University of London

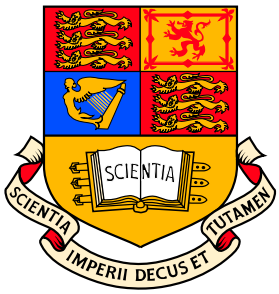

Imperial College of Science, Technology and Medicine

The Blackett Laboratory

Quantum Optics and Laser Science Group

Quantum Optics with a Single Trapped Ion

Hebe Frances Powell

Thesis submitted in partial fulfillment of the

requirements for the degree of

Doctor of Philosophy

of the

University of London

September 2002

To my parents.

Acknowledgements

I would like to thank my two supervisors, Dr. Daniel Segal and Dr. Richard Thompson, for their help and support during my time at Imperial College. I am grateful to Dr. Martijn Van Eikelenborg for his words of encouragement at difficult moments. Thanks also to my other colleagues in the Ion Trapping Group.

I am indebted to Dr Mike Damzen for many useful discussions and his kind advice during the writing of this thesis. I would also like to thank Laura Pennycuick for her invaluable friendship.

Special thanks to Ara Minassian, Graham and Kelly Verdi–Crofts, Sukee, Khalid and Aliki and all the other chaps for stress relief sessions at the bar!

Finally, I must thank my family for all of their patience and support throughout my studies.

I would like to acknowledge financial support from the Engineering and Physical Sciences Research Council.

Abstract

This thesis describes experiments carried out on small clouds and single ions of Magnesium confined in a Penning trap. The ions are laser cooled and observed by collection of resonance fluorescence from the cooling transition near 280 nm.

Initial work concentrated on the Quantum Zeno effect: the inhibition of the decay of an unstable system by frequent measurements. The experiment which was to have been completed involved a single $^{25}Mg^{+}$ ion. A theoretical overview of the phenomenon is given. The design and analysis of the trap intended for use in this investigation is presented.

The quantum jump statistics for the three stable isotopes of Mg^{+} have been studied experimentally. The average time which the ion spends fluorescing, 'on' time, was compared to the average time it spends in the dark state, 'off' time to find the *On to Off ratio*. For both $^{24}Mg^{+}$ and $^{26}Mg^{+}$ this value was found to be 16.0 $\pm$0.7, in agreement with a theoretical value of 16.0.

The presence of hyperfine structure in $^{25}Mg^{+}$ has two consequences. Firstly, while the jump rate for $^{24}Mg^{+}$ and $^{26}Mg^{+}$ remains unaltered for both available cooling transitions, for $^{25}Mg^{+}$ the on to off ratio is predicted as 11.8 and 22.8 for the lower and upper transitions respectively. The experimentally measured ratios were: 10.2 $\pm$1.5 and 22.0 $\pm$3. Secondly, is the appearance of *nuclear quantum jumps*. These jumps occur rarely, thus although the data indicate some evidence for nuclear jumps, no firm conclusions can be drawn due to the small number of events observed.

The first demonstration of the axialization of laser cooled ions in a Penning trap is reported. Axialization allows the coupling of the two radial modes present in the Penning trap, the cyclotron and magnetron motions. Laser cooling is enhanced, causing a substantial reduction in the radius of the magnetron motion. An ICCD camera was used to image the axialization process for the first time. For a single

ion the decrease of the magnetron amplitude corresponds to a reduction in ion temperature to an upper limit of order 10 mK.

The laser cooled, axialized system exhibits some interesting dynamics which depend critically on the axial drive frequency and amplitude. These were studied using a photon-photon correlation technique.

Contents

List of Tables

List of Figures

CHAPTER 1

Introduction

Bridging the gap between scientific theory and experimental reality presents enormous difficulties. Theorists have a habit of demanding highly idealised conditions: particles at rest, particles undisturbed by stray electomagnetic and gravitational fields, or simply single, isolated particles. None of these things are within our usual experience of The Possible. An easy solution to this problem would be to dismiss any theory requiring testing in conditions which do not occur in everyday reality; they are merely curiosities arising from taking certain principles to extremes. However, experimentalists are not easily beaten and have in the ion trap found an environment so nearly free from bothersome external influences that we can begin to test these extreme limits of fundamental theory.

As a research tool the ion trap is proving its worth in numerous fields. The high resolution enabled in the ion trap environment means that the main impact of the ion trap has been in the field of spectroscopy [1]. Ion traps are widely used in the field of frequency standards [2, 3]. A frequency standard is the base for a high precision clock, and indeed the construction of an ionic clock based on optical transitions in Yb^+ in an RF (radio frequency) trap is at the centre of much research at the National Physical Laboratory [4, 5]. The elecromagnetic trap has also permitted

increased accuracy in the measurement of atomic constants, such a the electronic g-value [6].

The precision of measurements made in ion traps is greatly improved if the trapped particles are cooled: storage time is increased and effects such as first order Doppler shifts are reduced. A technique which can be easily applied to damp motions over a broad frequency range is buffer gas cooling. This method is propagated by collisions between the trapped species and other colder atoms. For many applications buffer gas cooling is sufficient: micro-wave frequency standards have been made using buffer gas cooled Hg^+ ions [7]. However, cooling by means of collisions is not ideal as it can cause perturbations of the energy levels and leads to the loss of ions from the trap.

Laser cooling is often seen as the method of choice as sub–Kelvin temperatures and strong confinement are easy to achieve. Techniques such as Laser Raman cooling [22] and EIT (Electromagnetically Induced Transparency) cooling [23, 25] have enabled the cooling of ions to the motional ground state. The disadvantage of laser cooling is that it is only applicable to a limited number of ion species [2]. One way round this is to use "sympathetic cooling" where laser cooled ions are used to cool other particles. In this way even molecular ions may be cooled [12, 13]. Like buffer gas cooling, this method also works through collisions between particles, but is more effective than simple buffer gas cooling. Very low temperatures of sympathetically cooled particles have been demonstrated. In reference [14] a cloud of highly charged Xe^+ ions are sympathetically cooled (using $^9Be^+$) to the point of crystallization. Efficiency of cooling is best achieved by ensuring that only a small difference exists between the charge to mass ratios of the laser and sympathetically cooled species. In the case of isotopes of the same ion where only one isotope is directly laser cooled all are found to reach the same minimum temperature. This was demonstrated in [15] for the isotopes of Mg^+.

An interesting result of sympathetic cooling is that particles of different masses become spatially separated [16, 17]. In a combined trap (which uses a both static and RF electric fields plus the magnetic field) this phenomenon can be exploited to simultaneously trap particles of different masses and opposite charges. The confinement of both electrons and protons at the same time has been achieved in this way [18].

As methods for cooling trapped particles have improved, other areas of research have opened. The facility with which single ions can be trapped means that the quantum realm is well within access: the observation of phenomena such as quantum jumps (instantaneous atomic transitions) is one of the most celebrated successes of the ion trap. More recently ion traps have created a great deal of interest in the field of quantum information processing [3].

Strongly cooled trapped ions will become spatially ordered: crystallized. This phenomenon has been observed in both RF [17, 21] and Penning traps [22, 23]. The bcc structure of large ion crystals has been investigated using optical Bragg diffraction [24]. The localization of ions in a crystal is such that two laser cooled ions can act as coherent point sources in analogy with the classical Young's slits experiment. Two Hg^+ ions were investigated in this way and interference fringes were observed in the fluorescence emitted [25].

Low temperature and highly localized particles mean that long decoherence times are expected in ion traps. In this way it has been possible to observe purely quantum phenomena such as entanglement [26]. From their motional ground state, ions can be coherently manipulated enabling the development of usable "quantum" logic gates [27–29].

The RF trap is probably considered the most adaptable for use in quantum information processing. In such traps it is relatively easy to reach the Lamb–Dicke regime and the Linear RF trap can be used to prepare strings of ions allowing for

the addressing of individual ions. The complex motion of ions within a Penning trap would make this a more difficult, yet there is no fundamental reason why a Penning trap could not be used instead.

The properties of the Penning trap mean that the ion/trap system is in itself quite interesting. Ions confined within the trap can be considered as a non-neutral plasma, the properties of which are determined by the plasma density and trapping voltages. The ion cloud shape, density and rotation frequency, the static properties of the plasma, have been investigated in detail principally at NIST [1]. The dynamic properties of Penning trap plasmas and single ions in a Penning trap are also well studied [22, 32, 33] the detection of ion motional frequencies being the basis of many spectroscopic techniques [8] and the reduction of their amplitude being essential in others [35].

The interest of this thesis lies in the use of Penning traps for the investigation of quantum phenomena. The key to this is the development of techniques which improve the trapping regime within the Penning trap: specifically increasing the efficiency of laser cooling.

The original focus of the work described in this thesis was an investigation of the quantum Zeno effect, involving a single ion confined in a Penning trap. The phenomenon arises from the strangeness of the measurement process in quantum mechanics: how to describe the interaction between a microscopic quantum system and a macroscopic measuring instrument.

The experiment at Imperial college has been through many alterations and reincarnations. The Zeno effect can be investigated by the measurement of a driven atomic transition. The atomic system upon which our experiment is based is provided by a single trapped magnesium ion.

The main body of the thesis begins in Chapter 2 which is in two parts. The first part contains a brief overview of the principles behind the Penning trap and the

dynamics of the trapped particles. In the second part laser cooling is discussed with particular reference to the problems of cooling the complex ion motion in a Penning trap.

Chapter 3 contains a discussion of the quantum Zeno effect. The problems of measurement in quantum theory are set out and the ideas of interaction free measurement and the wavefunction collapse are introduced. There follows a summary of earlier experimental work completed on the Zeno phenomenon and the controversy produced. To end the chapter the experiment proposed at Imperial college is outlined.

The special considerations for the quantum Zeno experiment are discussed in Chapter 4. The experiments described in this thesis were completed in two different systems: one based around a conventional electromagnet and the other based around a superconducting magnet. The advantages of both systems are discussed. Peripheral systems such as the laser and data collection software and hardware are also described.

What could be termed the system characterization is described in Chapter 5. A detailed experimental examination of the quantum jump statistics of Mg^+ was carried out. Particular problems of trapping single ions and specific isotopes were investigated. The conclusions of this study were important in furthering the quantum Zeno experiment.

Chapter 6 explores the problems of laser cooling in the Penning trap. In particular, an experimental technique known as axialization is described. Axialization enables the elimination of one of the two types of radial motion present in the Penning trap (the magnetron motion) thereby increasing the laser cooling efficiency for the trapped ions. The method is demonstrated to work and the minimum temperatures achieved are measured. The process of axialization generally improves the stability of the trapped ions and it was hoped that its implementation might increase

the chances of completing the Zeno experiment successfully.

Due to unforseen circumstances (multiple breakages of vital equipment) the Zeno experiment was not completed. The final Chapter draws together all the results and produces some conclusions. Suggestions for the improvement of the system and future direction are discussed briefly.

References

[1] D. J. Wineland, *Precision Measurement and Fundamental Constants II.* **Spec. Publ. 617**, 83 (1984)

[2] J. J. Bollinger, J. D. Prestage, W. M. Itano and D. J. Wineland, *Phys. Rev. Lett.* **54**, (1985)

[3] J. J. Bollinger, D. J. Heinzen, W. M. Itano, S. L. Gilbert and D. J. Wineland, *IEEE Tran. Instrum. Meas.* **40**, 126 (1991)

[4] P. Taylor, S. V. Gateva-Kostova, R. B. M. Clarke, G. P. Barwood, W. R. C. Rowley and P. Gill, *Phys. Rev. A.* **56**, 2699 (1997)

[5] M. Roberts, P. Taylor, S. V. Gateva-Kostova, R. B. M. Clarke, W. R. C. Rowley and P. Gill, *Phys. Rev. A.* **60**, 2867 (1999)

[6] R. S. Van Dyck Jr., P. B. Schwinberg and H. G. Dehmelt, *Phys. Rev. Lett.* **59**, 26 (1987)

[7] L. S. Cutler, C. A. Flory, R. P. Giffard and M. D. McGuire, *Appl. Phys.* **B39**, 251 (1986)

[8] C. Monroe, D.M. Meekhof, B. E. King, S. R. Jefferts, W. M. Itano and D. J. Wineland, *Phys. Rev. Lett.* **75** , 4011 (1995)

[9] G. Morigi, J. Eschner, C. H. Keitel, *Phys Rev Lett.* **85**, 4458 (2000)

[10] C. F. Roos, D. Leibfried, A. Mundt, F. Schmidt-Kaler, J. Eschner and R. Blatt *Phys. Rev. Lett.* **85**, 5547 (2000)

[11] R. C. Thompson, *Adv. Atom. Molec. Phys.* **3**, 53 (1993)

[12] T. Baba and I. Waki, *Jpn. J. Appl. Phys.* **35**, 1134 (1996)

[13] M. A. Van Eijkelenborg, M. E. M. Storkey, D. M. Segal and R. C. Thompson, Phys. Rev. A, **60**, 3903 (1999)

[14] L.Gruber, J. P. Holder, J. Steiger, B. R. Beck, H. E. De Witt, J. Glassman, J. W. McDonald, D. A. Church and D. Schneider, *Phys. Rev. Lett.* **86**, 636 (2001)

[15] R. E. Drullinger, D. J. Wineland and J. C. Berquist, *Appl. Phys.* **22**, 365 (1980)

[16] D. J. Larson, J. C. Berquist, J. J. Bollinger, W. M. Itano and D. J. Wineland, *Phys. Rev. Lett.* **57**, 70 (1986)

[17] H. Imajo, K. Hayasaka, R. Ohmukai, U. Tanaka, M. Watanabe and S. Urabe, *Phys. Rev. A.* **53**, 122 (1996)

[18] J. Walz, S. B. Ross, C. Zimmermann, L. Ricci, M. Prevedilli and T. W. Hänsch, *Phys. Rev. Lett.* **75**, 3257 (1995)

[19] J. I. Cirac, P. Zoller, *Phys. Rev. Lett.* **74**, 4091 (1995)

[20] D. J. Wineland, J. C. Berquist, W. M. Itano, W. M. Bollinger and C. H. Manney, *Phys. Rev. Lett.* **59**, 2935 (1987)

[21] F. Diedrich and H. Walther, *Phys. Rev. Lett.* **59**, 2931 (1987)

[22] L. R Brewer, J. D. Prestage, J. J. Bollinger, W. M. Itano and D. J. Wineland, *Strongly Coupled Plasma Physics*, Plenum, **53** (1996)

[23] J. N. Tan, J. J. Bollinger, B. Jelenkovic and D. J. Wineland, *Phys. Rev. Lett.* **75**, 4198 (1995)

[24] W. Itano, J. J. Bollinger, J. N. Tan, B. Jelenkovic, X.-P. Huang and D. J. Wineland, *Science*, **279**, 686 (1998)

[25] U. Eichmann, J.C. Berquist, J. J. Bollinger, J. M. Gillingan, W. M. Itano and D. J. Wineland, *Phys. Rev. Lett.* **70**, 2359 (1993)

[26] C. A. Sackett, D. Kielpinsky, B. E. King, C. Langer, V. Meyer, C. J. Myatt, M. Rowe, Q. A. Turchette, W. M. Itano, D. J. Wineland, C. Monroe, *Nature* **406**, 256 (2000)

[27] C. Monroe, D. M. Meekhof, B. E. King, W. Itano, D. J. Wineland, *Phys. Rev. Lett.* **75**, 4714 (1995)

[28] Ch. Roos, Th. Zeiger, H. Rohde, H. C. Nagerl, J. Eschner, D. Leibfried, F. Schmidt-Kaler and R. Blatt, *Phys. Rev. Lett.* **83** , 4713 (1999)

[29] S. Schneider, D. F. V. James, G. J. Milburn, *J. Mod. Opt.* **47**, 499 (2000)

[30] L. R Brewer, J. D. Prestage, J. J. Bollinger, W. M. Itano, D. J. Larson and D. J. Wineland, *Phys. Rev. A.* **38**, 859 (1988)

[31] J. J. Bollinger, D. J. Heinzen, F. L. Moore, W. M. Itano and D. J. Wineland, *Phys. Rev. A.* **48**, 525 (1993)

[32] R. C. Thompson, D. C. Wilson, *Z. Phys. D.* **42**, 271 (1997)

[33] G. Zs. K. Horvath, J-L. Hernandez-Pozos, K. Dholakia, J. Rink, D. M. Segal and R. C. Thompson, *Phys. Rev. A.* **57**, 1944 (1998)

[34] L. Schweikhard and A. Marshall, *J. Am. Mass Spectrom.*, **4**, 433 (1993)

[35] R. C. Thompson, K. Dholakia, G. Zs. K. Horvath, W. Power and D. M. Segal, *J. Mod. Opt.* **41**, 1087 (1994)

CHAPTER 2

Ion Trapping in a Penning Trap

The introduction sought to demonstrate the importance of the ion trap as a tool in research physics. The Penning trap will now be looked at in detail: how this type of trap works and how ions can be laser cooled within it. The particular features of traps used in experiments described in the thesis are discussed later.

2.1 The Penning Trap

Earnshaw's theorem tells us that it is impossible to create a fully three dimensional electrostatic potential well in free space. This is a problem, but fortunately there are ways to overcome it. The starting point of any ion trap is the generation of a cylindrically symmetric quadrupole electric potential. Three electrodes of hyperbolic cross-section can be used for this purpose: two end-caps and a ring, as shown in figure 2.1. This configuration generates a saddle shaped potential of the form:

$$V_T(x, y, z) = \frac{U_0}{(R_0^2)}(2z^2 - x^2 - y^2) \tag{2.1}$$

where $R_0^2 = (2z_0^2 + r_0^2)$. This produces confinement along the the central z-axis of the trap.

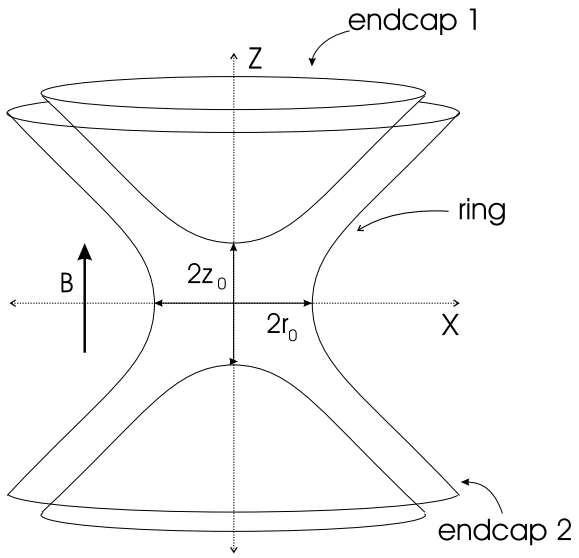

Fig. 2.1: A schematic diagram of a quadrupole ion trap.

To prevent the escape of particles in the unrestricted direction there are two options. A radio frequency (RF) field can be applied to one set of electrodes, this periodically (at the RF frequency) inverts the saddle point potential to make a Paul trap. Alternatively the trap can be placed in a static magnetic field, $\mathbf{B} = \mathbf{B_0}\hat{\mathbf{z}}$, with the trap oriented such that the magnetic field lines are directed along the z-axis: a Penning trap.

2.1.1 The Motion of Single Ions in a Penning Trap

The combined use of electric and magnetic fields produces complex motion of particles within the Penning trap. The electric saddle potential forms a one dimensional harmonic well in the axial direction resulting in simple harmonic motion along the z-axis. In the radial plane, however the magnetic confinement gives rise to two superimposed circular orbits: the modified cyclotron and magnetron motions. The first of these constitutes a small amplitude perturbed cyclotron rotation, where the pure cyclotron angular frequency is $\omega_c = eB/m$. The second arises due to the

velocity filter effect of the crossed electric and magnetic fields. Often termed the $\mathbf{E}\times\mathbf{B}$ drift it causes a slow precession of the modified cyclotron orbit about the trap centre.

Considering the forces acting in a Penning trap on a single particle of charge q and mass m, it is possible to derive equations of motion for that particle. The electrostatic potential has the form described by equation 2.1, while the magnetic field is uniform and directed along the z-axis: $\vec{B} = B_0\hat{z}$. The force on a charged particle resulting from the electric field is $\vec{F_E} = q\vec{E}$ (with $\vec{E} = -\nabla V$) and that resulting from the magnetic field is $\vec{F_M} = q\vec{v} \times \vec{B}$. The total force on the ion is the sum of these:

$$\begin{aligned} \vec{F_T} &= \vec{F_E} + \vec{F_M} \\ &= -q\nabla V + q\vec{v} \times \vec{B} \end{aligned} \tag{2.2}$$

Working this through and separating the variables, the equations of motion are:

$$\ddot{x} = \frac{2eU_0}{mR_0^2}x + \frac{eB}{m}\dot{y} \tag{2.3}$$

$$\ddot{y} = \frac{2eU_0}{mR_0^2}y - \frac{eB}{m}\dot{x} \tag{2.4}$$

$$\ddot{z} = -\frac{4eU_0}{mR_0^2}z \tag{2.5}$$

where $R_0^2 = r_0^2 + 2z_0^2$ (see diagram 2.1). The charge and mass of the trapped particles are e and m respectively. For particles with a positive charge, a negative trapping potential, U_0 is required. Following from equation 2.5, the simple harmonic motion in the z-direction will have a characteristic angular frequency, ω_z given by:

$$\omega_z = \sqrt{\frac{4eU_0}{mR_0^2}} \tag{2.6}$$

To examine motion in the radial plane it is convenient to decouple the x and y motions. This can be done by transforming to a frame of reference which rotates at half the cyclotron frequency, that is $\omega_c/2$. In this frame the magnetic field is effectively zero. This gives new expressions for the equations of motion in the radial plane:

$$\ddot{x} = (\omega_z^2/2 - \omega_c^2/4)x \tag{2.7}$$

$$\ddot{y} = (\omega_z^2/2 - \omega_c^2/4)y \tag{2.8}$$

The x and y motions can now be described as simple harmonic motion at an angular frequency of:

$$\omega_1 = \sqrt{(\omega_z^2/2 - \omega_c^2/4)} \tag{2.9}$$

These two simple harmonic motions through the origin can be expressed as the sum of two equal amplitude circular motions: one in the clockwise sense and one in the anti-clockwise sense, both at ω_1, about the origin. These correspond directly to motions in the laboratory frame: the modified cyclotron, at angular frequency, ω_c', and the magnetron at angular frequency, ω_m.

$$\omega_c' = \frac{\omega_c}{2} + \omega_1 \tag{2.10}$$

$$\omega_m = \frac{\omega_c}{2} - \omega_1 \tag{2.11}$$

Under normal working conditions the motion in the trap combines a large radius magnetron motion and a small radius modified cyclotron orbit. In the rotating frame this manifests itself as an elliptical orbit: the addition of a large amplitude (r_m) orbit at $-\omega_1$ and a small amplitude (r_c) orbit at $+\omega_1$. Diagram 2.2 shows what this looks like in each frame.

It is apparent that all the motional frequencies, apart from the cyclotron fre-

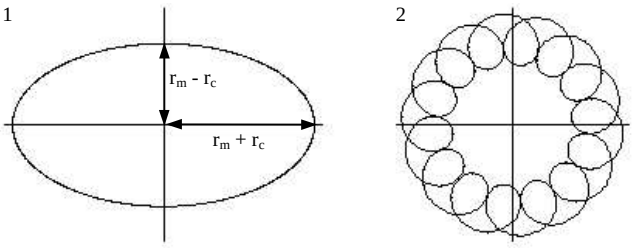

Fig. 2.2: On the left the form of ion motion in the rotational frame is shown. On the right the is the equivalent motion in the lab frame.

quency, ω_c, are dependent upon the trapping voltage. It should be noted that the sum of the magnetron and modified cyclotron frequencies is always equal to the true cyclotron frequency, $\omega_c = eB/m$.

The relationships between the motional frequencies impose limits upon the stability of the trap. If $\omega_z^2/2 > \omega_c^2/4$ then equation 2.9 has no real solutions. This implies that at voltages for which this condition would apply, the trap no longer functions. From figure 2.3, it is possible to see that for the trap modelled, and using magnesium ions, the trapping voltage must be no greater than 24 V. In practice, the limit for stability is at a slightly lower voltage. Knowledge of the limit on trap stability for the trapped ion species is useful. The mass dependence of ω_z means that equation 2.9 becomes unsovable at a lower voltage for particles of large mass than for those of small mass. The process of loading ions into the trap often results in the production of ions other than those which we intend to trap. Heavier impurity ions can be cleaned from the trap by raising the trapping voltage near to the stability limit for the desired species. The removal of heavier particles and the resulting decrease in the incidence of collisions within the trap improves storage lifetime and the cooling efficiency.

Figure 2.3 shows the voltage dependence of the motional frequencies for magnesium trapped in the "split-ring" trap (which is described in Chapter 4).

It is clear that as the trapping parameters are varied, specifically the relative

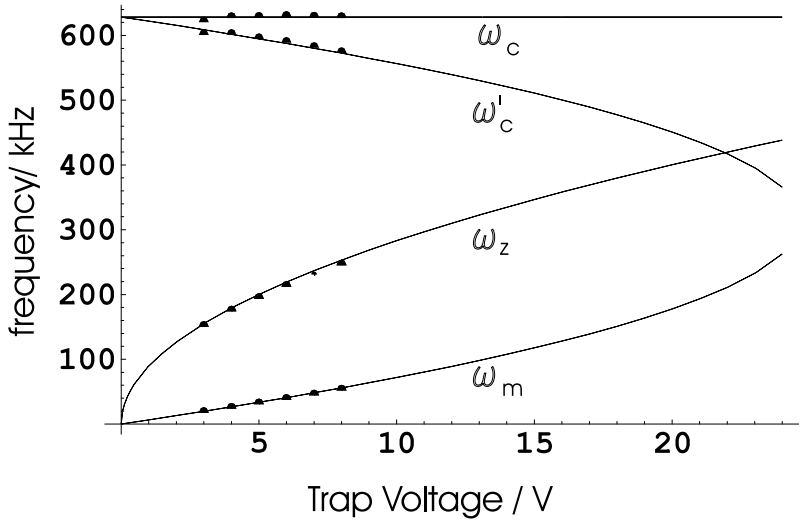

Fig. 2.3: A graph showing how motional frequencies of ions in a Penning trap alter with trap potential. Some experimental points for the split-ring trap are shown.

magnitude of the electric and magnetic fields, the *shape* of the trapping potential will alter. This can be understood by considering the relative amplitudes of the various ion oscillations within the trap under different trapping conditions. Assuming that thermal equilibrium exists between the axial and radial modes (these will be coupled by ion-ion collisions), then by altering say, the trap voltage it is possible to change the amplitude of the oscillatory motion. There are two extremes for the shape of the trap potential. At low trap voltages, axial confinement is weak in comparison to the radial confinement which means that the axial motion increases in amplitude (a pencil like trap potential). In the case where the trapping voltage is strong, an ion would be forced into larger radial orbits (a pancake like trap potential). On a practical level, it is desirable to have a nearly spherical potential as overlap between the ion trajectory within the trapping volume and the laser cooling beam is greatest under these conditions. Where more than one ion is present, the cloud shape is ultimately determined by the *plasma rotation frequency* (see section 2.1.2) and not by the shape of the trap potential. However, the trap potential does have

an influence on the cloud shape and it is generally true that greatest stability is obtained when the trap potential is spherical.

To determine the conditions for which the trapping potential is spherical is quite simple. It is again convenient to transform to a frame of reference rotating at $\omega_c/2$. In this frame the radial orbit is elliptical and can be described by the equations:

$$\ddot{x} = -\omega_1^2 \dot{y} \quad \text{and} \quad \ddot{y} = -\omega_1^2 \dot{y} \tag{2.12}$$

The axial motion is still described by equation 2.5. In thermal equilibrium, the potential is spherical when the axial oscillation frequency is equal to that of the radial motion in the rotating frame. It can then be shown that:

$$\begin{aligned} \omega_z^2 &= \omega_1^2 \\ \omega_z^2 &= \omega_c^2/6 \end{aligned} \tag{2.13}$$

Thus we can work out the value of U_0 required to give a spherical potential in a particular trap for any ion species.

2.1.2 The Plasma Description.

In the case where more than one ion is present in the trap a term describing the coulomb interaction between the ions must be added to the equations of motion. In general the total electrostatic potential present will be the sum of the trapping potential, any potential due to induced charges on the electrodes (contact potential) and the space charge potential. The analysis of plasma dynamics is complex. The effect of space charge is to quantitatively alter the dynamics of an ion cloud, the magnitude of these effects is largely dependent upon the density of the cloud. It is helpful if it can be assumed that we are dealing with a plasma of uniform density.

In the case of a laser cooled ion cloud this is generally true, however to assess the validity of this assumption we must define certain parameters, in particular the Debye wavelength, λ_D of the system. This is the distance over which the plasma density falls from its maximum to zero at the edge of the cloud:

$$\lambda_D = \left[\frac{\epsilon_0 kT}{n_0 e^2}\right] \tag{2.14}$$

where ϵ_0 is the electric permittivity of the vacuum and n_0 is the ion density. If the plasma can be described as having uniform density it should have a very sharply defined boundary such that $\lambda_D \ll$(plasma dimensions). This condition is true except where the ion cloud is crystalline, in which case the density of the cloud is not constant over distances comparable to $n_0^{-1/3}$. In general a plasma may be treated as having constant density if the inter-ion spacing is small compared to the plasma dimensions, which must be so for any cloud where the number of ions present > 1 (regardless of any structure within the ion cloud).

The ion density within the plasma is calculated as:

$$n_0 = \frac{2\epsilon_0 m\omega_r(\omega_c - \omega_r)}{e^2} \tag{2.15}$$

This is related to the plasma frequency ω_p by:

$$\omega_p^2 = 2\omega_r(\omega_c - \omega_r) \tag{2.16}$$

where, ω_r is the plasma rotation frequency (this is equivalent to the magnetron rotation for 1 ion). The plasma rotation frequency is independent of radius and is a rigid, uniform rotation of the entire cloud. From these relationships it can be seen that the ion density within the cloud is related to the plasma rotation frequency. The temperature will have very little effect on the volume of the plasma except in

that it affects the Debye wavelength: a hot plasma will have a very diffuse boundary and may have a large volume for this reason.

The space charge potential is an ellipsoid of revolution and has the following form:

$$V_I(r,z) = \frac{m\omega_p^2}{6e}[a(\alpha)r^2 + b(\alpha)z^2] \tag{2.17}$$

here α is the aspect ratio (the shape) of the ion cloud. If z_p and r_p are the axial and radial extent of the plasma, then $\alpha = z_p/r_p$. Poisson's equation requires that:

$$2a(\alpha) + b(\alpha) \quad = 3 \quad \text{where} \quad b(\alpha) \quad = Q_1^0 \frac{\alpha/(\alpha^2-1)^{1/2}}{(\alpha^2-1)} \tag{2.18}$$

here Q_1^0 is an associated Legendre function of the second kind [1].

The cloud aspect ratio is related to the cloud oscillation frequencies in the following way:

$$\frac{\omega_z^2}{\omega_p^2} = Q_1^0\left[\frac{\alpha}{(\alpha^2-1)^{1/2}}\right]/(\alpha^2-1) \tag{2.19}$$

This combined with the ω_p dependence reflect the effect of the plasma density on the behaviour of the system.

If the cloud is under constant trapping conditions, i.e trap voltage, magnetic field and the number of ions are left unchanged, then an equilibrium density should exist. It has been shown that density equilibria are allowed if $\omega_z < \omega_c/\sqrt{2}$, $\omega_m < \omega_r < \omega_c'$ [2]. A minimum density occurs for $\omega_r \gtrsim \omega_m$. The cloud aspect ratio will approach zero in this regime, which means that it will be pancake like. If the cloud rotation frequency is reduced further such that $\omega_r \to \omega_m$, the aspect ratio decreases; the radius of the cloud will expand outwards becoming infinitely thin in the z direction. Increasing ω_r on the other hand, has the effect of increasing the plasma aspect ratio by reduction of the cloud radius and a corresponding increase of cloud size in the z dimension. When the maximum aspect ratio is reached, the cloud is stretched

out along the axial direction. From equation 6.19, the maximum cloud density is obtained when $\omega_r = \omega_c/2$. In a frame of reference which rotates with the cloud we would normally expect to see the motion of individual ions consisting of circular orbits (modified cyclotron rotation). When the plasma rotation frequency reaches $\omega_c/2$ we find that the trajectories of the ions are transformed into straight lines. This is termed Brillouin flow and is comparable to the behaviour expected of an unmagnetized plasma. The situation is equivalent to the transformation to a frame of reference rotating at $\omega_c/2$, here the magnetic field is effectively zero, enabling the decoupling of radial modes of motion (see section 2.1.1).

The appearance of new motional frequencies is not unexpected. Compared to the single ion case, as well as centre of mass motion it is now possible to have relative motions between the ions. These relative motions result in not only rotation but vibration of the cloud. At Brillouin flow, for example the cloud rotation is accompanied by a vibrational breathing mode (at $\sqrt{3}\omega_1$). It can be shown that in the case of rotational motion, the relative and centre of mass oscillations have very similar form. A centre of mass motion for a cloud will have the same frequency as for the corresponding single ion motion. The frequencies of the relative motions, however, will be charge shifted to slightly higher values depending upon the density of the ion cloud. An investigation of this phenomenon, where the relative motions are studied using the photon-photon correlation technique, is contained in reference [23]. A more detailed analysis of the plasma modes which can be excited is contained in reference [22].

The relevant plasma parameters can be calculated for magnesium, to give minimum and maximum densities of $n_0(min)$= 4.4×10^{13} ions/m^3 and $n_0(max)$= 1.1×10^{14} ions/m^3 with corresponding Debye lengths of 1.04×10^{-5} m and 6.3×10^{-6} m (at around T = 1 K). In this thesis it is generally only single ions which are considered. At the level of 5-10 ions (see ICCD images in Chapter 6) the cloud dimensions are

only an order of magnitude greater than the Debye length. Even though the conditions for a uniform density plasma are still upheld it is clear that with so few ions single particle affects will begin to predominate over plasma effects. In this limit it is more appropriate to describe the ion dynamics in terms of the normal modes of motion for ions in a Penning trap. The motion of small numbers of ions in a Penning trap is discussed in reference [1].

2.2 Cooling Using Light

The cooling of trapped particles is of great importance. It not only increases storage times and improves precision measurements, but also allows for the observation of such phenomena as crystallization of the ion cloud which will only occur at very low temperature. Although there exist many techniques for cooling particles in an ion trap [6] one of the most effective is laser cooling.

The basic principle behind cooling using radiation pressure has quite a long history. When photons are scattered by atoms, momentum is transferred from the photons to the atoms. If we assume that the photons have an initially preferred direction but that those scattered by atoms are emitted in random directions, then it is clear that photons could be used to give a momentum kick in the preferred direction. The effect of this *scattering force* was first reported by O. Frisch [7] who used incoherent light from a sodium vapour lamp to deflect a beam of sodium atoms. Some twenty years later, A. Kastler [8] proposed the use of resonant light for cooling.

The first proposals for laser cooling of trapped particles date from 1975. Wineland and Dehmelt published proposals for the cooling of ions simultaneously with those of Hänsch and Schawlow for the cooling of neutral atoms [9, 10].

The process of laser cooling is in many ways analogous to that of optical pumping,

although in the former case we are seeking to pump the ion into lower motional energy levels rather than an electronic ground state. Bearing this in mind one requirement for laser cooling is that we have a closed two level atomic system. It must be possible to excite the ion from some state $|1\rangle$ into some other state $|2\rangle$ from which a single possible decay route returns the ion to $|1\rangle$. Such systems are non-existent, however there are a number of ions which can make serviceable approximations [2]. Magnesium ions in a Penning trap are an example of such a system: using the $2S_{1/2} \rightarrow 2P_{3/2}$, which is a strongly allowed dipole transition, the closed system is formed using σ-transitions ($\Delta m_J = \pm 1$). Other ions are not quite so simple requiring the use of additional lasers to address other transitions in order to maintain a closed loop. The cooling of ions is further complicated as suitable transitions are generally in the ultra violet range of the spectrum for which tunable laser sources do not exist.

2.3 The Cooling of a Free Particle

Let us now take a closer look at the physical picture of laser cooling [12]. Imagine an atom travelling in free space at a velocity v_a. These atoms possessing a ground and an excited state separated by an energy of $E_a = \hbar\omega_a$ are irradiated using a laser beam of frequency ω_l propagating in a direction opposed to that of the atom. In order for the atom to interact with the laser light, the laser frequency must be tuned just below that of the atomic absorption line such that: $v_a = (\omega_a - \omega_l)/k$ (where k is the modulus of the laser wave vector). The velocity of the atom means that the Doppler shift brings the laser light into resonance with the atomic transition which allows the atom to absorb one of the oncoming photons. This process increases the atom momentum by $\hbar\vec{k_l}$. Some time later the photon is re-emitted in some random direction (scattering). The atom momentum is altered

by re-emission, but the random nature of this spontaneous process means that the average change in momentum over many such events is zero. In this way the average change in momentum experienced by the atom in one *absorption + emission* cycle is $\hbar\vec{k_l}$ in the direction of laser propagation. As a result, the atoms experience a net force opposing their motion which over many cycles slows them down. If we assume that the atomic transition is strongly saturated then the force on the atoms may by expressed thus:

$$F_{max} = \hbar k_l \frac{\Gamma}{2} \tag{2.20}$$

where Γ= the natural linewidth of the transition.

If the laser photons and atoms moving in the same direction were to interact, then the net force experienced by the atoms would of course increase their velocity. Doppler cooling has an in-built asymmetry which prevents this "heating" from occurring. Just as atoms against the direction of laser propagation see the light Doppler shifted into resonance, those moving *away* see it red-shifted further to the low side of the absorption line. In this case scattering is greatly diminished. For a cloud of atoms moving with random velocities one laser beam can only cool one motional degree of freedom.

The residual heating effects due to recoil have so far been ignored. In the emission process the average change in momentum is zero, however the atom performs a random walk in momentum space since there is in fact a finite momentum transfer of $\hbar\vec{k_l}$ at each emission event (the rms value of momentum change is non-zero). The recoil energy can then be calculated as $R = (\hbar\vec{k_l})^2/2m$ (where m is the atomic mass). This is the kinetic energy which an atom initially at rest would gain/lose on the absorption/emission of a photon and it is a fundamental factor in limiting the minimum temperature attainable.

2.4 The Cooling of Trapped Particles

The problem of laser cooling trapped particles is well discussed in the literature, the most complete descriptions can be found in references [4, 12, 14].

If we consider a particle trapped in a harmonic well it is immediately possible to identify important differences between this case and that of a free particle: that is that the particle now has characteristic motional frequencies. Assuming that the particle is confined in a three dimensional well then it will posses three characteristic angular frequencies, ω_x, ω_y and ω_z. Let us consider the z direction only and assume that we are dealing with a two level ion for which the difference in energy between the ground and excited states is $\hbar\omega_0$. The rate at which the excited state decays to ground is Γ.

The harmonic motion of the trapped ion means that both the laser field as seen by the ion and the light emitted by the ion will be frequency modulated at the characteristic frequency ω_z. This means that side bands are present on the absorption spectrum of the ion. There exist two possible regimes: the weak binding limit and the strong binding limit. In the first instance $\omega_z < \Gamma$, and the optical side bands are unresolved. In the second instance $\omega_z > \Gamma$ and the optical side bands *are* resolved: the absorption spectrum of the ions is not continuous.

2.4.1 The Doppler Cooling Limit

The weak binding limit is the one which prevails in the experiments carried out for this study, so it shall be dealt with in detail. In a typical case where $^{24}Mg^{+}$ is confined in a Penning trap at 1T the axial motion is at $\omega_z \sim 200$ kHz, while $\Gamma = 43$ MHz (this being much less than the Zeeman splitting at such a field, which for the ground state, is equal to 28 GHz).

In this limit the ion may be treated essentially as if it were a free particle: the

axial oscillation brings the ion in and out of resonance with the laser light much more slowly than the time it takes for a photon to be absorbed and re-emitted. The following simple calculations can be used to obtain expressions describing laser cooling and ultimately find a minimum reachable temperature using Doppler Cooling.

Using the principles of energy and momentum conservation we can analyze a scattering event in which the ion travelling at a velocity v absorbs a photon from the laser beam [4, 12]:

$$m\vec{v'} = m\vec{v} + \hbar\vec{k_l} \tag{2.21}$$

$$\frac{1}{2}m\vec{v'}^2 + \hbar\omega_0 = \frac{1}{2}m\vec{v}^2 + \hbar\omega_l \tag{2.22}$$

where $\vec{v'}$ is the velocity of the ion after absorption. From equation 2.21 we find an expression for the difference of the squares of the ion velocity before and after absorption. This equation can be substituted into equation 2.22 to give:

$$\hbar\omega_l = \hbar\omega_0 + \frac{\hbar k_l}{2}(\vec{v'} + \vec{v}) \tag{2.23}$$

Looking first at the *absorption* process and returning to equation 2.21, everything can be expressed in terms of the ion initial velocity, $\vec{v}$:

$$\hbar\omega_l = \hbar\omega_0 + \hbar\vec{k_l}(\vec{v} + \frac{\hbar\vec{k_l}}{2m}) \tag{2.24}$$

The definition for R, the recoil energy is $R = (\hbar\vec{k_l})^2/2m$, thus:

$$\hbar\omega_l = \hbar\omega_0 + \hbar\vec{k_l} \cdot \vec{v} + R \tag{2.25}$$

The emission process can be treated in a similar way, expressing equation 2.21 in

terms of $\vec{v'}$, to give the following equation for the energy of the *emitted* photon:

$$\hbar\omega_e = \hbar\omega_0 + \hbar\vec{k_e} \cdot \vec{v'} - R \tag{2.26}$$

Taking the difference between equations 2.25 and 2.26 and averaging over the distribution of scattered photons ($\vec{k_e}$) we obtain an expression for the mean change in energy per *absorption + emission* cycle.

$$\langle \Delta E_k \rangle_{\vec{k_e}} = 2R + \hbar\vec{k_l} \cdot \vec{v} \tag{2.27}$$

This equation shows that there is cooling only if $\hbar\vec{k_l} \cdot \vec{v_a} < -2R$, otherwise the atom will experience an increase in kinetic energy. This means that only atoms with velocities opposing the laser beam propagation will be slowed.

The variation in kinetic energy per Cartesian degree of freedom can be calculated as:

$$\begin{aligned} \Delta E_i &= \frac{1}{2}mv_i^2 - \frac{1}{2}m(v')_i^2 && (2.28)\\ &= \frac{\hbar^2(k_i - k_{si})^2}{2m} + \hbar(k_i - k_{si})v_i && (2.29)\\ &= R(\hat{k_i}^2 - 2\hat{k_i}^2\hat{k_{si}}^2 + \hat{k_{si}}^2) + \hbar(k_i - k_{si})v_i && (2.30) \end{aligned}$$

where $i = x, y, z$ and the subscript, s, refers to the scattering process. It has been assumed that $k \sim k_s$.

Considering the angular distribution of the scattered photons. This depends on the orientation of the electric dipole moment for the transition with respect to the magnetic field. The probability of a photon being emitted into a solid angle $d\Omega$ in the direction $\hat{k_s}$ for a $\Delta M = \pm 1$ transition such as that used for laser cooling Mg^+

(M is the eigenvalue of the total angular momentum in the $\hat{B}$ direction) is:

$$P_s(\hat{k_s})d\Omega = \frac{3}{16\pi}(1+\cos^2\theta_s)d\Omega \tag{2.31}$$

where θ_s is defined relative to the direction of the magnetic field lines: $\hat{B}\hat{k_s} = \cos\theta_s$. The integral $\int P_s(\hat{k_s})d\Omega$ is normalized to 1.

Assuming the value of P_s is known, then equation 2.30 can be averaged over all angles of scattered photon:

$$\begin{aligned} \langle \Delta E_i \rangle_s &= \int_{\hat{k_s}} P_s(\hat{k_s})\Delta E_i d\Omega \\ &= R(f_i + f_{si}) + \hbar k_i v_i \end{aligned} \tag{2.32}$$

with

$$f_{si} \equiv \int P_s(\hat{k_{si}})\hat{k_{si}}^2 \tag{2.33}$$

and

$$f_i \equiv \hat{k_i}^2 \tag{2.34}$$

Equation 2.33 has a value of 1/3 in the case of isotropic scattering [4].

The average rate of change in energy is given by the product of the scattering rate γ_s and the average energy change per scattering event. The scattering rate itself is equal to the number of photons per unit area per unit time multiplied by the absorption cross section for photons of a particular polarization and propagation direction. If I is the energy flux of the incoming laser light and is equal to $c|E_0|^2/8\pi$ W/m^2, then the number of photons present is $I/\hbar\omega$. For atoms travelling at a particular velocity the absorption cross section, $\sigma(\omega, \vec{v})$ can be determined using

perturbation theory (in the case where $I <$ saturation intensity) [12].

$$\sigma(\omega, \vec{v}) = \frac{\sigma_0(\Gamma/2)^2}{[(\omega_0 + \vec{k} \cdot \vec{v} + \frac{R}{\hbar} - \omega)^2 + (\Gamma/2)^2]} \tag{2.35}$$

where $\sigma_0 = 6\pi \lambda\!\!\!^{-2}_0 |\hat{\epsilon} \cdot \hat{d_{eg}}|^2$, $\lambda\!\!\!^{-}_0 = c/\omega_0$. In this expression, ϵ is the polarization of the incident light and d_{eg} is the electric dipole moment of the transition. For the laser cooling transition in Magnesium, $2S_{1/2} \rightarrow 2P_{3/2}$, the value of $\sigma_0 = 3\pi \lambda\!\!\!^{-2}_0$ [4].

The Doppler cooling limit can be found using energy rate equations. Let us take the simplest case of cooling simple harmonic motion along the z-axis using a single laser beam directed along that axis. Motion in the radial plane shall, for the moment be ignored. The rate of change in energy in the z direction can be expressed as follows:

$$\frac{dE_z}{dt} = (\frac{I}{\hbar\omega})\langle\sigma(\omega, \vec{v})[\hbar k v_z + R(1 + f_{sz})]\rangle_v \tag{2.36}$$

In accordance with the principle of laser cooling, in the case of negative laser detuning ($\omega < \omega_0 + R/\hbar \simeq \omega_0$), $\sigma(\omega, \vec{v})$ is larger for negative v_z than for positive v_z until very low temperatures are reached. If the system has already undergone some degree of cooling, such that the Doppler broadening is much less than the natural linewidth and the detuning ($k(v_z)_{rms} \ll \Gamma/2$ and $k(v_z)_{rms} \ll (\omega_0 + (R/\hbar) - \omega)$) then equation 2.4.1 can be approximated using the following expansion evaluated for $v_z \rightarrow 0$:

$$\sigma(\omega, \vec{v}) = \sigma(\omega, v_z) + \vec{v}\frac{\partial\sigma(\omega, v_z)}{\partial v_z} \tag{2.37}$$

$$\sigma(\omega) = \sigma(\omega, v_z) \tag{2.38}$$

$$\sigma'(\omega) = \frac{\partial\sigma(\omega, v_z)}{\partial v_z} \tag{2.39}$$

thus:

$$\sigma(\omega) = \sigma_0 \frac{(\Gamma/2)^2}{[(\omega_0-\omega)^2+(\Gamma/2)^2]} \tag{2.40}$$

$$\sigma'(\omega) = \sigma_0 \frac{(\Gamma/2)^2(-2(\omega_0-\omega)\vec{k})}{[(\omega_0-\omega)^2+(\Gamma/2)^2]^{-2}} \tag{2.41}$$

$$\sigma(\omega, v_z) = \sigma_0(\omega)\Big(1-2\frac{(\omega_0-\omega)\vec{k}\cdot\vec{v}}{[(\omega_0-\omega)^2+(\Gamma/2)^2]}\Big) \tag{2.42}$$

Provided that there is equal probability that the ion is travelling towards or away from the laser photons then terms linear in v will cancel to give:

$$\langle\sigma(\omega,\vec{v})\rangle_v = \sigma_0 \frac{(\Gamma/2)^2}{[(\omega_0-\omega)^2+(\Gamma/2)^2]} \tag{2.43}$$

which is clearly equal to $\sigma(\omega)$. Thus, if the scattering rate:

$$\gamma_s = \frac{I}{\hbar\omega}\langle\sigma_0(\omega,\vec{v})\rangle_v \tag{2.44}$$

substituting equation 2.42 into expression 2.36 gives:

$$\frac{dE_z}{dt} = \gamma_s\Big\langle\Big(1-2\frac{(\omega_0-\omega)k\vec{v}}{(\omega_0-\omega)^2+(\Gamma/2)^2}\Big)[\hbar k v_z + R(1+f_{sz})]\Big\rangle_v \tag{2.45}$$

Once again we can make use of the assumption of a symmetric velocity distribution to cancel any terms which are linear in v_z. Thus equation 2.45 becomes:

$$\frac{dE_z}{dt} = \gamma_s\left[\Big(-2\frac{(\omega_0-\omega)k^2\langle v_z^2\rangle_v}{(\omega_0-\omega)^2+(\Gamma/2)^2}\Big) + R(1+f_{sz})\right] \tag{2.46}$$

Under the conditions set out, only motion in the z direction will reach a steady state. This occurs when the left hand side of equation 2.46 equals zero. Evaluating $\langle v_z^2\rangle_v$ for this condition we can find a steady state kinetic energy in the z direction. The

minimum value of kinetic energy is obtained when $(\omega_0 - \omega) = \Gamma/2$. Hence:

$$\begin{aligned} E_{Kz} &= \frac{1}{2} m \langle v_z^2 \rangle_v \\ &= \frac{\hbar(1 + f_{sz})\Gamma}{8} \end{aligned} \tag{2.47}$$

The Doppler limit for any particular particle can be calculated since we can define $E_{Kz}(min) = k_B T_z(min)/2$ assuming that scattering is isotropic ($f_{sz} = 1/3$). As an example, the Doppler limit for Magnesium is ~ 1 mK.

2.4.2 The Strong Binding Limit

The motion of a particle in a harmonic well can be described by the equation, $z = z_0 \sin(\omega_z t)$. In the centre of mass frame of reference the particle sees a frequency modulated laser field, the electric component of which can be expressed as:

$$\begin{aligned} E(t) &= E_0 \exp[i(kz - \omega_0 t)] \\ &= E_0 \exp[i(kz_0 \sin(\omega_z t) - \omega_0 t)] \end{aligned} \tag{2.48}$$

This expression can be expanded in a series of Bessel functions. In order to find the intensity absorption spectrum we must take account of the natural linewidth, Γ, of the transition thus:

$$I(\omega) = I_0 \sum_{n=-\infty}^{\infty} |J_n(kz_0)|^2 \frac{(\Gamma/2)^2}{(\Gamma/2)^2 + [\omega - (\omega_0 - n\omega_z)]^2} \tag{2.49}$$

In the strong binding regime the ion oscillation frequency is greater than the natural line width of the laser cooling transition, $\omega_z > \Gamma$. The discontinuous nature of the emission spectrum is then resolved and takes the form of a large, Doppler free carrier at ω_0, and side bands at $\omega_0 \pm n\omega_z$ (where ω_0 is the frequency of the laser cooling

transition).

To laser cool in this regime the laser frequency must be tuned to a red side band, $\omega_0 - n\omega_z$ and the recoil energy on photon absorption must be less than a quantum of the ion vibrational energy ($R < \hbar\omega_z$). Assuming the laser frequency is matched to that of the first lower side band, the ion absorbs photons of energy $\hbar(\omega_0 - \omega_z)$ and re-emits photons of average energy ω_0. With each scattering event the ion looses an average of one quantum of vibrational energy: $\Delta E = \hbar\omega_z$.

Off-resonance transitions will occur because the laser linewidth and the transition linewidth, Γ, are finite. These events produce a heating effect and most commonly involve absorption on the upper ($\omega_0 + \omega_z$) side band followed by emission on the carrier or absorption on the carrier followed by emission on the lower side band ($\omega_0 - \omega_z$). The low temperature limit for this so called side band cooling represents the balance between the on-resonance and off-resonance processes, it has been calculated as [6]:

$$k_B T_{min} = \frac{1}{4}(\alpha + \frac{1}{4})(\Gamma/\omega_0)^2 \tag{2.50}$$

where α is dependent upon the angular distribution of the photon emission and is close to 1.

In Penning traps it is generally difficult to obtain large cooling rates in the strong binding limit. One reason for this is simply that in most cases the trap oscillation frequency ω_z is of the order of 100-1000 kHz, while the linewidths of dipole transitions are around a few MHz. This necessitates the use of weaker transitions with a correspondingly low scattering cross section and consequently a low cooling rate. A Paul trap on the other hand can be engineered to work with a frequency chosen to fit the conditions for strong binding. A further consideration is that while a Paul trap gives essentially a three dimensional harmonic well with three near degenerate frequencies along each of the principal axes (x, y and z), the Penning trap is characterized by three distinct frequencies: $\omega_m < \omega_z < \omega_c'$ (see section 2.1.1). This

means that the Penning trap has a very complicated side band spectrum, possessing side bands at not only the fundamental motional frequencies (eg $\omega_0 \pm \omega_c'$), but also at intermodulation products ($\omega_0 + a\omega_m + b\omega_z + c\omega_c'$ where a, b and c are integers). There are two consequences of this, one, that the spectrum is in fact nearly continuous at high temperatures and two, that to minimize the vibrational energies for all three degrees of freedom requires three lasers.

The Lamb–Dicke Regime

This is defined as the case where the ion is confined to a space of dimensions comparable to the wavelength of the laser cooling radiation used. More precisely: $z_{rms} \ll \lambda_0/2\pi$. From equation 2.49 it can be seen that under conditions of very strong confinement where $kz_0 \leq 1$, the amplitude of the Doppler free component of the absorption spectrum (at ω_0) will increase with respect to that of the side bands. This is in fact the signature of the Lamb–Dicke regime.

In the micro-wave domain, where $\lambda_0 \sim 1$ cm, the Lamb–Dicke regime is easily reached, even for quite large numbers of ions. Unfortunately, in the optical region of the spectrum very low temperatures are required before such a degree of confinement is possible. There are ways around this problem, specifically with the use of high frequency RF traps.

In the absence of any static voltage, the maximum secular axial frequency of an ion in an RF trap is [15]:

$$\omega_z = \frac{2}{R_0^2}\left(\frac{eV_0}{0.908m}\right)^{1/2} \tag{2.51}$$

Strong confinement is implied by a high oscillation frequency, so it is clear that to achieve this, large voltages and small trap dimensions are necessary. Maximum voltages are limited by electrical break down. The degree of miniaturization of trap electrodes is dependent upon machining capability, which generally means that it is not possible to use parabolic or spherical electrodes. Some designs for miniature

traps are discussed in references [16–19].

As a result of the large oscillation frequencies used in miniature RF traps, the strong binding limit applies even for the use of dipole transitions. Oscillation frequencies of 60 MHz have been measured for Beryllium ions which have a strong dipole transition at 313 nm of linewidth 19 MHz [15]. The combination of strong confinement and the high cooling rates enabled by use of dipole transitions mean that cooling to the Lamb–Dicke regime is easily attained. Techniques such as Raman cooling and EIT (Electromagnetically Induced Transparency) can be used to cool further. The combination of severe confinement and very low temperature allow the possibility for many interesting experiments, specifically in the field of quantum information [3].

2.4.3 Cooling beyond the Doppler Limit

Raman Cooling

In this method of cooling, the single photon transition is replaced by stimulated Raman transitions between metastable levels (such as hyperfine levels). As there is no need for narrow, single photon transitions this technique is applicable to many ion species and even neutral atoms. In the unresolved side band regime very low temperatures have been achieved with weakly bound neutral atoms [21]. In the experiment which shall be described here, Beryllium ions in a Paul trap were cooled to their motional ground state using resolved side band Raman cooling [22]. Figure 2.4 shows the scheme which was used.

Before Raman cooling can be effective, the ion must already be in a sufficiently low vibrational energy level: $\langle n_v \rangle \sim 1$. At this point the ion should be in the Lamb–Dicke regime. The Raman beams cycle between vibrational states, the ion energy being reduced by one vibrational quantum with each cycle. Referring to

figure 2.4, the transition labelled D2 provides the Doppler "pre-cooling" (with the ion vibration frequency $\omega_v \simeq \Gamma$) necessary to reduce the vibrational energy of the ion leaving it in the Lamb–Dicke regime. The additional beams D1 and D3 are also required respectively to prevent optical pumping to the $F = 1$ ground state and to deplete the $|F, m_F\rangle = |2, 1\rangle$ ground state. Once the ion is in the Lamb–Dicke regime, it is prepared in the $|2, 2\rangle$ state by switching off D2.

The Raman beams are detuned to the first red motional side band ($\Delta = \omega_0 - \omega_v$) and have a difference frequency approximately equal to the hyperfine splitting of the $^2S_{1/2}|F = 2\rangle$ and $|F = 1\rangle$ ground state. When the Raman beams are switched on the ion is transferred from $|2, 2\rangle|n_v\rangle \rightarrow |1, 1\rangle|n_v - 1\rangle$. Beams D1 and D2 induce a further Raman transition which returns the ion to state $|2, 2\rangle|n_v - 1\rangle$. This cycle is repeated along the three principal axes (x, y and z), to reduce $n_v \rightarrow 0$ in three dimensions. In this stage of the cooling process $\Gamma_{Ram} \ll \omega_v$, where Γ_{Ram} is the Raman transition linewidth. As with conventional side band cooling off-resonance transitions on the carrier and blue motional side band will produce some heating.

To generate two beams of controllable frequency difference, light from a single laser source is passed through an acousto-optic modulator (AOM). The fundamental and first order diffracted beams act as the two Raman beams, alteration of the modulation frequency allowing tunability of the frequency between the two. By altering the relative tuning of the Raman beams the effective laser linewidth can be made very narrow. This has considerable advantages over conventional laser cooling.

To assess how far n_v has been reduced, the asymmetry of the motional side bands on the Raman transition is probed using beam D2. To do this, the Raman detuning is first set to $\Delta = \omega_0 + \delta_{pr}$. A probe transition is then driven between the states, where $\Delta n_v = 0, \pm 1$. The probability of driving this probe transition is then determined by applying a π-pulse between levels $|2, 2\rangle|n_v\rangle \leftrightarrow |1, 1\rangle|n_v - 1\rangle$ and then driving the $^2S_{1/2}|2, 2\rangle \rightarrow {}^2P_{3/2}|3, 3\rangle$ transition (D2). This cycle is repeated (at $\sim$ 4 kHz)

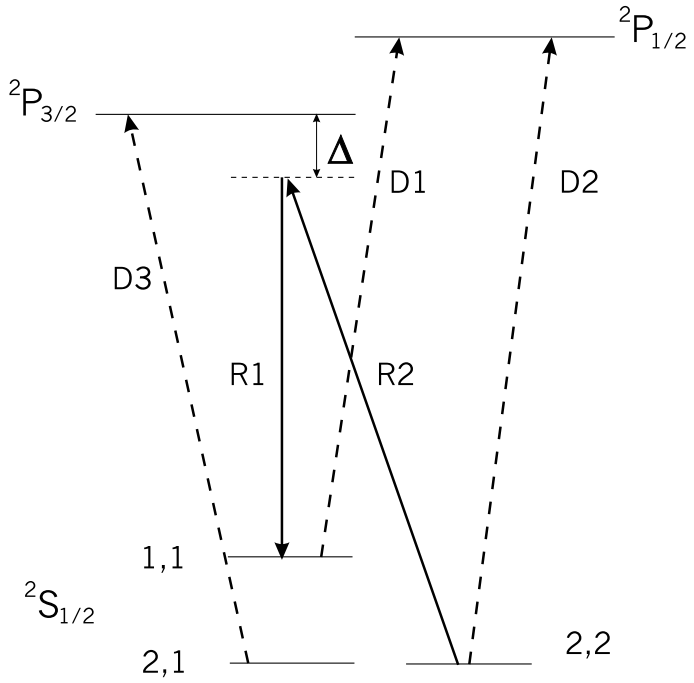

Fig. 2.4: The energy levels of Be^+ used in resolved side band Raman cooling. The value of Δ is ~ 12 GHz. The relative detuning of the two Raman beams (R_1 and R_2), is of the order of the hyperfine splitting of the $^2S_{1/2}$ state; this is $\omega_0/2\pi = 1.2$ GHz.

while sweeping δ_{pr} to obtain the Raman absorption spectrum. There is a Raman carrier frequency at ω_0 ($\delta_{pr} = 0$) with red and blue side bands in all three dimensions. These side bands are at $\delta_{pr} = \pm\omega_v$, representing the transitions between vibrational energy levels: $|2,2\rangle|n_v\rangle \leftrightarrow |1,1\rangle|n_v - 1\rangle$. If the ion is mostly in the lowest vibrational state, it is expected that the red side band should be very much reduced compared to the blue: the only possible transitions being $|2,2\rangle|n_v = 0\rangle \rightarrow |1,1\rangle|n_v + 1\rangle$.

Figure 2.5 shows the first set of side bands in the x-direction. The solid points show the strengths of these side bands after Doppler pre-cooling, the hollow points show the result of Raman cooling. After Raman cooling the red side band is no longer visible and the blue side band is correspondingly enhanced.

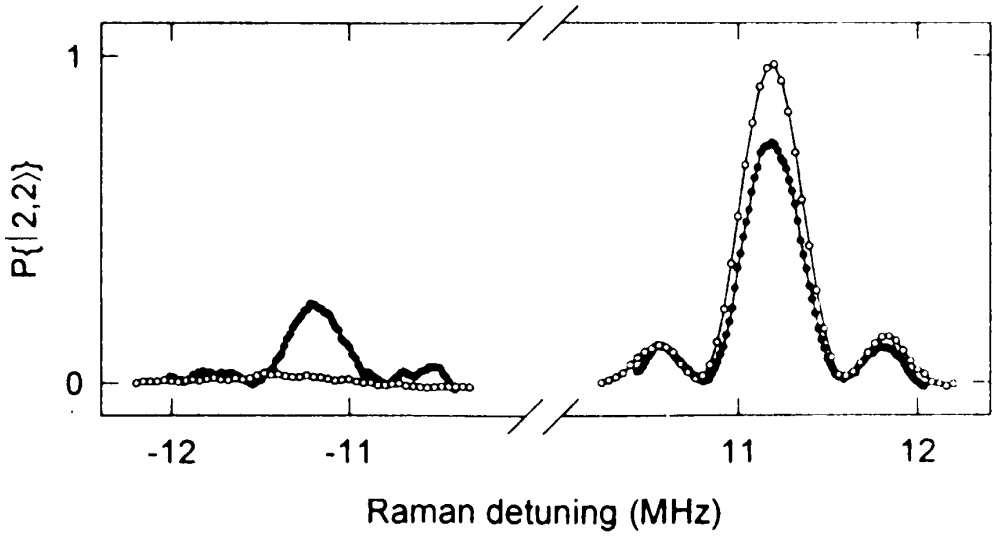

Fig. 2.5: The first order red and blue side bands of the absorption spectrum for Raman cooled Beryllium (x-direction only).

If n_v is thermally distributed then it can be shown that:

$$\frac{I_{red}}{I_{blue}} = \frac{\langle n_v \rangle}{1 + \langle n_v \rangle} \tag{2.52}$$

From this the vibrational occupation number of $\langle n_v \rangle$ can be obtained. After Doppler pre-cooling it was calculated as, $\langle n_v \rangle = 0.47$, reduced to $\langle n_v \rangle = 0.014$ after Raman cooling. This value of $\langle n_v \rangle$ corresponds to the ground state being occupied 98 % of the time. Highest ground state occupation can be achieved by cooling all three of the motional degrees of freedom. If the cooling cycle is applied, in turn, on each of the three motional side bands (at $\omega_0 - \omega_x$, $\omega_0 - \omega_y$ and $\omega_0 - \omega_z$) it was found that the ion could be cooled to the $\langle n_v \rangle = (0.033, 0.022, 0.029)$. This indicates that the ground state is occupied roughly 92 % of the time.

Cooling using Electromagnetically Induced Transparency.

A recently developed technique involves the phenomenon of electromagnetically induced transparency (EIT) [23]. The process of EIT can occur in any system of three or more energy levels and it is defined as the cancellation of the absorption of one transition by the simultaneous, coherent driving of another. The phenomenon can be understood as the destructive interference between two pathways to the excited state. It has been demonstrated in a number of systems [24].

This method of cooling has a number of advantages over side band techniques as it works by eliminating the carrier frequency in the atomic absorption spectrum. Off-resonance transitions on the carrier and the blue motional side band are a source of heating in both conventional side band and Raman cooling. The occurrence of off resonant transitions is more frequent at higher laser intensities, which imposes a limit on the laser intensity and so the rate of cooling. Because EIT removes the carrier there is no limitation on the amount of laser intensity which can be used making it possible to achieve large cooling rates. A further advantage of the technique is that it enables the simultaneous cooling of more than one mode of vibration. The method of EIT cooling also has another advantage over simple side band cooling in that the scheme does not require strong confinement: dipole transitions are used neither of which has to satisfy the relation $\Gamma << \omega_z$.

Referring to figure 2.6, this shows a simple atomic system in a λ configuration. The excited state $|e\rangle$, of linewidth, γ is coupled to both the ground state, $|g\rangle$ and the metastable state, $|r\rangle$ by dipole transitions. If a strong *coupling* laser, of frequency $\omega_r = \omega_{re} + \Delta_r$ (where ω_{re} is the frequency of the bare atomic transition $|r\rangle \rightarrow |e\rangle$) and Rabi frequency, Ω_r is used to excite the $|r\rangle \rightarrow |e\rangle$ transition then driving the $|g\rangle \rightarrow |e\rangle$ transition produces an absorption spectrum of the the form shown in figure 2.6 (inset). The probe laser is termed the *cooling* laser and has a frequency $\omega_{ge} + \Delta_g$

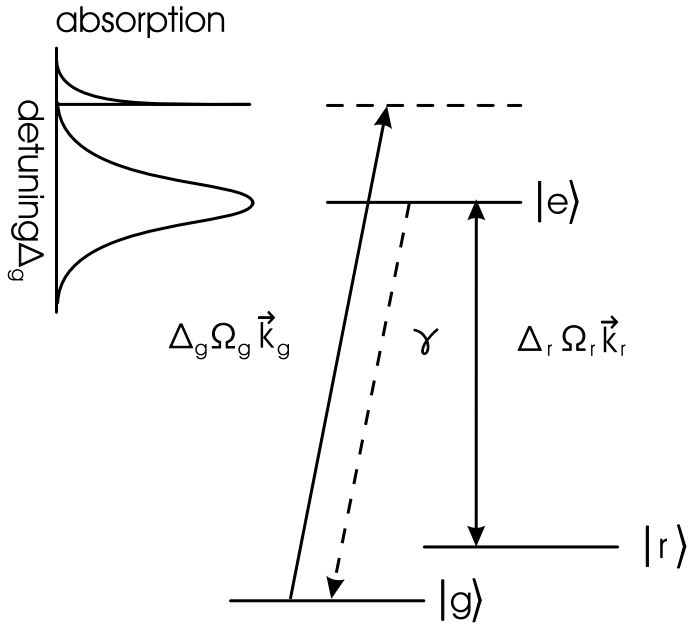

Fig. 2.6: A schematic energy level diagram showing the EIT process. On the left is shown the absorption profile produced when the cooling laser ($|g\rangle \rightarrow |e\rangle$) is used to probe the dressed states of the atom/coupling laser field. After reference [23]

(where ω_{ge} is the frequency of the bare atomic transition $|g\rangle \rightarrow |e\rangle$)and Rabi frequency, Ω_g.

The absorption spectrum has a zero at $\Delta_g = \Delta_r$ and is asymmetric for $\Delta_r \neq 0$. The two peaks, one narrow and one broad, correspond to the dressed states of the atom + coupling laser (the dressed state energy level diagram is shown in figure 2.7, graph 2). The strong coupling laser induces an ac Stark shift of magnitude δ, this moves the absorption maxima away from Δ_r.

$$\delta = \frac{1}{2}(\sqrt{\Delta_r^2 + \Omega_r^2} - |\Delta_r|) \tag{2.53}$$

It is now appropriate to take into account the effect of harmonic motion in the trap. The zero in the absorption spectrum corresponds to the $|g, n\rangle \rightarrow |e, n\rangle$ transition (ie the carrier frequency) which is eliminated. By careful choice of laser

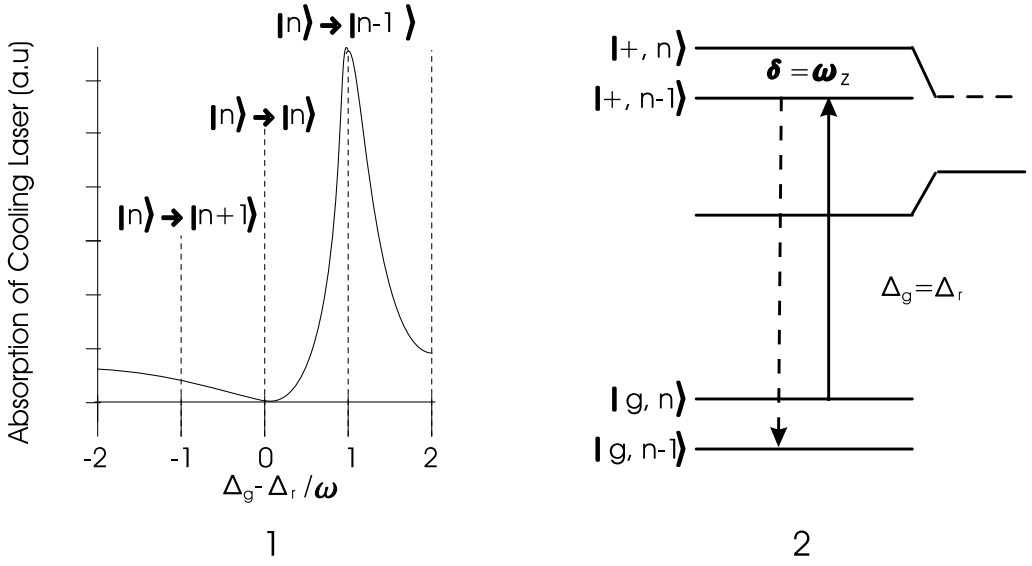

Fig. 2.7: Graph 1 shows a schematic diagram showing the characteristic absorption profile for EIT. By adjusting the laser parameters the profile can be shifted such that the appropriate atomic transitions coincide with the minima and maxima of absorption. In graph 2, the dressed energy levels are shown. After reference [23]

parameters a value of $\Delta_r > 0$ can be determined which will move the red side band: $|g, n\rangle \rightarrow |e, n-1\rangle$, to the maximum of the narrow absorption peak. Under these conditions the blue side band will fall in a region of the spectrum where there is little chance that it will be excited. This is shown in figure 2.7, graph 1. To fulfill both the condition for removing the carrier frequency and enhancement of the red side band the laser parameters must be adjusted according to the following:

$$\Delta_g = \Delta_r \quad \text{and} \quad \delta = \omega_z \tag{2.54}$$

If the frequencies of vibrational modes (in the x , y and z-directions) within the trap are similar it is possible that the side bands for more than one oscillator will fall within the width of the absorption peak at Δ_r. If this is so, then it is possible to cool all of these modes simultaneously. This result in itself is not surprising, what is remarkable is that it has been shown that the theoretical cooling limit (the minimum

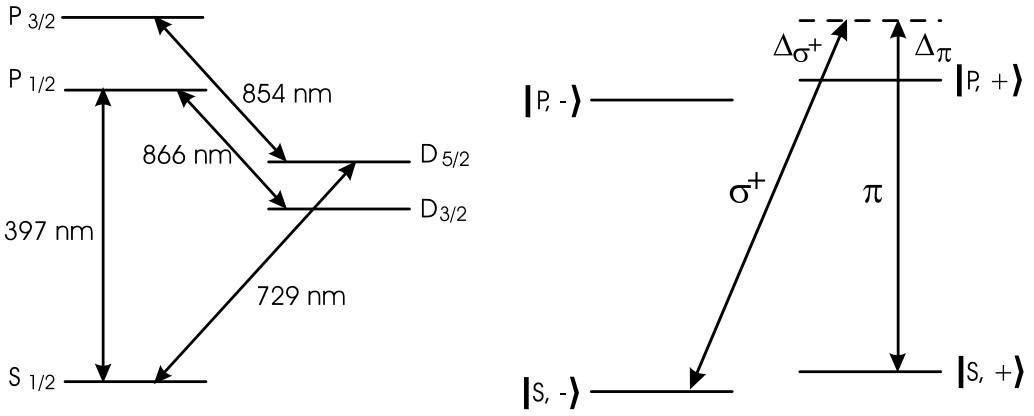

Fig. 2.8: The energy levels used to achieve EIT cooling of $^{40}Ca^{+}$. The Λ–system is formed by $S_{1/2}$,$(m_J = 1/2) \rightarrow P_{1/2}$, $(m_J = 1/2)$ and $S_{1/2}$,$(m_J = -1/2) \rightarrow P_{1/2}$, $(m_J = 1/2)$. These are labelled π and σ_+ which are respectively, the cooling transition and the coupling field. For EIT cooling, $\Delta_{\sigma^+} = \Delta_{\pi}$.From reference [25].

motional energy level reached) in any one direction is not determined by the angle between the laser beams and the motional axis [23]. This is in complete contrast to any other method of cooling.

The theory of this method of cooling was first put into practice by Roos et al. In their 2000 paper [25] they describe how a single ^{40}Ca^{+} ion is cooled to the ground state by exploiting EIT.

The energy level diagram for ^{40}Ca^{+} in an RF trap is shown in figure 2.8. Normal Doppler cooling takes place on the $S_{1/2} \rightarrow P_{1/2}$ transition. The coupling laser, here termed σ_+, creates the required absorption profile when probed by the π, cooling laser. The two beams are produced by the same laser at 397 nm. The difference in frequency between the coupling and cooling lasers is made with the use of a pair of AOMs and is set to equal the Zeeman splitting of the $|S, \pm\rangle$ levels in the quantization B-field. This means that the absorption profile can be created at roughly 75MHz above the $|P, +\rangle$. The stark shift $\delta = 1/2(\sqrt{\Delta_{\sigma^+}^2 + \Omega_{\sigma^+}^2} - |\Delta_{\sigma^+}|)$ is tuned by altering the intensity of the coupling laser and is set at the frequency of the vibrational mode which is to be cooled.

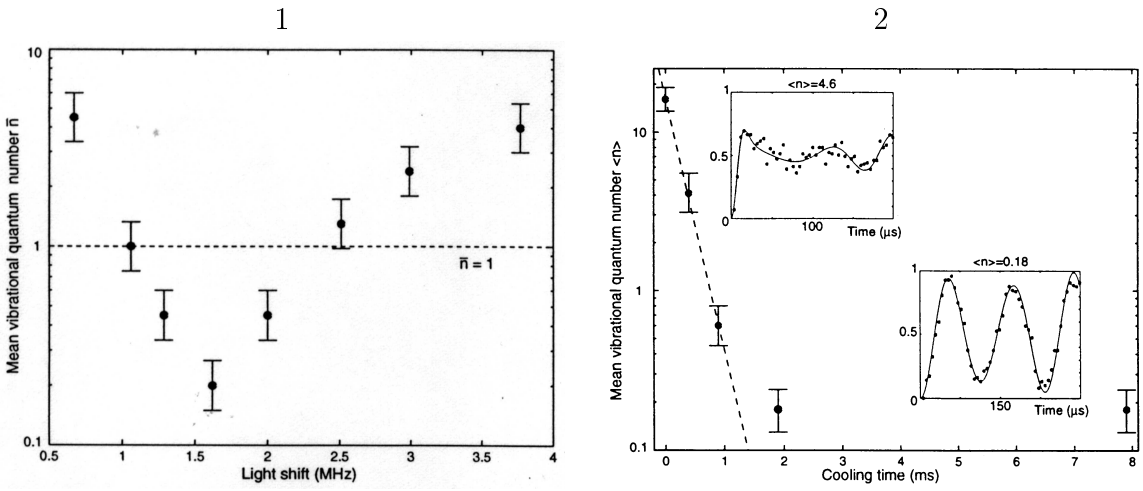

Fig. 2.9: Graph 1 shows the variation in final ground state occupation as a function of stark shift. Graph 2 shows the mean vibrational quantum number $\langle n_y \rangle$ vs EIT cooling pulse length. The insets show the result of exciting Rabi oscillations on the $|S,+\rangle \rightarrow D_{5/2}$ motional side band, first after very little EIT cooling and then after the maximum cooling time

In the experimental scheme the ion is first Doppler cooled to the Lamb–Dicke regime. The EIT beams are then applied for some time. The occupation of the vibrational mode can be assessed by spectroscopy of the $S_{1/2} \rightarrow D_{5/2}$ quadrupole transition. Once the EIT beams are shut off the ion is pumped into the $|S,+\rangle$ state from which Rabi oscillations are excited on the blue side band of the $|S,+\rangle \rightarrow D_{5/2}$ transition. By fitting to the expected form of the Rabi oscillations the ground state occupation can be determined. Figure 2.9, graph 1, shows how the mean ground state occupation of the y-mode of oscillation varies according to the length of time for which EIT cooling is applied: after 0.4 ms (left) and after 7.9 ms (right). This compares to the initial thermal distribution which gives a mean vibrational occupation number $\langle n_y \rangle = 16$. The lowest recorded mean vibrational number $\langle n_y \rangle = 0.18$, and 84% probability of ground state occupation. Figure 2.9, graph 2, shows how the final value of $\langle n_y \rangle$ varies with the stark shift, δ. Clearly the most efficient cooling occurs when δ matches ω_y.

An important prediction of the theory is that more than one mode of vibration can be cooled simultaneously. In reference [25], it is described how both the y and z modes of vibration are cooled. The frequencies of these modes are $\omega_y = 2\pi \times 1.6$ MHz and $\omega_z = 2\pi \times 3.3$ MHz, the value of δ was chosen to be an average of ω_y and ω_z. After 7.9 ms the ion was found to have ground state occupation probabilities for the y and z modes of 58% and 74% respectively.

Applying either Raman cooling or EIT cooling in a Penning trap would be difficult for the same reasons as conventional side band cooling is difficult: the complex motional spectrum. However, this is not to say that it would be impossible. The special features of EIT cooling: not requiring strong binding and the simultaneous cooling of more than one vibrational mode make it most attractive. With EIT cooling it is also possible that, making use of an ion with multiple energy levels it might be possible to "design" a spectrum with numerous dark transitions to eliminate frequencies besides the carrier: complete removal of blue motional side bands for instance.

2.4.4 Cooling in a Penning Trap

The complexity of the motion of ions in the radial plane of a Penning trap makes it difficult to laser cool these degrees of freedom. To fully appreciate this it is necessary to look at the kinetic and potential energy of the ion motion within the trap. The equations of motion were derived earlier in this chapter (see equations 2.3, 2.4 and 2.5), from these it is possible to obtain expressions for the kinetic and potential

energies, E_T being the sum of the two:

$$\begin{aligned} E_k &= \frac{1}{2}(mr_m^2\omega_m^2 + mr_c^2\omega_c'^2) + mr_m r_c \omega_m \omega_c' \cos(\omega_m t - \omega_c' t + \Theta_m - \Theta_c) + \\ &\quad \frac{1}{2} mr_z^2 \omega_z^2 \sin^2(\omega_z t + \Theta_z) \qquad (2.55) \\ E_p &= \frac{1}{2} m\omega_z^2 [r_z^2 \cos(\omega_z t + \Theta_z) - \frac{1}{2}(r_m^2 + r_c^2) - \\ &\quad r_m r_c \cos(\omega_m t - \omega_c' t + \Theta_m - \Theta_c)] \qquad (2.56) \\ E_T &= \frac{1}{2} mr_z^2 \omega_z^2 + m\frac{1}{2}(\omega_c' - \omega_m)(\omega_c' r_c^2 - \omega_m r_m^2) \qquad (2.57) \end{aligned}$$

where Θ_m, Θ_c and Θ_z are phase angles. From these equations it is apparent that if the magnetron energy decreases there will actually be an increase in the magnetron radius. The magnetron motion is unstable and therefore requires very different cooling conditions from other ion motions. Even the term "cooling" in this case is controversial as the word is normally associated with the removal of energy from a system. In order to keep ions confined within the trap it is beneficial to decrease the amplitude of any ion motion. As far as the Penning trap is concerned, the term "cooling" simply reflects this, it is not a reduction in the total energy of the particle motion.

Bearing in mind the peculiarities of the Penning trap, rather than looking at the change in energy experienced by a trapped ion when it scatters photons it is better to examine what happens to the amplitude of the ion motion. Allowing that all the same conditions hold as were used to consider the case of a harmonically bound atom: the ion is two level, these states being connected by an electric dipole transition the upper state life time of which is $\Gamma >>$ the frequency of ion motion (which in the Penning trap means $\Gamma >> \omega_c' > \omega_z > \omega_m$). At time $t = t_0$, the ion absorbs a photon of wave vector $\vec{k}$. Later the ion emits a photon of wave vector $\vec{k_s}$, the change in its velocity in one of the principal directions (i = x , y or z) will be $\Delta\vec{v} = \hbar(\vec{k} - \vec{k_{si}}/m)$. In the scattering process the squares of the radii of the ion

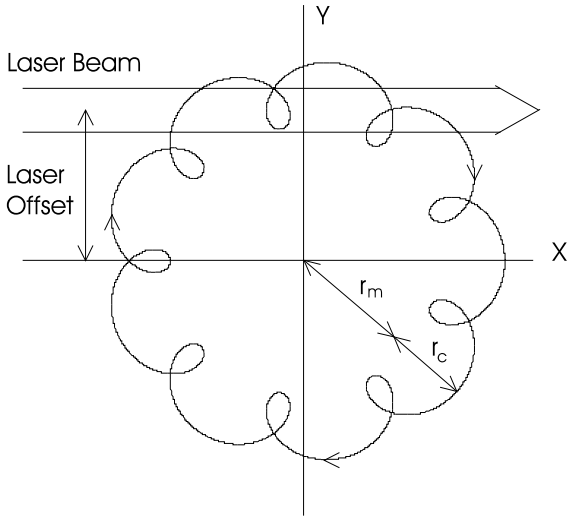

Fig. 2.10: The scheme for laser cooling of radial motion in a Penning trap.

motion change thus:

$$\Delta r_z^2 = (\Delta v_z/\omega_z)^2 - (2r_z\Delta v_z)/\omega_z)\sin(\omega_z t_0 + \Theta_z) \quad (2.58)$$

$$\Delta r_m^2 = [(\Delta v_x)^2 + (\Delta v_y)^2]/4\omega_1^2 + (r_m/\omega_1)[\sin(\omega_m t_0 + \Theta_m)\Delta v_x + \cos(\omega_m t_0 + \Theta_m)\Delta v_y] \quad (2.59)$$

$$\Delta r_c^2 = [(\Delta v_x)^2 + (\Delta v_y)^2]/4\omega_1^2 - (r_c/\omega_1)[\sin(\omega_c' t_0 + \Theta_c)\Delta v_x + \cos(\omega_c' t_0 + \Theta_c)\Delta v_y] \quad (2.60)$$

where $\omega_1 = \frac{1}{2}(\omega_c' - \omega_m)$. These are formulated from the equations of motion for an ion in a Penning trap (equations 2.3, 2.4 and 2.5) and their time derivatives.

In the axial direction there is a harmonic potential, thus equation 2.58 is equivalent to equation 2.30. The equations for the radial motions are very different. In order to determine what might be the cooling conditions for the modified cyclotron and magnetron motions it is necessary to find a set of circumstances for which equations 2.60 and 2.59 have the same form as equation 2.58. In the former case this requires that $\delta v_y \to 0$ and δv_x be *positive*, in the latter case $\delta v_y \to 0$ and δv_x should

be *negative*. The two conditions seem irreconcilable. Fortunately, because the magnetron is of such large radius compared to the modified cyclotron there is a way around the problem: if the laser beam is placed on one side of the magnetron orbit where this rotation takes the particles away from the laser photons (making Δv_x negative) the smaller modified cyclotron will take the ions through several cycles while inside the laser beam, this way the ions will move towards the laser photons (making Δv_x positive) at least some of the time. The conditions for cooling the modified cyclotron motion can be considered similar to those required to cool harmonic motion. From here we come to the familiar configuration for cooling in the Penning trap with the laser beam detuned to the red (to cool the modified cyclotron motion), and the beam position offset from the trap centre in order to fulfill the requirements for reduction of the magnetron motion. This result is discussed fully in reference [4]. Figure 2.10 shows the radial motion in a Penning trap and how the cooling beam should be set up.

With the basic model for laser cooling in the Penning trap now established I shall go on to look briefly at the *recipe* for ideal cooling which is developed in reference [7]. This work is of particular relevance as it was used to incorporate the effects of laser cooling into the computer simulations of axialisation discussed in Chapter 6.

A Simple Model for Laser Cooling in the Penning Trap.

The purpose of this model is primarily to look at the rate of damping of the ion motion which can be achieved with different detunings and beam offsets. It ignores the effects of re-emission, so cannot be used to gauge the minimum temperature reached by the laser cooled ion. A simple rate equation approach is used to describe the scattering process. In this way the average force experienced by the ion is the momentum imparted per photon ($\hbar k$) times the scattering rate, R. The value of R

is:

$$R = \frac{SA}{2}\frac{1}{1+S+(2\Delta/\Gamma)^2} \tag{2.61}$$

where A is the Einstein A-coefficient, Δ the effective laser detuning (dependent upon the ion velocity through the Doppler effect), Γ is the linewidth of the cooling transition and S is the saturation parameter. For a Gaussian laser beam S is:

$$S = S_0 \exp(-2((y_0 - y)/w^2)) \tag{2.62}$$

where S_0 is the saturation parameter at the beam centre, y_0 is the radial offset of the laser from trap centre, y is the position of the ion relative to trap centre and w is the laser beam waist.

If we determine that the laser beam enters the trap along the x-axis with an offset of y_0, then the rate of laser cooling for a trapped ion is dependent upon its instantaneous y coordinate and the component of its velocity in the x direction. It follows then that the total force experienced by the ion will be the combined effect of a position dependent term in y and a velocity dependent term in $\dot{x}$:

$$\begin{aligned} F_T &= F_y + F_{\dot{x}} && (2.63)\\ &= \hbar k\Big(\frac{\partial R}{\partial y}\Big) y + \hbar k\Big(\frac{\partial R}{\partial \dot{x}}\Big)\dot{x} && (2.64) \end{aligned}$$

We are not concerned with the cooling of the axial ion motion as this is generally not cooled directly but by collisions and as a result of misalignments.

Recalling the radial equations of motion for a trapped ion, equations 2.3 and 2.4. In the presence of laser cooling these become:

$$\begin{aligned} \ddot{x} &= \frac{\omega_z^2}{2}x + \omega_c\dot{y} + \alpha y - \beta\dot{x} && (2.65)\\ \ddot{y} &= \frac{\omega_z^2}{2}y - \omega_c\dot{x} && (2.66) \end{aligned}$$

In order to solve these equations analytically the asymmetry between the x and y directions should be removed. This can be done if we rotate the x and y-axes by 45° and make the approximation that $\alpha << \omega_z^2$ and that $\beta << 2\omega_c$. The equations then become:

$$\ddot{X} = \omega_c\dot{Y} + (\omega_z^2/2)X + (\alpha/2)Y - (\beta/2)\dot{X} \tag{2.67}$$

$$\ddot{Y} = -\omega_c\dot{X} + \omega_z^2 Y - \omega_c\dot{X} \tag{2.68}$$

The solutions to these equations are of the form $X = X_0\exp(pt)$ and $Y = Y_0\exp(pt)$. To first order, this gives values of p:

$$p = i\Big(\frac{\omega_c}{2} \pm \omega_1\Big) - \frac{\beta}{4} \pm \frac{1}{2}\sqrt{-4\omega_1^2 + \beta^2/4 - i(\beta\omega_c - 2\alpha)} \tag{2.69}$$

$$= i\frac{\omega_c}{2} - \frac{\beta}{4} \pm \frac{\alpha - \beta\omega_c/2}{4\omega_1} \tag{2.70}$$

with $\omega_1 = \sqrt{\omega_c^2/4 - \omega_z^2/2}$.

The ion oscillation frequencies are unchanged by the presence of laser cooling (the imaginary part of p), however, they have different damping rates (the negative of the real part of p). The two damping rates can be found by rearrangement of expression 2.70: γ_m (using the lower signs) for the magnetron motion and γ_c (using the upper signs) for the modified cyclotron motion:

$$\gamma_m = \frac{\alpha - \beta\omega_m}{4\omega_1} \tag{2.71}$$

$$\gamma_c = \frac{\beta\omega_c' - \alpha}{4\omega_1} \tag{2.72}$$

These equations show explicitly what we already know; that the magnetron motion is cooled principally by the spatial variation in laser intensity–laser offset (α) while the modified cyclotron motion is cooled mainly as a result of the frequency dependence

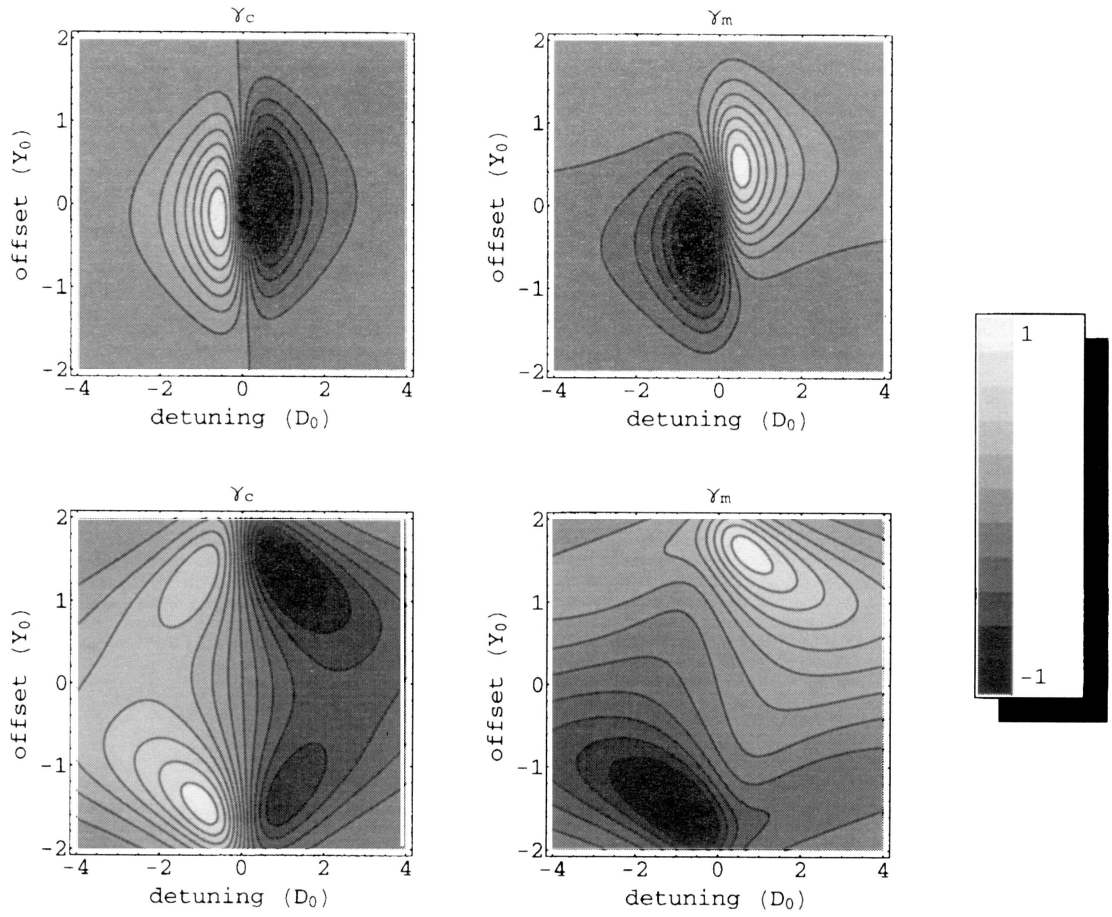

Fig. 2.11: Contour plots showing how the rates of cooling of the magnetron (right) and cyclotron motions (left) are affected by the laser parameters of detuning and beam offset. The top two plots are for low levels of saturation ($S_0 = 0.1$), while the bottom two plots show what happens when the intensity of the laser is increased ($S_0 = 15$).

of the interaction with the laser beam (β). In order to have damping of both motions then $\beta\omega_m < \alpha < \beta\omega_c'$. This is the general requirement of laser cooling which has been derived before by other means [4].

It is interesting to note that:

$$\beta = 2(\gamma_m + \gamma_c) \tag{2.73}$$

$$\alpha = 2(\omega_c'\gamma_m + \omega_m\gamma_c) \tag{2.74}$$

The first of these equations is equivalent to what one would expect for the one dimensional case ($\gamma_m + \gamma_c = \gamma$), the second shows how the available cooling power is essentially divided between the two radial motions in a manner dependent upon α.

The contour diagrams in figure 2.11 show how the damping rates alter with laser detuning and laser beam offset. The upper two plots show the low intensity case and the lower two plots show the high intensity case. It is clear that it is impossible to simultaneously maximize the cooling rates for both the modified cyclotron and the magnetron oscillations. Instead it is the product of the two damping rates which is maximized for optimal cooling of the both radial motions. The division between heating and cooling is a near vertical line close to zero detuning, which is unaffected by changes in laser intensity. The main practical difference between the low and high intensity cases is that at higher intensities the region for which cooling of the complete radial motion is maximized is larger than in the low intensity case. At low intensity ($S_0 = 0.1 \equiv 0.9$ μW), the maximized cooling rate occurs for $Y_0 = 1.0$ and $D_0 = -0.5$ which gives $\gamma_c = 2\pi \times 4.4$ kHz and $\gamma_m = 2\pi \times 0.27$ kHz. The same laser parameters at high intensity ($S_0 = 15 \equiv 140$ μW) give $\gamma_c/2\pi = 24$ kHz and $\gamma_m = 2\pi \times 1.5$ kHz. The second instance is closest to experimental conditions, although it is likely that both the laser offset and the detuning would generally need

to be greater than predicted: in the first case to avoid regions where the detuning would tend to heat the magnetron and in the second to prevent heating of the modified cyclotron in the range of $D_0 \to 0$.

Damping rates can be measured experimentally by plotting the phase difference between a weak driving field and the driven ion motion as a function of frequency, close to resonance. The frequency interval, $\Delta\nu$ between the points where the phase difference is $\pi/4$ and $3\pi/4$ is related to γ as $\Delta\nu = \gamma/\pi$, where γ is the damping rate of the particular motion being driven. For magnesium the damping rates have been found to be: $\gamma_c = 2\pi \times 50$ kHz while $\gamma_m = 2\pi \times 3.5$ kHz [27]. This is quite typical with the cooling rate for the modified cyclotron motion an order of magnitude greater than that of the magnetron motion. In Chapter 6, a method for extending the more efficient cooling of the modified cyclotron radius to the magnetron radius is explored. This method, termed axialization, works by coupling the two radial motions. In the presence of laser cooling the exchange of energy between the two motions results in a decrease in magnetron radius, leading ultimately to the elimination of this orbit.

References

[1] L.R.Brewer, J. D. Prestage, J. J. Bollinger, W. M. Itano, D. J. Larson and D. J. Wineland, *Phys. Rev. A.* **38**, 859 (1988)

[2] *Adv. At. Mol. Phys.* **3**, 53 (1967)

[3] K. Dholakia, G. Zs. K. Horvath, D. M. Segal, R. C. Thompson, D. M. Warrington and D. C. Wilson, *Phys. Rev. A.* **47**, 441 (1993)

[4] J. J. Bollinger, D. J. Heinzen, F. L. Moore, W. M. Itano and D. J. Wineland, *Phys. Rev. A.* **48**, 525 (1993)

[5] D. C. Wilson and R. C. Thompson, *Z. Phys. D.* **42**, 271 (1997)

[6] W. Itano, J. C. Berquist, J. J. Bollinger and D. J. Wineland, *Phys. Scripta*, **T59**, 106 (1995)

[7] O. Frisch, *Z. Phys.* **86**, 42 (1933)

[8] A. Kastler, *J. de physique et le radium*, **11**, 255 (1950)

[9] D. J. Wineland and H. G. Dehmelt, *Bull. Am. Phys. Soc.* **20**, 637 (1975)

[10] T. W. Hänsch and A. C. Schawlow, *Opt. Commun.* **13**, 68 (1975)

[11] R. C. Thompson, *Adv. Atom. Molec. Phys.* **3**, 53 (1993)

[12] D. J. Wineland, W. Itano, *Phys. Rev. A.* **20**, 1521 (1979)

[13] W. Itano and D. J. Wineland, *Phys. Rev. A.* **25**, 35 (1982)

[14] S. Stenholm, *Rev. Mod. Phys.* **58**, 699 (1986)

[15] S. R. Jefferts, C. Monroe, A. S. Barton and D. J. Wineland, *IEEE Trans. Instrum. Meas.* **44**, 148 (1995)

[16] P. Straubel, *Naturwissenschaften*, **42**, 506 (1955)

[17] R. G. Brewer, R. G. DeVoe and R. Kallenbach, *Phys. Rev. A.* **46**, R6781 (1992)

[18] C. A. Schrama, E. Peik, W. W. Smith and H. Walther, *Opt. Comm.* **101**, 32 (1993)

[19] R. G. DeVoe, *Phys. Rev. A.* **58**, 910 (1998)

[20] J. I. Cirac, P. Zoller, *Phys. Rev. Lett.* **74**, 4091 (1995)

[21] M. Kasevich and S. Chu, *Phys. Rev. Lett.* **69**, 1741 (1992)

[22] C. Monroe, D.M. Meekhof, B. E. King, S. R. Jefferts, W. M. Itano and D. J. Wineland, *Phys. Rev. Lett.* **75** , 4011 (1995)

[23] G. Morigi, J. Eschner, C. H. Keitel, *Phys Rev Lett.* **85**, 4458 (2000)

[24] J. P . Marangos, *J. Mod. Opt.* **45**, 471 (1998)

[25] C. F. Roos, D. Leibfried, A. Mundt, F. Schmidt-Kaler, J. Eschner and R. Blatt *Phys. Rev. Lett.* **85**, 5547 (2000)

[26] R. C. Thompson and J. Papadimitriou, *J. Phys. B.* **33**, 3393 (2000)

[27] M. A. van Eijkelenborg, K. Dohlakia, M. E. M. Storkey, D. M. Segal and R. C. Thompson, *Opt. Commun.* **159**, 169 (1999)

[28] J. J. Bollinger, D. J. Heinzen, F. L. Moore, W. M. Itano and D. J. Wineland, *Phys. Rev. A.* **48**, 525 (1993)

CHAPTER 3

The Quantum Zeno Effect

3.1 Zeno's Paradox

The quantum Zeno effect is a strange phenomenon owing its name to a Greek philosopher who had quite an unusual view of the world. The philosopher was of course Zeno of Elea who was convinced that motion is impossible– an illusion. To illustrate his point Zeno proposed a number of paradoxes the most famous of which concerns a race between Achilles and a Tortoise. It is explained that the tortoise, if given a head start can not be overtaken by the faster Achilles. Imagine that the tortoise is initially ahead by say, ten rods (to use the non-S.I. unit of the time). To overtake the tortoise Achilles must first cover this distance, by which time the tortoise has moved further on by some smaller distance which Achilles must then cover, by which time the tortoise is ahead by a yet smaller distance and so on. In this way Achilles can never overtake the tortoise and is doomed to ignominious defeat.

Zeno is very popular amongst mathematicians as his problems revolve around the conceptualization of infinity. Inspired by Zeno, Lewis Carroll [1] wrote an amusing piece called "What the Tortoise said to Achilles" which describes the scene after the race in which of course, Achilles has beaten the tortoise. The two characters

discuss the propositions of Euclid starting from two basic premises which imply a hypothetical third and end up in an infinite and infinitely logical loop in which more and more premises are added before the third can be accepted logically. It is an interesting exploration of thought processes and worth reading. This dialogue and a few others in which even Zeno himself appears can be found in "Gödel, Escher, Bach: an Eternal Golden Braid" by D. Hofstadter [2].

Everyday experience leads us to find Zeno's reasoning suspect, if amusing. The frustration of Achilles is easily be dispelled when we tell him that the sum of an infinite series is finite and since all of Zeno's paradoxes do in fact contain the same basic ingredient of dividing space or time into ever smaller portions to frustrate progress then why not dismiss the whole thing?

Of Zeno's paradoxes the one which most closely resembles our problem is that of Zeno's Arrow [3–5]. Zeno states that when the arrow occupies a place just its own size it must be at rest. Imagine now, an arrow in flight, at every moment of its flight it will occupy a place just its own size. So we must conclude that the arrow is at rest and by implication all motion is impossible. It is as if, by defining the position of the arrow at a particular moment we deny it the possibility of occupying any other.

Although an observer is not mentioned explicitly, the problem does recall the old adage that "a watched pot never boils". It seems that Zeno has actually exposed quite a fundamental difficulty in our perception of the world. To describe an evolving system it is usual to look at the state of that system at a particular instant. The evolution is then mapped out in a series of snap-shots in which the system is "frozen". How does the system get from one stage to the next if it is frozen whenever we look at it? To explain this an entirely different description is required in which the evolution is in a continuous flow and the notion of ascribing a particular state to the system is meaningless. The time intervals between the snap-shots can become

infinitesimal, but it will still be true that each time the system is deemed to have a particular state it becomes momentarily frozen. So, watched pots can never reach the boil and arrows don't move. This still seems fairly ridiculous and even Zeno would have to admit that in the Classical World arrows do not become frozen in flight. In Quantum Mechanics, however, we often have to disregard our intuitive understanding of the world: ideas such as entanglement, superposition of physical states and the Heisenberg Uncertainty Principle have no parallel in the world of our senses. Quantum mechanics may well be one of the most robust theories produced by physics, yet it contains much which makes it at odds with the world we perceive. In particular, quantum mechanics is unable to describe the process of measurement in a satisfactory, non-paradoxical way. Schrödinger's cat still suffers because of this!

Zeno made a debut appearance in physics in relation to nuclear decay of unstable isotopes. The essentials of the argument, assuming our ability to make perfect measurements, is that the decay of a nucleon can be inhibited by frequent observations of its non-decay, and all time evolution is frozen if continuous measurement is achieved.

Subsequently many areas of physics have begun to look at the Zeno phenomenon as a real feature of the physical world. There have been suggestions for many experiments to prove the reality of the Zeno effect. These have looked at position measurement of particles, neutron spin rotation in a magnetic field, and the particular concern of this thesis: the decay of an excited state of an atom. A couple of experiments have claimed to show, beyond doubt, the existence of the Zeno effect; these and the controversy they have raised will be discussed.

3.2 Theory

As has been set out, the Quantum Zeno phenomenon was first described in connection with nuclear decay [6]. The argument can be explained quite simply in the following way. Taking an array of radioactive nuclei which have a decay rate proportional to t^x for short times, the probability of survival to time t_0 is:

$$P_s(t_0) = 1 - k(t_0)^x \tag{3.1}$$

where $k(t_0)^x \ll 1$.

If an intermediate measurement of survival is made at time $t_0/2$ the probability of survival is:

$$P_s(t_0/2) = 1 - k(t_0/2)^x \tag{3.2}$$

After a further period of $t_0/2$ the survival probability is:

$$\begin{aligned} P'_s(t_0) &= (1 - k(t_0)^x)^2 \\ P'_s(t_0) &= 1 - k(t_0)^x/2^{x-1} + k^2(t_0/2)^{2x} \end{aligned} \tag{3.3}$$

If t_0 is small the last term can be ignored and it follows that if $x > 1$, the probability of decay is reduced by a factor of 2^{x-1}. If n measurements are made then a further reduction in the probability of decay is achieved: by a factor of n^{x-1}. In this way, by taking an infinite number of measurements we can decrease the probability of decay to zero. For a more rigorous treatment we must look at the paper by B. Misra and E. Sudarshan [7], generally taken to be the seminal paper on this subject.

In essence, the premise which Misra and Sudarshan work on is that although quantum mechanics can tell us much about the state of for instance, an atomic particle, at a particular juncture in time, it can tell us nothing of what happens

to the particle during a certain time *interval*. Thus quantum mechanics does not seem to allow for the possibility of continuous measurement, despite the fact that there appears to be no fundamental objection to this concept– such as an indivisible, smallest unit of time. It is tempting to conclude on finishing this paper that the intrinsic problem is simply that we have not yet found a satisfactory way to describe the measurement process in quantum mechanics. This is perhaps quite true. The question is can the Zeno effect be dismissed as a quirk of the mathematics in which we have chosen to frame the problem and will it disappear as soon as a better frame work is available?

The approach that Peres [8] takes in his article, written not long after that by Misra and Sudarshan, is informative. He takes a very pragmatic view, leaving the reader to decide whether the result is in fact *paradoxical* or not. The author seeks to separate the Zeno paradox from the specifics of what he terms *measurement theory*. This is useful, since measurement is itself not a fundamental concept; the results of a measurement arise from interactions between the matter in the measured and measuring systems, these being governed by fundamental laws. In this way, Peres shows how the Zeno phenomenon can arise directly from the Schrödinger equation, by looking at the quadratic time dependence of the decay from one quantum state to an adjacent state.

That the Zeno effect might be an artefact of our imperfect understanding is the source of much controversy especially since a few experiments have now been completed which appear to show that the result is a physical reality. Interpretational problems arise principally from three sources: the projection postulate which is used to describe the measurement process in reference [7], what exactly is *continuous* in the context of a measurement process and how can a measurement be made without disturbing the system such that the outcome of a *measurement* is simply a variable of the measuring device.

There have been many articles since Misra and Sudarshan set the ball rolling. As yet there is no unanimous view as to whether the quantum Zeno effect is a real phenomenon. This is principally due to the fact that there is no consensus on exactly what the intrinsic factors in the effect might be. Some of these issues are looked at in the following section; more detailed, general discussions of the subject are included in references [9–12].

3.2.1 The Trouble with Copenhagen

A measurement process involves a set of interactions between a system and a measuring device, these interactions obeying the Schrödinger equation. The one problem here is that the Schrödinger equation predicts that, after a measurement, the measuring device will be left not in one physical state, giving a unique result, but in a superposition state of all possible outcomes of that particular measurement process. This is contrary to our usual experience of taking measurements. There are a number of ways to get round this difficulty, the most convenient of which is the "projection postulate" as formulated by Von Neumann, which is associated with the Copenhagen Interpretation of quantum mechanics. In this interpretation the system/measuring-device interaction follows the Schrödinger equation until the final stage of the measurement process. At this final point another phenomenon takes over whereby the wave function of the combined system *collapses* into one or other of the states available.

The Von Neumann interpretation is very useful, but it is in no way a satisfactory description of the measurement process. Why should a system develop according to the Schrödinger equation under normal circumstances while at a measurement it follows the collapse postulate? This is almost as difficult to understand as the possibility of a system being in a superposition of states.

In forming the quantum Zeno paradox the projection postulate was used to

describe the measurement process. This leaves the idea open to the criticism that it depends on a very special, some would say erroneous, version of quantum mechanics. Once the first experiment [13] (which shall be described in full at a later point) claiming to prove the existence of the Zeno effect was completed this argument gained momentum. This is because the system which was used, a V-scheme atomic energy level configuration, could be analyzed without any recourse to the projection postulate to give the same answers. The problem is that if a system is perturbed sufficiently by a measuring device then the arrested time evolution characteristic of the Zeno effect is merely a result of random decoherence and does not deserve a special name [14, 15].

Bearing in mind the objections outlined above it has been said that both the Zeno effect and the projection postulate itself could be disproved. Although the converse could be true, as a group in Japan did attempt to show [16]. Unfortunately the argument that the experiment of reference [13] is explainable by other means is quite solid and even the original experimenters agree that this is so [17]. The question is have the experimentalists erred in this case: a study of this kind simply is not adequate to demonstrate the Zeno effect, or if it does, what does this say about the projection postulate? Or perhaps, rather than getting knotted in a debate about interpretation we should get to the bottom of how to describe and most importantly, make good measurements.

3.2.2 The Limit for Continuous Measurement and a Time scale for the Quantum Zeno Effect.

What does the concept of continuous measurement actually mean? In their paper, Misra and Sudarshan cite the recording of the particle decay by a bubble chamber as an example of continuous measurement ... but the tracks left in the bubble cham-

ber do not appear to show that the decay process is slowed by the measurements made. We could describe the process as a succession of discrete measurements, in which case measurement is certainly not continuous, but then how do we achieve continuous measurement? It has been suggested that complete suspension of time evolution (and by implication, the achievement of continuous measurement) should be treated as an unrealizable ideal [18, 19]. There are indeed physical realities which must preclude continuous measurement such as the recovery time or dead time of a detector. Unfortunately, this still does not answer the question of why we do not see even a semi-Zeno effect in the case of the bubble chamber.

Part of the answer lies in the time scales involved. If we look at any decay process we find that there are two distinct forms of time evolution: over long time intervals it appears exponential, however on short time scales it is quadratic. The *shortness* of the time interval in this case relates to the coherence time of the state we are looking at.

In Fermi's Golden Rule we have an equation which tells us the decay rate for an unstable system:

$$\Gamma = \frac{2\pi}{\hbar}|u_k\langle\widehat{H}'\rangle u_s|^2\rho_E \tag{3.4}$$

here, ρ_E is the density of states and u_s and u_k are the initial and final states of the system.

Consider a system with a decay rate governed by equation 3.4. The probability that such a system survives in its initial state through a time interval Δt is:

$$P_s(\Delta t) = 1 - \Gamma\Delta t \tag{3.5}$$

If we look at the system n times at regular intervals, then equation 3.5 gives us the

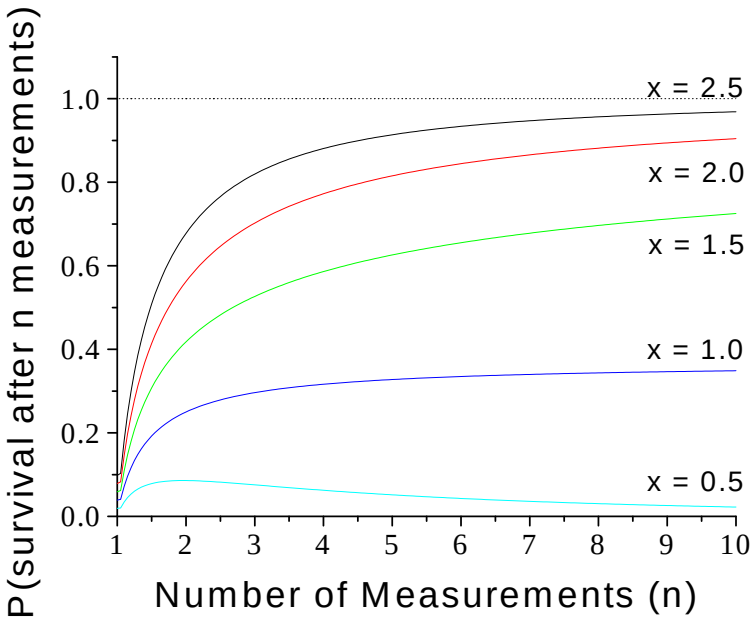

Fig. 3.1: A graph of the probability of survival for a system with decay probability dependent upon t^x. As x increases above 1, the probability of survival is enhanced by large numbers of measurements.

exponential decay rate which we expect:

$$\begin{aligned} P_s(N\Delta t) &= \Big[1-\Gamma\Delta t\Big]^n \\ &= \Big[1-\Gamma\Big(\frac{T}{n}\Big)\Big]^n \\ &\simeq \exp(-\Gamma T) \end{aligned} \tag{3.6}$$

where $T = n\Delta t$. The survival probability decreases exponentially and it will approach 0 as we take more measurements.

Unfortunately as $\Delta t \to 0$, the approximations which allow us to derive Fermi's Golden Rule are not admissible. This being the case we must integrate the time dependent Schrödinger equation [8] to give us another decay rate. This gives us a

different probability for the survival of the system through the time interval Δt:

$$P'_s(\Delta t) = 1 - a(\Delta t)^2 \tag{3.7}$$

where a is a constant.

If we attempt to make n equally spaced measurements on a system evolving with this kind of time dependence, then:

$$P'_s(\Delta t) = \left[1 - a\left(\frac{T}{n}\right)^2\right]^n \tag{3.8}$$

Because the decay rate is proportional to t^2, as n increases then $P_s(n\Delta t) \to 1$, as we saw in the example towards the beginning of this chapter.

The argument can be illustrated graphically. In figure 3.1 the survival of a system with decay probability dependent upon t^x is shown. The value of x is varied from 0.5 through 1 (the case of exponential decay) to 2.5 in steps of 0.5. The number of measurements taken, n, goes from 1 to 10. It is only when $x > 1$, that reduction of the decay probability is achieved.

3.2.3 Interaction-free measurement, Non-Locality and the Quantum Zeno Effect Or, What is a Good way of Measuring Things?

To prove the Zeno effect requires us to make measurements which leave the system we are measuring in a pure state. Such a measurement must be instantaneous. In the real world the only way to achieve this is by using what is often termed an *interaction free* measurement. When the Zeno paradox was originally proposed, the measurement taken was of the non-decay of a nucleon. In this case the simple presence of a measuring device capable of registering the decay of the nucleon is

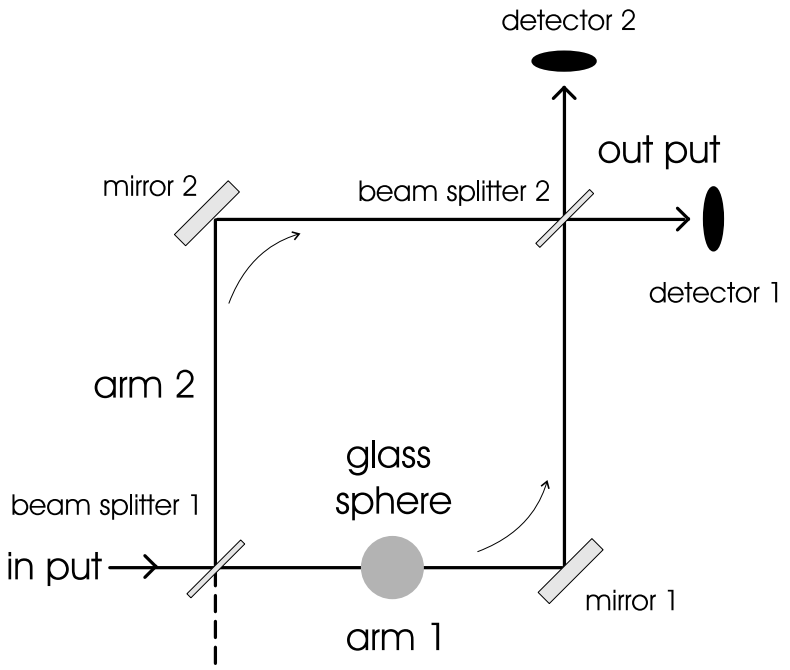

Fig. 3.2: A diagram of a Mach-Zehnder interferometer, consisting of two beam splitters, two mirrors and two detectors. The difference in optical path length between the two arms of the interferometer determines the interference pattern at the out put and consequently which detector registers the arrival of a photon.

responsible for inhibiting that decay. There is no physical interaction between the nucleon and the detector.

As a further example of interaction free measurement consider the experiment described in reference [12]. This describes a method of sorting two types of glass bulb, one of which contains some substance which will explode on interaction with a single photon. The idea is to try to do this without destroying the explosive bulbs. Surprisingly, this can be done with up to a 99.9 % success rate. All that is required is a Mach-Zehnder interferometer.

Referring to figure 3.2, initially both arms of the interferometer are equivalent and light entering at the input will always be detected at output 1 (by detector 1). If one of the glass bulbs is placed in, say arm 1 of the interferometer there are two possibilities. Taking the case where the bulb is empty (non-explosive), the

path length of arm 1 remains unaltered and any photon entering the system will be registered at detector 1. When a full bulb (explosive) is placed in arm 1, however, this will alter the path length. In this instance any photon which travels through the interferometer without destroying the bulb must go to detector 2. So, with a bulb in position, a photon at detector 1 gives us no information, but a photon at detector 2 is an unambiguous sign that the bulb under test is explosive. This allows us to sort out some of the explosive bulbs, repeating the experiment on those bulbs which gave inconclusive results further increases the percentage of explosive bulbs which can be recovered.

What is important in both the original scheme and that of reference [12] is that there is no sense in which the measurement process takes up any time: the nucleon's "decision" not to decay and the photon's "decision" on which path to take are instantaneous. A further point is that both are null measurements: information is gained by observation of a non-event. This has the bonus (which relates to the topics discussed in the previous section) that there is no detector dead time for this kind of measurement so we can reach a truly continuous regime of measurement. This means that by using an interaction free technique we can make perfect measurement and measure continuously.

There are now two questions to answer. Firstly, are all null measurements in fact interaction-free. Secondly, does the Zeno effect require interaction free measurement or is *good* measurement a sufficient condition.

To answer the first point, take the experiment performed by Itano et al at NIST [13]. Here we have an experiment which it seems you can do in two ways, one making an interactive measurement (where fluorescence is produced) and one making a null measurement, where no fluorescence is produced. The problem is, does the second type of measurement qualify as interaction-free, as the ion is still bathed in pulses of electromagnetic radiation. Those who have written about the subject certainly

don't appear to think there is any substantial difference between the two forms of the experiment and if we look at references [18, 20] we find that they are right. The difference between the NIST approach and the other interaction-free processes described is the use of laser *pulses* to measure the atomic state. These pulses must necessarily have some finite duration and it is this which is the root of the problem whether the atom fluoresces or not. In this case the null measurement is not also interaction free.

The second question is perhaps most important. Some authors [21] have suggested that the interaction-free measurement is a requirement for the Zeno effect as the true *phenomenon* is essentially non-local. The effect must consist of an unstable system and a measuring device which are macroscopically separated.

Non-locality is a purely quantum phenomenon, and is associated with the concept of entanglement. What is unusual about the Zeno effect is that the *entanglement* between the unstable system and the measuring device seems to have been established without there having been even any initial contact, as is generally required.

That the Zeno effect should necessarily be classed as non-local does not seem entirely convincing. To introduce this idea does perhaps even confuse the issue further. What is more important is that measurements made are good: ideally this means that the system should be left in a pure state at the end of the measurement process. Measurements will never be perfect, thus a more realistic and ultimately more satisfactory approach is to make certain that any measurement made approaches the ideal.

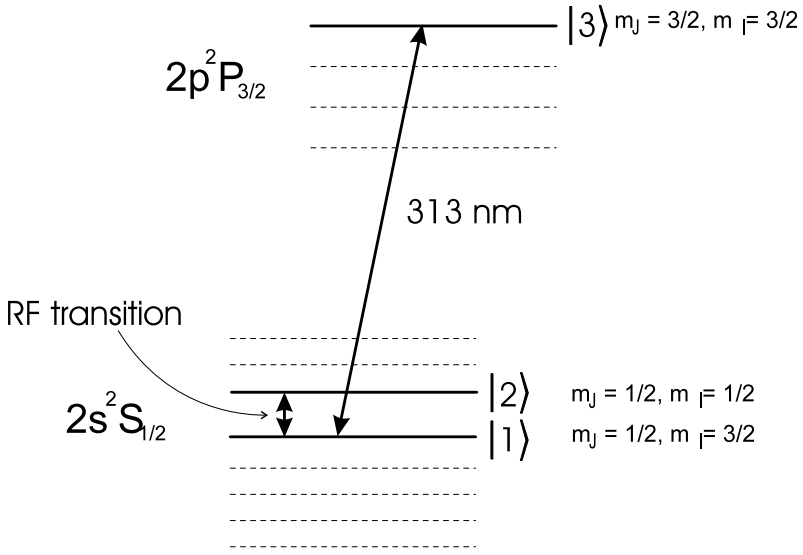

Fig. 3.3: A schematic diagram showing the physical realization of the three level Zeno scheme with a $^9Be^+$ ion. The relevant levels are labelled.

3.3 Evidence for the Zeno Phenomenon

3.3.1 The Quantum Zeno Effect with an Ensemble of Ions

With all the considerations discussed in the last section it seems an impossible task to actually test for the Zeno effect: not only do we need to approach the limit of continuous measurement but also devise a method by which measurement takes place without disturbing the system under observation. The first experiment which sought to prove the existence of the Quantum Zeno effect was undertaken by Itano et al at NIST [13]. Their experiment was based on an idea set out by Cook in his paper of 1988 [22]. Since this time there have been a number of further experiments and simulations attempted both in support and in contradiction to the original. In this section I shall outline a few of the experiments which have been done and also look at the proposals for others with reference to some of the objections that have been raised to the initial experiment.

The experiment performed by Itano and co-workers was performed on a large cloud of Beryllium ions in a Penning trap. The set of atomic levels used for the "unstable system" and "the measurement device" was a V-scheme: the ion could make transitions from the common ground state $|1\rangle$ to a metastable level $|2\rangle$ or to an upper excited state $|3\rangle$. The scheme is shown in figure 3.3 as it was achieved using $^9Be^+$. The system to be measured is the $|1\rangle \rightarrow |2\rangle$ hyperfine transition (the Zeno transition) at 320.7 MHz. Measurements are made by interrogating the system using a pulses of laser light resonant with the ($|1\rangle \rightarrow |3\rangle$) transition. This transition is a strongly allowed dipole transition and doubles as the laser cooling transition. If the Zeno transition is weakly driven, application of a measurement pulse will find the ion in either state $|1\rangle$ or state $|2\rangle$. In the first case, the ion can interact with the laser photons and fluorescence from the dipole transition is detected. In the second case, no fluorescence can be detected as the transition from the metastable level to the ground state is not resonant with the laser wavelength.

To test for the Zeno effect, the system could be driven with a π-pulse which, under normal conditions would transfer the population of level $|2\rangle$ into $|1\rangle$. The time evolution of a driven system is sinusoidal (Rabi oscillation) and is therefore approximately quadratic for $t \sim 0$. The Zeno effect can be produced if the system is interrogated at a frequency relating to the initial, quadratic period of evolution. If this is done each measurement projects the ion into the initial state. Figure 3.4 shows this process.

To fully understand the experiment we must look in greater detail at the mathematical description. Assuming the ion begins in state $|1\rangle$, if the transition $|1\rangle \leftrightarrow |2\rangle$ is driven using an on resonance RF (radio frequency) π-pulse of duration $T = \pi/\Omega$ (where Ω is the Rabi frequency of the driving field) then the populations of each level at the end of the driving pulse can be determined using a vector representation of the two level system. On transforming to a rotating frame of reference in which

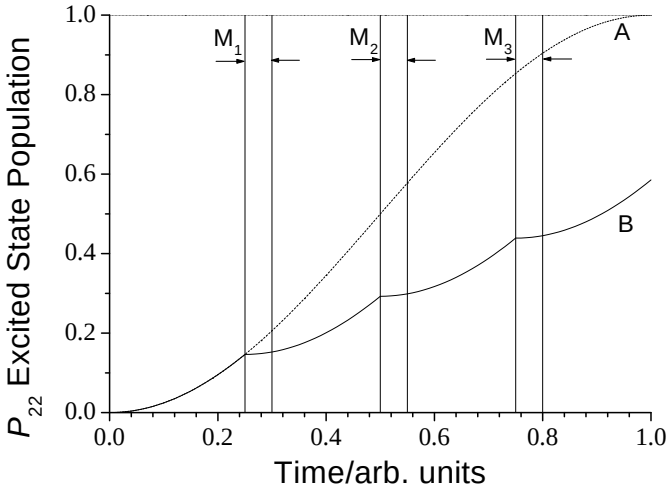

Fig. 3.4: A schematic representation of a two level driven system undergoing frequent measurement. The dashed curve, A, shows the driven evolution of the population from the ground state to the upper state. At each measurement, $M_1, 2, 3$ the evolution is interrupted and the system is *reset*. The time evolution with measurement is curve B [12].

the RF perturbation is stationary we can describe the system in terms of a vector $\mathbf{R} = (\mathbf{R_1}, \mathbf{R_2}, \mathbf{R_3})$.

$$\mathbf{R_1} = \rho_{12} + \rho_{21} \tag{3.9}$$

$$\mathbf{R_2} = i(\rho_{12} - \rho_{21}) \tag{3.10}$$

$$\mathbf{R_3} = \rho_{22} - \rho_{11} = P_1 - P_2 \tag{3.11}$$

here ρ is the density matrix and P_1 and P_2 are respectively, the probability of finding the ion in state $|1\rangle$ and that of it being in state $|2\rangle$. For an ion initially in state $|1\rangle$, in the case where no measurement pulses are applied the probability $P_2 = 1$ at time $\tau_0 = T$. If n measurement pulses are applied at times $\tau_k = kT/n = k\pi/(n\Omega)$, where $k = 1, \ldots, n$, then the value of $\mathbf{R}$ shortly before the first measurement pulse can be calculated.

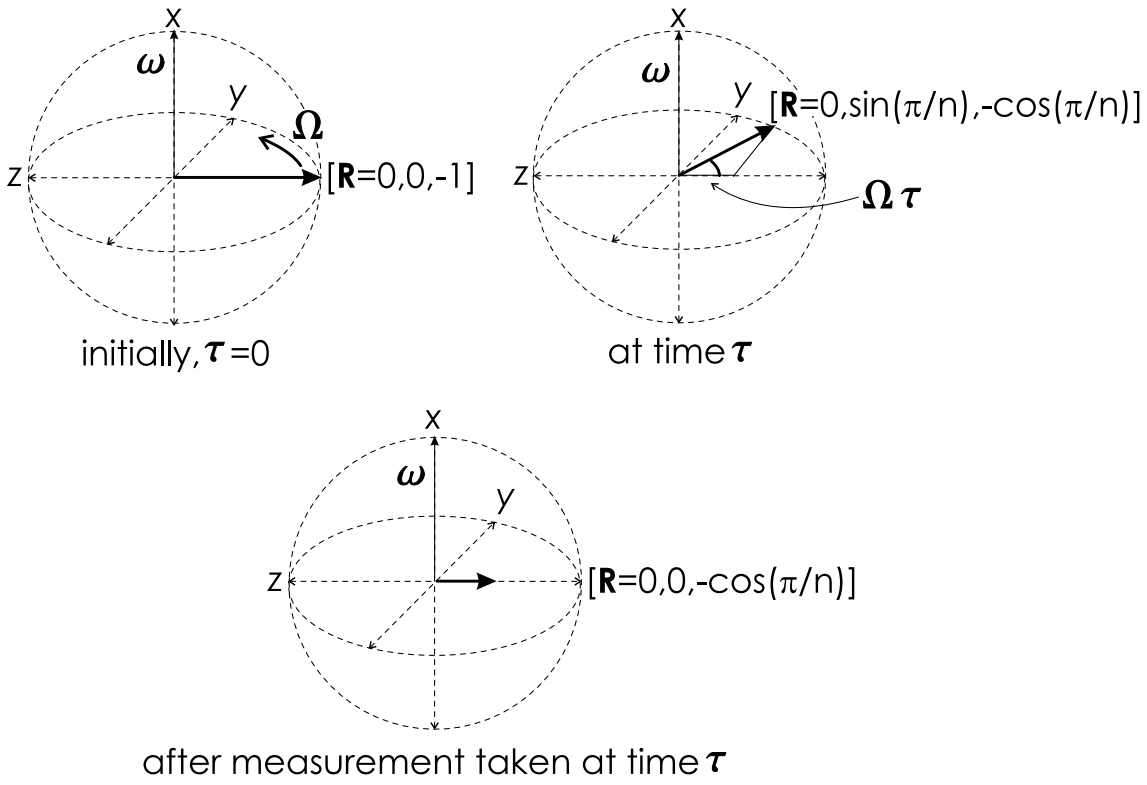

Fig. 3.5: A pictorial representation of the measurement process, see text.

The equation of motion for $\mathbf{R}$ is:

$$\frac{d\mathbf{R}}{dt} = \omega \times \mathbf{R} \tag{3.12}$$

where $\omega = (\Omega, 0, 0)$. With $\mathbf{R} = (0, 0, -1)$ at time $\tau = 0$, then at time $\tau = \pi/n\Omega$ just before the first measurement pulse is applied:

$$\mathbf{R} = [0, \sin(\Omega\tau), -\cos(\Omega\tau)] \tag{3.13}$$

$$\mathbf{R} = [0, \sin(\pi/n), -\cos(\pi/n)] \tag{3.14}$$

At the end of the measurement pulse the ion is left (the authors of reference [13] choose to say it is *projected*) in either level $|1\rangle$ or level $|2\rangle$. Both $\mathbf{R_1}$ and $\mathbf{R_2}$ are set to zero (the coherences ρ_{12}, $\rho_{21} = 0$) while $\mathbf{R_3}$ remains unaltered: after the first

measurement pulse $\mathbf{R}$ is the same as before the pulse but it is reduced in magnitude by a factor of $\cos(\pi/n)$. After n measurements the value of $\mathbf{R}$ is:

$$\mathbf{R} = [\mathbf{0}, \mathbf{0}, -\mathbf{cos^n}(\pi/\mathbf{n})] \tag{3.15}$$

this is shown pictorially in figure 3.5.

To determine what happens to the probability of finding the ion in state $|2\rangle$ we can use equation 3.11 and the conservation of probability $P_1 + P_2 = 1$.

$$P_2 = \frac{1}{2}(1 + \mathbf{R_3}) \tag{3.16}$$

Substituting in the value of $\mathbf{R_3}$ from equation 3.15 this becomes:

$$\begin{aligned} P_2 &= \frac{1}{2}[1 - \cos^n(\pi/n)] \\ &\simeq \frac{1}{2}[1 - \exp(-\frac{1}{2}\pi^2/n)] \quad \text{for large } n \end{aligned} \tag{3.17}$$

The experimental procedure can be divided into three phases; preparation of the initial state, measurement and assessment.

1. Preparation: The ions must be prepared in either the ground or the metastable states. If the 313 nm radiation is applied for ~ 5 seconds it was assumed that the majority of ions were in the ground state, the additional application of an RF π-pulse at 320.7 MHz was used to prepare the ions in the metastable state.

2. Measurement: This stage began immediately after preparation.
   The ground $\rightarrow$ metastable transition (or alternatively the metastable $\rightarrow$ ground) was driven with an RF π-pulse (of length T = 256 ms) while simultaneously applying n laser measurement pulses. The measurement pulses were of length $\tau_p = 2.4$ms, with separation T/n.

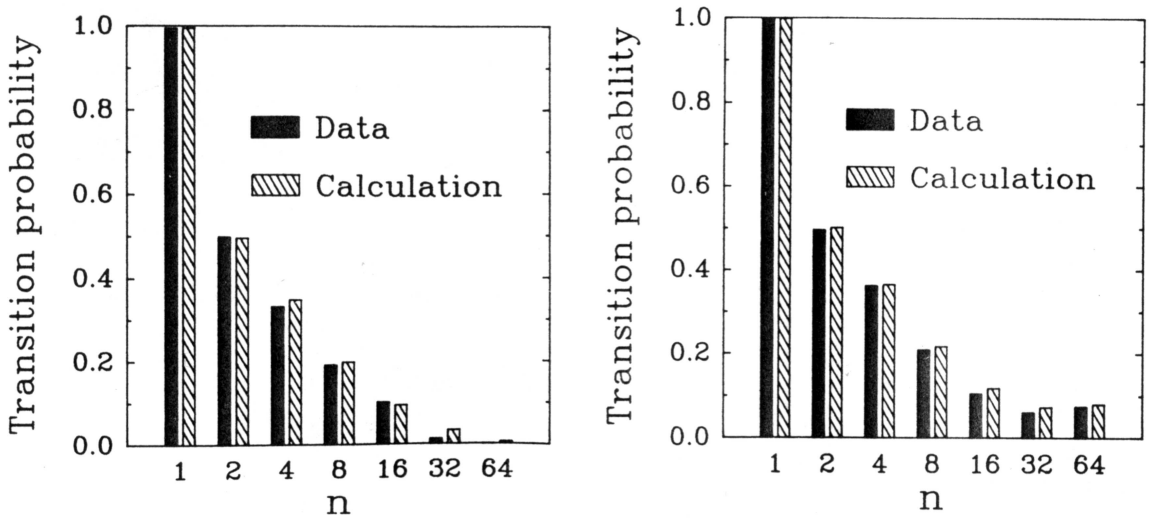

Fig. 3.6: Graphs showing the results for driving the ground → metastable transition (left) or the metastable → ground transition (right) when n measurements are made.

3. Detection: a final measurement pulse (of duration 100 ms) was applied to determine which state the ions were in. The number of photons detected was assumed to be proportional to the number of ions in the ground state at the end of the measurement phase of the procedure.

Note that the results of each individual measurement were not kept. The authors of reference [13] argue that this is not necessary as the emitted photons would be recorded by the electromagnetic field.

In order to determine whether the Zeno effect occurs the effect of different numbers of measurements (n = 1, 2, 4, 8, 16, 32 and 64) was investigated. Both transitions into and out of the metastable level (the latter being a case of a null measurement experiment in that if the ion is in fact frozen in the metastable level it can not fluoresce) were driven. It was found that a decrease in the probability of decay was seen for increasing numbers of measurements under both experimental regimes. The results are shown in figure 3.6.

The problem with this experimental approach is that although it follows the

original idea of Cook quite closely it differs in one important respect. Cook envisaged that the experiment should be done with one ion, however the experiment in reference [13] was carried out using a very large cloud. This leads to two related problems, one in the description of the experiment, namely the validity of the projection postulate and secondly the assumption that the laser pulses used could give accurate information on the state of the ions. Is performing the experiment once on an ensemble equivalent to performing it many times on a single ion? If not then this means that we can not actually tell the difference between the effect of measurement and of decoherence.

It is possible to derive the optical Bloch equations as if the atomic V-scheme and the laser field were included in one larger system. This is done in reference [14]. Analyzing the system in this way gives the same results as Itano found experimentally. The difference is that there is clearly no need to resort to the concept of wave function collapse. In this model the laser pulses merely cause random decoherence of the system and can not properly be described as measurements. This renders the results of the Itano experiment entirely unremarkable: as Ballentine writes in no uncertain terms, "... the quantum Zeno effect is not really a consequence of continuous observation, but rather of an excessively strong perturbation by an inappropriate apparatus..." [15].

The Bloch equations are part of the ensemble approach to quantum mechanics, an interpretation which does not admit the use of the projection postulate. Their use in analysis of Itano's experiment is entirely valid, but to say then that this can completely demystify the Zeno effect ignores an important fact: in the case of a single trapped ion, as in the original proposal the Bloch equations would be inappropriate precisely because they are associated with an ensemble. Thus to dismiss the Itano experiment purely on this point is hasty.

It is important that the Bloch equations show that while the calculated density

matrix for the ensemble is (mostly [1]) diagonalized at the end of a measurement pulse it does not allow us to make any assumptions about the particular states of individual atoms. This means that we can not interpret a lack of fluorescence as an indication that all the atoms are in state $|2\rangle$ or the detection of fluorescence as an indication that all the atoms are in state $|1\rangle$. An approach which does allow us unambiguous knowledge of individual atomic states uses the idea of *quantum trajectrories*. Quantum trajectories can be applied equally to single particle problems and ensemble systems. In fact the Bloch equations can be derived starting from the quantum trajectory description of a single radiating atom [23].

References [18, 23] use the quantum trajectory approach to describe Cook's atomic V-scheme system. For the laser pulse to be an effective measuring instrument in the Zeno effect experiment, the length of the laser pulse, τ_p, must clearly be much shorter than the length of the π-pulse, T_π. However it needs to be long enough and strong enough such that there is a high probability of producing fluorescence from level $|1\rangle$. It is also important that there is enough time between probe pulses for any population left in the excited state (level $|3\rangle$) to decay to the ground state. This means that the inverse Einstein coefficient, A_3^{-1} of level $|3\rangle$ must be small in comparison to the interval between measurement pulses: $A_3^{-1} \ll T_\pi - \tau_p$. Taking the case where the probe (RF) and measurement pulse are applied simultaneously, these considerations lead to the following restrictions on the experimental parameters:

$$\epsilon_p = \frac{A_3\Omega_2}{\Omega_3^2} \ll 1 \tag{3.18}$$

$$\epsilon_d = \frac{\Omega_3^2}{A_3^2} \ll 1 \tag{3.19}$$

$\Omega_{2,3}$ are the Rabi frequencies for the π-pulse and the probe pulse respectively.

These lead to the conclusion that in order to perform good state measurements

[1] Incomplete diagonalization is a result of the finite length of the measurement pulses.

the length of the laser pulse, τ_p must be such that:

$$\tau_p \gg \max[A_3^{-1}, \frac{A_3}{\Omega_3^2}] \tag{3.20}$$

Applying these conditions to a system of ions undergoing an experiment such as that performed by Itano et al gives results remarkably close to those found by the Bloch equation approach. The quantum trajectory method, however does ultimately give more information. Not only does the Zeno effect emerge as expected but the effect is enhanced as the laser pulses approach "ideal" measurements. In this regime the results of simulations show close correlation with those found using the projection postulate. The conclusion to be drawn is that laser pulses can, under certain conditions, be regarded as near perfect measurements and the projection postulate is adequate to describe the process.

The authors of reference [24] also use the method of quantum trajectories to study the case of a single atom. The evolving atomic system under scrutiny (two of the levels in the complete V-scheme) is treated as if it were embedded within the system-detector arrangement. In this way, a detuning exists between the measured system and the detection system. The amount of detuning is dependent upon the duration and strength of the pulse applied to drive the $|1\rangle \leftrightarrow |2\rangle$ transition and it is this same detuning which determines whether the pulse will actually provide information about the state of the ion so constituting a measurement. The Zeno effect emerges only when true measurement pulses are used.

The length of the measurement pulses used in the Itano experiment is governed by the length of time it would take every ion in the cloud to interact with the laser beam and scatter at least one photon. The pulses used were deemed to be good measurement pulses as each one could be expected to scatter ~ 72 photons. Following reference [23] it is possible to asses whether this was a good enough condition

by calculation of ϵ_p and ϵ_d. These values are 4.1×10^{-4} and 2.5×10^{-4} respectively. Since these numbers are clearly much less than 1 as required, we must conclude that the measurements they made were in fact good. It is still the case, however, that the only way to rid the experimental procedure of interpretational ambiguities is to use a single particle.

3.3.2 The Zeno Effect for Non-Atomic Systems

The main interest of this thesis lies in the area of trapped ions and therefore the experimental procedure outlined by Cook is of greatest relevance. However no discussion of the Zeno effect would be complete without some consideration of other schemes suggested for the experimental verification of the phenomenon.

Neutron Spin Flipping

This very interesting approach to the Zeno problem was suggested by a Japanese group [16]. Part of the motivation for this work is to prove that the work of Itano et al did not show evidence of the Zeno effect because the photons produced in the intermediate phase of the experiment were not explicitly recorded. It is argued that the absence of these measurements means that the wave function was not properly collapsed at each stage: no measurement was made. A scheme (shown in figure 3.7) is devised and modelled, whereby the spin rotation of a neutron in a magnetic field is inhibited [16, 25].

If a neutron finds itself in a magnetic field with direction perpendicular to its spin state then the nuclear spin of the neutron precesses about the magnetic field lines. In the experiment a spin up neutron traveling along the x-axis encounters a sequence of magnetic field "zones". The direction of the magnetic field within these zones is perpendicular to the spin state of the neutron in order to produce spin rotation: any neutron passing through the complete sequence of zones would

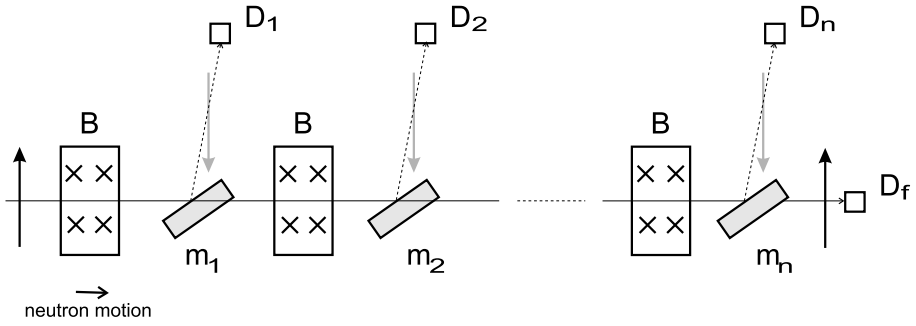

Fig. 3.7: Here a set up for demonstrating the Zeno effect is shown. The unstable system is the rotation of a neutron spin in a magnetic field. Spin rotation can occur in the areas, labelled B, where a magnetic field is present. Magnetic mirrors, $m_{1,2,\ldots,n}$, which allow the passage of spin-up neutrons are placed after each magnetic field zone so that any spin-down neutrons will be deflected and detected by detectors, $D1, 2, \ldots, n$. The neutron motion is from left to right, if it passes through the system without undergoing spin rotation it will reach the final detector, D_f. After reference [16].

be *flipped* from spin-up to spin-down. These "zones" are located within a second field of direction parallel to the neutron spin state, so that in between each zone the neutron spin is stable. Magnetic mirrors are placed between the magnetic field "zones" so that, if at any stage, the neutron spin is flipped it will be reflected and consequently registered by a suitable detector. There is also a final detector to determine whether the neutron passes through the system.

The action of the magnetic mirror is viewed as analogous to the action of the laser beam pulses in reference [13], the one collapses the neutron state into spin-up or spin-down where the other collapses the ion energy state into one of two available energy levels. The difference between this scheme and the Itano scheme is that intermediate measurements can be made owing to the presence of the detectors. Reference [16] follows the evolution of the system where detectors are in place and also with them omitted. Interestingly it is found that performing intermediate recordings makes no difference to the outcome of the experiment. However it is proposed that the two experiments are fundamentally different: with no detectors in place then coherence is maintained throughout the evolution, the neutron wave function is never collapsed,

while the presence of detectors means that coherence is lost, the wave function *is* collapsed at every stage. The conclusion drawn is that the Itano experiment does not prove the Zeno effect because it is analogous to the first regime. The argument is that the concept of wave function collapse is so intrinsic to measurement and consequently the Zeno effect that any process which can be discussed without the mentioning wave function collapse can not show the Zeno effect. This is certainly an original angle.

Position Measurement

This simulation [26] which looks at particle positions within a double well potential was developed with the intention of disproving the existence of the Zeno effect. At first glance it seems to succeed. On further reflection, however it not only shows evidence for the Zeno effect but makes a good illustration of the universality of the good measurement regime concepts explored in reference [24].

If a particle is trapped in one of the minima of a double potential well there is a finite probability that this particle will tunnel through the potential barrier into the other minima. Under conditions of free evolution the characteristic time constant for the tunneling process is T, and the particle oscillates back and forth between the two potential minima with a period of 2T. A Gaussian meter (that is a meter which can detect the particle over a certain distance, $-x \rightarrow x$, with a sensitivity which varies according to a Gaussian distribution over that distance.) is used to determine the position of the particle. The accuracy of the meter, i.e its width, and the frequency of measurements were varied.

The result of taking ever more frequent measurements on this system is actually found to produce what might be termed an anti-Zeno effect. The authors "improve" the accuracy of their meters and find that this makes the situation even clearer: frequent measurement undoubtedly helps the particle to tunnel. But could there be

another explanation for these results?

The obvious question with this work is: what of the Uncertainty Principle? In measuring the position of a particle to an arbitrary degree of accuracy an uncertainty is conferred to the particle momentum. The more accurately the position is measured, the more uncertain is the momentum. This means that two consecutive measurements are highly unlikely to give the same result. The authors do not seem to see the Uncertainty Principle as an intrinsic problem with their scheme. It is stated, however, that the measurement strength was chosen to minimize the uncertainty relationship.

Gagen et al re-examine the problem of position measurements in their 1993 paper [27]. The principal thrust of this work is the definition of a more sophisticated and indeed, realistic, model for the measurement process. In considering the measurement interaction they determine that for reasons connected to the uncertainty relationship there is what they term a "measurement back action". This means that as a result of a measurement the particle will on average gain some energy. The stronger and more accurate ($\Delta x \to 0$) the measurement the more energy is gained. In this way, after some number of measurements, the model of the double potential as a two level system breaks down as the particle has sufficient energy to pass over the potential barrier rather than tunnel through it. It is concluded that the results reported by Fearn and Lamb are a consequence of an inappropriately strong measurement regime: the particle wave packet becomes highly energetic very quickly and is not localized in either of the potential minima for a significant length of time. At an optimum measurement strength, the authors of reference [27] are able to show that the double well system does in fact exhibit the Zeno effect.

Collisional Relaxation.

There are few experimental investigations of the Zeno effect, two of which will be outlined here. They are very different in approach to the experiment proposed by Cook, and do not perhaps have the same appeal as they lack simplicity. However, they form an interesting digression.

The earlier of the two experiments [28] concerns inhibition of nuclear spin state relaxation (from ortho to para) of CH_3F molecules caused by collisions acting as measurements. The idea was first proposed in reference [29].

In this set up there is an equilibrium where multilevel molecules exist, some in an ortho and some in para nuclear spin states (the ratio is $\sim 1:1$). If a suitable electric field is applied, a Stark shift produces ortho and para energy level mixing which results in spin conversion. The idea is that the natural relaxation from one state to the other is slowed by frequent *measurement collisions*. The incidence of these collisions can be made to increase by raising the gas pressure.

In reference [13] the authors discuss the possibility of whether a collision might be a sufficient process to be called a measurement. They come to the conclusion that, as a collision "does not tend to project a single quantum system ... into one state or another", it can not be described as a measurement. The authors of the paper presently under discussion [28] do not specifically look at this question, however Block and Berman do discuss the issue in reference [14].

Looking at figure 3.8, the states within each subspace f or s are the eigenstates of the particle Hamiltonian, $\widehat{H_0}$. The curved arrows indicate transitions between levels within each subspace produced directly by collisions with the environment (other CH_3F molecules and background gases). Transitions between subspaces are allowed owing to $\widehat{V}$, the intramolecular perturbation. Thus the complete Hamiltonian of the

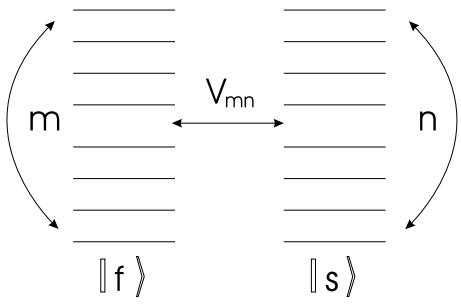

Fig. 3.8: The figure shows a multilevel system whose quantum states fall into two separate subspaces in which the observable $\widehat{O}$ has eigenvalues f and s. After reference [28].

free particle becomes:

$$\widehat{H} = \widehat{H_0} + \widehat{V} \tag{3.21}$$

The question asked is: if some test particles are introduced initially in one of the subspaces f or s, how will they relax and eventually reach an equilibrium distribution between sub-spaces? Reference [28] explains that there are two possible modes of relaxation: Classical or Quantum. The former is described as the process by which coupling to the environment via a collision produces direct transitions between sub-spaces f and s. This process is described by the relevant scattering cross-sections. The latter case of quantum relaxation, which produces transitions between sub-spaces, is not produced directly, but owing to mixing by the system's own Hamiltonian. This process of relaxation is expected to suffer the quantum Zeno effect as the result of interruption (measurement) due to collisions.

In the experiment, particles are prepared in a test chamber with a measured degree of enrichment of the ortho molecules. An electric field is applied to produce a Stark shift capable of mixing particular ortho and para states such that there is a $1/p$ dependence in the relaxation rate at low p (where p is the CH_3F pressure). As soon as the field is turned on the relaxation process begins. The experiment was repeated at various pressures and the ortho $\rightarrow$ para decay rate was found to decrease with increasing pressure. It is proposed that each time a molecule undergoes

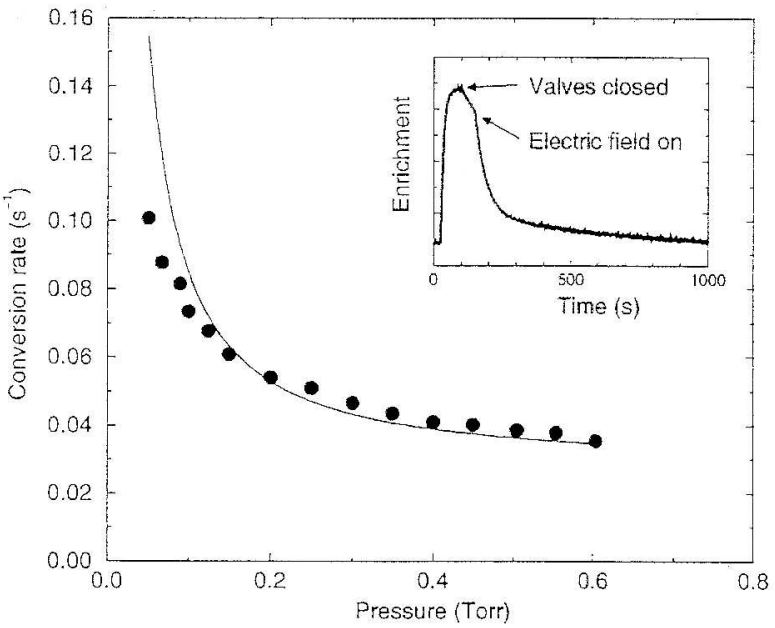

Fig. 3.9: A graph showing the conversion rate of CH_3F molecules from the ortho to para state at various pressures [28]. The inset shows a typical decay curve for a single experimental run.

a collision, the relaxation process stimulated by the electric field is interrupted and the molecule is projected back into its initial state. In this way it could be said that the electric field is analogous to the RF π-pulse in reference [13], mixing the ortho and para states of the molecules just as the RF mixes the metastable and ground states of the ions. The collisions then must be seen as analogous to the measurement pulses of the Itano experiment.

Figure 3.9 illustrates how the decay rate of the ortho molecules to para molecules appears to be decreased as pressure is increased.

The experimental scheme does have limitations however in the high pressure regime. At high pressures spin conversion due to direct transitions: classical relaxation, takes over. This process, which is linear with pressure, results in the destruction of the good measurement regime.

Inhibition of Quantum Tunneling.

This experiment looks at the inhibition of quantum tunneling [30]. In this case ultra cold Sodium atoms are confined within an accelerating, periodic optical potential. The rate at which the optical potential accelerates can be controlled to make the state of the system stable (such that tunneling is unlikely to occur), or unstable (so that the atoms will tunnel). The experiment consists of alternating unstable and stable periods. The periods of stability are used to assess how many of the atoms have tunnelled out of the trap. The time scales for the experiment were previously investigated to establish over what period the probability of tunneling is expected to be quadratic [31]. It was found that when the unstable regime was interrupted frequently within this quadratic region the rate of tunneling was significantly diminished compared to the case of free evolution.

The actual measurement process consisted of switching off the trapping beams and allowing ballistic expansion of the atom cloud. The distance moved by each atom during this period is proportional to the velocity of that atom at the time the beams were switched off. Those atoms still trapped at the time of switch off will be slower than those which have tunnelled out. The difference in velocity means that the *trapped* and *tunnelled* atoms will be spatially separated. A fluorescence image of the cloud can be used to determine the number of atoms which remain trapped at the end of the tunneling period. The duration of the measurement period is determined by the time required to obtain a sufficiently resolved image of the tunnelled and trapped atoms.

The calculated minimum interruption length to obtain good resolution of atom numbers is stated as 30 μs, which is why interruptions of shorter duration do not produce any effect. For the results shown in figure 3.11 the authors chose interruption lengths of 50 and 40 μs. It is not explained why these time durations were

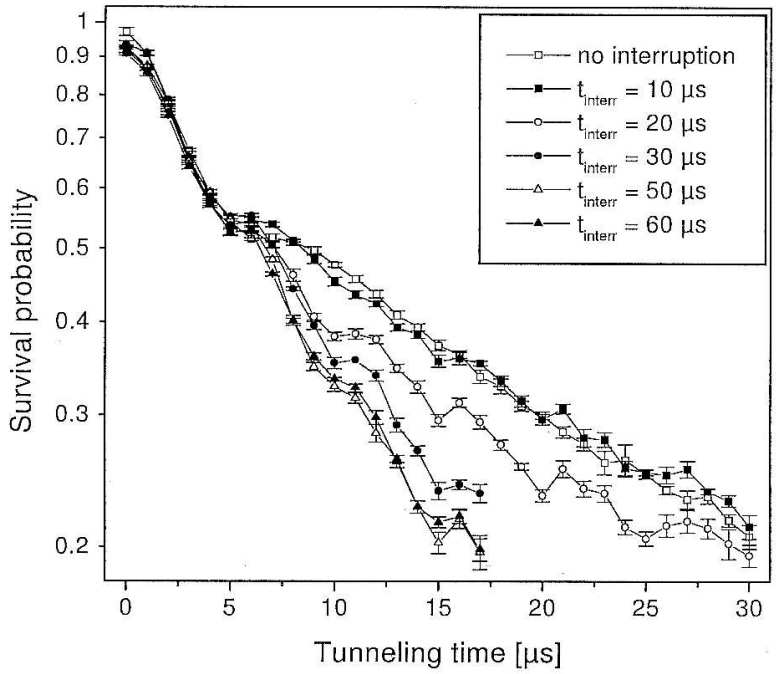

Fig. 3.10: The graph shows the tunneling probability as a function of the duration of tunneling acceleration. The hollow squares show the free evolution of the system. The other curves denote sequences where interruption of the time evolution occurred. These interruptions are of finite duration but there length varies as indicated. The time between interruptions remains constant at 5μs.

chosen and from previous reading it seems that intuitively one should choose the shortest possible measurement period to avoid the situation where the measurement interaction is inappropriately strong. The authors claim that in switching between unstable and stable regimes the initial state is re-established at the beginning of each new tunneling period regardless of how long the measurement period is. Once the threshold for sufficiently good resolution is reached the measurement time should have no effect on the strength of Zeno effect seen.

The effect of altering the measurement period is investigated. The results are shown in figure 3.10. It is actually done for the anti-Zeno effect (which will be explained later) and shows that the longer the measurement period, the stronger the anti-Zeno effect becomes. This is not surprising and it can be assumed that the

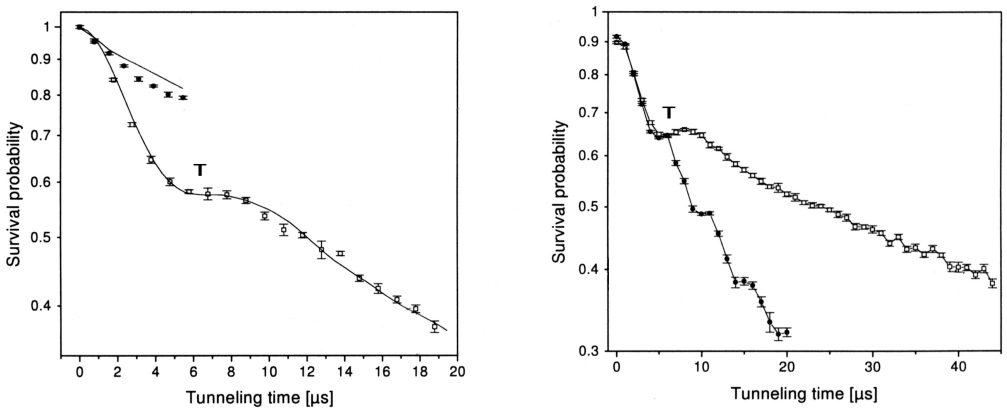

Fig. 3.11: The results of interrupting the evolution of a system of atoms tunneling out of a potential well, see text. On the left the Zeno effect is observed. On the right an "anti"-Zeno effect is seen [30]. In both graphs the hollow squares show the survival probabilities for an uninterrupted sequence while the solid circles show the experimental results for an interrupted time evolution.

result can be generalized to their investigation of the Zeno effect itself: increasing the measurement period is equivalent to increasing the measurement strength such that it is able to produce state reduction. The results seem to show that measurement periods which are shorter than 20 μs have no effect, measurement periods of lengths between 20 and 30μs have most effect, and once this minimum time duration is reached there appears to be no further advantage in further increase (the curves for 50 an 60 μs are very similar).

This experiment is most interesting as it looks at the spontaneous decay of an unstable state, rather than a driven transition: the quantum Zeno effect in its purest form. In figure 3.11, the Zeno and so called anti-Zeno effect are compared. Consider the uninterrupted time evolution for the system: there are clearly two distinct regimes of tunneling probability. Initially there is a quadratic region, this is followed by a distinct transition to an exponential region (marked as "T" on the graphs). The graph on the left shows experimental results for the case where the evolution of the system has been interrupted every 1 μs, i.e. while the system is

governed by the quadratic dependence. The other graph on the right shows how the rate of decay can actually be increased, here interruptions take place every 5 μs, that is after the system has reached the exponential regime. Unfortunately it is only in these two extremes that the authors look at the effect of altering the frequency of measurement. One of the predictions associated with the Zeno effect is that increased measurement frequency further enhances the effect, it is a pity that they did not explore this feature.

3.4 Further Work on the Cook/Itano System

In the following discussion the atomic scheme is that proposed by Cook [22]: a V-scheme consisting of a dipole transition for measurement, $|1\rangle \leftrightarrow |3\rangle$ and a transition to a metastable state, $|1\rangle \leftrightarrow |2\rangle$. This second is the "Zeno transition", which is inhibited.

3.4.1 An Experiment with a Single Ion

This experiment takes a novel approach though it is still essentially the same as the proposal by Cook [22]. A single $^{172}Yb^{+}$ ion is used. The Zeno transition is the $^2S_{1/2} \leftrightarrow {}^2D_{5/2}$ transition (at 411nm) while the measurement pulses drive the $^2S_{1/2} \leftrightarrow {}^2P_{1/2}$ transition (at 369nm). This is shown in figure 3.12.

The system is first prepared in the $^2S_{1/2}$ state. A series of alternating drive and measurement pulses then follow, as shown in figure 3.12. The drive pulses at 411 nm are of length $\tau = T_\pi(1 + 1/n)$, where T_π is the length of a π-pulse and n is an integer[2]. The probe pulses at 369 nm collapse the wavefunction of the ion at the end of each drive pulse. The ensemble average is recovered by repeating this sequence numerous times. The result of an individual measurement is either an "on" (there is fluorescence) or an "off" (no fluorescence). The probability of consecutive

[2]That the pulses are in fact of length $T_\pi(1 + 1/n)$ is a minor detail and will not be referred to again. It is the additional fraction of a π-pulse which is important.

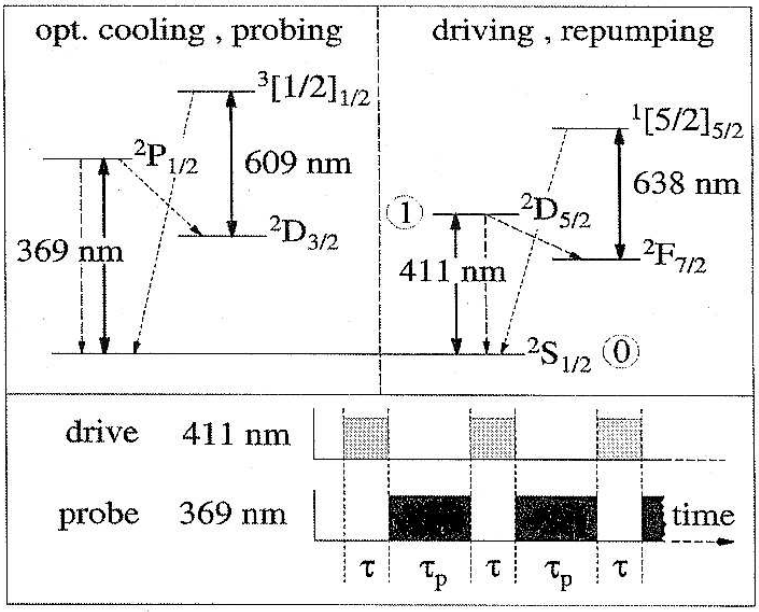

Fig. 3.12: The transitions in $^{172}Yb^+$ used for this investigation of the Zeno effect, the levels which form the V-scheme are indicated using the usual numbering convention. The measurement sequence is also shown in schematic form [32], where τ and τ_p are the respective lengths of the drive and measurement pulses.

measurements being the same depends on how closely spaced the measurements are: the closer they come the higher the probability that long strings of the same result occur: the Zeno effect.

To assess the effect of increasing measurement frequency the authors of this paper use an interesting approach. Rather than simply setting the length of the π-pulse and decreasing the length of time between measurement pulses, they choose to keep the measurement sequence unaltered while changing the length of a π-pulse for each experimental run. This is done by changing the detuning of the drive light: as the light becomes further detuned the length of a π-pulse for the system becomes longer and the time between measurements naturally constitutes a decreasing fraction of a π-pulse thereby effectively increasing the measurement frequency. In figure 3.13 the dependence of the transition rate upon detuning is shown.

Three detunings, labelled 5, 6 and 7 on figure 3.13 are chosen and explored

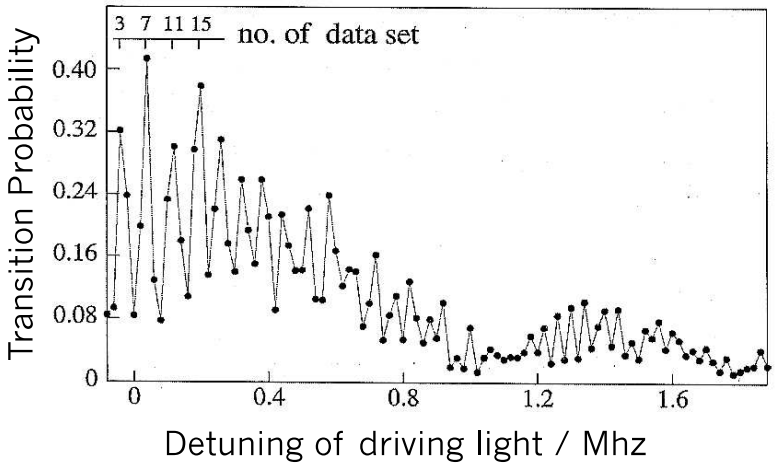

Fig. 3.13: The $|1\rangle \rightarrow |2\rangle$ transition probability changing as a function of the detuning of the driving radiation (411 nm) [32].

experimentally. The results in each case are shown in figure 3.14.

Referring to figures 3.13 and 3.14, first consider what happens when the drive radiation (411 nm) is on resonance (7). Here we expect that the measurement time is some large fraction of a π-pulse and so the probability of the population being driven into the dark state is high. The results are most likely to be a long series of "off" measurements. Taking a detuning which gives half the maximum transition probability (6), then the ion will be "on" and "off" with equal probability. Lastly, consider the case where the driving resonance is far enough from resonance to give a minimum transition probability (5). The time between measurements is now a minute fraction of the π-pulse and the measurements are effectively more frequent than in either of the previous cases. In this last case we expect the ion to be trapped in the ground state and the likelihood of long strings of "on" measurements to be greatly increased. This is indeed so, and the Zeno effect is demonstrated.

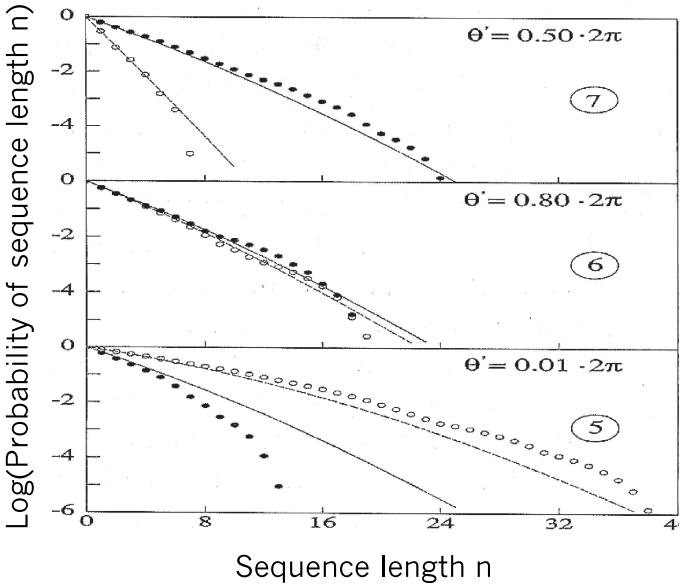

Fig. 3.14: The probability of seeing the ion in either state $|1\rangle$ (on) or state $|2\rangle$ (off) on consecutive readings for different detunings of the driving radiation i.e. different measurement frequencies [32]. The filled circles indicate "off" measurements while the hollow circles indicate "on" measurements. The numbers 5,6 and 7 refer to points on the transition probability versus detuning graph in figure 3.13. Here $\Theta' + 2\pi n = \sqrt{\Omega^2 + \Delta^2}\tau$, where Ω, Δ, τ and n are the Rabi frequency, detuning of the driving radiation, the length of the drive pulse and the number of measurements respectively.

3.4.2 A Proposal for an Experiment in the Continuous Regime

In this proposed experiment [20] a single ion is taken and subjected to *continuous* excitation on the Zeno transition whilst being simultaneously interrogated by frequent measurement pulses. The paper explores what happens as the time span between measurement pulses becomes vanishingly small and the continuous regime of measurement is approached.

The dynamics of a single ion are treated using the quantum trajectory approach, to avoid recourse to the projection postulate. In their earlier work [18, 23] the projection postulate is discussed for its usefulness as a simple tool, though like all simplifications it has limitations. The projection postulate assumes that measurements are "ideal", the quantum trajectory approach allows the authors to look at

what effect non-ideal measurements (such as laser pulses) would have on the evolution of the system.

As for other tests of the atomic Zeno effect the V-scheme proposed by Cook [22] is used. Rather than driving the Zeno transition with a π-pulse, the excitation field is on for an indeterminate time while the measurement pulses are applied. It is the time between measurements, Δt which is related to the length of a π-pulse: $\Delta t = T_\pi/n$, where n is the number of pulses delivered while the excitation field is on. The duration of the probe pulse, $\tau_p \ll \Delta t$ is governed by the conditions required to make it a good measurement pulse (see equation 3.20).

A weak drive on the $|1\rangle \rightarrow |2\rangle$ is provided by a continuously applied excitation field (where the length of a π-pulse is: $T_\pi = \pi/\Omega_2$ and Ω_2 is the Rabi frequency of the applied radiation field.). After a single measurement pulse ($|1\rangle \rightarrow |3\rangle$), there is an equal probability of finding the ion in either state $|1\rangle$ or state $|2\rangle$. Applying a series of measurement pulses results in a stochastic series of readings of the ion in either state $|1\rangle$ or state $|2\rangle$. The more closely spaced the measurements become the greater the chance that consecutive measurements will be the same. The results of computer simulations of the system are shown in figure 3.15.

The periods over which the ion is observed to be in state $|1\rangle$ are termed the *light* periods since the ion can fluoresce as the $|1\rangle \rightarrow |3\rangle$ transition is resonant with the measurement pulse. Those periods during which the ion remains in state $|2\rangle$ are termed *dark* periods because in this state the ion is unable to interact with the measurement pulse. The duration of these periods are respectively T_L and T_D. In the ideal case, when the time between measurements: $\Delta t \rightarrow 0$ it is expected that a continuous series of readings of the ion occupying either state $|1\rangle$ or state $|2\rangle$ will be observed. The lengths of the light and dark periods are found to be:

$$T_L \simeq T_D = \frac{4}{\Omega_2^2 \Delta t} \tag{3.22}$$

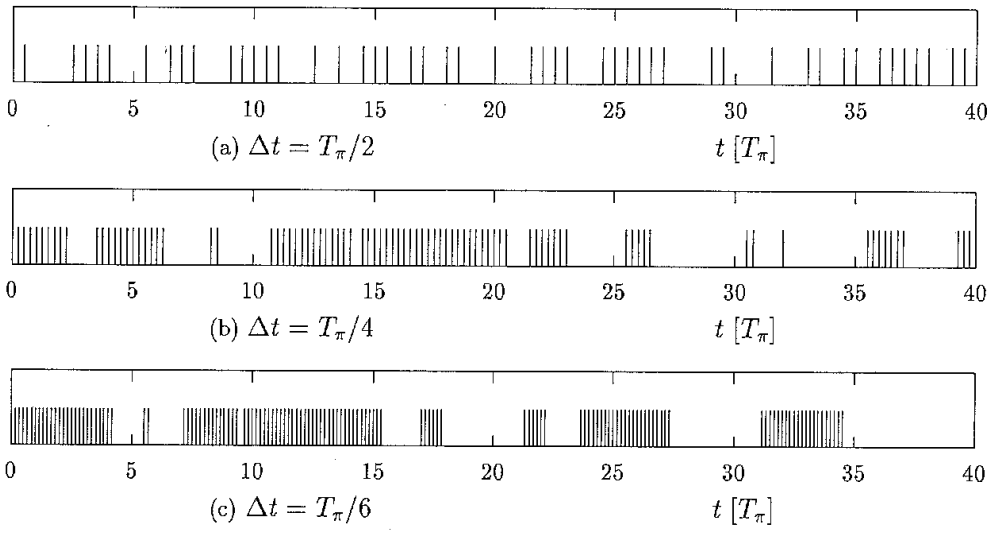

Fig. 3.15: The results of simulations of the Zeno system carried out with different spacings between probe pulses [20]. These show stochastic sequences of light and dark readings, the lines represent readings of the ion in the ground state and it emits a radiation burst. The length of a π-pulse is: $T_\pi = \pi/\Omega_2$.

Unfortunately, measurements will never be entirely ideal and this should be taken into account. The situation is described as follows: at the end of a probe pulse the system will be either in level $|1\rangle$ or it will be in level $|2\rangle$. Taking the first instance, during the probe pulse the ion will emit photons, and the last emission will indeed leave it in the ground state. There is however a possibility that the ion will have acquired small state $|2\rangle$ component for the duration of the probe pulse, it will also have a small state $|3\rangle$ component which decays rapidly at the end of the pulse. In the second case a small state $|1\rangle$ component is present due to the finite duration of the probe. This means that the density matrices describing the ion state after a probe pulse will be very close but not equal to $|1\rangle\langle 1|$ and $|2\rangle\langle 2|$ respectively. This small correction means that the lengths of light and dark periods are now:

$$T_L \simeq T_D = \frac{\tau_p + \Delta t}{\Delta t} \frac{4}{\Omega_2^2 \Delta t} \tag{3.23}$$

This clearly approaches the case for ideal measurements when $\tau_p \ll \Delta t$.

The ultimate limitation on the extent to which the ion state can be frozen is governed by the conditions imposed on Δt: ie that $\Delta t \gg A_3^{-1}$ (where A_3^{-1} is the inverse Einstein coefficient of level $|3\rangle$), see section 3.3.1. This means that Δt can not in fact reach the limit $\Delta t \to 0$ which gives a finite maximum length to the light and dark periods observed.

$$\lim_{\Delta t \to 0} T_L = \frac{A_3^2 + 2\Omega_3^2}{\Omega_2^2 A_3^3}\Omega_3^2 \tag{3.24}$$

$$\lim_{\Delta t \to 0} T_D = \frac{\Omega_3^2}{\Omega_2^2 A_3} \tag{3.25}$$

where Ω_3 is the Rabi frequency of the measurement laser (driving $|1\rangle \to |3\rangle$).

To conclude, this paper describes a possible way of assessing the Zeno effect using a theoretical base which does not rely on the projection postulate. The limitations of the set up are also well investigated, specifically the effect of taking imperfect measurements. This yields the result that just as the projection postulate is an idealized/simplified description of the measurement process the results which it predicts: the total freezing of the atomic state, is an ideal and can not be achieved.

3.4.3 Approaching the Ideal: The Zeno Effect in a Spontaneously Decaying System

One of the principal difficulties with investigating the Zeno phenomenon in its truest form, i.e the inhibition of a spontaneous decay process, is that the time scales involved are so short. As a result, in order to investigate the effect it has been necessary to resort to looking at driven transitions for which the "Zeno susceptible" time interval is significantly longer. The ultimate challenge would be to test the theory on a system which, even if it could not be spontaneously decaying at least

showed decay properties that greatly resembled that process: or more so than the Rabi-oscillation of the Cook [22] proposal. Steps towards achieving this goal are discussed in reference [33]. The authors propose a system which is similar to the familiar V-scheme, however, by inducing a linewidth in state $|2\rangle$ the behaviour of the driven transition is altered. In the usual case, driving the $|1\rangle \rightarrow |2\rangle$ transition of the V-scheme forces the population into Rabi oscillation. If however, level $|2\rangle$ has a finite linewidth (as does a spontaneously decaying level), then the population initially in state $|1\rangle$ will decrease exponentially. This type of behaviour is similar in form to that of spontaneous decay, but the time scale for the quadratic behaviour, which the Zeno effect requires, is much longer and also controllable.

In the following the terminology is slightly altered from normal in that the measurement transition is now between states labelled $|1\rangle$ and $|5\rangle$. The Zeno transition remains the $|1\rangle \rightarrow |2\rangle$ transition.

In order to produce an effective linewidth in state $|2\rangle$ new energy levels, into which the population of state $|2\rangle$ can be transferred, are added to the original V-scheme. In the simplest case state $|2\rangle$ decays spontaneously into a state $|3\rangle$. A slightly more sophisticated approach allows tuning of the decay parameters: by making the $|2\rangle \rightarrow |3\rangle$ a driven transition and introducing a further level (or levels) into which level $|3\rangle$ can spontaneously decay. By alteration of the Rabi frequencies of the lasers driving the $|1\rangle \rightarrow |2\rangle$ and the $|2\rangle \rightarrow |3\rangle$ transitions, both the time constant of the exponential behaviour and the length of the short time scale quadratic regime can be changed. This is in contrast to the simplest case (spontaneous decay of $|2\rangle \rightarrow |3\rangle$) where all parameters are fixed by the decay constant of the third level. Figure 3.16 shows two of the three atomic schemes proposed in this paper. The work was conceived with the intention that it should be implemented using a trapped ion.

The authors examine the time evolution for the two systems for both short and

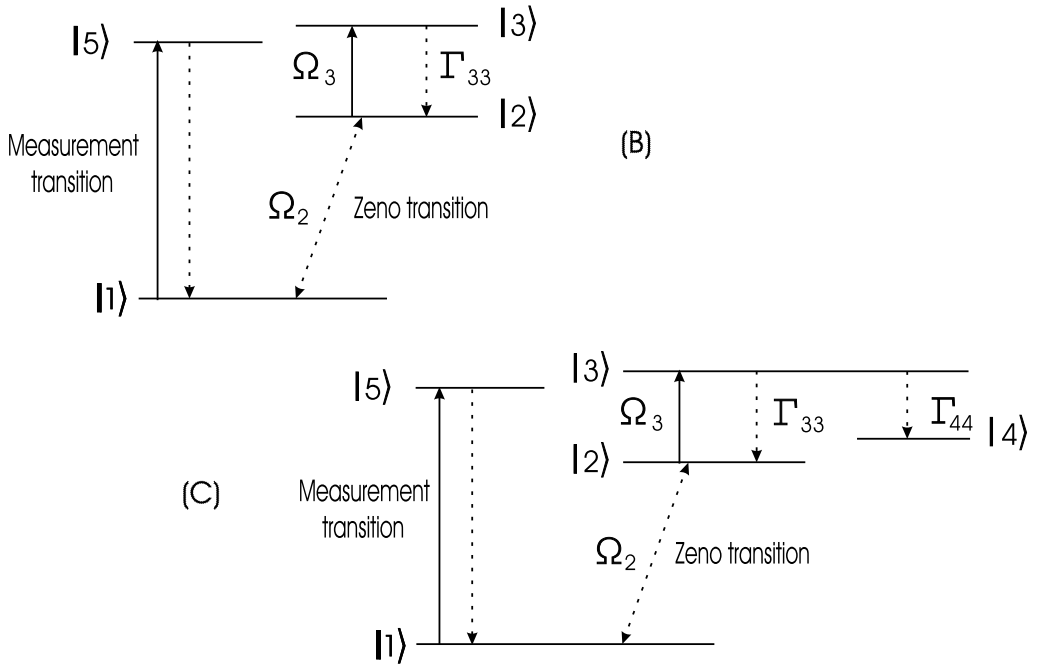

Fig. 3.16: Two "tunable" schemes proposed to investigate the Zeno effect using a pseudo-spontaneously decaying system [33]. The values Γ and Ω are the decay constants and Rabi frequencies for the various transitions.

long time scales and arrive at expressions for the expected time dependence of ρ_{11}, the population of level $|1\rangle$. For long time scales (t $> 200\Gamma_{33}^{-1}$, where $Gamma_{33}^{-1}$ is half the Einstein coefficient of the $|1\rangle \rightarrow |3\rangle$ transition) the population ρ_{11} is indeed found to decrease exponentially to a value of 0.5 when the $|1\rangle \rightarrow |2\rangle$ transition is driven. This is the case for both structure B and C, although the exact nature of the population evolution varies for each scheme. The short term time dependence (t $> 200\Gamma_{33}^{-1}$) is:

$$\rho_{11}(t) = 1 - \frac{\Omega_2^2}{4} t^2 \tag{3.26}$$

This is the same for both of the schemes treated and clearly shows the desired quadratic relationship with time. The length of the quadratic region can be shown to be:

$$T_q \sim 4\frac{\Gamma_{33}}{\Omega_3^2} \tag{3.27}$$

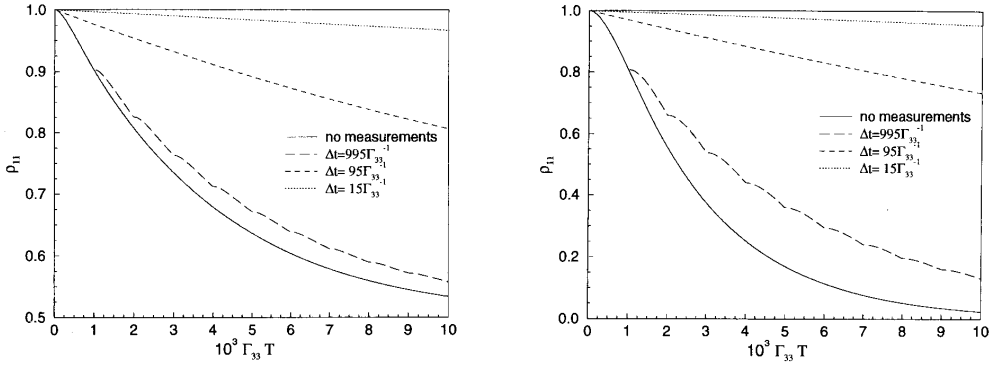

Fig. 3.17: The results of simulations of the behaviour of the configurations B and C [33]. The parameters used were the similar in both cases: $\Omega_2 = 0.0012\Gamma_{33}$ and $\Delta_2 = \Delta_3 = 0$. For structure C $\Gamma_{33} = \Gamma_{44}$. The Rabi frequency of the measurement pulse is $\Omega_5 = 4\Gamma_{33}$ and the decay constant of the upper state of the measurement transition (level $|5\rangle$)is $\Gamma_{55} = \Gamma_{33}$. The duration of the measurement pulse is $\tau_p = \Gamma_{33}^{-1}$ while the pulse separation is given by Δt.

The results of modelling systems B and C are reproduced in figure 3.17. The unperturbed time evolution of the two systems (solid lines) is clearly very different to what is usually expected for a coherently driven system. Assuming that the population is initially in the ground state, if radiation resonant with the $|2\rangle \rightarrow |3\rangle$ transition is applied, then on driving the Zeno transition ($|1\rangle \rightarrow |2\rangle$) with a π-pulse, the ground state population is expected to undergo initially quadratic then exponential decay. This new type of behaviour, resulting from the induced linewidth in the upper state, looks very much like spontaneous decay. However, unlike a true spontaneously decaying system, the rate of decay can be altered and the quadratic region extended sufficiently to perform an investigation of the Zeno effect.

The effect of applying measurement pulses was investigated for both structures B and C. Three different measurement frequencies were chosen (dotted lines on figure 3.17). For both structures, as the number of measurements increases the decay of ρ_{11} is increasingly inhibited. This seems a clear manifestation of the Zeno effect.

To conclude, in this section three experimental investigations of the atomic Zeno

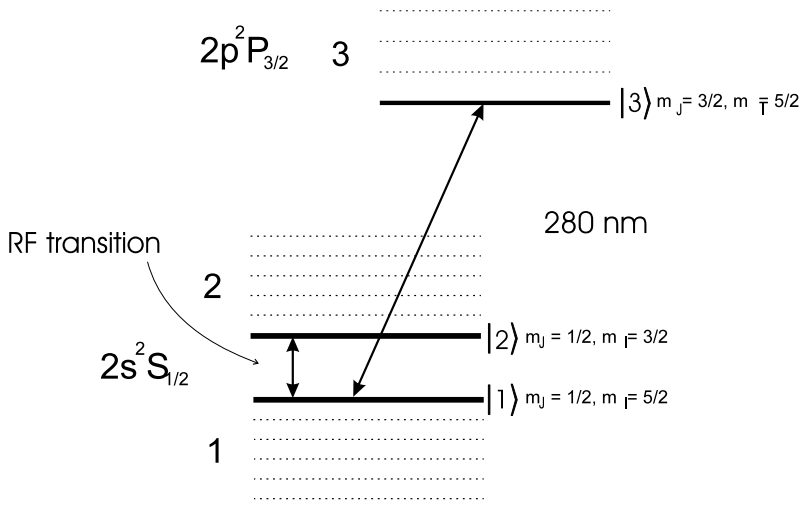

Fig. 3.18: The energy levels of $^{25}Mg^{+}$ required for a realization of the quantum Zeno effect.

effect, one actual and two proposed, were discussed. These experiments deal only with single ions where a transition to a metastable state is inhibited due to frequent interrogation by a laser pulse. The results, experimental and simulated show clear evidence for the Zeno effect. The action of a laser pulse as a measurement has been well characterized and the use of single particles means that the interpretation of the results is free from the ambiguities surrounding the original experiment of Itano et al. So, the results should be uncontroversial.

3.5 Experimental Outlook

It was hoped that it might be possible to first complete a set of investigations along the lines proposed by Beige [20]. The system of choice was $^{25}Mg^{+}$; the energy levels involved are shown in figure 3.18. Of course, $^{9}Be^{+}$, as used by Itano et al [13] would be equally viable. In fact $^{9}Be^{+}$ was used in the preliminary stages of this investigation, but it was decided that greater success could be achieved by switching to $^{25}Mg^{+}$. The principal reason for this switch was laser stability: the minimum

Table 3.1: The On:Off ratios for quantum jumps in $^{25}Mg^{+}$ varying with magnetic field.

B-field/T	lower trans.	upper trans.
1	11.80	22.80
1.3	12.69	20.79
1.8	13.90	19.27

frequency jitter in the stabilized laser frequency could only be reduced to 12 MHz (in the U. V). For $^{25}Mg^{+}$, the laser cooling transition has a linewidth of 43 MHz; this is several times greater than the frequency instability, so minor excursions in the laser frequency make little difference to the fluorescence level observed from the ion. On the other hand, the natural linewidth of the $^{9}Be^{+}$ laser cooling transition is 19 MHz which meant that stable signal was very difficult to achieve with this ion.

The quantum jump statistics of Mg^{+} are discussed in chapter 5. These naturally occurring transitions to a dark state will interfere with the Zeno statistics. Fortunately, with Mg^{+} we have the option of cooling on two different transitions, and importantly, in the case of $^{25}Mg^{+}$ there is a different characteristic quantum jump rate associated with each transition. Generally it is convenient to talk of On:Off ratios, this is the ratio of the times the ions spends fluorescing to that which it spends in the dark state. The two laser cooling transitions are $^{2}S(m_J = 1/2, m_I = 5/2) \rightarrow ^{2}P(m_J = 3/2, m_I = 5/2)$ (upper) and $^{2}S(m_J = -1/2, m_I = -5/2) \rightarrow ^{2}P(m_J = -3/2, m_I = -5/2)$ (lower). At a magnetic field of 1 T, the On:Off ratio for the lower transition is approximately half that for the upper transition. At high magnetic fields the two On:Off ratios approach the value for the isotopes without hyperfine structure (16:1). The respective jump rates at three different values of magnetic field are shown in table 3.1. In order to minimize the interference of the natural quantum jumps the upper transition would be used for cooling. The magnetic field was chosen to keep the laser cooling transition

frequency near a recognizable feature of the Iodine spectrum.

A further consideration for moving to the use of Mg^+ in this experiment was to do with the trap itself. The R_0^2 value for the trap used was such that at the magnetic field chosen, for the light Be^+ ions several hundred volts would be required to produce a spherical potential within the trap and such high voltages are inconvenient. The heavier ion, Mg^+ requires a much lower voltage to reach the same trapping regime.

The systems highlighted in the proposal of Plenio [33] could also be experimentally implemented. It is suggested that the first of these, labelled system B in figure 3.16, could be realized in $^{24}Mg^+$ at a field of 1 T: level $|1\rangle$ is the $m_J = -1/2$ sublevel of the $^2S_{1/2}$ state with level $|2\rangle$ as the $m_J = 1/2$ of the same state, level $|3\rangle$ has to be the $m_J = 3/2$ state of the $^2P_{3/2}$ level (as it decays exclusively to level $|2\rangle$). Levels $|1\rangle$ and $|2\rangle$ are separated by ~ 10 GHz at 1 T. The measurement transition is the laser cooling transition: $^2S(m_J = -1/2) \rightarrow {}^2P(m_J = -3/2)$. The other configuration, system C in figure 3.16, would be possible using $^9Be^+$, at a 1 T field. In this case the transition between levels $|1\rangle$ and $|2\rangle$ are within the $2s^2$ $S_{1/2}$ manifold: level $|1\rangle$ is $(m_J = 1/2, m_I = 3/2)$ and level $|2\rangle$ is $(m_J = 1/2, m_I = 1/2)$. These two levels are separated by roughly 312 MHz. Level $|3\rangle$ is the $(m_J = 1/2, m_I = 1/2)$ sublevel of $^2P_{1/2}$; this state can decay to level $|2\rangle$ or to level $|4\rangle$ which is the $(m_J = -1/2, m_I = 1/2)$ sublevel of $^2S_{1/2}$. The upper state of the measurement transition is the $m_J = 3/2$ sublevel of $2p$ $^2P_{3/2}$, which can be excited exclusively if circularly polarized light is used.

If these experiments could be realized, not only would the quantum Zeno effect could be shown to exist independent of the projection postulate and other formalities of quantum mechanical interpretation, it might also be shown that it is a real phenomenon present in incoherent decay processes: the true Zeno effect. This could have implications in the study of many atomic processes: the quantum Zeno effect has been suggested as a mechanism in lasing without inversion [34] and also as

a means of preventing decoherence in quantum computational applications (error prevention [35]).

References

[1] Lewis Carroll, Mind, 4, (1895)

[2] D. R. Hofstadter,*Gödel, Escher, Bach an Eternal Golden Braid*, Penguin Books, (1999)

[3] T. L. Heath, *A History of Greek Mathematicians 1*, Oxford (1931)

[4] S. M. Cohen, *http://faculty.washington.edu/smcohen/320/ZenoArrow.html*

[5] J. J. O'Connor and E. F. Robertson, *http//www-gap.dcs.st-and.ac.uk/∼history/mathematics/Zeno_of_Elea.html*

[6] C. B. Chiu, E. C. G. Sudarshan and B. Misra, *Phys. Rev. D* **16**, 520 (1977)

[7] B. Misra and E. C. G. Sudarshan, *J. Math. Phys* **18**, 756 (1977)

[8] A. Peres, *Am. J. Phys* **48**, 931 (1980)

[9] I. Singh and M. A.B.Whitaker, *Am.J. Phys* **50**, 882 (1982)

[10] H. Nakazato, M. Namiki, S. Pascazio, H. Rauch, *Phys. Let. A* **217**, 203 (1996)

[11] D. Home, M. A. B. Whitaker, *J. Phys. A* **19**, 1847 (1986)

[12] A. Shenzle, *Cont. Phys.* **37**, 303 (1996)

[13] W. M. Itano, D. J. Heinzen, J. J. Bollinger and D. J. Wineland, *Phys. rev. A* **41**, 2295 (1990)

[14] E. Block and P. R. Berman, *Phys. Rev. A* **44**, 1466 (1991)

[15] L. E. Ballentine, *Phys. Rev. A* **43**, 5165 (1990)

[16] S. Inagaki, M.Namiki and T. Tajiri, *Phys. Let. A* **166**, 5 (1992)

[17] W. M. Itano, D. J. Heinzen, J. J. Bollinger, *Phys. Rev. A* **43**, 5168 (1990)

[18] A. Beige, G. C. Hegerfeldt and D. G. Sondermann, *Quant. SemiClass. Opt* **8**, 999 (1996)

[19] Z. Hradil, H. Nakazato, M, Namiki, S. Pascazio, H. Rauch, *Phys. Let. A* **239**, 333 (1998)

[20] A. Beige and G. C. Hegerfeldt, *J. Phys. A* **30**, 1323 (1997)

[21] D. Home and M. A. B. Whitaker, *An. Phys* **258**, 237 (1997)

[22] R. Cook, *Phys. Scr* **T21**, 49 (1988)

[23] A. Beige and G. C. Hegerfeldt, *Phys. Rev. A* **53**, 53 (1996)

[24] M. J. Gagen and G. J. Milburn, *Phys. Rev. A*, 1467 **47** (1993)

[25] S. Pascazio, M. Namiki, G. Badurek and H. Rauch, *Phys. Let. A* **179**, 155 (1993), 155-160

[26] H. Fearn and W. E. Lamb (Jr), *Phys. Rev. A* **46**, 1199 (1992)

[27] M. J. Gagen, H. M. Wiseman and G. J. Milburn, *Phys. Rev. A* **48**, 132-142 (1993)

[28] B. Nage, L. J. F. Hermans and P. Chapovsky, *Phys. Rev. Lett* **79**, 3097 (1997)

[29] P. L. Chapovsky, Physica (Amsterdam), **233A**, 441 (1996)

[30] M. C. Fischer, B. Gutiérrez-Medina and M. G. Raizen, *quant-phot/0104035*, (2001)

[31] S. R. Wilkinson, C. F. Bharucha, M. C. Fischer, K. W. Madison, P. R. Morrow, Q. Nlu, B. Sundaram and M. G. Raizen, *Nature* **5**, 575 (1997)

[32] Ch. Balzer, R. Huesman, W. Neuhauser, P. E. Toschek, *Opt. Comms* **180**, 115 (2000)

[33] M. B. Plenio, P. L. Knight, R. C. Thompson, *Opt. Comm* **123**, 278 (1996)

[34] F. B. de Jong, R. J. C. Spreeuw and H. B. van Linden van den Heuvell, *Phys Rev A* **55**, 3918 (1997)

[35] L. Vaidman, L. Goldenberg and S. Weisner, *Phys Rev A* **54**, R1745 (1996)

CHAPTER 4

The Experimental Set Up

The experiments described in this thesis were carried out in two different systems, one based around a superconducting magnet (the Zeno system) and the other based around a conventional electromagnet (the split-ring system). The Zeno experiment itself requires the stability of field produced by a superconducting magnet. Preliminary work: the investigation of quantum jump statistics of magnesium, could be carried out in the split-ring system. The work on axialization was to have been completed in the Zeno system, however, owing to unforeseen circumstances this work was also done in the split-ring system.

The first and second sections of this chapter will look at the two systems individually. Special attention is paid to the Zeno system owing to the unconventional trap design and because certain features have undergone major redesign since the trap was initially built. The split-ring system on the other hand is already well documented. The final sections will deal with those pieces of apparatus which were common to both arrangements: the laser, data collection and the techniques used to trap single ions.

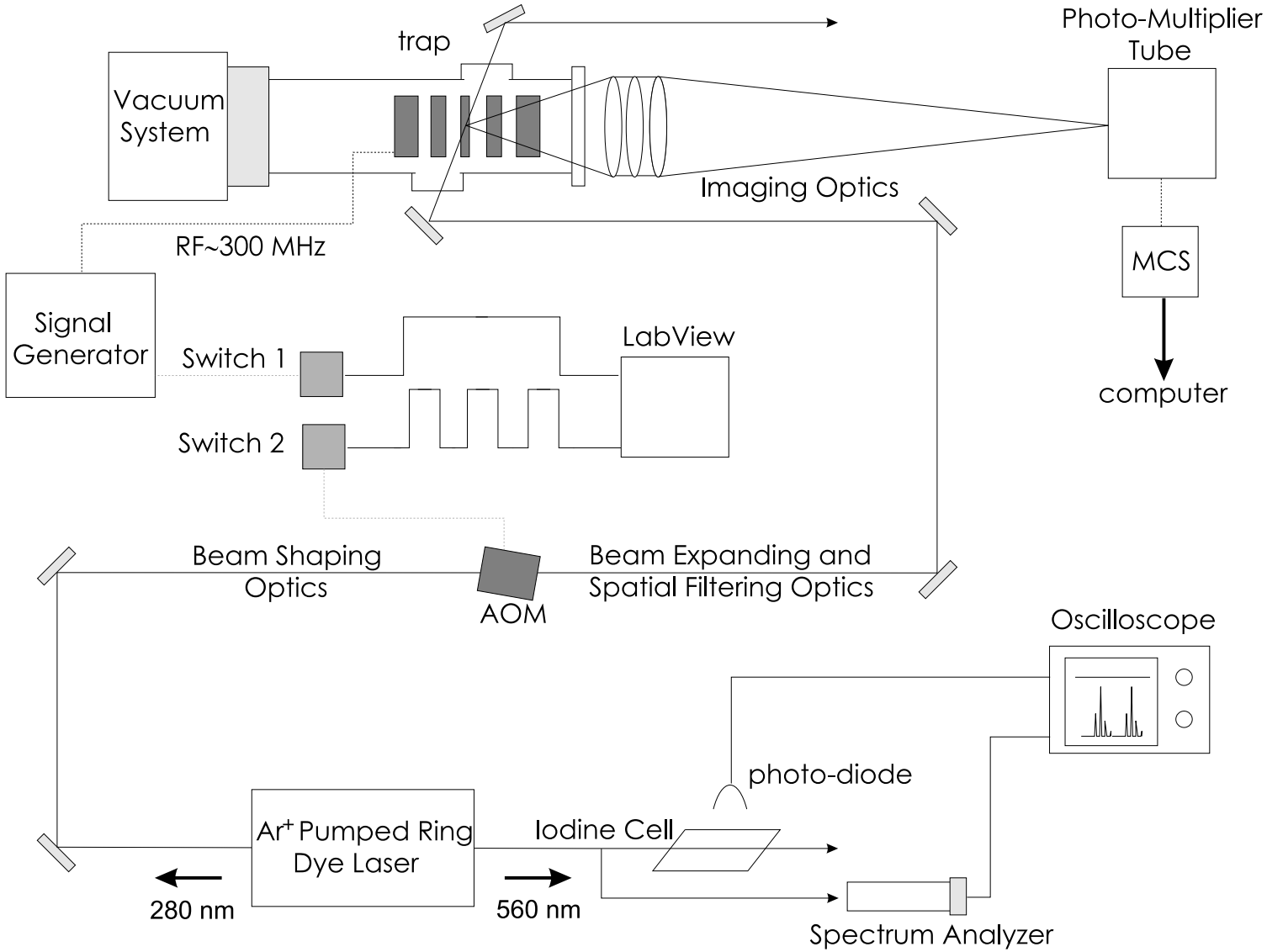

Fig. 4.1: A schematic diagram of the experimental set up.

4.1 The Zeno System

As explained, our demonstration of the Zeno Effect relies on being able to accurately address a specific hyperfine level. The frequency of the transition must remain constant on the time scale of the experiment, thus a magnetic field which fluctuates rapidly and unpredictably, such as one produced by an electro-magnet is clearly unsuitable. The field of a superconducting magnet on the other hand is extremely stable and decays very slowly at a calculable rate, this results in a small variation in the frequency of the hyperfine transition on a time scale of days. A schematic diagram of the system is shown in figure 4.1.

4.1.1 The Superconducting Magnet

The magnet used in this experiment has a vertical bore into which the trap can be inserted. The magnetic field lines are parallel to the bore of the magnet and the field strength has a maximum at a particular height (27 cm) up the bore. The trap must be co-axial with the magnet and sit with its centre at the point of maximum field strength. A diagram of the magnet is shown in figure 4.2.

The arrangement produces certain logistical difficulties with positioning of laser cooling beams and imaging optics. The trap is inaccessible once it is in the correct position for trapping. This means that the passage of the laser beam through the trap and the imaging optics must be optimized before the trap goes inside the magnet. At present the trap and all the optics are arranged on a frame work of studding; the entire ensemble can then be moved up and down parallel to the bore of the magnet. In this way, adjustments can be made before the trap is in position and the alignment will not be lost when the trap is raised into the magnet.

The magnetic field produced can be as great as 2.5 T and it has been calculated that the decay of the field after energizing is of the order of 1×10^{-7} T/hour.

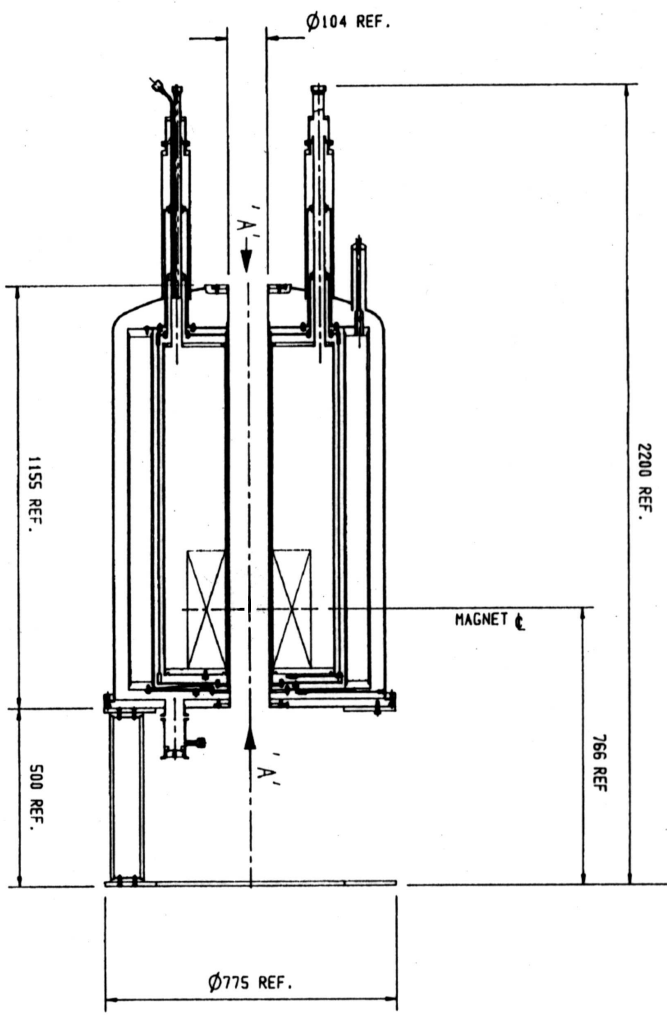

Fig. 4.2: A schematic diagram of the superconducting magnet.

As an indication of the stability of the field some preliminary data to find the $2^2S_{1/2}(m_I{=}3/2,m_J{=}1/2)\rightarrow 2^2P_{3/2}(m_I{=}3/2,m_J{=}3/2)$ hyperfine transition in Beryllium is included in figure 4.3. The width of the transition under the driving conditions used is 25 Hz, such experiments can be completed using the field of an electromagnet [1, 2], but in these cases the width of the transition is nearer a few hundred kHz.

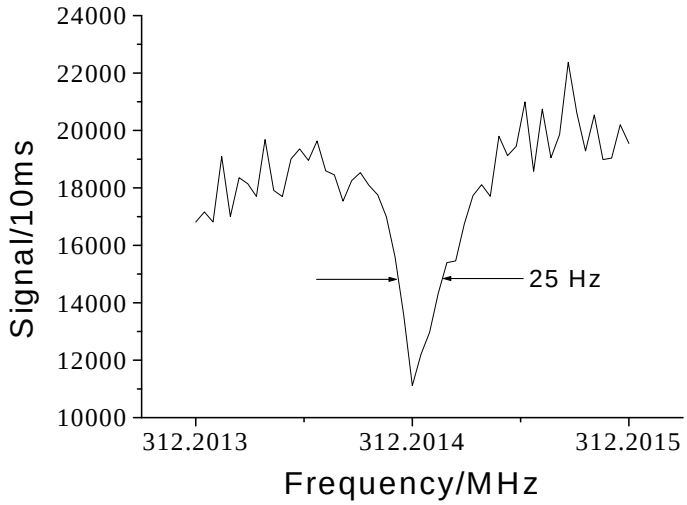

Fig. 4.3: The hyperfine transition in Beryllium. The transition frequency was calculated using the Breit-Rabi equations and found by scanning a range of frequencies around the expected value. In this case a range of 200 Hz was scanned using an rms drive amplitude of 100mV.

4.1.2 A Cylindrical Penning Trap

First Considerations in the Trap Design

The design of the trap aims to fulfill the need for good access for laser cooling and high visibility of the trapped ions. Considering the dimensions of the magnet the only way to achieve these goals is with an open-end-cap trap, the imaging can then be along the axis of the trap. The trap was originally designed and constructed by a previous student of the group, J. L. Hernández Pozos [3]. Considerable changes have since been made to the original set up: the mounting of the trap within the vacuum can, the mounting and design of ovens and filaments. The dimensions and separations of the trap electrodes were not altered and the introduction of a split ring electrode in the later stages of the project was not expected to have a significant effect on the behaviour of the trap. The laser cooling beams are directed first down (parallel to the trap/magnet axis) then diagonally up through the centre of the trap.

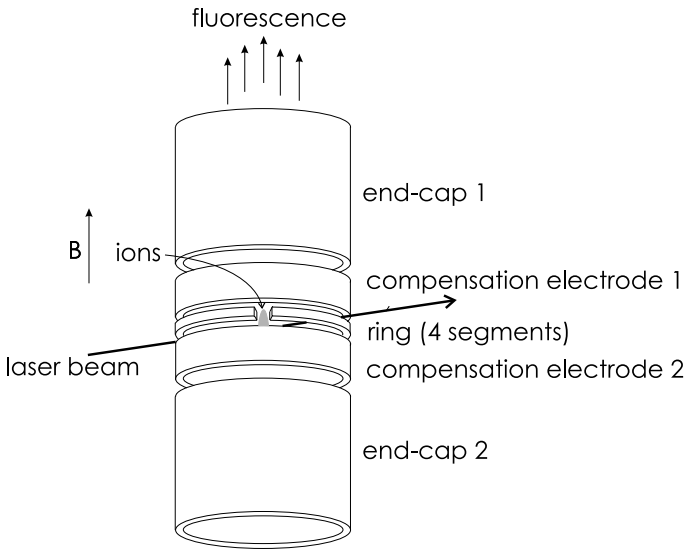

Fig. 4.4: The Zeno trap. The ring diameter is 12 mm while the distance from trap centre to the end-caps is 8.25 mm. The value of R_0^2 for this trap has been found experimentally as 3.2×10^{-4} m^2.

The trap is shown in figure 4.4. There is space for two atomic beam ovens to be fitted, one on either side of the ring. The ovens are made using pieces of tantalum tube (outer diameter = 1.02 mm), a small pin-hole is pierced into the wall of the tube and once the tube is filled it is folded at each end. The ovens are spot welded onto a length of tantalum wire (diameter = 0.25mm). When current is passed through the wire, the oven is heated and a beam of atoms leaves the pin-hole and is directed across the centre of the trap. The ionizing electron beam is produced by a V-shaped filament of thoriated tungsten. The filament is seated beneath the lower end-cap with the point of the V directed upwards towards the trap centre. The electrons emitted from the filament are accelerated across the centre of the trap along a path parallel to the magnetic field lines when a potential is applied to the electrodes. The potential on the electrodes is set such that when the electrons reach the trap centre and collide with the atomic beam they have just sufficient energy to cause single ionization.

The electrodes of the Zeno trap are made using Oxygen Free High Conductivity

Copper. When the trap was initially built the ring-electrode was made of a single piece. This was changed for a segmented ring cut radially into four: to enable axialization of the trapped ions. Electrical isolation between the four sections was achieved by placing small spacers made of alumina into holes drilled into the electrode sections. The intention was to ensure that all four sections could lie in the same plane, however the difficulty of drilling 1 mm holes into pieces only 1.5 mm thick means that this is probably not the case. It seems unlikely that the small misalignments of the ring sections would prevent the trap from working (at the time there were problems with the laser beam pointing stability and possibly with the imaging) however the trap has never functioned satisfactorily with the split-ring in place. Owing to the thickness of the ring electrode there is no easy solution to this problem.

Inspiration for the Design

The principal source for the design of the trap is a paper by Gabrielse et al [4]. In this paper they set out the design of a cylindrical Penning trap with open end-caps. The feature of the trap which makes it particularly interesting is it's *orthogonality*, that is to say, anharmonic terms in the trap potential are not present owing to the relative dimensions of the trap electrodes. The effectiveness of the use of compensation electrodes has been proven in the field of mass spectrometry. In reference [5], a compensated cylindrical trap is used to achieve mass resolving powers of 1×10^5.

To understand better what is meant by an orthogonalized trap we should look in detail at the equations describing the potential formed by a cylindrical trap. Ideally a Penning trap should have hyperbolic electrodes in order to produce a quadrupole potential; by flattening all the surfaces and boring holes in the end-caps the potential becomes distorted and a compensating potential needs to be sought in order to re-

approach the ideal. Thus the idea of the *compensation electrode* is introduced.

The potential at the centre of a Penning trap can be expressed using Legendre polynomials in the following way:

$$V = \frac{1}{2}V_0 \sum_{k_{even}=0}^{\infty} C_k \left(\frac{r}{R_0}\right)^k P_k(\cos\Theta) \tag{4.1}$$

here V_0 is the trapping potential and the characteristic distance $R_0^2 = r_0^2 + 2z_0^2$. Legendre polynomials are used since the cylindrical trap has azimuthal symmetry.

If the potential were perfectly quadrupolar the coefficient C_2 would be equal to 1, while all other coefficients (apart from C_0 which is a constant throughout and can be neglected) would equal zero. This is the regime we are aiming for in the cylindrical trap.

To best analyze the compensated cylindrical trap the potential described in equation 4.1 can be taken to be formed of two components: that produced by the simple end-cap and ring configuration and that due to the compensation electrodes. If we apply V_0 to the ring and V_c to the compensation electrodes then the full potential can be written thus:

$$V = V_0\Phi_0 + V_c\Phi_c \tag{4.2}$$

Φ_0 and Φ_c are solutions of Laplace's equation and can be expanded near the centre of the trap as:

$$\Phi_0 = \frac{1}{2}\sum_{k=0}^{\infty} C_k^{(0)} \left(\frac{r}{d}\right)^k P_k(\cos\Theta) \tag{4.3}$$

and (4.4)

$$\Phi_c = \frac{1}{2}\sum_{k=0}^{\infty} D_k \left(\frac{r}{d}\right)^k P_k(\cos\Theta) \tag{4.5}$$

Equating 4.1 and 4.2 then the C_k coefficients can be calculated thus:

$$C_k = C_k^{(0)} + D_k \frac{V_c}{V_0} \tag{4.6}$$

The equation governing the characteristic axial frequency of particles in the trap is:

$$\begin{aligned} \omega_z^2 &= \frac{qV}{mR_0^2} \\ &= \frac{qV_0}{mR_0^2} C_2 \end{aligned} \tag{4.7}$$

where m is the particle mass and q is its charge. Ideally all of the C_k coefficients should be zero apart from C_2, which should equal 1 (equation 4.1). It can be seen that the effect of non-zero C-coefficients is to cause the axial frequency, ω_z, to vary with the amplitude of that motion. In other words, the motion is *anharmonic*. This is clearly undesirable.

Using equation 4.6 it is possible to see how the lowest order anharmonicities could be compensated for: that is setting by $C_4 = 0$.

$$-\frac{C_4^{(0)}}{D_4} = \frac{V_c}{V_0} \tag{4.8}$$

However, unless there is some way of fixing $C_2 = 1$, the axial frequency will alter as a function of compensation electrode voltage. The condition where C_2 is fixed in this way is termed *orthogonality* and can be only be achieved if $D_2 = 0$. It is possible to achieve this with a suitable choice of trap geometry. Essentially, for any compensation electrode size z_c/z_0 there is a specific trap radius r_0/z_0 for which $D_2 = 0$.

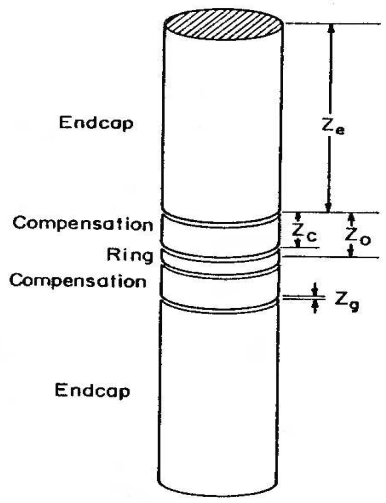

Fig. 4.5: A schematic diagram of a cylindrical trap.

Modifications to the Gabrielse Design: How the New Design Compares

To adapt the Gabrielse design to one which is usable in our situation a number of points needed consideration. First of all, our trap is an optical trap so spacings between electrodes must be sufficiently large to allow laser beams through the trap. The requirement for the trap to be inside the magnet bore at a specific position also enforces certain constraints on trap dimensions. Other decisions as to the dimensions of the trap have been driven by the imaging optics and collection efficiency (maximizing the solid angle for photon collection). Table 4.1 summarizes the differences between the trap currently used at Imperial college (the *Zeno Trap*) and the design of Gabrielse et al. The dimensions referred to are shown in diagram 4.5. The effects of modifying the original Gabrielse design were studied previously [3]. However, the difficulties of working with this trap, especially once the split ring electrode was in place, prompted a more rigorous investigation.

In the original paper by Gabrielse, a graph is shown which gives the ratio r_0/z_0 required to orthgonalize a compensated trap. Using the equations given in reference

Table 4.1: The trap relative dimensions of the Zeno trap compared with the Gabrielse design.

	r_0/mm	(r_0/z_0)	(z_c/z_0)	(z_e/z_0)	(z_g/z_0)
Gabrielse	6.0	1.024	0.835	4.327	0.030
Zeno Trap	6.0	0.727	0.909	1.455	0.182,0.121

Table 4.2: The C_k^0 and D_k coefficients for the Zeno trap and that designed by Gabrielse et al. The results were obtained using the equations detailed in reference [4] and figures calculated for the Gabrielse trap are in agreement with those detailed in the paper.

	Gabrielse Trap C_k^0, D_k	Zeno Trap C_k^0, D_k
k=2	0.545, 0.0001	0.548, 0.328
k=4	-0.212,-0.557	-0.460,-1.273
k=6	0.164, 0.431	0.728, 1.473

[4], this graph was reproduced and extrapolated to extend to a larger range. It is shown here in figure 4.6. Looking at graph 1 to begin with, the point at which the original design by Gabrielse et al fits is indicated. The dimensions of the Zeno trap do not fit onto the graph: it is not an orthogonal trap. Looking at table 4.2 we can see the effect this has on the C_k^0 and D_k coefficients: the criteria for orthogonality is that D_2=0, which is clearly not the case. As explained, a non-orthogonal trap will produce variation in the axial frequency, ω_z, with compensation voltage. Taking the differential of equation 4.7, the influence of the compensation electrode voltage upon the axial frequency can be quantified. For the Zeno trap at V_0 = 120V (ω_z=395 kHz), which is a realistic trapping voltage for $^{24}Mg^+$, the change in axial frequency/V is 1 kHz/V. The same parameter at the same voltage (ω_z=690 kHz) for the Gabrielse trap is 0.6 Hz/V. For our purposes it is not necessarily important that the Zeno trap be orthogonal since the anharmonicities of the trap can be minimized regardless: by altering the compensation electrode voltage. Fluctuations in the compensation electrode voltage could be a problem for high precision work, as they might introduce

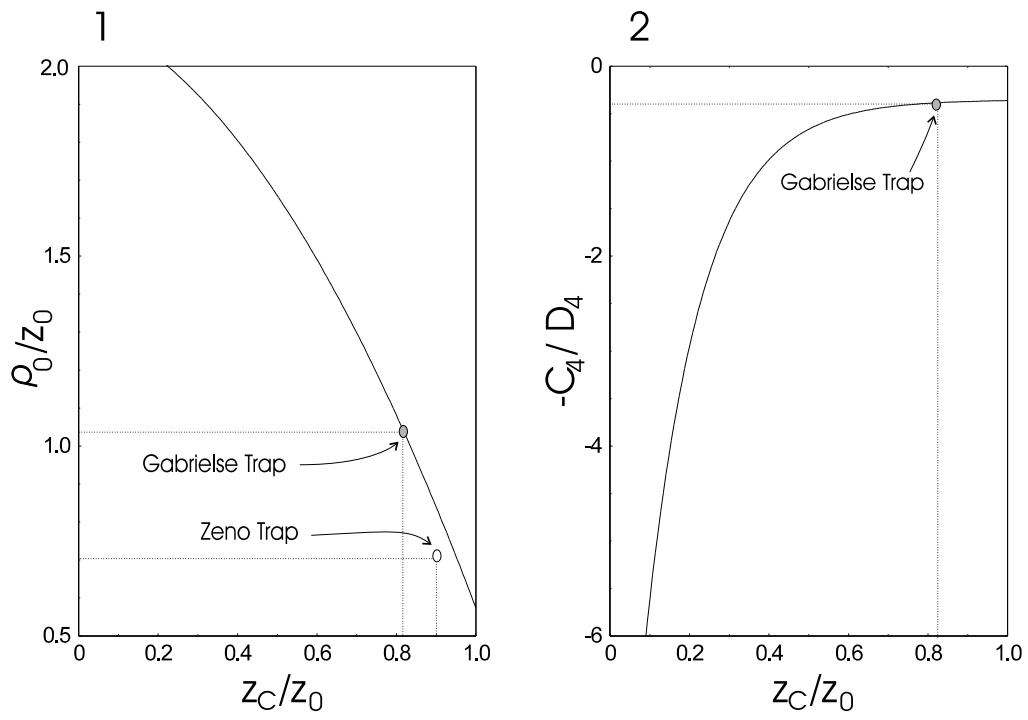

Fig. 4.6: Graphs showing the relative trap dimensions required to produce an orthogonalized trap (1) and the compensation electrode voltage needed to make C_4 equal to zero (2).

unquantified heating effects. The non-orthogonality of the Zeno trap may become of greater relevance considering that future experiments may require highly efficient cooling, involving a second laser to cool the axial motion directly and the coupling of the axial motion to the magnetron oscillation: to reduce the magnetron radius in a similar process to axialization. Naturally this will become difficult and less effective if the axial frequency is changing.

Referring to graph 2 in figure 4.6, the Gabrielse trap is compensated by application of V_C = -0.38 V_0. The value for the Zeno trap must be found from equation 4.8 as it is a non-orthogonal trap: the required compensation is -0.36 V_0. It has been calculated that the dimensions of the Zeno trap if correctly compensated give a value of $C_4 = 5.55\times10^{-17}$, which seems quite adequate.

The effect of introducing larger gaps between the electrodes and the truncation

of the end-caps has been looked at [3]. The major problem with large gaps between electrodes is distortion of the quadrupole field, fortunately these effects are minimal at the centre of the trap. The length of the end-caps would seem to be a greater worry. Throughout reference [4] it is assumed that the electrodes are infinitely long. This is clearly unrealistic and in order to approach this ideal it is sufficient to ensure that the end-cap length is several times the internal trap radius (r_0), indeed the C_k coefficients are within 1% of the infinite end-cap limit when $z_e/r_0 < 3$. In the case of the Zeno trap this ratio is 2, which is rather smaller than desirable.

Evaluation of the shape of the electric potential along the z-axis using the dimensions of the two traps shows that for the same trapping voltage the Zeno trap is relatively shallower than the Gabrielse trap. The two potentials are compared in

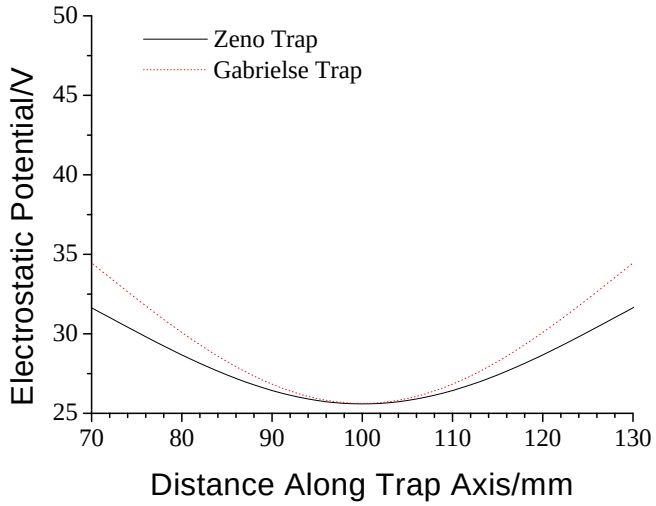

Fig. 4.7: A comparison of the electrostatic potential generated by the trap described by Gabrielse et al and the Zeno trap. The curves were calculated with a voltage of 120 V applied between the end-caps and the ring.

figure 4.7. The only real disadvantage of the trap being so shallow is the need to generate very high voltages to get comparable confinement to other traps. This reflects the high R_0^2 value of the Zeno trap (3×10^{-4} m^2), which is an order of magnitude

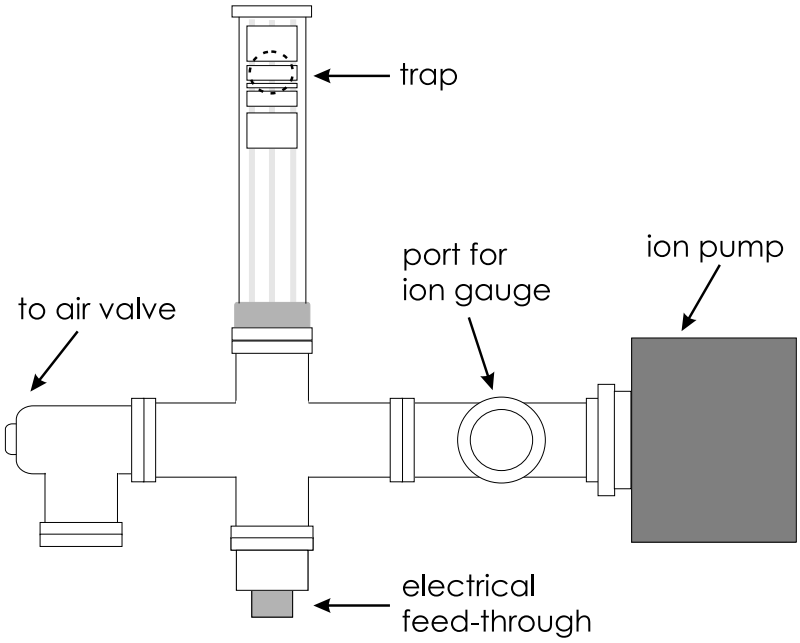

Fig. 4.8: The vacuum system for the Zeno trap. The lateral view is shown.

larger than is usual.

4.1.3 The Vacuum System

The dimensions of the magnet impose severe restrictions on the nature of the vacuum system. In order to accommodate the trap and the necessary beam steering mirrors inside the magnet bore, a specially built vacuum can was required. At the time the best solution was provided by a vessel made entirely of glass. In this way, input ports for the laser and a window for imaging could all be integrated into the main container for the trap. The rest of the system was then made from off the shelf U.H.V. (Ultra High Vacuum) compatible components. The system is shown in figure 4.8.

To reach the vacuum pressures needed for ion trapping (1×10^{-10} mbar), the system is first roughed out (to 1×10^{-7} mbar) using a turbo-molecular pump. To reach lower pressures requires baking to a temperature of at least 150 ^{o}C. The length

of this procedure can vary, but lasts until the pressure stabilizes (generally, over a 48-72 hour period). The system is then cooled and the ion-pump fired.

4.1.4 The Optical System

Optics for Beam Shaping and Steering

The beam which emerges from the laser is elliptical, such a beam is not ideal for sharp focusing at the trap centre thus cylindrical optics are used to shape the beam. A telescope of cylindrical lenses diminishes the longer axis of the beam and a second telescope, this time comprising spherical lenses, expands the beam once again. At the focus of the second telescope is a pin-hole of 20μm radius which acts to spatially filter the beam.

Focusing into the trap was done using a single lens of ~ 1 m focal length. The position of the focus could be tuned either by moving this lens or alternatively, by changing the divergence of the beam using a telescope arrangement. The sharpness and position of the focus can be judged from watching how the beam is apertured by the trap electrodes.

The fast switching of the laser beam required for the Zeno experiment was done using an acousto-optic-modulator (AOM) in the beam path. The acoustic grating is produced by means of a radio frequency (RF) oscillator at 80 MHz. It is the first order diffracted beam which is sent to the trap, this beam can be effectively switched on and off using a computer controlled RF–switch which periodically interrupts the RF drive to the AOM. The pulse sequences required to do this were generated using LabView.

In order to make the switching as clean as possible the beam is double passed through the AOM. There is always some residual acoustic grating in the acousto-optic crystal, even when the RF supply is nominally off, this means that there will

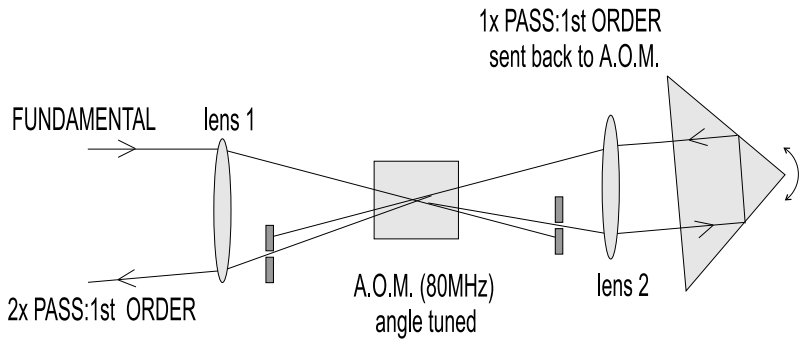

Fig. 4.9: The scheme for double passing through the acousto-optic modulator. The AOM is initially angle tuned in order to optimize the first pass, the emerging first order diffracted beam is then retroreflected. Due to the presence of lens 2, by rotating the corner cube the angle of the return beam can be optimized with respect to the acoustic grating. With this method efficiencies of up to $\sim 60\%$ transfer on the second pass were achieved.

be leakage of the fundamental into the first diffracted order at all times. This *leak beam* is weak but sufficient to cause decoherence of the atomic state being measured. Double passing the laser beam through the AOM is a way of reducing the leakage to negligible levels.

The Imaging Optics

Light emitted by a cloud of trapped ions is collected by a lens system which sits above the trap, outside the vacuum container. The lens system which comprises three lenses was specially designed to be give an aberration free image of the ions at trap centre with a magnification of $\times 20$. The image is cast at the upper end of the magnet bore, where there is sufficient space for a photomultiplier to be positioned. The photomultiplier is shielded from the magnetic field by a μ-metal tube. Although the lenses are intended for use with Beryllium at 313 nm, there was no appreciable loss of image quality when working with Magnesium at 280 nm.

The main reason for using high magnification is to produce large signal to noise ratios (since background, scattered light is not focused while light from ions at the trap centre is). There is a downside to the set up: the area imaged is extremely

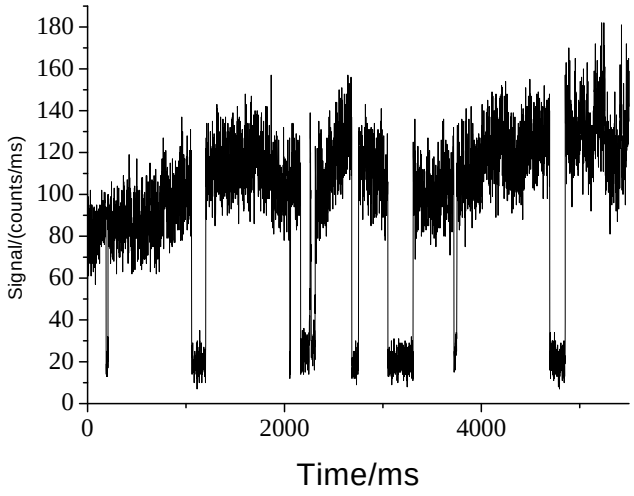

Fig. 4.10: The quantum jumps of a single Beryllium ion. The signal to noise is about 10:1 (bin size is 1ms), this is the advantage of using a high magnification system. In other traps using a magnification of 1, the greatest signal to noise ratio achieved was 5:1 (see later).

small, thus it can be quite difficult to locate ion clouds within the trap. To illustrate this, if the photomultiplier aperture is set at 1cm diameter then it is possible to image only 500 μm of the trap centre, with typical cloud sizes of around 100 μm it is a common experience that even after a cloud has been located the process of cooling causes that cloud to shrink out of view. To illustrate the high signal to noise ratio a trace of quantum jumps in Beryllium obtained using the Zeno trap is included in figure 4.10.

4.2 The Split-Ring System

This system is a tried and tested set-up, so it will be discussed only briefly here, further details are in reference [6]. The use of an electromagnet rather than a superconductor makes the arrangement of optics (for imaging and beam steering) comparatively simple: there is no need for custom designed vacuum cans.

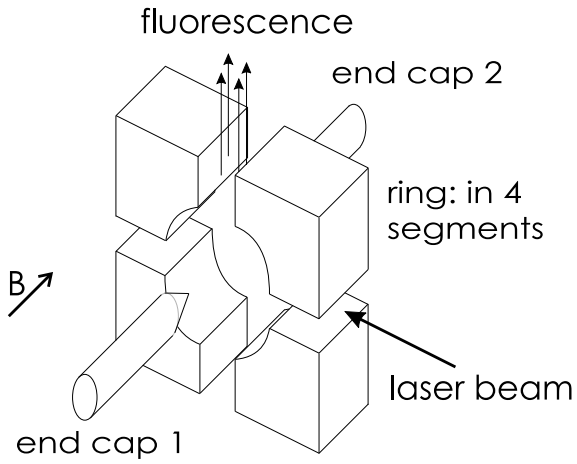

Fig. 4.11: A schematic diagram of the Split-Ring trap. The diameter of the ring is 10 mm and the distance from trap centre to the end-caps is 3.5 mm. The value of R_0^2 for this trap has been measured experimentally as 5.12×10^{-5} m^2.

4.2.1 The Trap and Vacuum System

The trap is of a typical design: possessing two end caps and a ring electrode. The ring electrode is split radially into four segments (figure 4.11) and for ease of machining, all the electrodes are of triangular profile. The electrodes are made using Copper-Beryllium. Electrical insulation of the ring electrode segments is provided by 1 mm ceramic washers secured using ceramic screws. The trap is described fully in references [6, 21].

The ovens are of the same design as those in the Zeno trap. They are situated on either side of the split ring, with a direct line of sight to the centre of the trap. The filaments are housed inside small cavities within the end-cap electrodes. Holes are drilled into the end-caps which allow the electrons to travel across the trap.

Once assembled the trap is fitted into a four way cross piece of the stainless steel vacuum system. The trap is oriented so that the ring is vertical and the laser beam can pass through the trap in the horizontal plane. The laser beam enters the system via a flat view-port window and exits through a Brewster window. Imaging is then

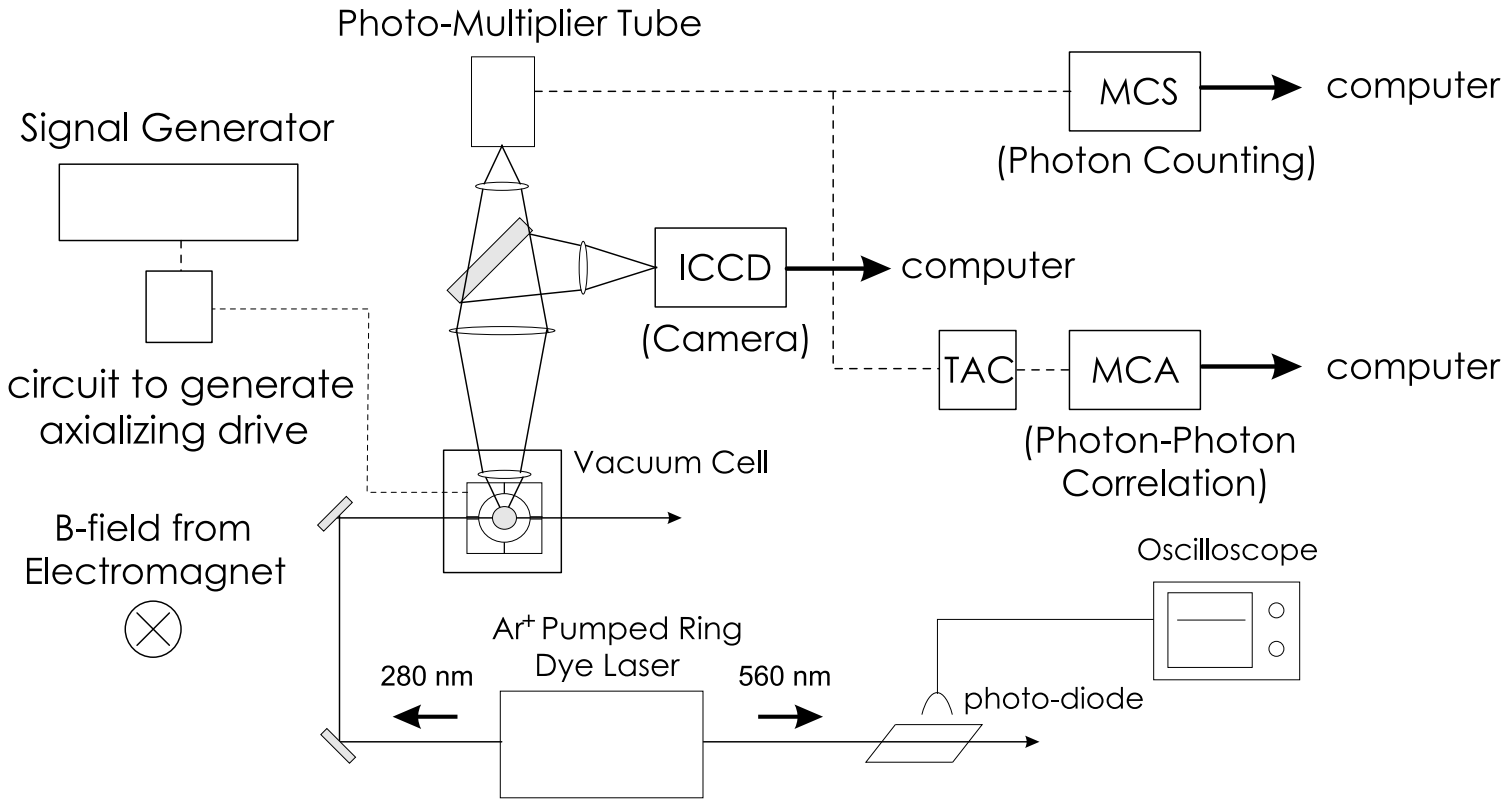

Fig. 4.12: The split-ring system.

done in the vertical plane, through a flat view-port window. The vacuum system housing the trap is placed between the poles of an electromagnet, such that the magnetic field lines are along the axis of the trap. A diagram showing the essential features of the system is shown in figure 4.12.

4.2.2 The Optical Systems

The comparatively short beam path combined with the use of a shorter focal length lens (30 cm), means that unlike the Zeno system no beam shaping or spatial filtering is necessary. The signal to noise ratio for this system was assessed with and without the presence of cylindrical optics and spatial filtering: it was found that there was no advantage to be gained from their use.

The laser passes through the trap via conical holes cut into the split-ring electrode and light from the ions fluorescing within the trap emerges from another conical hole also cut in the split-ring. The fluorescent signal is collected and imaged into the photomultiplier by a system of three lenses (as indicated on figure 4.12). The system has a magnification of $\times 1$. Signal to noise is generally of the order of 1:5, as can be seen from quantum jump traces in chapter 5.

To image using the ICCD camera, the first two lenses of the original optical system are used. The light emerging from the second lens is diverted towards the camera using a mirror which can be flipped in and out of position. A final lens focuses the light onto the ICCD array. The magnification has been calculated as ~ 1.

4.3 The Laser

To cool and detect trapped ions a tunable laser source at an appropriate frequency is required. The laser cooling frequencies of Beryllium and Magnesium are both in

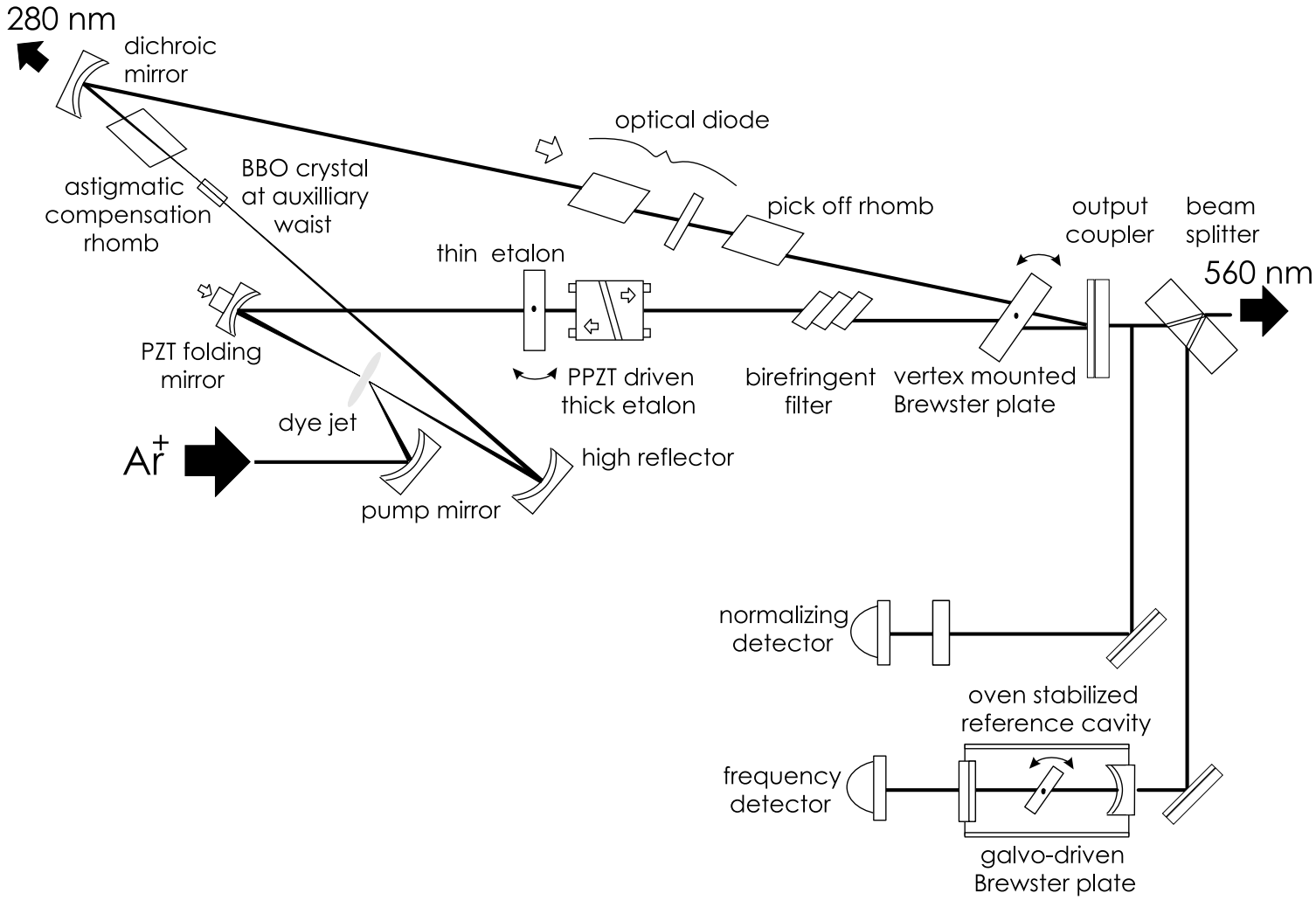

Fig. 4.13: The dye laser.

the ultra-violet. For Beryllium the $^2\mathrm{P}_{3/2}(m_I = -3/2, m_J = -3/2) \rightarrow {}^2\mathrm{S}_{1/2}(m_I = -3/2, m_J = -1/2)$ transition at 313 nm is used while for Magnesium it is the $^2S_{1/2} \rightarrow {}^2\mathrm{P}_{3/2}$ transition at 280 nm. To reach this region of the spectrum frequency doubling is required and the only laser capable of producing the appropriate visible wavelength is a dye-laser.

The laser system used for the experiments in this thesis consists of an Ar^+ laser (Coherent Innova 400) pumped, stabilized ring dye laser (Coherent 699R). The ultra-violet light is produced by intra-cavity frequency doubling the dye-laser out put using an angle tuned *Beta* Barium Borate (BBO) crystal. Up to 150 μW of U.V power can be produced in this way. A schematic diagram of the dye laser is included in figure 4.13.

Cooling transitions are located using absorption spectroscopy of molecular Iodine. In order to monitor the laser frequency stability a spectrum analyzer (FSR = 300 MHz) was used.

4.3.1 Intra-Cavity Frequency Doubling of the laser Using a Brewster Cut Crystal

The second harmonic generation in this system is achieved by placing the frequency doubling crystal at an auxiliary focus within the dye-laser cavity. Historically this has been done using a crystal cut with plane faces which have been anti-reflection coated. This has numerous problems, principally damage to the anti-reflection coatings owing to the high intra-cavity light intensity. The damage leads to short timescale power instability and ultimately degredation of the laser performance over the space of weeks. Additionally, since it is not possible to independently optimize the dye-laser and the second harmonic generation there may have been some impact on the frequency stability of the system, especially once large areas

of the crystal coatings had been damaged. In experiments requiring high levels of laser frequency and power stability, such as the Zeno experiment this puts severe limitations on the length of data run possible and tends to decrease the signal to noise ratio.

Ideally the system should be re-designed to involve an external cavity for frequency doubling. An interim solution, however is to use a doubling crystal which has Brewster cut end faces. The disadvantage of this is that it alters the astigmatism of the cavity. To solve this problem requires knowledge of the initial cavity astigmatism (before insertion of the crystal). This is already compensated by the presence of a silica rhomb inside the laser cavity. Therefore, the amount of astigmatism in the cavity can be calculated using the length of this rhomb and its refractive index at the fundamental frequency (560 nm). Once the Brewster cut BBO crystal is inserted it is then a simple matter to calculate the length by which the existing compensating rhomb would have to be shortened in order to accommodate the doubling crystal.

4.3.2 Calculation of the Astigmatism Compensation

The source of astigmatism in a ring cavity is the oblique incidence of light on any curved mirror surfaces. It arises because, for a beam of light arriving at any angle other than normal to the mirror surface, the radii of curvature which it sees differ in the planes parallel (x-plane) and perpendicular (y-plane) to that of the ring. If we were to analyze the situation in terms of ray transfer matrices, we would find that the system could be described using two such matrices: one for the x and one for the y-plane. Following reference [8] it can be shown that other optical elements, including inclined plates (such as a Brewster cut crystal), will also introduce astigmatism into a cavity. Careful cavity design can ensure that the astigmatism present is minimized. In the dye-laser, the astigmatism of the mirrors is counterbalanced by that of a silica rhomb with faces inclined at Brewster's angle (see figure 4.13).

Table 4.3: The values used to calculate the length for a new astigmatism compensating element (silica rhomb (2)) if the original element (silica rhomb (1)) is removed to accommodate a frequency doubling crystal (7 mm BBO crystal). The combined astigmatism of the BBO crystal and new element are as closely matched to the initial values as is possible.

	Silica Rhomb (1)	BBO crystal	Silica Rhomb (2)
d_x/mm	8.76	2.90	5.90
d_y/mm	3.75	1.14	2.50
l/mm	22	7	14.88

In reference [9], expressions are derived to calculate the the amount of astigmatism in the x and y directions, d_x, d_y. These are:

$$d_x = t\sqrt{(n^2-1)}/n^2 \tag{4.9}$$

and

$$d_y = t\sqrt{(n^2-1)}/n^4 \tag{4.10}$$

where the thickness of the astigmatic element is t and the refractive index of that element is n. The definition of t is shown in figure 4.14. The figure indicates how the value of t is translated into a length of crystal, l, through which the laser light should travel in order to become fully compensated .

If the initial values for the silica rhomb are d_{sx} and d_{sy} then:

$$d_{sx} = d_{bx} + d'_{sx} \tag{4.11}$$

$$d_{sy} = d_{by} + d'_{sy} \tag{4.12}$$

where $d_{bx,by}$ and $d'_{sx,sy}$ are the corresponding values in the BBO crystal and the new silica rhomb. The values of refractive index for fused silica and BBO at 560 nm are 1.54 and 1.65 respectively. The lengths t and l are related as shown in figure 4.14. Once these dimensions were obtained for the original silica rhomb equations 4.9 and

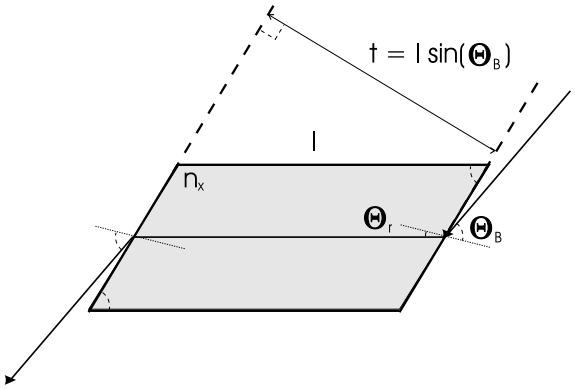

Fig. 4.14: A schematic diagram of a Brewster cut crystal for frequency doubling. The relationship between the distances l and t is shown.

4.10 could be used to calculate d_{sx} and d_{sy}. Similar calculations were made to obtain d_{bx} and d_{by} (i.e to find out how much of the compensation could be done with the 7 mm BBO frequency doubling crystal). Equation 4.12 was then used to calculate the remaining astigmatism which could be compensated by a new length of silica suitably cut. The values from this set of calculations are summarized in table 4.3.

4.4 Data Collection

4.4.1 The Photo-Multiplier and the ICCD Camera

Fluorescence from the trapped ions could be collected using a Thorn EMI photo-multiplier or an Andor Technology ICCD (Intensified Charge Coupled Device) camera. Every photon arriving at the photo-multiplier results in the production of a TTL pulse. These pulses could be sent to one of the data aquisition cards (MCA or MCS) which are desribed later. The photo-multiplier is of high quantum efficiency and can be used to monitor the ions in real time. In the case of the ICCD camera photons arriving at the intensifier fall onto a photo-cathode, electrons are produced and multiplied as they pass through a series of micro-channel plates. The data is

sent to a PCI controller card and the image can be viewed using the appropriate software. The software interface allows the user to alter parameters such as the exposure time. The camera is of variable gain, using this feature and by altering the exposure time it is possible to image even single ions.

4.4.2 The Multi Channel Scaler (MCS)

To look at the real time evolution of the trapped ions, pulses from the photo-multiplier are sent to a MCS card (EG and G–Ortec). This card counts the number of photons arriving in a specific time interval. We can then observe a *photon count rate per bin time*. Bin times as low as 2 μs can be used, however it was usual to use between 500 μs and 10 ms. The display consisted of up to 8000 channels as a plot of the number of photons collected versus the channel number.

4.4.3 The Multi Channel Analyzer (MCA) and Time to Amplitude Converter (TAC)

These devices allow us to look at photon-photon correlations. The stream of TTL pulses from the photo-multiplier are sent to the start and stop gates of a TAC (EG and G–Ortec). The first pulse starts the TAC timer and the next pulse stops it, the time delay between the pulses is converted into an analogue voltage that is proportional to the length of the delay. The voltage pulse is then sent to the MCA (a software controlled EG and G–Ortec MCB (multi channel buffer) card). The MCA has 2048 channels, each of which corresponds to a specific time delay between photons. The resolution can be calculated as (number of channels)/(TAC time delay), thus it is determined by the full scale time delay set on the TAC (usually 100-200 μs). When a voltage pulse is received, the counter for the relevant channel is incremented. In this way a distribution of time delays present can be formed.

4.4.4 LabView

Automation of the data aquisition can be achieved using National Instruments LabView: this package consists of a PCI card, computer interface and Input/Output board (comprising both analogue and digital inputs and outputs which are software configured). So called *virtual instruments* (such as pulse generators) can be constructed using a graphical programming language. The Real-Time System Integration (RTSI) bus on the LabView card enables synchronous triggering of several events. Both the ICCD camera and the MCS can accept a trigger from LabView in the form of a TTL pulse. Using a GPIB card, our signal generator can be controlled via a LabView program.

4.5 Techniques For Ion Trapping

Methods used to capture clouds of ions are discussed in earlier work by the group. The technique developed for the loading of single ions will be described here.

Initially the starting parameters for oven and filament current and the accelerating bias for the electron beam must be found. The bias will differ depending upon the ionization potential of the ion to be loaded (for Beryllium this is 9.3 eV and for Magnesium it is 7.6 eV) and the trapping voltage used. Ideally the bias voltage should be set at a level where the electrons are accelerated to an energy which will only produce *singly* ionized particles. Suitable currents for the ovens also depend upon the ion used: the temperature to evaporate Beryllium is nearly twice that needed in the case of Magnesium. Filament currents depend on the material used and method of construction of the filaments. The length of time for which ovens and filaments are run is more easy to standardize. As a guide, ovens were run first for 20 seconds, then the filament + bias were run (with the oven still on) for a further 10 seconds, the complete loading process taking 30 seconds. Before loading the laser

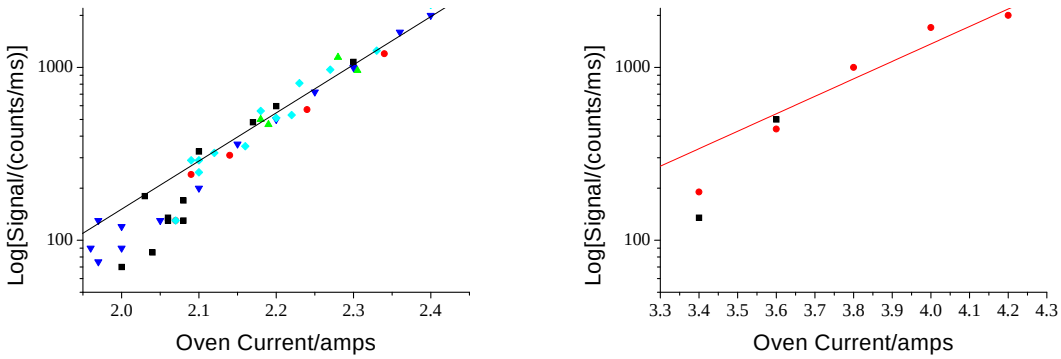

Fig. 4.15: Oven characterization, showing how the oven current may be decreased to reduce the number of ions loaded into the trap. Graph 1 shows data for $^{24}Mg^{+}$ and graph 2 shows data for $^{9}Be^{+}$.

beam was set to scan a frequency range of 1 GHz up to the resonant frequency. The position of the laser beam was set to one side of trap centre, as is required for laser cooling in a Penning trap.

To load single ions the best method is to begin by loading a large cloud. This is done in order to find the optimum laser frequency and beam position . Once the best conditions are found, the laser beam is left in place and another cloud is loaded with the oven set at a lower current than before. All other parameters are kept constant. Once the ions are in the trap the laser beam position is re-optimized for the smaller cloud. Successive loads are made, each time with a lower oven current. Generally, the oven current is reduced in increments of 0.1 A. With practice single ions can be loaded within half an hour.

The method was first used with Beryllium and has proved to be more reliable than other methods such as cloud reduction by driving motional frequencies. The graphs in figure 4.15 show how cloud size, inferred from the fluorescence rate, decreases with oven current for Magnesium and Beryllium.

4.6 Electrical Connections and Other Circuitry

The traps are built onto a vacuum compatible electrical feed through. This enables electrical connection of the electrodes, ovens and filaments, via BNC connectors. In the case where it is necessary to apply RF to the trap this can be done by applying a signal directly to whichever electrode is at the common ground (generally the ring electrode).

For the axialization experiments, described in chapter 6, it was necessary to build a circuit capable of delivering two out of phase signals of the same frequency and amplitude. The circuit, a diagram of which can be found in Appendix D, consisted of an inverting and a non-inverting amplifier of equal gain. The frequency response of the circuit is governed by a third amplifier of gain up to 0.9, designed to give equal gain over a range a frequencies up to 1.5 MHz.

References

[1] J. J. Bollinger, J. S. Wells, D. J. Wineland, W. M. Itano, *Phys. Rev. A.* **31**, 2711 (1985)

[2] W. M. Itano and D. J. Wineland, *Phys. Rev. A.* **24**, 1364 (1981)

[3] J. L. Hernández Pozos, PhD thesis, University of London, Unpublished (2001)

[4] G. Gabrielse, L. Haarsma and S. L. Rolston, *Int. Journal. Mass Spectrom. and Ion Proc.* **88**, 319 (1989)

[5] H. Raimbault-Hartmann, D, Beck, G. Bollen, M. König, H.-J. Kluge, E. Schark,*Nuc. Instum. and Methods in Phys. Res. B.* **126**, 378 (1997)

[6] M. E. M. Storkey, PhD Thesis, University of London, Unpublished (2001)

[7] M. A. van Eijkelenborg, M. E. M. Storkey, D. M. Segal, R. C. Thompson, *Int. J. Mass. Spectrom.* **188**, 155 (1999)

[8] D. C. Hanna, *IEEE J. Quantum Electronics*, **QE-5**, 483 (1969)

[9] H. W. Kogelnik, E. P. Ippen, A. Deines and C. V. Shank, *IEEE J. Quantum Electronics*, **QE-8**, 373 (1972)

CHAPTER 5

Characterization of Magnesium$^+$

5.1 Motivation

In our experiment the three level system required to carry out an investigation of the quantum Zeno phenomenon is provided by a Magnesium ion. The transition to the metastable state, which is driven in the Zeno experiment does actually occur naturally. This natural jumping to the metastable state does not interfere with the Zeno effect (although it will modify the statistics) for an ensemble of atoms, however, as we hope to perform the experiment on a single ion it is a factor which must be well understood and accounted for. The results from this investigation are published in reference [1].

In this chapter I will first discuss the nature of quantum jumps and explore why they are interesting to study. I shall then go on to discuss the studies completed at Imperial College.

5.2 What is a Quantum Jump?

The possibility of a so called Quantum Jump was first postulated by Bohr. It can be described as a process by which an atomic system makes an instantaneous transition between two quantum states. Quantum jumps can be observed in a V-scheme system consisting of a strong dipole transition and a weak transition to a metastable level. If the strong transition is driven with resonant radiation, fluorescence will be observed. Depending on the ion species involved, quantum jumps may be produced in one of two ways; the metastable transition can be weakly driven or as in the case of magnesium the ion is transferred into the metastable state by a spontaneous Raman process. When the system jumps to the metastable level it is no longer able to interact with the incident laser light and will not fluoresce. For large ensembles of ions the process is unobservable; quantum jumps occur randomly in both directions such that the average level of fluorescence remains constant. In the case where single ions or small numbers of ions are isolated quantum jumps may be seen as one or, in the latter case, a few discrete steps in the fluorescence level.

5.2.1 Studies of Quantum Jumps

Nowadays the trapping of single ions is quite routine and the observation of quantum jumps in various ion species has been reported by a number of groups [2–7]. A summary of early quantum jump experiments can be found in reference [8].

It was Dehmelt [9] who first proposed a use for the quantum jump. Terming it *electron shelving*, Dehmelt suggested that it could be an amplification mechanism for the detection of weak transitions in single atom spectroscopy. A further interest in quantum jumps lies in the fact that these rare transitions to metastable levels can be exploited as frequency standards. Amongst the first recorded observations of quantum jumps were for Barium and Mercury ions.

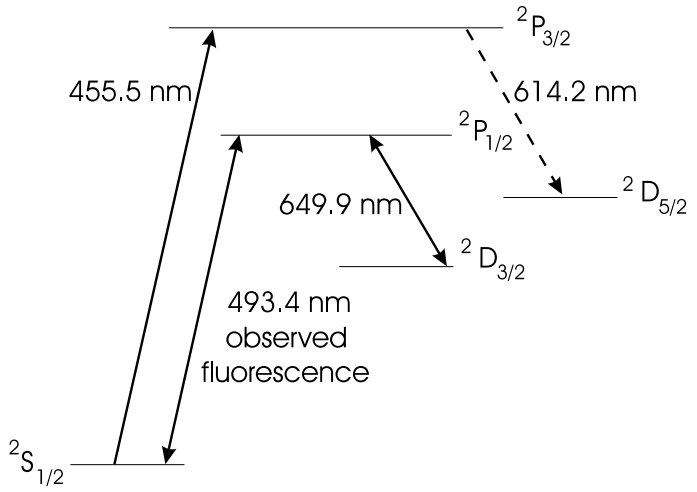

Fig. 5.1: The energy levels of $^{56}Ba^+$. The laser cooling transition is indicated by the bi-directional arrows. The quantum jump transition is into the 5d $^2D_{3/2}$ state, via the 6p $^2P_{3/2}$.

Quantum Jumps in Barium Ions

Quantum jumps in Barium are produced by spontaneous Raman-Stokes transitions [2, 10], but for experimental purposes it is generally easier to stimulate them using light from a hollow cathode lamp [11]. The ion is laser cooled using two lasers at 493.4 nm and 649.9 nm and the shelving state is the 5d $^2D_{5/2}$. Light from the hollow cathode lamp is used to drive the $^2S_{1/2} \rightarrow {}^2P_{3/2}$ transition from which the ion can decay spontaneously into the shelving state. The scheme is shown in figure 5.1. The lifetime of the 5d $^2D_{5/2}$ metastable level was measured as $\tau = 32 \pm 5$ s, giving a linewidth of 5 mHz. Such a narrow linewidth makes Barium an obvious candidate for a frequency standard. However, the system is limited by the frequency width of the radiation source used to drive the quantum jump transition. Ideally a laser tuned to 1.76μm would be used to drive the $^2S_{1/2} \rightarrow {}^2D_{5/2}$ transition directly. Attention has turned to the use of other ions owing to the difficulties in fabricating sufficiently narrow linewidth lasers at the desired frequency.

In reference [10], the authors look at the quantum jumps of two and three trapped

ions. Analysis showed that the number of events when two and three ions jumped simultaneously was much larger than expected. This phenomenon has been called *cooperative quantum jumping*. Explanations of the process are based on the idea that individual ions are coupled to the radiation field and consequently coupled to each other. Early proposals [12, 13] relied on radiative interactions between ions. These require the ions to be separated by a few hundredths of a wavelength of the driving radiation ($\sim$ nm) which is clearly impossible to achieve experimentally due to Coulomb repulsion. Recently, the possibility of dipole-dipole interactions between the ions has been suggested as a more realistic mechanism for cooperative jumps. In this scheme the ions only need to be at separations of 10 times the wavelength of the strong transition [14].

Unfortunately, no other experimental groups have been able to observe cooperative quantum jumping. In a recent publication by Skornia et al [15] it is shown how spontaneous decay inhibits the dipole entanglement of the ions. This process depends upon the strength with which the weak transition is driven, which may explain why many groups have failed to see any enhancement of multiple jumps.

Quantum Jumps in Mercury Ions

To observe quantum jumps in Mercury ions requires a similar set up to that used for Barium (see figure 5.2). As with Barium, the use of driving radiation is a matter of experimental convenience; jumps can occur spontaneously.

In reference [16] the authors look at photon anti-bunching in the emission from the metastable level. A distribution, $g_d(\tau)$ is used to denote the probability that the emission of a 281.5 nm photon is followed by the emission of another 281.5 nm photon after a time τ has elapsed. If this distribution is plotted for the experimental data it is found to go to zero at $\tau = 0$. This implies the occurrence of photon anti-bunching.

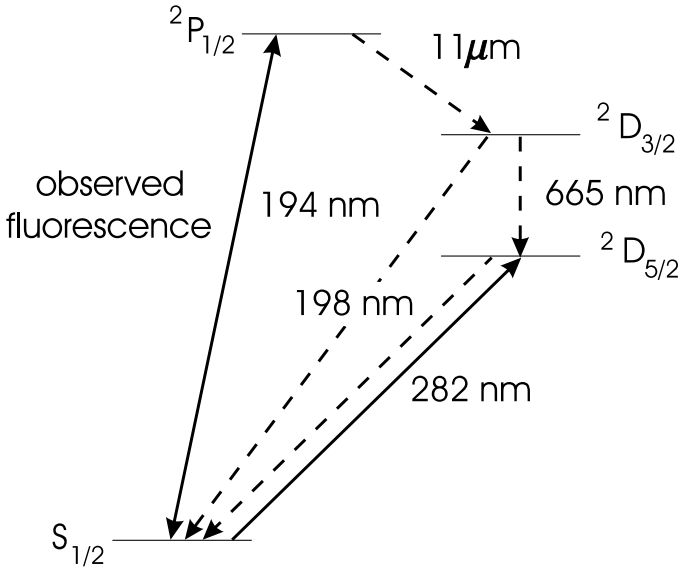

Fig. 5.2: The energy levels of $^{198}Hg^+$. A laser tuned to the $5d^{10}6s\ ^2S_{1/2} \rightarrow 5d^{10}6p\ ^2D_{5/2}$ will result in quantum jumps in the fluorescence observed on the laser cooling transition at 194 nm. The lifetime of the $5d^{10}6p\ ^2D_{5/2}$ metastable level is $\tau = 90 \pm 30$ ms [16].

There are other mechanisms which remove the ion from the laser cooling cycle. These so called background events might be collisions with background molecules or, more interestingly, spontaneous decay from the upper excited level of the laser cooling transition to the $^2D_{3/2}$ state (see figure 5.2). Both the apparent jump rate and the length of the "jumps" observed will be influenced by background processes. The effect of the $^2D_{3/2}$ level was studied in reference [17] and a branching ratio for the two decay routes from this level was evaluated.

If the quantum jumps in the fluorescence from the 194 nm transition are analyzed a plot of the number of jumps versus the length of jumps can be produced. For a single *jump route*, this would be a single exponential. Owing to the fact that there are two decay processes occurring, by fitting two exponentials (one for each of the possible decay channels) a normalized branching ratio can be calculated.

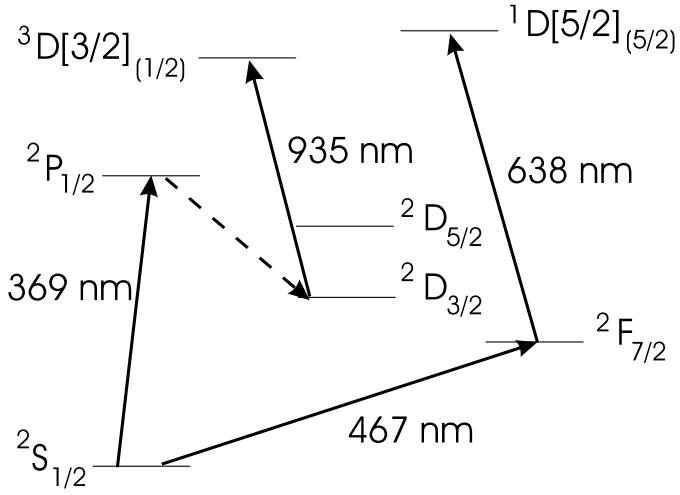

Fig. 5.3: The energy levels of $^{172}Yb^+$. Laser cooling takes place on the $^2S_{1/2} \rightarrow {}^2P_{1/2}$ transition (369 nm). There is a high probability that the ion will decay from the $^2P_{1/2}$ state into the $^2D_{3/2}$, to depopulate this level and maintain the cooling cycle a laser at 935 nm is required to bring the ion into the ground state via the $^3D[3/2]_{1/2}$. The $^2S_{1/2} \rightarrow {}^2F_{7/2}$ is the octopole transition and is expected at 467 nm.

Quantum Jumps in Ytterbium Ions

One of the most astounding quantum jump experiments concerns the observation of the electric octopole transition (see figure 5.3) in Ytterbium [18], with an estimated lifetime of 10 years.

In order to find the frequency of the quantum jump transition, the ion was interrogated using a high intensity laser source at the expected transition frequency. Because the lifetime is expected to be so long, when the ion makes the transition to the metastable level it can not be left to decay spontaneously, instead it was driven back to the ground state via the $^1D[5/2]_{5/2}$ level. Doppler broadening of the jump transition was eliminated by confining the ion to the Lamb-Dicke regime [19]. In order to avoid broadening of the ground state the cooling (369 nm) and interrogating (467 nm) lasers were chopped in anti-phase.

Quantum jumps were seen over a 1 MHz section of a 16 MHz scan. The frequency of the transition was determined as 642116785.3 MHz and from the rate of observed

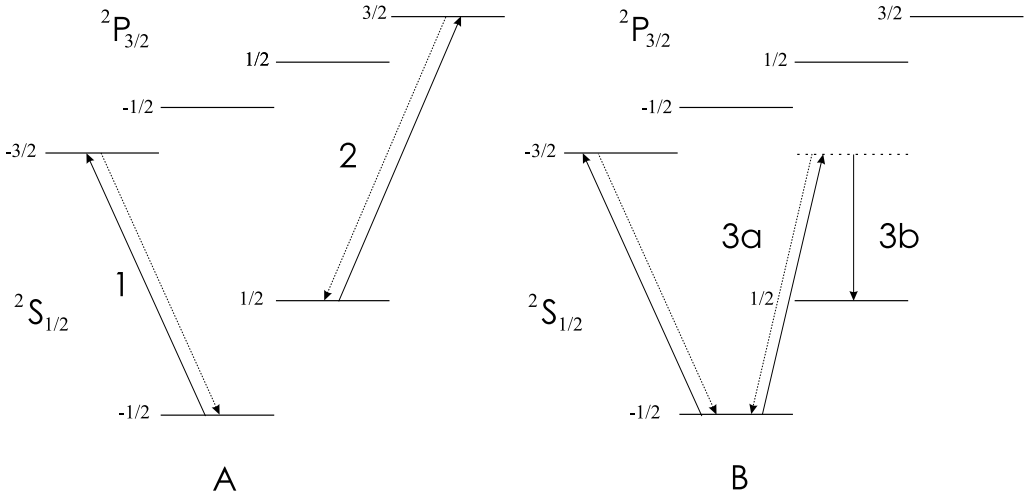

Fig. 5.4: The energy levels of Mg^+. The laser cooling transitions are shown in (A), either 1 or 2 could be used. If laser cooling takes place on transition 1, then quantum jumps may occur via transitions 3a and 3b (B).

transitions and the laser parameters the lifetime of the $^2F_{7/2}$ level was calculated as 3700 days. There is good reason to believe that this transition could become the basis of an extremely accurate frequency standard and, as the authors of reference [18] suggest, the longevity of this state could make it useful for applications in quantum computation.

5.3 Quantum Jumps in Magnesium Ions

We turn now to the focus of this particular study. The quantum jump process in magnesium requires only one wavelength of radiation to drive transitions between the $^2S_{1/2}$ and $^2P_{3/2}$ states, which in the Penning trap, are Zeeman split. There are two possible transitions which could be used for laser cooling of magnesium, marked as 1 and 2 in figure 5.4.

Looking at the lower transition initially (1), the laser is tuned between the $S_{1/2}$, (m_J = -1/2) and the $P_{3/2}$, (m_J = -3/2) states and is linearly polarized with its electric vector perpendicular to the magnetic field. The transition is strongly allowed

according to dipole selection rules so the ion will cycle nearly continuously between these two levels producing a steady rate of fluorescence. However, since the radiation is linearly polarized, an additional selection rule applies: $\Delta m_J = \pm 1$ (σ-transitions). This makes it possible for the ion to make transitions to the $P_{3/2}$ ($m_J = 1/2$) state, despite this being far off resonance. In emission the ion is not restricted to making a σ-transition and as a result there are *two* possible decay routes: referring to figure 5.4, back to the $S_{1/2}$, (m_J = -1/2) state (transition 3a) or to the $S_{1/2}$, ($m_J = 1/2$) state (transition 3b). Should the ion decay to the $S_{1/2}$, ($m_J = 1/2$) state then it is removed from the resonant cycling loop and fluorescence will cease. A second off resonance transition: $S_{1/2}$, ($m_J = 1/2$) $\rightarrow$ $P_{3/2}$, (m_J = -1/2) $\rightarrow$ $S_{1/2}$, (m_J = -1/2), takes the ion back into the cooling cycle where it once again scatters light. These processes result in the characteristic light and dark periods in the fluorescence produced by a single ion.

The situation is more complicated for the case of $^{25}Mg^+$ (I = 5/2) where hyperfine structure is present. The magnetic field used was of magnitude 0.98 T, thus the strong field regime applies. In $^{25}Mg^+$, this results in the Zeeman levels being split into six hyperfine components as shown in figure 5.5.

Laser cooling now takes place between the lower hyperfine levels of the original cooling scheme: $^2S_{1/2}$, (m_J = -1/2, m_I = -5/2) $\leftrightarrow$ $^2P_{3/2}$, (m_J = -3/2, m_I=-5/2). Jumping occurs when the ion is transferred to the $^2S_{1/2}$ ($m_J = 1/2, m_I = -5/2$) state. This process involves $\Delta m_I = 0$ and is therefore equivalent to that which occurs in $^{24}Mg^+$. Weak hyperfine mixing of the states means that transitions of the type $\Delta m_I = \pm 1$ are also allowed, although they are extremely rare.

It has been postulated [9] that such events do occur, if infrequently, leading to longer than "normal" quantum jumps, so called *nuclear quantum jumps*. Two distinct types of nuclear jump are predicted, to $^2S_{1/2}$ (m_J =-1/2, m_I =-3/2) or $^2S_{1/2}$ (m_J =1/2, m_I =-3/2). Referring to figure 5.5, these are transitions IIa and IIb

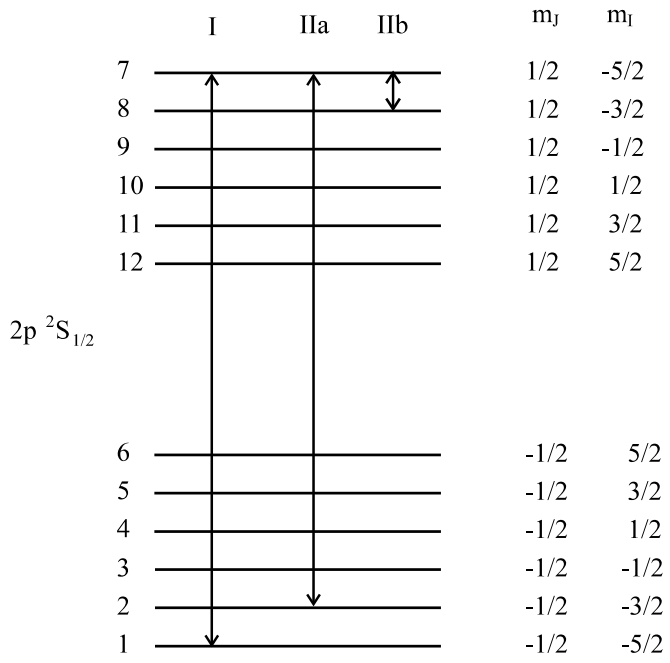

Fig. 5.5: The Hyperfine Levels of $^{25}Mg^+$ with the transitions associated with nuclear quantum jumps.

respectively.

Although the quantum jump process is random, statistical analysis shows that there is, on average, a constant ratio between the time which the ion spends fluorescing (on time) and the time for which it is in the metastable level (off time). The rate of quantum jumping for a particular ion can be established by a density matrix analysis. This has been done in detail for $^{24}Mg^+$ [21, 22]. Alternatively a simple rate equation approach can be applied. In this method, steady state level populations are obtained and expressed in terms of laser detuning and transition width from which the mean duration of fluorescence on and off periods can be determined. The ratio of the on time to off time (on to off ratio) can be obtained from the ratio of the detunings of transitions into and out of the dark state. It is found that the On to off ratio is independent of laser power and magnetic field while it is weakly dependent upon detuning. On to off ratios for the different ionic isotopes can be found by

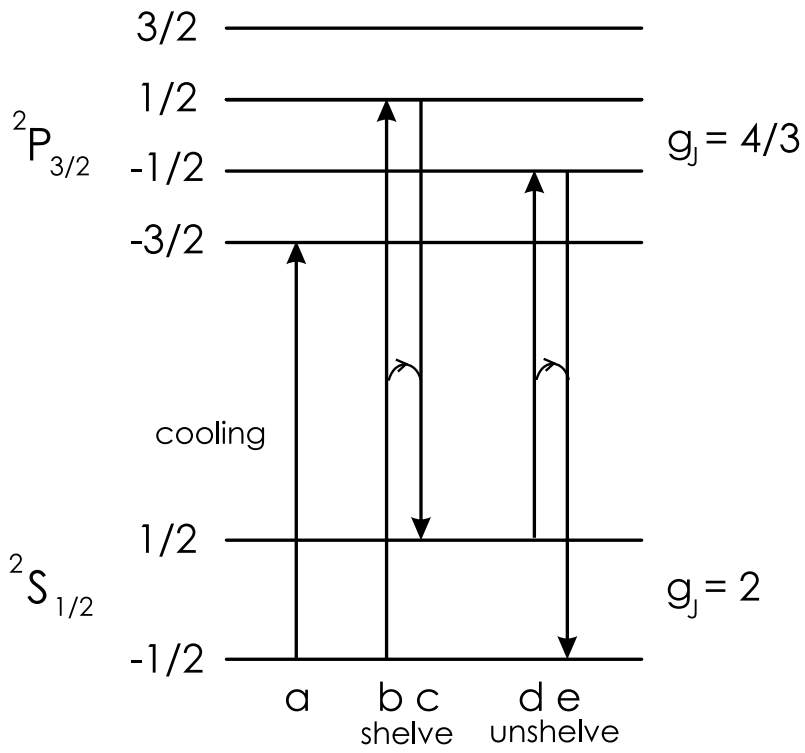

Fig. 5.6: The energy levels of $^{24}Mg^+$ with the transitions associated with quantum jumps.

considering the frequency shifts in the energy levels; in $^{26}Mg^+$ these cancel out to give a ratio which is the same as $^{24}Mg^+$, while for $^{25}Mg^+$, owing to the presence of hyperfine structure, the effect is to reduce the ratio from 16.0 to 11.8 for a 0.98T field.

An appreciation of how the on to off ratio is calculated and how it is altered by hyperfine structure can be obtained very simply by looking at the detunings of the transitions involved. Consider the formula describing the energy of an electronic Zeeman level:

$$E = g\mu_B \mathrm{m}_J B \tag{5.1}$$

where μ_B is the Bohr magnetron and g the Lande g factor which for the $^2S_{1/2}$ level is 2 and for the $^2P_{3/2}$ level is 4/3.

The on to off ratio can be found by calculating the rate of population transfer

between fluorescing and shelving states. Referring to figure 5.6, the transitions into and out of the shelving state are labelled respectively b, c and d, e. If we let the population of the ground state $^2S_{1/2}$(-1/2) = N_-, and the population of the metastable state $^2S_{1/2}$ (1/2)) = N_+, where $N_- + N_+ = N_0$ (a constant), then in the steady state:

$$\frac{dN_-}{dt} = \frac{dN_+}{dt} = 0 \tag{5.2}$$

$$R_e N_+ = R_b N_- \tag{5.3}$$

where, R_b denotes the rate of transitions into the shelving state while R_e denotes the rate out of the shelving state. From perturbation theory, these rates are:

$$R_i = \alpha \frac{(\Gamma/2)^2}{\Delta_i^2 + (\Gamma/2)^2} \tag{5.4}$$

In this equation α is a constant containing information about the atomic core and the fundamental constants involved. Γ is the transition width and i = a, b, c, d, e. The quantum jump transitions are driven far from resonance so we can assume that the detunings $\Delta_{b,e} >> \Gamma/2$. Thus it can be shown that:

$$\frac{N_+}{N_-} = \frac{R_b}{R_e} = \frac{\Delta_e^2}{\Delta_b^2} \tag{5.5}$$

Equation (5.1) can be used to find the detunings of the transitions which, in the case of $^{24}Mg^+$, turn out to be in a ratio of 4:1. Thus the on to off ratio is 16. Clearly an isotope shift in energy levels has no effect on the shape of the problem so $^{26}Mg^+$ has the same ratio as $^{24}Mg^+$, however for the odd isotope a second term in the energy equation is required to take account of the hyperfine splitting:

$$E = g\mu_B \mathrm{m}_J B + A\mu_I \mu_J \tag{5.6}$$

Table 5.1: The detunings of the $^{25}Mg^{+}$ transitions used to calculate the On to Off ratio.

Transition	$^2S_{1/2} \rightarrow {}^2P_{3/2}(m_J, m_I)$	Δ	ON : OFF
a	$-28B - (-14B + A5/4)$	-13.25	
b	$-B28/3 - (-14B + A5/4)$	5.42	$(-10.85)^2 : (37.35)^2$
c	$-B28/3 - (14B - A5/4)$	-24.10	
d	$B28/3 - (14B - A5/4)$	-5.42	1 : 11.85
e	$B28/3 - (-14B + A5/4)$	24.10	

where $A = -596$ MHz for the S level, while for the P level this value is small enough to be ignored in these calculations. The effect of the additional term is to alter the detunings and hence the on to off ratio, which becomes 11.8 for the lower cooling transition in a field of 0.98 T.

To clarify the calculations described above table 5.1 shows how the detunings are worked out for $^{25}Mg^{+}$ for a field of 0.98 T.

At this point it is appropriate to mention the possibility of laser cooling Mg^{+} using its higher frequency transition: $^2S_{1/2}$, ($m_J = 1/2$, $m_I = 5/2$) $\rightarrow$ $^2P_{3/2}$, ($m_J = 3/2$, $m_I = 5/2$). The separation of this transition from the lower one is 27.44 GHz in a magnetic field of 0.98 T. At this higher frequency the on to off ratio for $^{24}Mg^{+}$ and $^{26}Mg^{+}$ is unaltered but it has the effect of raising the ratio (from 11.8 to 22.8) for $^{25}Mg^{+}$.

5.4 Outline of the Experimental System

The experiments described here were carried out using a Penning trap with a split ring electrode, described briefly in Chapter 4 (see also reference [21]). The U.V. laser power was between 36 and 77 mW (continuously monitored). The majority of data were collected with up to 60 counts per ms for a single ion, above a background count of 10 counts per ms. The average length of a quantum jump was recorded as ~ 2 ms.

The source of magnesium was a natural abundance atomic oven, the ratio of species $^{24}Mg^+$: $^{25}Mg^+$: $^{26}Mg^+$ being 8:1:1. Ions are created when the atomic beam from the oven is crossed with a beam of electrons from a heated filament. The oven was characterized such that it was possible to load small clouds (containing around 10 ions), and single ions with relative ease and repeatability. The method for loading is explained in Chapter 4. Single ions of the most abundant isotope could be loaded directly, but it was found that the most reliable way of obtaining single ions of $^{25}Mg^+$ and $^{26}Mg^+$ was to load a small cloud and then selectively cool the desired isotope. The other isotopes present were sympathetically cooled. The large collision rate resulting from this regime led to reduced storage times and increased noise on quantum jump traces for $^{25}Mg^+$ and $^{26}Mg^+$ compared to those for $^{24}Mg^+$. Typically the signal was $\sim 20\times10^3$ counts per second for the two less abundant species while for $^{24}Mg^+$ it was $\geq 55\times10^3$ counts per second (against similar background count levels).

5.5 Results

5.5.1 Initial Analysis

Data files containing the quantum jump information in the form of counts versus time were analyzed using a Turbo Pascal program (see Appendix A). The program produces a histogram of the number of times particular count rates are recorded. This produces a double peaked distribution: a small peak at the background count rate and a large peak at the signal level corresponding to single ion fluorescence.

The program also produces a distribution of the number of jumps recorded of a particular length, which takes the form of an exponential decay with respect to increasing jump length. To determine what constitutes a quantum jump the program

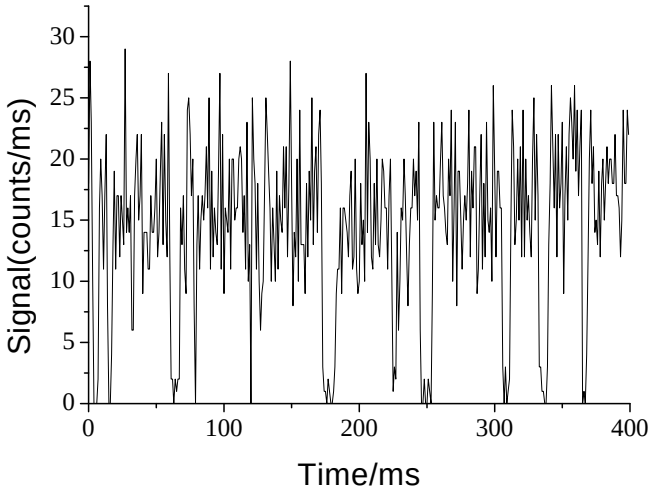

Fig. 5.7: Signal from a single $^{25}Mg^{+}$ ion.

is given a *threshold* value: if the signal falls bellow this value during a time bin the ion is considered to be in the off state and a jump is counted. An example of some experimental data is shown in figure 5.7. Results from the initial analysis of this data are shown in figure 5.8. The ion involved is $^{25}Mg^{+}$.

Data produced by two or three ions can also be analyzed in this way and where the signal to noise ratio is sufficiently good the histograms produced have three and four peaks respectively. This is a result of the fact that traces for two and three ions have two and three distinct signal levels above background. Some sample data traces and their histograms are included in Appendix B.

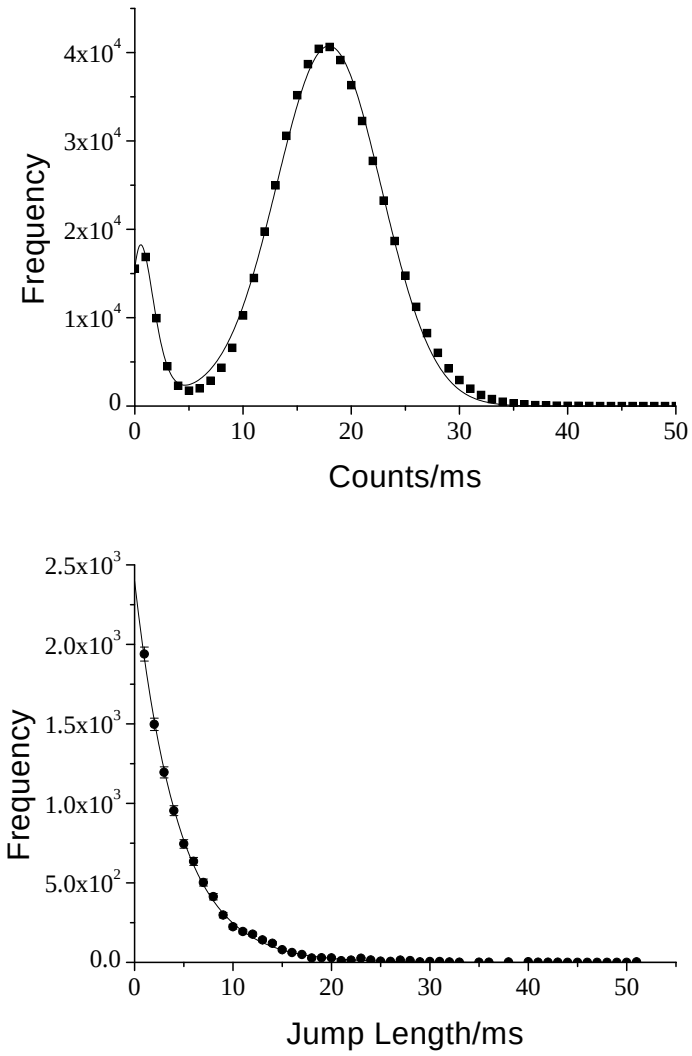

Fig. 5.8: The quantum jumps of a single $^{25}Mg^{+}$ ion. Top: The photon statistics for the raw data shown at the top of the page. Bottom: Jump length distribution from the raw data shown at the top of the page.

5.5.2 Construction of the Model

If the threshold could be set so as to give an unambiguous distinction between the on and off states this would provide an excellent method for finding the on to off ratio. Referring to the graph showing the photon statistics in figure 5.8 as an example, the areas beneath the peaks at the signal and background count rates represent the time the ion spends in the on state compared to the time it spends in the off state respectively. The on to off ratio could be found from the ratio of the areas under the respective peaks. In the absence of all noise sources, the threshold would be set at half the average signal level. Unfortunately signal noise is such that it is often unclear where the threshold level should be set. An indication of whether a good threshold level has been set is obtained from the graph of jump length distribution. As a result of laser noise, too high a setting can result in an excessively large number of short jumps being recorded. These "jumps" are in reality merely statistical fluctuations in signal level. If a log plot of the jump length distribution is made then the anomalous point, at the shortest recorded jump length, is clearly far away from the general trend of the data. Despite this there is still a range of possible values which the threshold might reasonably take.

In order to eliminate some of the uncertainty of estimating the threshold, a more sophisticated approach must be taken. It can be shown that the on to off ratio may be calculated as:

$$\frac{\langle T_{on} \rangle}{\langle T_{off} \rangle} = \frac{\bar{x}_w - M_b}{M_s - \overline{x}_w} \tag{5.7}$$

where $\bar{x}_w$ is the weighted mean of the whole distribution. M_b and M_s are the mean background and signal counts respectively.

For an accurate determination of the mean signal and background levels it is important to find a suitable way of dealing with intermediate count levels, counts which can not be considered either true on counts or true off counts. These counts

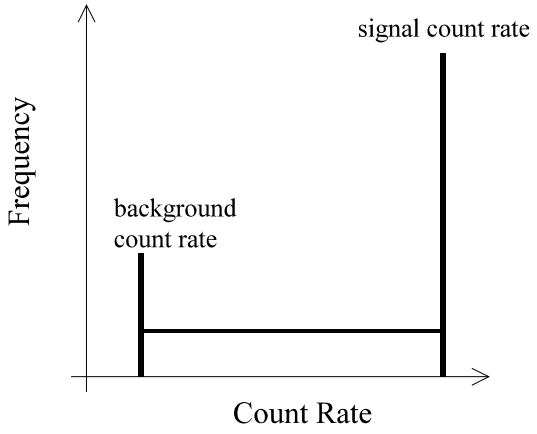

Fig. 5.9: The theoretical distribution of photons collected from a single ion undergoing quantum jumps.

need to be eliminated from the calculation of the two means, whilst the entire distribution is considered in finding $\bar{x}_w$. Noise filtering was done in two different ways; one involved a program loop which discarded any events where the ion switched from above to below the threshold (method (1)). The other involved the introduction of a second threshold (method (2)), such that the fluorescence rate had to be above one threshold to be regarded as on while it had to be below the second threshold to be counted as off. Both of these methods were found to remove some of the arbitrariness from the choice of threshold.

Finally a third method was developed: a curve was generated and fitted to the data. Ideally, since there are only two possible states in which the ion can find itself, the photon statistics should produce two delta functions: one at background signal level and a second one at the single ion signal level, as shown in figure 5.9.

The data, however, is binned and there is a finite possibility that the ion will in fact switch between states during one bin time. This results in a range of intermediate values being recorded which are distributed between the two delta functions, we therefore introduce a *correction function*. The area beneath the correction function is expected to be twice the number of quantum jumps recorded, an obvious

consequence of the fact that if the ion is observed making n jumps then it switches between states $2n$ times.

The exact form of the intermediate distribution can be determined by consideration of the types of processes and their respective probabilities which would produce these points. For example the ion may switch from on to off during a bin or it may switch on to off to on again. Both produce intermediate count rates but the former process is more likely, as bin size was chosen to be shorter than the average expected jump length. This analysis gives a distribution which is essentially a top hat function although it does in fact have a tendency to be skewed in favour of the higher values.

The model must be refined to take account of noise. The most significant sources of noise are the counting statistics, laser power and laser frequency fluctuations. In the absence of laser noise, the form of the data and its discrete nature suggests that a Poisson distribution would be a suitable model for both peaks. However, this was found to be unsatisfactory, in particular in fitting to the signal peak. This made further consideration necessary; while the laser power fluctuation will affect both peaks, the frequency fluctuation (frequency jitter of ~ 6 MHz) can only affect the signal peak. The additional broadening of the signal peak led to the conclusion that it would be best modelled with a Gaussian distribution.

The central distribution, the correction function, was taken to be flat topped. The rate at which it rises to its maximum is governed at the lower (off) end by the width of the Poissonian background distribution and at the higher (on) end by the width of the Gaussian signal distribution. This is illustrated in figure 5.10, which shows data from a single $^{24}Mg^{+}$ ion which, as one of the least noisy traces, best illustrates the development of the model.

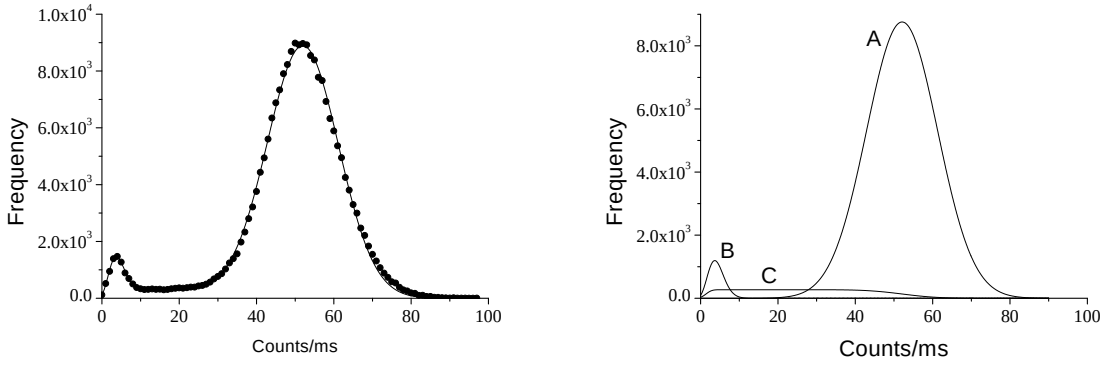

Fig. 5.10: The development of the model using data for a single $^{24}Mg^{+}$ion. Right: the labels A, B, and C refer to the curves for the signal peak, the background peak and the correction function respectively.

The form of the correction function was first approximated empirically, thus:

$$H \times \left[\frac{1}{\exp(-4(x - M_b)/\sqrt{M_b})} - \frac{1}{\exp(-4(x - M_s)/\sigma_s)} \right] \tag{5.8}$$

here, x is the photon count rate, M_b and M_s are the means of the background and signal distributions respectively and σ_s is the width of the signal distribution. H is roughly the maximum height of the distribution. The constant 4 was chosen to best fit the data.

An appropriate correction function can be derived analytically by the convolution of two Gaussians to give the following:

$$\frac{H}{2} \times \left(\mathrm{erf}\Big[\frac{x - M_b}{\sqrt{2M_b}}\Big] - \mathrm{erf}\Big[\frac{x - M_s}{\sigma_s\sqrt{2}}\Big] \right) \tag{5.9}$$

The three distributions are added and then fitted to the data. The height of the correction function was fixed in order to fulfill the requirement that the area beneath the correction function should be twice the number of quantum jumps seen. This analysis is similar to the approach taken independently by Roos [24].

As has been mentioned, the areas under the two peaked distributions are representative of the time the ion is observed in the off state and the on state. The correction function is present owing to the switching between states during one bin: considering this process it is expected that on average the ion will be in the on state during half the bin and in the off state during half the bin. Consequently, since the total area under the correction function equals twice the number of jumps observed, half of its area should be added to the off time while half should be added to the on time thus:

$$\frac{\langle T_{\text{on}} \rangle}{\langle T_{\text{off}} \rangle} = \frac{A_{\text{on}} + (A_{\text{corf}}/2)}{A_{\text{off}} + (A_{\text{corf}}/2)} \tag{5.10}$$

The model gave consistent results, however it might be argued that as with the other methods it is open to some error on the grounds that it still relies on the value of the threshold being set correctly. As explained, if the threshold is set too high large numbers of short "jumps" are counted which are in fact fluctuations in signal level. These spurious jumps mean that the area under the correction function will be set too high, which not only gives a poor fit but also an artificially low on to off ratio.

5.5.3 Results Obtained

Table 5.2 shows a summary of the results obtained. Methods (3a) and (3b) refer to the curve fitting methods using the analytical (equation 5.9) and empirical (equation 5.8) correction functions respectively. Results obtained by use of equation 5.7 are also included in the table, the methods ((1) or (2)) indicate which noise filtering technique was employed.

The data are grouped according to the laser power and time bin length used for each set α to δ. The errors are generated by considering the standard deviation of sub-samples of data sets α, β, γ, and δ and also that between data sets for the same isotope. Since the value of the On:Off ratio for $^{25}Mg^{+}$ is affected by which cooling

Table 5.2: The On to Off ratios for the three stable isotopes of Mg^+: calculated and experimental values.

Ion Species	Run Time/s	On:Off				
		Theoretical	method 1	method 2	method 3a	method3b
$^{24}Mg^+(\alpha)$	112	16.0	15.8±0.2	16.2±0.2	16.6±0.8	16.0±0.2
$^{24}Mg^+(\beta)$	320	16.0	14.6±0.1	15.9±0.5	15.9±0.8	15.9±0.8
$^{24}Mg^+(\gamma)$	320	16.0	14.5±0.7	16.0±0.5	16.4±0.8	16.4±0.8
$^{25}Mg^+I(\alpha)$	276	11.8	10.0±1.0	12.0±0.6	10.0±1.0	10.4±0.4
$^{25}Mg^+I(\beta)$	480	11.8	9.6±0.5	10.0±1.0	10.0±1.0	9.8±0.5
$^{25}Mg^+I(\gamma)$	384	11.8	10.0±0.5	12.0±1.0	10.0±1.5	9.7±0.5
$^{25}Mg^+I(\delta)$	384	11.8	10.0±1.0	11.0±1.0	11.0±1.5	11.0±0.6
$^{26}Mg^+$	480	16.0	15.2±0.2	16.1±0.5	15.0±1.5	16.6±0.8
$^{25}Mg^+II$	128	22.8	19.0±3.0	22.0±2.0	22.0±4.0	22.0±2.0

transition is used, I denotes the lower transition and II denotes the upper transition (respectively transitions 1 and 2 on figure 5.4).

Results obtained by all methods are consistent with the prediction that the even isotopes should have similar jump rates while $^{25}Mg^+$ has a lower rate at the lower transition and a higher rate at the upper transition. The curve fitting methods, however were deemed to be the most accurate, as they rely less on an accurate choice of threshold: the greatest errors in this case arising more from differences in results from sub-samples of the data sets. Taking averages over all the values obtained by both methods 3a and 3b the on to off ratios for the three isotopes are found. These turn out to be, for $^{24}Mg^+$ 16.1 ±0.8, for $^{25}Mg^+$ 10.2 ±1.5 (lower transition) and 22.0 ±3 (upper transition), while for $^{26}Mg^+$ it is 15.8 ±0.7. The ratios for the two even isotopes are the same, with a mean of 16.0 ±0.7 within the limits of experimental accuracy. These results are shown graphically in figure 5.11

The systematically low ratio obtained at the lower $^{25}Mg^+$ transition is not readily explainable. However two factors in particular might be responsible: one is the low signal for $^{25}Mg^+$ in comparison to that for the $^{24}Mg^+$ data; this meant that slightly

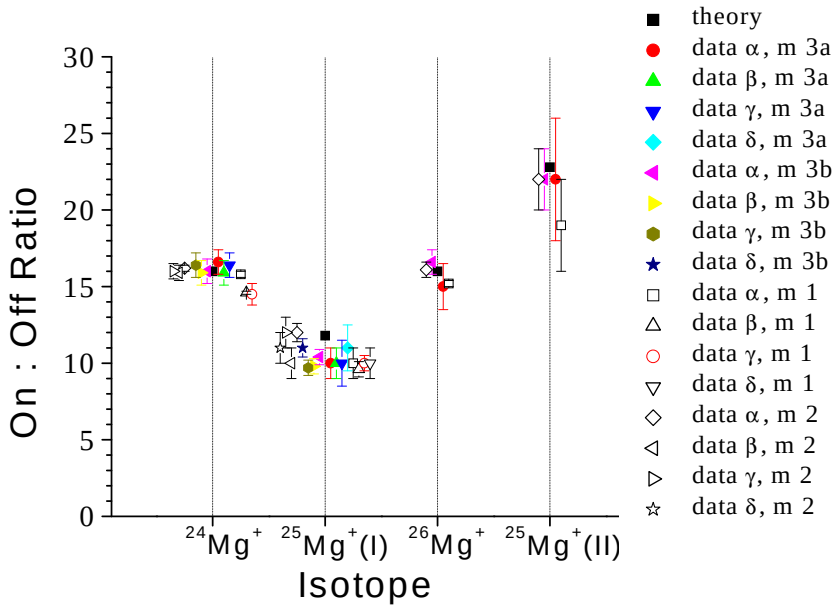

Fig. 5.11: A graphical representation of the results on table 5.2 to show how they cluster about the theoretical values.

longer bin times (1 ms instead of 0.5 ms) were often required to maintain a reasonable signal to noise ratio for $^{25}Mg^{+}$. As a result the average jump length is more similar to the bin size used in the case of the $^{25}Mg^{+}$ data as compared to the $^{24}Mg^{+}$ data. The result is less well separated, highly broadened peaks, which make the curve fitting routine difficult and imprecise for these traces.

Besides problems in analyzing the data there are physical factors which could affect the jump rate to give a lower than expected on to off ratio; these include the laser detuning [21] and polarization vector of the incoming laser light. Of these two the latter is by far the most important, since the presence of polarization components both perpendicular and horizontal to the axial magnetic field enables the ion to make both σ-transitions (1→5→2) and π-transitions (1→4→2). The number of π-transitions made is clearly dependent on the proportion of laser light present which is polarized parallel to the magnetic field. Reformulation of the rate equations with these additional transitions included results in a reduced on to off ratio [26]. The

relationship between the on to off ratio and the polarization rotation is of the form:

$$\frac{R'_e}{R'_b} = R\frac{1+x}{1+7x} \tag{5.11}$$

R'_e and R'_b are the new rates of transition into and out of the shelving state. R is the theoretical on to off ratio. The parameter x relates to the polarization rotation: it is the fraction of light which is polarized parallel to the magnetic field:

$$x = \frac{I_{\|}}{I} = \frac{|E|^2\cos^2(\Theta)}{|E|^2(\cos^2(\Theta)+\sin^2(\Theta))} \tag{5.12}$$

The polarization of laser light entering the trap was tested and it was found that the polarization vector was rotated by 4° from the desired orientation. That the polarization vector suffered no further rotation on traveling through the trap was also tested. The degree of rotation of the polarization is not significant enough to have caused the difference observed since it would only account for a 2.4% change in the on to off ratio, from 11.8 to 11.5 in the case of the lower $^{25}Mg^+$ transition.

5.5.4 Were there any Nuclear Jumps?

The quantum jump process can be considered largely equivalent in all three isotopes of magnesium which have been studied. However the presence of hyperfine structure in the odd isotope, $^{25}Mg^+$, opens up the possibility for other jump transitions through hyperfine mixing of states. Whether or not these other jump transitions occur can be determined from the distribution of observed jump lengths: since the hyperfine mixing is small (the mixing coefficient being of the order of 0.02) the nuclear jump transitions will be rare; they are also predicted to be longer than normal jumps. As a consequence the jump length distribution for $^{25}Mg^+$ should show a longer tail off at long jump durations in comparison to the distributions for

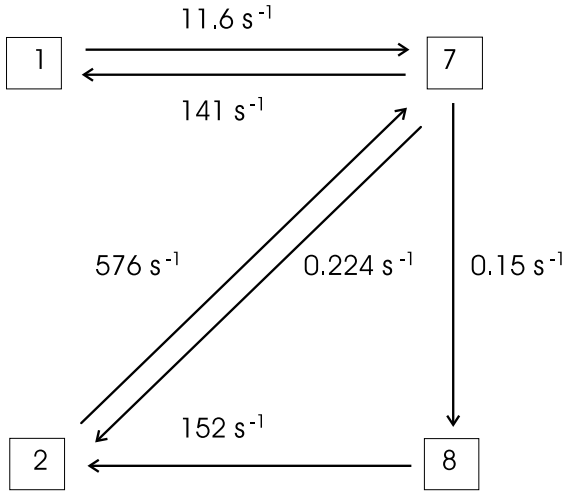

Fig. 5.12: A schematic diagram for quantum jumps in $^{25}Mg^{+}$. The levels involved are labelled 1, 2, 7 and 8 from figure 5.5. The transition rates between the four levels are indicated, these can be used to calculate the steady state populations of each level.

the other two isotopes. It is expected that whereas the jump length distributions for $^{24,26}Mg^{+}$ can be modelled by single exponential decay curves the distribution for $^{25}Mg^{+}$ will be best described by the sum of two terms: one of similar characteristics to that used in the other two cases (indicating a jump process common to all three isotopes) and a second low amplitude, slowly decaying curve (for the nuclear jump process, peculiar to $^{25}Mg^{+}$). In figure 5.12 the paths for each type of quantum jump are shown along with the rate at which they occur.

To determine the rate and duration of the different types of jump occurring the rate equation approach can be used, this time taking into account the new decay routes available. Transition probabilities between the levels involved were calculated and the ratios of state populations taken [9].

$$\frac{N_7}{N_1} = 0.0822 \tag{5.13}$$

$$\frac{N_8}{N_1} = 1.00 \times 10^{-3} \tag{5.14}$$

$$\frac{N_2}{N_1} = 6.40 \times 10^{-4} \tag{5.15}$$

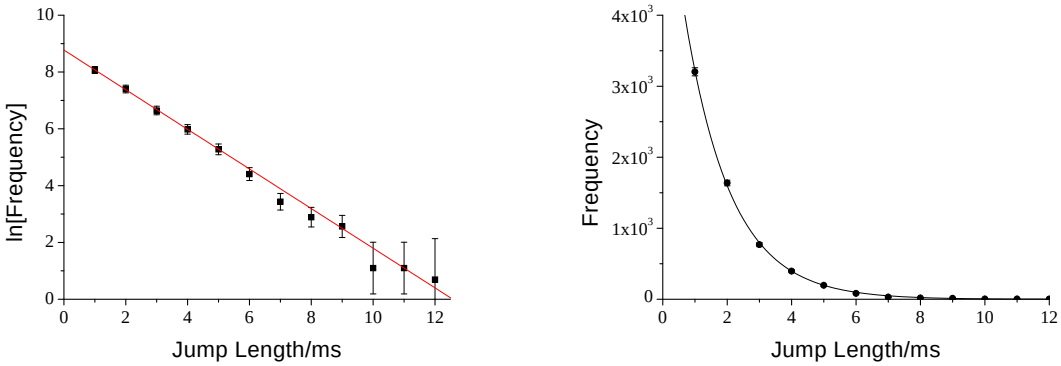

Fig. 5.13: Left: a log-plot of the jump length distribution for $^{24}Mg^{+}$. Right: the raw data (from set α).

where $N_{1,2,7,8}$ are the populations of levels 1,2,7 and 8 respectively (see figure 5.5).

Equation 5.13 clearly represents the predominant process (that equivalent to the jumps observed in the even isotopes), while equations 5.14 and 5.15 show two very small effects which would be indistinguishable from each other in the experimental data.

Using the transition probabilities we can calculate that only 0.27 % of jumps will be nuclear (1 in 370 jumps). Jump lengths are predicted to be 3.2 t and 2.2 t (where t is the length of normal jumps which is $\sim$ 2 ms for the powers used) [9]. The average length of a nuclear jump is 2.7 t = 5.4 ms.

The jump length distribution for normal jumps can be described by a simple exponential of the form: $K\exp(-t/\tau_j)$, where τ_j describes the average jump length for the distribution and K is a constant. The nuclear jump process however, involves several stages. Each of these stages has a characteristic time constant, thus the jump length distribution will not be a simple exponential decay. Assuming that all jumps are normal and fitting an exponential to data for all three isotopes gives an initial idea of the qualitative differences between the three.

Figures 5.13 and 5.14 show the jump length distributions of two different isotopes,

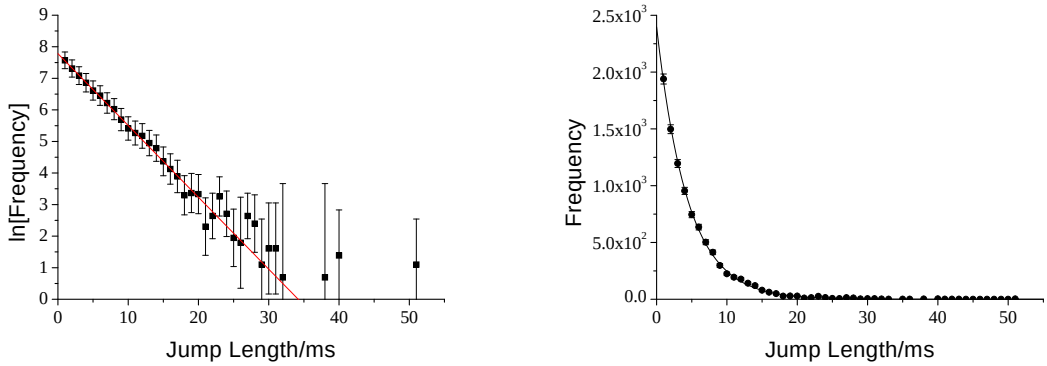

Fig. 5.14: Left: a log-plot of the jump length distribution for $^{25}Mg^{+}$. Right: The raw data (from set α). In contrast to the plot for $^{24}Mg^{+}$, the exponential decay model is not entirely adequate, in particular at longer jump lengths.

$^{25}Mg^{+}$ and $^{24}Mg^{+}$ respectively, for comparison. As can be seen, while the data for $^{24}Mg^{+}$ is well described by a single exponential, such a curve is clearly not adequate for the $^{25}Mg^{+}$ data.

The main difficulty in analyzing the data is the fact that the nuclear jumps are predicted to be so rare: the average number of jumps observed in a single data set was 5000, of these we expect only 13.5 to be nuclear jumps. As a result any contribution from the nuclear jumps to the overall jump length distribution is small and although we can clearly see that there is a difference between the distributions for the odd and even isotopes it is difficult to make any firm conclusions due to the unreliability of the curves fitted to the data.

Direct Observation of Nuclear Quantum Jumps

As has previously been discussed the infrequency of nuclear quantum jumps makes it very difficult to apply any statistical analysis to the data which was collected. It can be estimated that 10 hours of data would yield 1×10^{6} jumps, of which 3×10^{3} are predicted to be nuclear jumps. Such a number of nuclear jumps would enable a proper statistical fit to be made from which both the amplitude and the time

constant of the nuclear jumps process could be determined.

An alternative approach might be to increase the incidence of nuclear jumps by driving the process with RF (radio frequency) radiation at the hyperfine transition frequency. To this end the split ring trap was refurbished and fitted with an enriched $^{25}Mg^{+}$ oven (in order to be able to load this isotope directly so avoiding the problems of collisional heating referred to earlier in this chapter). There are two possible approaches, both of which were explored. In the first approach, a small cloud or ideally, a single ion would be trapped and the hyperfine transition probed. The dip in fluorescence which would result from driving should show a characteristic recovery time which is related to the rate of nuclear jumping. The other approach would involve capturing single ions and simply allowing them to perform quantum jumps, with the RF drive on the probability of those jumps being nuclear would be enhanced. On studying the jump length distribution the nuclear jump process would have a much greater influence on the shape of the distribution than under normal circumstances.

Of the two nuclear jump processes only one can be driven directly (the other involves a forbidden transition). This is transition IIb on diagram 5.5, its frequency is 285.7538 MHz, as calculated using the Breit-Rabi formula [27]:

$$\Delta E(F,M) = -\frac{h\Delta\nu}{2(2I+1)} - g_I'\mu_B BM \pm \frac{h\Delta\nu}{2}\left(1+\frac{4Mx}{2I+1}+x^2\right) \qquad (5.16)$$

here $x = g_J'\mu_B B/h\delta\nu$, $\delta\nu = 3A$, where $A = -596$ MHz, $g_J' = g_J - g_I'$ and g_J is the Lande g factor and $g_I' = 9.299\times10^{-5}g_J$ [28]. M refers to the value of $m_F = m_I + m_J$, μ_B is the Bohr magnetron, h is Plank's constant and B the magnetic field, which in this case was 0.98 T. The value of I for magnesium is 5/2 and the $\pm$ in equation 5.16 refers to transitions between levels with $m_F = I + 1$ (+), or between levels with $m_F = I - 1$ (-).

From previous experience driving hyperfine transitions in Beryllium, the transition was expected to be quite narrow: 50 - 100 kHz (taking into account the fact that the electromagnet field is many times less stable than the superconductor field). The RF was amplified and coupled into the trap using a stub-tuner.

Despite numerous attempts, the hyperfine transition was not successfully driven using this set-up. When the magnetic field stability was tested, by driving motional frequencies of the ion cloud, it was found to be of the order of $\Delta B = \pm 0.01$ T. Using the differential of the Breit-Rabi formula at 0.98 T the expected change in transition frequency with magnetic field was estimated to be ± 150 kHz. This meant that in order to see the transition very long, broad frequency sweeps should be executed. Of course this might then result in further power broadening of the transition. An additional problem at this stage was that the fluorescence signal from the ions could not be kept constant for such long periods as were required. It is thought that the dye-circulator may have developed some problems which fed through into dye-jet instabilities causing beam pointing problems which were at times quite severe. This combined with the fact that the transition is weak and possibly very broad, meant that it could not be detected. As a result it was decided that the project should be abandoned.

References

[1] H. F. Powell, M. A. van Eijkelenborg, W. Irvine, D. M. Segal and R. C. Thompson, *J. Phys. B.* **35**, 205 (2002)

[2] Th. Sauter, R. Blatt,W. Neuhauser and P. E. Toschek, *Phys. Scripta*, **T22**, 128 (1988)

[3] R. G. Hulet, D. J. Wineland, J. C. Berquist and W. M. Itano, *Phys. Rev. A.* **37**, 4544 (1988)

[4] R. Blatt and P. Zoller, *Eur. J. Phys.* **9**, 250 (1988)

[5] P. A. Barton, C. J. S. Donald, D. M. Lucas, D. A. Stevens, A. M. Steane, D. N. Stacey, *Phys. Rev. A.* **3**, 2503 (2000)

[6] G. Ritter and U Eichman, *J. Phys. B.* **9**, L141 (1997)

[7] A. A. Madej, J. D. Sankey and A. R. W. McKellar, *J. Mod. Opt.* **2**, 373 (1992)

[8] R. J. Cook, *Progress in Optics*, vol 27, ed. Wolf (Amsterdam, Elsevier), p 316, (1990)

[9] H. G. Dehmelt, *Bull. Am. Phys. Soc.* **20**, 60 (1975)

[10] Th. Sauter, R. Blatt,W. Neuhauser and P. E. Toschek, *Opt. Commun.* **60** (1986), 287 (1986)

[11] W. Nagourney, J. Sandberg and H. G. Dehmelt, *Phys. Rev. Lett.* **56**, 2797 (1986)

[12] M. Lewenstein and J. Javanainen, *Phys. Rev. Lett.* **59**, 1289 (1988)

[13] G. S. Agarwal, S.V. Lawande and R. D'Souza, *IEEE J. Quant. Elec.* **24**, 1413 (1988)

[14] S. U. Addicks, A. Beige, M. Dakna and G. C. Hegerfeldt, *Euro. Phys. J. D.* **15**, 393 (2001)

[15] C. Skornia, J. von Zanthier, G. S. Agarwal et al, *Euro. Phys. Lett.* **56**, 665 (2001)

[16] J. C. Berquist, R. G. Hulet, W. M. Itano and D. J. Wineland, *Phys. Rev. Lett.* **57**, 1699 (1986)

[17] W. M. Itano, J. C. Berquist, R. G. Hulet and D. J. Wineland, *Phys. Rev. Lett.* **59**, 2732 (1987)

[18] M. Roberts, P. Taylor, G. P. Barwood, P. Gill, H. A. Klein and W. R. C. Rowley, *Phys. Rev. Lett.* **78**, 1876 (1997)

[19] R. H. Dicke, *Phys. Rev.* **89**, 472 (1953)

[20] D. J. Bate, PhD Thesis, University of London, Unpublished (1991)

[21] R. G. Hulet and D. J. Wineland, *Phys. Rev. A.* **36**, 2758 (1987)

[22] R. J. Cook and H. J. Kimble, *Phys. Rev. Lett.* **54**, 1023 (1985)

[23] M. A. van Eijkelenborg, M. E. M. Storkey, D. M. Segal, R. C. Thompson, *Int. J. Mass. Spectrom.* **188**, 155 (1999)

[24] C. Roos, PhD Thesis, University of Innsbrick, (2000)

[25] W. T. Irvine, *Third Year Lab Report On Quantum Jumps*, Imperial College, Unpublished (1999)

[26] D. C. Wilson, PhD Thesis, University of London, Unpublished (1992)

[27] G. K. Woodgate, *Elementary Atomic Structure*, Clarendon Press, Oxford, (1980)

[28] W. M. Itano and D. J. Wineland, *Phys. Rev. A.* **24**, 1364 (1981)

CHAPTER 6

Axialization of Single Ions and Small Clouds

6.1 Motivation

This chapter describes work which was to have been carried out in the Zeno trap. It was hoped that the technique, if successfully applied, would aid the stability of single trapped ions: making them less sensitive to laser power and frequency fluctuations leading to a greater signal to noise ratio. In the event the experiments described were actually done in the split-ring trap which was used for the quantum jump work. The main motivation in this case was to demonstrate the possibility of using the technique of axialization with a laser cooled system and to investigate its limitations. The results would then be useful in the ongoing project involving laser cooled Calcium ions.

6.2 Axialization as a Technique in Ion Trapping

With the growing interest in quantum information processing there has been an increasing need to develop technology which might enable the implementation of the ideas proposed. Very low temperatures can be reached in ion traps using laser cooling, but the minimum temperature can be limited by the nature of the trapping method itself. The two most widely used types of ion trap are the Paul (radio frequency) trap and the Penning trap [2]. The principles behind each of these traps are explored briefly at the beginning of Chapter 2. The two traps differ in the manner in which they provide radial confinement of ions: the former uses an electric field oscillating at a radio frequency while the latter uses a static magnetic field. This means that in the Paul trap the ion motion is simple harmonic in all directions but in the radial plane of the Penning trap the action of the combined electric and magnetic fields results in a complex orbital motion: a superposition of two rotations, the magnetron and the cyclotron rotation [1].

Until now much work in the area of quantum information science has focused on the use of linear Paul traps which allow the preparation of stationary strings of ions and strong confinement to the Lamb-Dicke regime [3]. Unfortunately, the low temperature limit of the Paul trap can be affected by the "micro-motion" of the trapped ions, which arises as a result of the trapping field and cannot be completely avoided. The Penning trap has no such limitation. However, the nature of the motion in the radial plane of the Penning trap complicates the laser cooling process [4–7]. Specifically, it is difficult to decrease both the magnetron and modified cyclotron amplitudes simultaneously. Problems arise because the magnetron motion is unstable: its total energy is negative so energy must be supplied in order to reduce the magnetron radius. It can be shown that the magnetron motion is reduced only when the laser is placed at the point where its rotation moves the ions *in the same*

direction as the laser photons. Even so the modified cyclotron motion is minimized considerably more efficiently than the magnetron orbit. This is due to the relatively small gradient of laser intensity across the centre of the trap [7]. Laser cooling in a Penning trap is discussed in Chapter 2.

Axialization, as the terminology implies, is the process by which particles in a Penning trap are driven towards the central axis of the trap [8]. It occurs when the efficient cooling of the cyclotron motion is effectively extended to the magnetron motion by means of a coupling between the two induced by a weak external field oscillating at the true cyclotron frequency, ω_c. This makes the conditions within the Penning trap approach those of the Paul trap, but without micro-motion. As a result it is expected that very low temperatures may be reached. This makes the Penning trap a serious contender for quantum information processing applications, especially where a magnetic field is required [9].

6.2.1 Manipulation of Ions in a Penning trap

From Chapter 2, section 2.1.1, there are three frequencies which can be used to describe the motion of ions in a Penning trap. The first of these, ω_z, describes simple harmonic motion in the axial direction. The other two frequencies are associated with motion in the radial plane, the modified cyclotron, ω_c', and the magnetron, ω_m.

The ion motional frequencies are related by the following equations:

$$\omega_z = \sqrt{\frac{4eU_0}{m(r_0^2 + 2z_0^2)}} \tag{6.1}$$

$$\omega_c' = \frac{1}{2}\omega_c + \frac{1}{2}\sqrt{\omega_c^2 - 2\omega_z^2} \tag{6.2}$$

$$\omega_m = \frac{1}{2}\omega_c - \frac{1}{2}\sqrt{\omega_c^2 - 2\omega_z^2} \tag{6.3}$$

where e is the electronic charge, B is the magnetic field strength, m is the ion mass

and U_0 is the trapping voltage. The values r_0 and z_0 define the distance from trap centre to the electrodes in the radial and axial directions respectively. The sum of the magnetron frequency and the modified cyclotron frequency is always equal to the true cyclotron frequency, $\omega_c = eB/m$. In our trap the characteristic frequencies have been measured for $^{24}Mg^+$ as: $\omega_z' = 2\pi\times283$ kHz, $\omega_m = 2\pi\times72$ kHz and $\omega_c' = 2\pi\times557$ kHz (with trapping voltage $U_0 = 10$ V and magnetic field of $B = 0.97$ T). The derivation of the expressions for motional frequencies and a graph showing their voltage dependence can be found in Chapter 2.

The motional frequencies of the trapped ions can be probed by measuring the response of the ion cloud to a small oscillating drive voltage applied to the trap electrodes. Here we are concerned with a laser cooled system, thus the changing shape of the ion cloud as a result of resonant driving is reflected in the fluorescence intensity emitted by the ions. By scanning a range of drive frequencies close to one of the ion motional frequencies a dip or peak will be observed in the fluorescence at the resonant frequency. Drive voltages can be applied to the trap electrodes in a number of configurations, which offer different ways of manipulating and detecting the cloud oscillations [10].

Of interest here is a scheme termed *azimuthal quadrupolar excitation*: axialization. This requires that the ring electrode be split radially into four electrically isolated segments each of which is supplied with an oscillating voltage of frequency, ω_c. A phase difference of π is introduced between the supplies to adjacent segments (see figure 6.1). The quadrupole field allows energy to be coupled between the modified cyclotron and magnetron motions [8]. With the additional presence of suitable damping, the radius of the magnetron motion decays, leaving the ions axialized. In this state the ion cloud becomes insensitive to the laser beam position which can now be moved to the trap centre for most efficient ion confinement.

The greatest interest in this form of quadrupole driving has been in the field

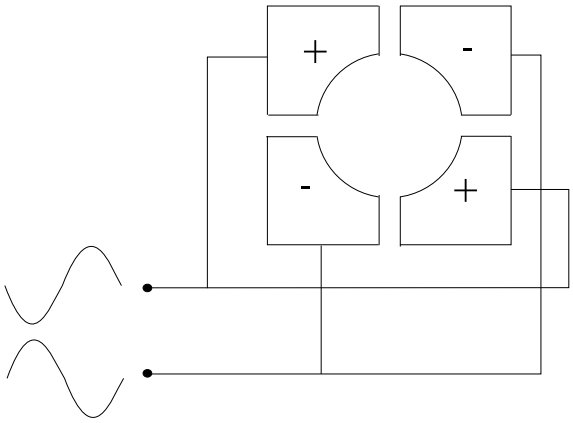

Fig. 6.1: A schematic diagram of the segmented ring electrode required for axialization. The apropriate electrical connections are as shown.

of Fourier Transform - Ion Cyclotron Resonance (FT-ICR) spectroscopy. In these experiments the trapped ions are buffer gas cooled. The motional frequencies of the trapped ions are excited using RF (radio frequency) radiation and can be detected by a variety of means. A commonly used detection method involves the examination of image currents produced between a pair of trap electrodes, these image currents contain frequency components corresponding to the motional frequencies of the ions [11]. Another method is time of flight in which excited ions are ejected from the trap and allowed to drift through an inhomogeneous magnetic field to a detector. Those ions which have been driven on resonance possess more energy than others and so reach the detector fastest [12].

For mass analysis the modified cyclotron and the magnetron modes must be excited individually. The sum of these two frequencies then gives the cyclotron frequency from which the ion mass is deduced. The use of a quadrupole drive at the cyclotron frequency however, is a clear improvement on this technique as it allows direct mass identification [12].

A full experimental investigation of axialization in buffer gas cooled systems is given in [12]. Such systems have no means of suppressing the magnetron orbit, this

means that ions are quickly lost from the trap. Axialization is an effective means of extending storage times. The mass dependency of the cyclotron frequency means that the axialization can also be used as a mechanism for producing isotopically pure ion clouds. These benefits have led to the possibility for increased precision measurements. In reference [13] the measurement of g_J values is discussed. Axialization is used in conjunction with other techniques to reduce ion temperature so improving the experimental signal to noise ratio. This produced results two orders of magnitude better than in previous experiments.

In our case of a laser cooled system there is no issue of storage time, however the increased cloud densities produced are equally beneficial to signal to noise ratio. Axialization is not the only technique which is capable of increasing the density of an ion cloud. As is described in Chapter 2, section 2.1.2, the density of a plasma depends upon its rotation frequency, ω_r. Minimum plasma density occurs when the $\omega_r \gtrsim \omega_m$, while maximum density is reached when $\omega_r = \omega_c/2$. The rate at which a plasma rotates can be increased by applying a suitable torque. This can be done using the radiation pressure of a weak laser beam [14, 15] or by using what is termed a "rotating wall", where the cloud rotation frequency is locked to an external drive [16]. In this last scheme a rotating quadrupole, perpendicular to the magnetic field, is produced by a ring electrode which has been radially segmented into six sections. Large ion clouds are treated ($\sim 1 \times 10^6$ ions) and it is shown that if a drive rotating at an angular frequency ω_d is applied, then provided it is of sufficient amplitude the ion cloud will be forced to rotate with the drive. The mechanism which produces this behaviour involves interactions between the quadrupole drive and charges on the surface of the trapped plasma which result in a torque. This force is coupled to the interior of the cloud by Coulomb interactions causing rotation of the whole cloud at the driving frequency. In the case of strongly coupled plasmas the cloud rotation is exactly matched to the drive frequency.

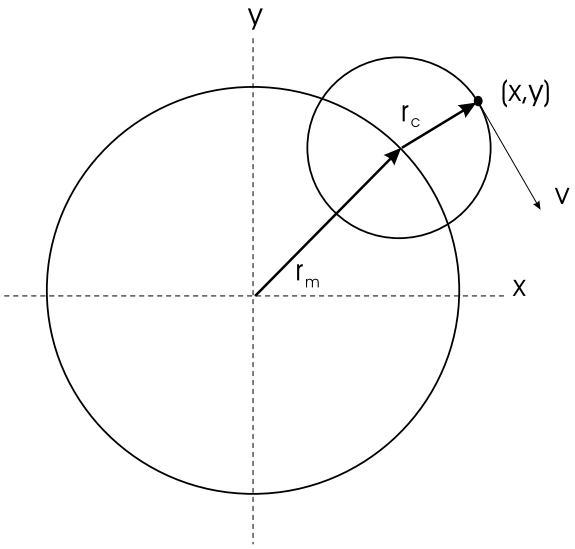

Fig. 6.2: The motion of ions in a Penning trap resolved into two uncoupled circular modes. The large radius orbit is the magnetron motion while the smaller radius orbit is the modified cyclotron motion.

The particular advantage of axialization as far as this experiment is concerned is the improved laser cooling efficiency. It should be stressed also that axialization is a single particle phenomenon whereas the rotating wall exploits plasma processes. This means that our method is well suited for use in quantum information processing where small clouds and especially single ions are required.

6.3 A Theoretical Description of Axialization

A full mathematical treatment of axialization is given in reference [8], the main points of which will be outlined here.

For this problem it is convenient to take motion in the radial plane as consisting of two uncoupled circular modes (the magnetron and modified cyclotron) as in

figure 6.2 such that:

$$x = r_c \sin(\omega_c' t) + r_m \sin(\omega_m t) \tag{6.4}$$

$$y = r_c \cos(\omega_c' t) + r_m \cos(\omega_m t) \tag{6.5}$$

The total energy of the system is the sum of the energies of each mode of oscillation (see Chapter 2). Since the problem concerns motion in the radial plane, consider E_R, the energy of the radial motion only:

$$E_R = E_c + E_m \tag{6.6}$$

where E_c and E_m are energies associated with the cyclotron and magnetron motions. These consist of both kinetic and potential energy:

$$\begin{aligned} E_c &= \frac{m}{2}\omega_p \omega_c' r_c^2 \\ &= (n_c + \frac{1}{2})\hbar\omega_c' \end{aligned} \tag{6.7}$$

$$\begin{aligned} E_m &= -\frac{m}{2}\omega_p \omega_m r_m^2 \\ &= -(n_m + \frac{1}{2})\hbar\omega_m \end{aligned} \tag{6.8}$$

where $\omega_p = \omega_c' - \omega_m$ and n is an integer ≥ 1.

The quantum mechanical result is found by using the model of an ion confined in an isotropic, 2 dimensional well characterized by the frequencies ω_c' and ω_m. A full quantum mechanical description of ion motion in a Penning trap can be found in references [17, 18].

What effect should driving at the cyclotron frequency have on the behaviour of a trapped ion? Referring to figure 6.3 which shows the energy levels for the two radial motions, the change in energy of the system when a single quantum of energy

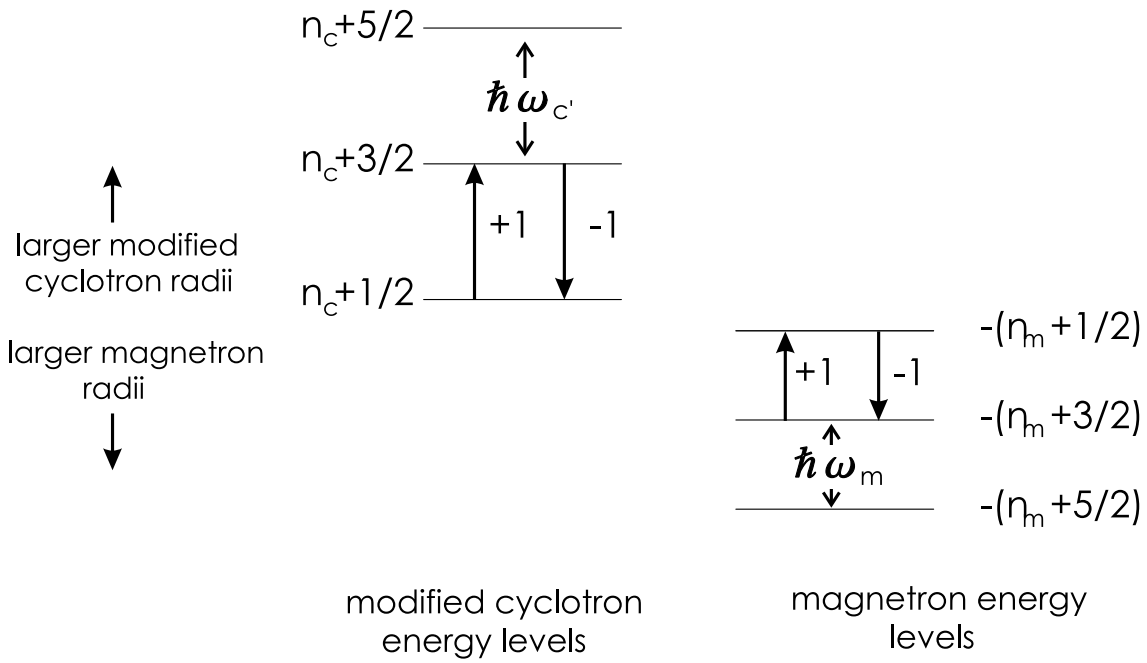

Fig. 6.3: The energy levels corresponding to the individual radial motions. The instability of the magnetron motion means that its energy levels are inverted with respect to those of the modified cyclotron motion. This means that when energy is removed from the system the magnetron motional quantum number will actually increase.

is absorbed is given by: $E_R = (n_c+\frac{1}{2})\hbar\omega_c' - (n_m+\frac{1}{2})\hbar\omega_m \rightarrow (n_c+\frac{3}{2})\hbar\omega_c' - (n_m-\frac{1}{2})\hbar\omega_m$. The total change in energy for the system on absorption (or loss) of a quantum of energy is then equivalent to $\pm(\omega_c' + \omega_m)\hbar = \pm\omega_c\hbar$. The quadrupole drive at the cyclotron frequency, shown in figure 6.4, provides the requisite excitation energy.

In the absence of any damping, energy will simply swap between the modes of motion and the driving field. In this process the ion motion evolves from one pure mode (either modified cyclotron or magnetron) to the other at a rate determined by the strength of the driving field. In many ways the situation is analogous to the evolution of coherently driven atomic states: Rabi flopping.

Assuming that there is no damping, the rate of energy change during the driving

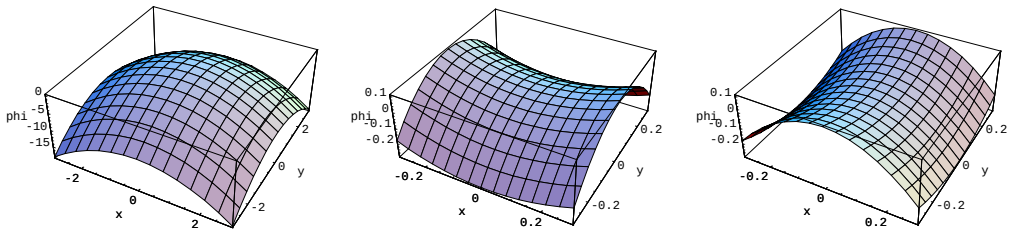

Fig. 6.4: On the far left the repulsive form of the static trap potential in the x-y plane is shown. To the right, how the axializing drive alters the static trap potential (the amplitude of the drive has been exaggerated for effect). The field flips between the two possible orientations shown at the drive frequency.

process can be expressed as follows:

$$\omega_m \frac{dE_c}{dt} = \omega_c' \frac{dE_m}{dt} \tag{6.9}$$

From this it can be determined that the rate of change in the radii of the two orbits will be:

$$\frac{1}{r_m}\frac{dr_c}{dt} = -\frac{1}{r_c}\frac{dr_m}{dt} \tag{6.10}$$

where r_c and r_m are respectively the radius of the modified cyclotron motion and that of the magnetron motion.

The rate of change in the energies and therefore the radii of the two orbits is ultimately related to the strength of coupling to the driving field: δ. Equating both sides of equation 6.10 to δ, gives two coupled differential equations to describe the ion motion:

$$\dot{r_c} = \delta r_m \tag{6.11}$$

$$\dot{r_m} = -\delta r_c \tag{6.12}$$

The solution to these equations is easily found:

$$r_c = r_m(0)\sin(\delta t) + r_c(0)\cos(\delta t) \tag{6.13}$$

$$r_m = r_m(0)\cos(\delta t) - r_c(0)\sin(\delta t) \tag{6.14}$$

where δ must have units of frequency and $r_c(0)$ and $r_m(0)$ are respectively, the initial amplitudes of the modified cyclotron and magnetron orbits.

In reference [8], δ, is termed the *beat frequency* as it is this parameter which determines the rate at which energy swaps between the modified cyclotron mode to the magnetron mode. The time, t, which it takes for ion motion to evolve from pure cyclotron to pure magnetron is $t = \pi/2\delta$. To find a numerical value for δ the power absorbed by the system over one cycle of the excitation drive must be calculated. It can be shown that $\delta = eC/2m\omega_c$ where $C = 3V_d/4R_0^2$ for a quadrupole trap (V_d is the amplitude of the drive voltage and $R_0^2 = r_0^2 + 2z_0^2$).

Since we are considering a laser cooled system, damping will be present. Defining damping coefficients, γ_c and γ_m for the modified cyclotron and magnetron motions, expressions 6.13 and 6.14 become [19]:

$$\dot{r_c} = \delta r_m - \gamma_c r_c \quad , \quad \dot{r_m} = -\delta r_c - \gamma_m r_m \tag{6.15}$$

where r_c and r_m are the radii of the cyclotron and the magnetron orbits respectively, γ_c and γ_m are the corresponding damping coefficients and δ is the coupling constant of the axializing drive.

Assuming that both r_c and r_m evolve as $\exp(-\Gamma t)$, we obtain an expression for the damping coefficient Γ:

$$\Gamma = \frac{-(\gamma_c + \gamma_m) \pm \sqrt{(\gamma_c + \gamma_m)^2 - 4(\gamma_c\gamma_m - \delta^2)}}{2} \tag{6.16}$$

Consideration of this expression shows us that axialization is in fact only one of a number of outcomes, the most important of which are enumerated here:

1. If $\gamma_c = \gamma_m = 0$ the system oscillates between pure cyclotron and pure magnetron motion with no reduction in energy.

2. If either γ_c or γ_m is large and positive (with the other one small) such that $\delta^2 > -\gamma_c\gamma_m$, then: $r_c, r_m \to 0$ as t $\to \infty$

3. If $\delta^2 = -\gamma_c\gamma_m$ with $\gamma_c > \delta > 0, \gamma_m < 0$ then we obtain a stable orbital radius such that: $r_m/r_c = \gamma_c/\delta = |\delta/\gamma_m|$

4. If $\delta^2 < -\gamma_c\gamma_m$ then the orbit expands, so reducing the damping coefficients, until condition 3 is met.

Axialization will occur only when condition 2 is met. The final set of conditions, 4, is the main difference between buffer gas cooled and laser cooled systems. With buffer gas cooling, the damping coefficients have a fixed ratio and are constant for a given buffer gas pressure. With laser cooling, the ratio of the two damping rates (and even their signs) can be varied by changing the laser frequency and/or position. In addition, both damping rates reduce if the motion of the ions takes them outside the laser beam. Therefore the stable orbital radius mentioned above can only be achieved in the case of laser cooling [20].

A simple computer simulation (see Appendix C) was written in order to explore the possibilities set out. For single ions all conditions can be shown, the parameters for which they occur matching well to experimental values. The results are shown in figure 6.5

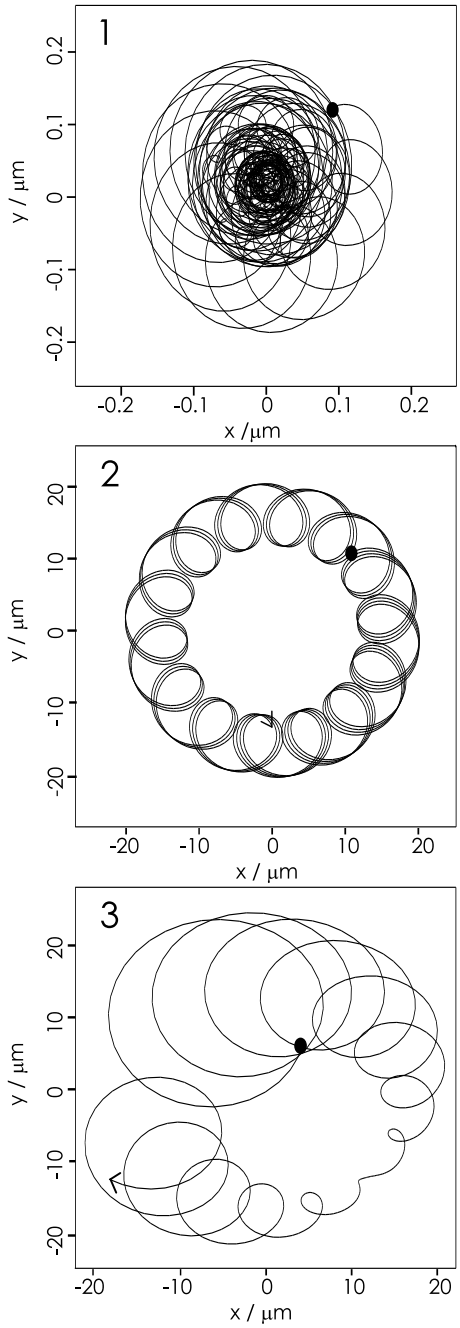

Fig. 6.5: 1 Axialization: $\delta^2 > -\gamma_c\gamma_m$ with $\delta^2 \simeq 1\times10^4$. 2 A large stable orbit: $\delta^2 < -\gamma_c\gamma_m$ with $\delta^2 \simeq 2\times10^2$. 3 No damping: $\gamma_c = \gamma_m = 0$. A realistic value was chosen for ratio of the two damping coefficients: $\gamma_c/\gamma_m = -10$, with $\gamma_m \sim -10$

6.4 Outline of the Experimental Set Up

Both the trap and additional set up are described more fully in Chapter 4. The trap is a simple end-cap/ring electrode configuration, with the additional feature that the ring electrode is divided into four segments [21]. The optical system was arranged such that the fluorescence from the ions could be collected by the photomultiplier (with a magnification of $\times 1$) and sent either to the MCS card or to the MCA card. When required, a mirror could be flipped into place to divert the light to an ICCD camera (with a magnification of ~ 1). The light is focused onto the CCD array which has a pixel size of 13 μm. The exposure time for each of the images was set as 10 s. The axializing field is provided by a small op-amp circuit which comprises an inverting and a non-inverting amplifier of equal gain (gain = 0.4). The circuit was designed to give constant gain up to 1.5 MHz. A diagram of the circuit can be found in Appendix D.

6.5 Results and Discussion

6.5.1 Achieving Axialization

In order to produce an axialized cloud the trap is initially loaded with a small number of ions. With the 280 nm laser frequency detuned by approximately 400 MHz the cyclotron drive is applied at a peak to peak amplitude of 0.4 V (after amplification). If the signal is monitored by the photo-multiplier an increase in fluorescence is observed. This increase in the count rate is immediate and can be explained by the cloud becoming more dense when the drive is applied: its Doppler width and radial extent being reduced by the drive field. Parameters are then optimized, the laser beam position is moved to the centre of the trap and the 280 nm laser detuning

is decreased: generally to near 100 MHz. Signals can be seen to increase by as much as three times their initial level. The signal level is also more stable than for an unaxialized cloud at similar laser detunings.

The effect is greatest for larger clouds and minimal for single ion: under normal conditions, when a large cloud is trapped one might expect a large fraction of the ions to be outside the laser beam at any one time, however the spatial extent of the single ion orbit will rarely take it out of the laser beam so greater confinement makes little difference to the signal level. Maximum signal and full axialization are achieved when the laser frequency approaches resonance and the beam is central within the trap.

When the drive frequency is scanned from below to above the cyclotron frequency a resonance peak can be observed in the ion fluorescence. It was found that the width of the cyclotron resonance depends strongly upon the position of the laser beam. Figures 6.6 shows the cyclotron resonance for a single ion (confirmed by monitoring quantum jumps). Initially (trace 1), when the laser beam is in its usual position for laser cooling the resonance is broad: 20 kHz (FWHM). Once the beam position is moved to the centre of the trap (trace 2) the resonance narrows: < 200 Hz (FWHM).

The beam position dependence of the resonance width is difficult to understand, but could perhaps be explained in terms of the competing heating and cooling effects at work. In both the traces in figure 6.6, the signal drops to near background levels away from resonance. The reduced signal is thought to be the result of off resonance heating effects: the quadrupole drive can only axialize the ions when its frequency coincides with that of the true cyclotron frequency, ω_c. When the beam is set up for normal laser cooling applying an on resonance quadrupole drive will improve laser cooling conditions producing a small increase in ion fluorescence. If the drive frequency is then stepped either up or down in frequency the ions will begin to suffer RF heating, however by virtue of the beam position there is still some cooling

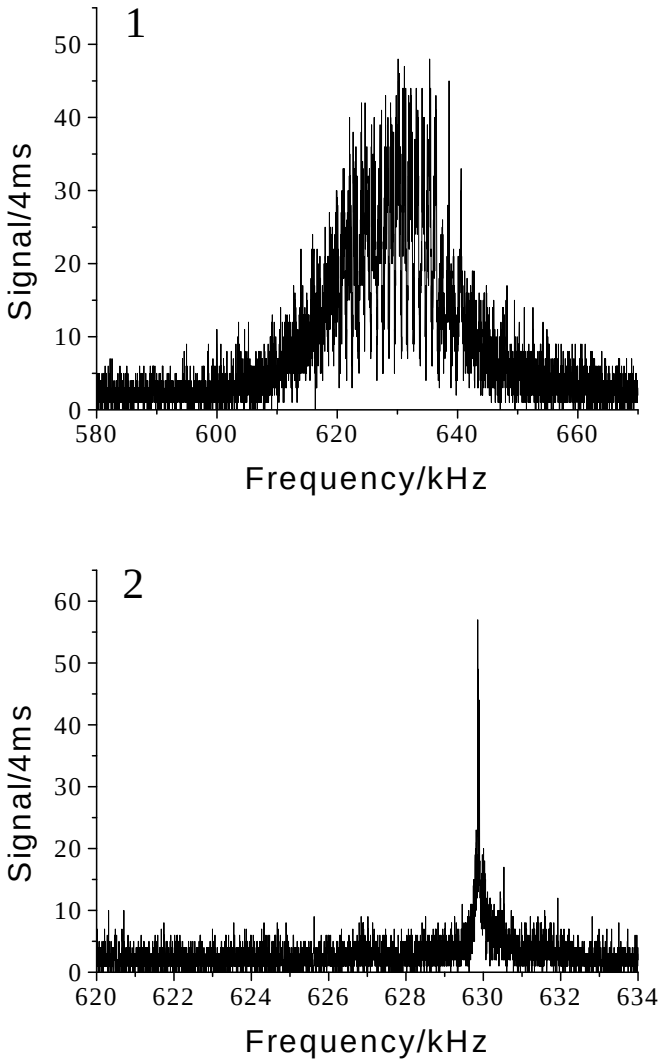

Fig. 6.6: The alteration in cyclotron resonance width with the laser beam position for a single ion (see text). Drive voltage amplitude, V_d, was optimized to obtain the narrowest resonance without significantly weakening the response. For trace 1, V_d = 30 mV and for trace 2, V_d = 141 mV. Note that the *modulation* on the signal is a product of the pseudo-continuous frequency scan of the particular function generator used.

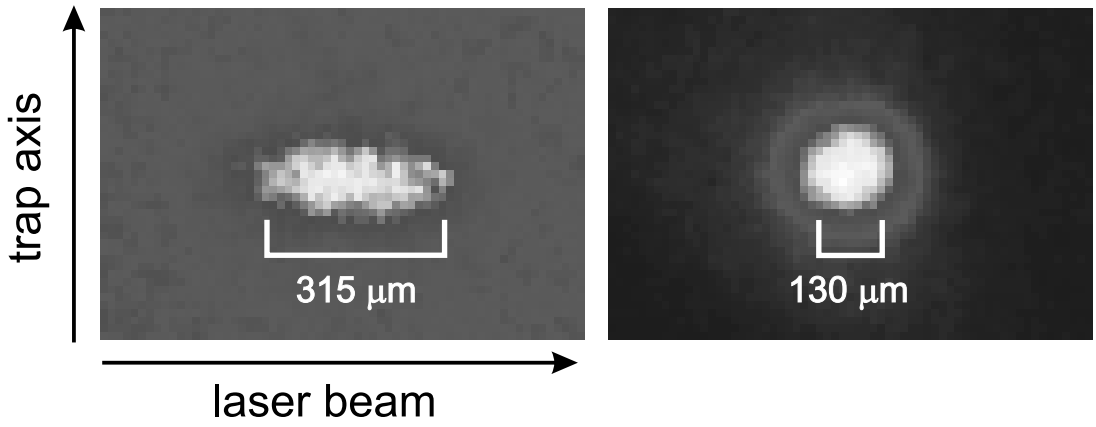

Fig. 6.7: The application of the cyclotron drive to a small ion cloud. From the fluorescence rate, the cloud size is ~ 5 ions. Laser detuning and beam position are the same for both images. The dimensions given correspond to the image plane [19].

and therefore the fluorescence does not immediately drop. It would seem that the RF heating effect of the quadrupole drive only becomes significant when the drive frequency is very far from resonance so producing the broad response observed. Moving the laser beam to a central position in the trap means that there is optimal cooling of the modified cyclotron motion when the drive is on resonance. These same conditions without the drive will however lead to magnetron expansion. Thus, when the drive is non-resonant the ion experiences not only RF heating but also laser heating. As a result the cyclotron resonance is very narrow.

6.5.2 Imaging Axialization

Using the ICCD camera the process of axialization can be observed. Referring to figure 6.7: the left hand image shows a laser cooled cloud with no drive present, while the right hand image shows the same cloud immediately after the drive is applied. There is an instant reduction in cloud radius by a factor of ~ 2.4. Optimizing the laser parameters further decreases the cloud radius (see figure 6.10). It is thought

that the size of the cloud observed is not limited by the size of the laser beam waist as this was measured as 140 μm. The substantial reduction in cloud radius is a clear demonstration of the effectiveness of axialization. For single ions results are even more spectacular.

The presence of single ions in the trap was confirmed by monitoring quantum jumps. Single ions were trapped and their behaviour under different driving conditions was investigated. The various situations which may arise as a result of varying the coupling strength, δ with respect to the damping coefficients of the radial motions, γ_c and γ_m are discussed in section 6.3. Those predictions which are most experimentally relevant are axialization: $\delta^2 > -\gamma_c\gamma_m$ and the appearance of large stable orbits: $\delta^2 = -\gamma_c\gamma_m$. In figure 6.8 a single ion is shown unaxialized, axialized and also in a large stable orbit.

A transition from the axialized state into a stable orbit can be provoked by reducing the drive amplitude or by driving at a frequency $\omega_d \neq \omega_c$. Both of these approaches effectively result in a reduction of the coupling strength. It should be equally possible to achieve this result by alteration of the laser detuning or frequency in order to raise the damping coefficients, but this was found to be less controllable. What is most interesting of course is the low temperature limit which can be achieved with axialization. This is discussed in the next section.

An Estimate of the Temperatures Reached

The volume occupied by a cold ion cloud is determined by its plasma rotation frequency and the ion number [22]. In the limit of a single ion however, the plasma description is no longer applicable. In this case, we can speak of reduction of the magnetron radius as "cooling" and the concept of an effective temperature can be associated with the size of the magnetron orbit.

The modified cyclotron motion is directly cooled by the laser, thus the radius of

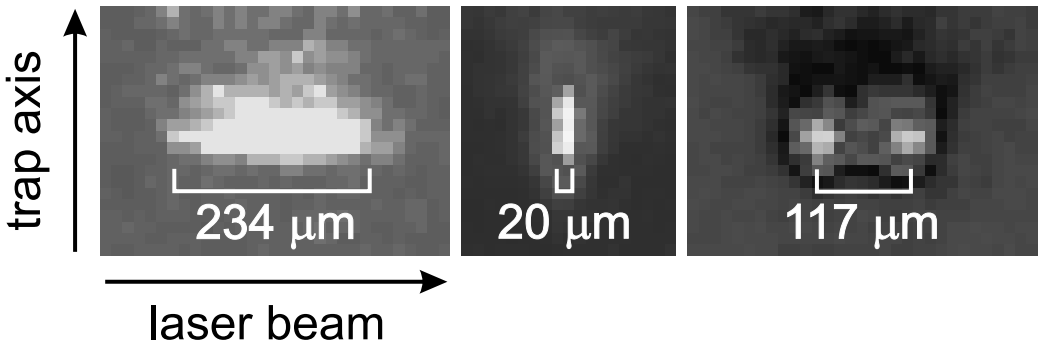

Fig. 6.8: Single ions, from left to right, unaxialized, axialized and in a large magnetron orbit.

this orbit is always smaller than that of the magnetron. We can then assume that the extent of an ion orbit in the radial plane is principally due to the radius of the magnetron motion. The size of the radial orbit measured from an ICCD image can be used to calculate the kinetic energy of the ion. The kinetic energy of the ion can be expressed in terms of either velocity or temperature:

$$E_k = \frac{3}{2}k_B T = \frac{1}{2}mv^2 \tag{6.17}$$

Thus, once the ion velocity is known this can be used to calculate an upper limit for the ion temperature:

$$T = 3\frac{mv^2}{k_B} \tag{6.18}$$

where k_B is Boltzman's constant and T is the temperature, m and v are the ion mass and velocity respectively.

From the image shown in figure 6.8, it can be established that in the absence of an axializing drive the radial extent of a single ion trajectory is around 230 μm. This indicates a temperature of order $\sim$ 1 K. In figure 6.9 a single, axialized ion is shown. In the radial direction the size of the image is 20 μm (1.5 pixels). Allowing

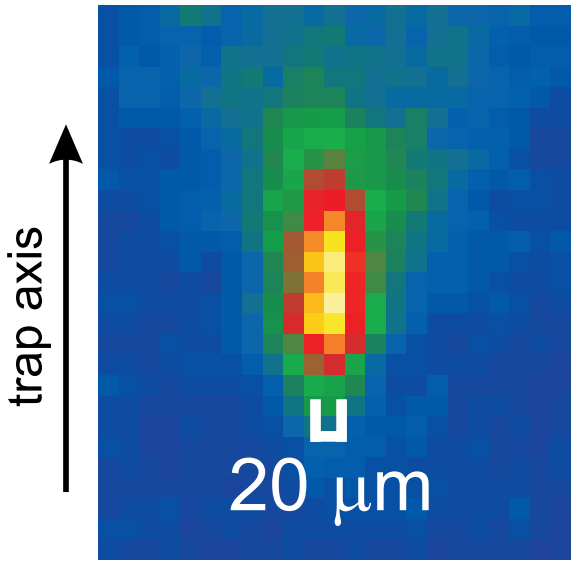

Fig. 6.9: A single axialized ion [19].

for the finite resolution of the camera, this gives an estimate for the ion temperature of order 10 mK. Aberrations in the imaging optics will tend to increase the image size, thus all temperature calculations should be considered an upper limit. In our trap geometry the axial motion receives no direct cooling thus its amplitude and therefore its temperature is greater than in the radial plane.

6.5.3 Cloud Dynamics.

The theoretical approach outlined earlier in this chapter is clearly only applicable to the case of a single ion, thus initial work focused upon the use of single ions. Larger clouds have been axialized and images of these clouds show the minimum magnetron radius scaling upwards with increasing ion numbers as shown in figure 6.10. This is in accordance with the limitations on maximum cloud density imposed by space charge effects.

If the cloud is considered as a non-neutral plasma (as discussed in Chapter 2) it

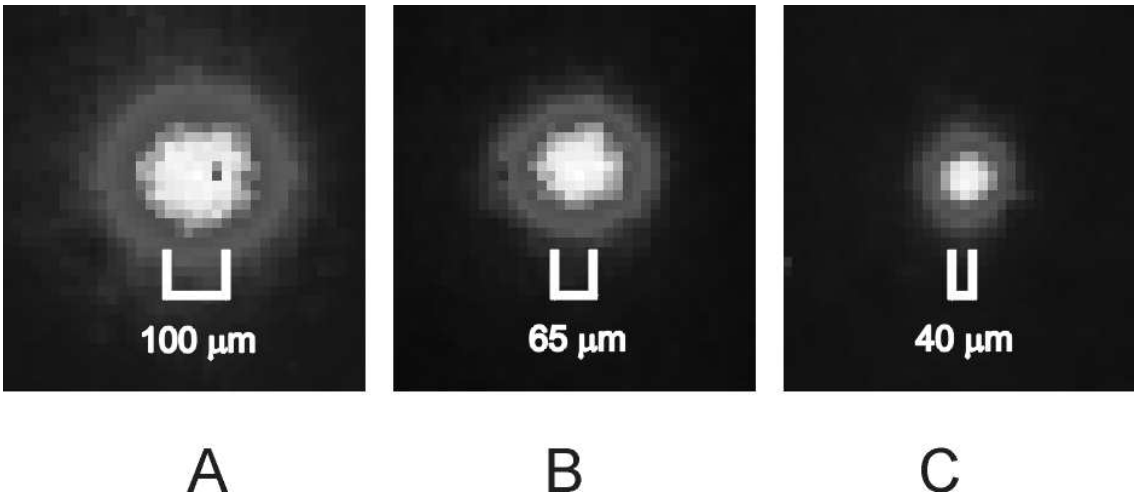

Fig. 6.10: Three axialized clouds, to compare the physical sizes of clouds containing (from A to C) approximately 10, 5 and 1 ion. All pictures were taken after the laser detuning and beam position were optimized.

is possible to obtain an expression for a maximum cloud density, n_0:

$$n_0 = \frac{2\epsilon_0 m\omega_r(\omega_c - \omega_r)}{e^2} \tag{6.19}$$

where ω_r is the cloud rotation frequency. The maximum cloud density occurs when $\omega_r = \omega_c/2$, which for magnesium ions gives $n_0 = 1.1 \times 10^{14}$ ions/m^3. The actual densities reached can be found by considering the cloud diameters measured from the ICCD images and assuming that the cloud is roughly spherical. For the 10 ion cloud a density of 3.0×10^{13} ions/m^3 is obtained and for the 5 ion cloud the density is 1.0×10^{14} ions/m^3.

In studying the interaction of larger clouds with the quadrupole drive, it is perhaps not axialization which is the most interesting phenomenon but rather the production of the stable orbits. Whereas it is straight forward to predict the effects of space charge in the case of axialization it is far from clear what structure the cloud might take on where stable orbits are formed.

The first evidence for large orbits in clouds of ions was seen in certain dynamic

processes, specifically when sweeping the drive frequency through resonance. Later in this chapter the behaviour of a large cloud is shown, figure 6.17, as the cyclotron resonance is swept. It is clear that the ion cloud is forced into large orbits on either side of resonance. This is in accordance with theory, as discussed in sections 6.3 and 6.5.2. The exact nature of these orbits could not be determined from the ICCD images alone. There were considered to be two possibilities: either the cloud forms a ring of roughly equally spaced ions centred on the trap centre, or the ions travel together as a dense cloud in a large orbit about trap centre. To investigate these possibilities photon-photon correlation was used.

6.5.4 Photon-Photon Correlation

The level of fluorescence emanating from a cloud of laser cooled ions will be modulated as a result of the ion motion. The Doppler effect means that as the ions oscillate they will periodically go further in and out of resonance, also large amplitude motion may take the ions out of the laser beam altogether; because motion in an ion trap is governed by certain characteristic frequencies, these frequencies will appear in the modulation of the resonance fluorescence. To see the modulation directly would require the collection of many photons per oscillation period and with ion frequencies in the kHz range this is not possible. Instead, taking advantage of the relatively low collection efficiency, the statistics of the photon pulse train itself can be examined: photons emitted by the same ion will be correlated, the intervals between them being related to the characteristic frequencies of the trapped ion. Taking a fast Fourier transform of the spectrum of intervals between photons allows information about the ion oscillation frequencies to be extracted [23]. A typical photon-photon correlation spectrum for magnesium ions in a Penning trap is shown in figure 6.11.

It is not normally expected that any correlation should exist between photons

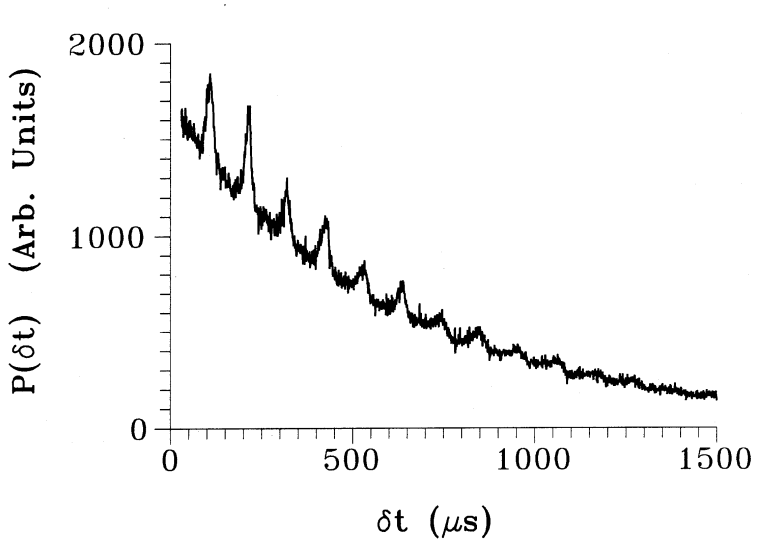

Fig. 6.11: Typical photon-photon correlation data for a cloud of magnesium ions in a Penning trap. The principal frequency on the trace is twice the magnetron frequency giving $\omega_m = 2 \times \pi 5$ kHz. The data is taken from [24].

emitted by different ions. This is because of the phase difference between the secular motion of any two ions within the trap. The time dependence of this phase difference is unpredictable as it arises from the dynamic behaviour of the ions. As the number of ions within a cloud increases, it becomes less likely that two photons from the same ion should be detected consecutively. As a result any features in the correlation spectrum become washed out. This means that the technique of photon-photon correlation is generally only suitable for small clouds (of up to 10 ions).

An advantage of the technique is that it is non-invasive, there is no need to drive any motional frequencies. Because it is only possible to observe correlation between photons emitted by the same ion, the method enables the determination of oscillation frequencies of a single ion within a cloud of other ions i.e the space charge modified oscillation frequencies which each ion in the cloud will experience [23]. Generally it is only the centre of mass frequencies which can be probed by excitation of centre of mass modes of oscillation.

Data Collection

In order to implement the photon-photon correlation technique in this experiment, clouds of ions were first loaded and axialized. The axializing voltage was then reduced until the ion cloud formed a large stable orbit. The pulses generated by the emitted photons were sent to the TAC and subsequently the MCA card. It is the time between consecutively arriving photons, (Δt), which is examined (the scheme is described in Chapter 4, section 4.4.3). If the photons emitted by the ion cloud arrived randomly then the MCA trace would be an exponentially decaying function of (Δt). In the case where fluorescence modulation is present as a result of ion motion, the MCA trace will comprise approximately sinusoidal components at the frequencies of ion motion. The spectrum which is collected experimentally consists of both correlated and uncorrelated data: sinusoidal modulations superimposed over an exponential decay curve. The choice of TAC time delay was between 200 and 100 μs, this allowed frequency resolution of 5 and 10 kHz respectively. To avoid aliasing when the fast Fourier transform of the spectrum is taken, the MCA bin width must be less than half the period of the fastest oscillation present, in this case the highest frequency is the cyclotron frequency at $\sim$ 630 kHz. With the TAC delay used, the bin width would be between 0.05 and 0.1 μs therefore aliasing will occur only if the frequency exceeds 10 MHz.

To determine as much as possible about the nature of the ion orbits seen, different cloud sizes were investigated each at different drive strengths and trapping voltages. In figures 6.12 and 6.13 typical traces and their fast Fourier transforms (FFT) are shown. The cloud sizes were $\sim$ 50 and $\sim$ 5 ions respectively.

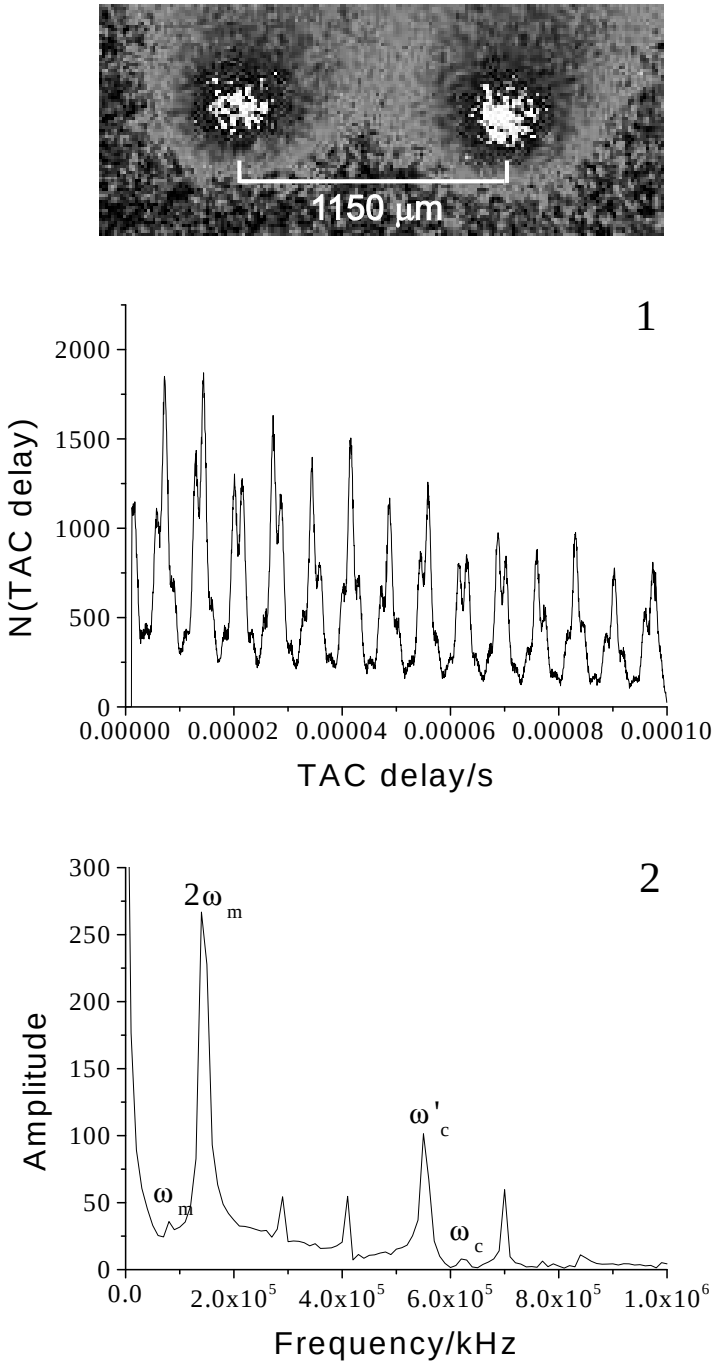

Fig. 6.12: Data 1: ICCD image of a ~ 50 ion cloud in a large orbit, beneath are a typical photon correlation trace (1) and its FFT (2) for such a cloud. Trap voltage was 10 V, making $\omega_m = 2\pi \times 72$ kHz and $\omega_c' = 2\pi \times 557$ kHz. The value of $\omega_c \sim 2\pi \times 630$ kHz and the drive amplitude was 0.36 V.

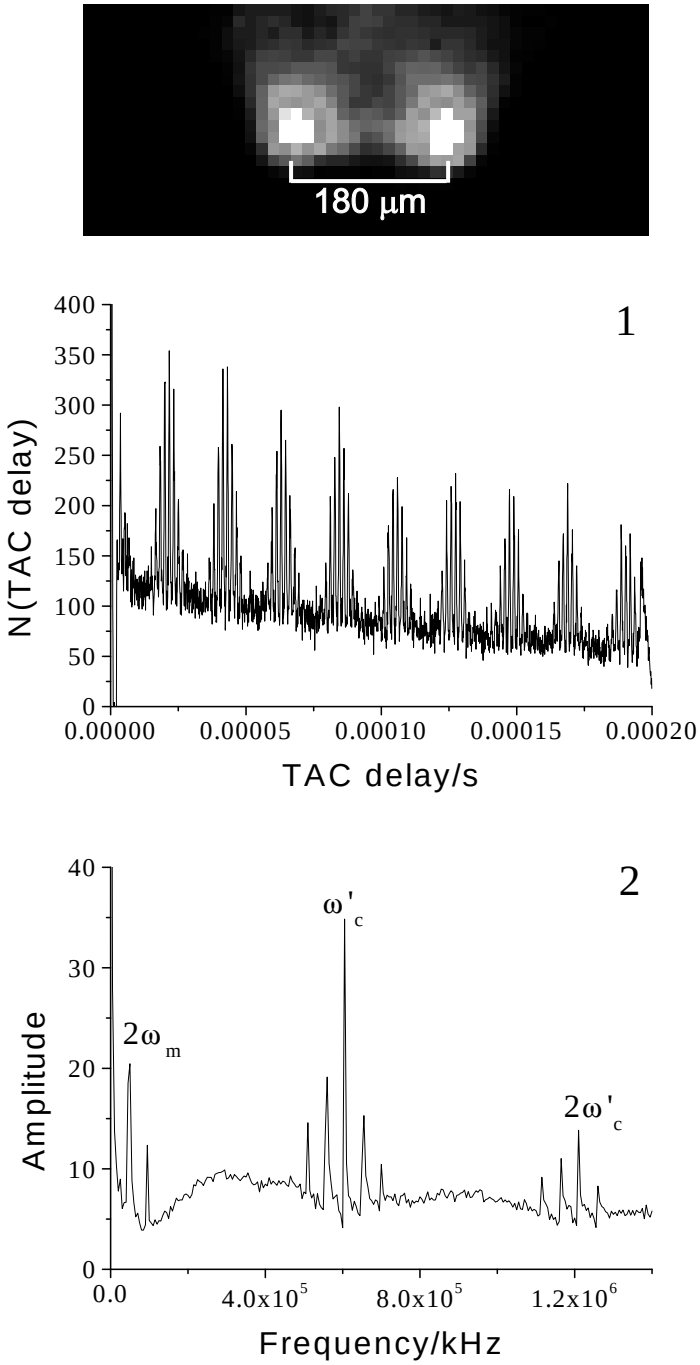

Fig. 6.13: Data 2: ICCD image of a ~ 5 ion cloud in a large orbit, beneath are a typical photon correlation trace (1) and its FFT (2) for such a cloud in a stable orbit. Trap voltage was 4 V, making $\omega_m = 2\pi \times 27$ kHz and $\omega_c' = 2\pi \times 601$ kHz. The value of $\omega_c \sim 2\pi \times 630$ kHz and the drive amplitude was 0.04 V.

6.5.5 Analysis of the Correlation Spectra

A Model for the Emitted Fluorescence

The form of the fluorescence signal emitted by the ion cloud can be expressed as follows:

$$F = A + B\Big((1 + \alpha_1 \cos(2\omega_m t))(1 + \alpha_2 \cos(\omega_c' t))\Big) \tag{6.20}$$

The appearance of twice the magnetron frequency as opposed to simply the magnetron frequency is a result of the fact that the ion cloud passes through the laser beam twice in each orbit. There may be other much smaller contributions at the magnetron frequency itself and at the true cyclotron. The amplitudes A and B are the average levels of background scatter and signal (fluorescence) respectively, α_1 accounts for the slow modulation resulting from the magnetron orbit and α_2 results from the modified cyclotron motion. Both types of modulation result from the Doppler effect bringing the ions in and out of resonance with the laser photons. The magnetron orbit, being of larger amplitude than the cyclotron, produces much deeper modulation. In the particular case seen here, because the orbit radius is often very large compared to the laser beam waist (the laser beam waist has been measured as 140 μm while the diameter of the orbit is $\sim$ 1000 μm), the magnetron modulation is further enhanced. The position of the laser beam means that the modified cyclotron should be strongly damped. Any residual motion at the modified cyclotron frequency results in a small modulation superposed over the main magnetron modulation. The α coefficients could be described as *visibility* parameters for the modulation peaks if the signal varies by $\pm\alpha$ about a mean fluorescence level.

The correlation spectrum which is collected represents the auto–correlation of the fluorescence signal, equation 6.20. In this way, we can determine an expression

which should describe the correlation spectrum:

$$f(s) = A^2 + B^2\left[(1 + \frac{1}{2}\alpha_1^2\cos(2\omega_m s))(1 + \frac{1}{2}\alpha_2\cos(\omega_c' s)\right] \tag{6.21}$$

In order to make a good fit to the correlation data, the fact that large time delays between photons are less likely than small time delays needs to be reflected. This is done by multiplying equation 6.21 by a suitable exponential decay curve.

As a result of the fact that the ion cloud physically moves in and out of the laser beam the fluorescence signal is telegraph–like. Equation 6.21 uses sinusoidal components, thus it is not entirely adequate to describe the correlation spectrum. This becomes more apparent as the number of ions in the cloud is reduced, comparing data samples 1 and 2, in the first the correlation trace does seem to contain sinusoidal functions, however in the second the function is nearer to a square wave. In order to better simulate the nature of the correlation function the low frequency modulation was fitted with the square of a sinusoid oscillating at half the magnetron frequency. The final form of the fitting function was as follows:

$$\begin{aligned} f(x) \;=\; & \Big[A^2 + B^2(1 + \frac{1}{2}\alpha_1^2\cos^2(\omega_m x)) \\ & (1 + \frac{1}{2}\alpha_2^2\cos(\omega_c' x))\Big]\exp(-Fx) \end{aligned} \tag{6.22}$$

where all values are as previously defined.

The values of the frequencies required for fitting can be estimated by taking a fast Fourier transform (FFT) of the photon correlation spectrum. The principal frequency components of $2\omega_m$ and ω_c' are labelled on figures 6.12 and 6.13. Other components at higher harmonics of the magnetron frequency are artefacts of the sharpness of the correlation trace. The amplitudes and frequencies found using equation 6.22 are summarized in table 6.1.

Table 6.1: A table of the amplitudes used to curve fit to the data in figures 6.12 and 6.13.

	A	B	F	α_1	α_2	$\omega_m/2\pi$	$\omega_c'/2\pi$
Data 1	1.00	180.00	0.01	1.30	0.20	71.5	551
Data 2	8.00	5.00	0.01	4.00	1.10	24.00	600.00

Alternative Models for the Ion Motion

Considering data sample 1 (50 ions), the strength of modulation present in the correlation spectrum is quite unexpected for this number of ions. It tends to indicate that the photons arriving at the TAC come in well defined bursts as would be characteristic of very small clouds. In fact the spectrum corresponds to what might be expected of one or two ions. This leads to the conclusion that the ions are in an ordered configuration consisting of either one or two dense clouds orbiting the trap centre.

It is highly counterintuitive that the ion should form any kind of coherent structure under non-ideal conditions. The radius of the expected orbit as determined by solution of equation 6.16 is for a single ion. In a cloud each ion is perturbed by the presence of all the others, thus while the mean radius for the orbit of the whole cloud might be that predicted, the individual ions would have a distribution of orbital radii about this mean. It also seems likely that the density of the ions in this type of cloud would be uniformly distributed around the circumference of the orbit. Since the orbit is so much larger than the size of the laser beam focus, an image of the cloud would indeed look like those which were observed: two bright spots showing where the cloud interacts with the laser beam. The problem with this picture is that there is nothing ordered about its structure, thus as far as the photon-correlation is concerned there would be nothing to distinguish it from an ion cloud under normal laser cooling conditions.

The solution which seems most seductive, is that the ions do in fact all have

the same orbital radius, that is they form an equally spaced ring. Starting with an initially axialized cloud, as the drive is lowered every ion in the cloud is forced to the same orbital radius. The Coulomb repulsion between the ions would keep them evenly separated.

To determine whether this situation might hold, a number of things require consideration. Firstly, are the correlation spectra consistent with what might be expected for a ring of evenly spaced ions? Secondly, what are the effects of space charge on the size of orbit radii which might be seen and also on the motional frequencies recorded in the correlation spectra?

Initially, let it be assumed that the ions do form a stable ring, what might be inferred about the possible form of the photon-correlation spectrum? Each time an ion passes through the laser beam a photon will be emitted and each one will correlate with every other. This would give a correlation trace containing the $(N\omega_m)$ and $(2N\omega_m)$ harmonics of the magnetron frequency, where N is the number of ions, as reported in [23]. Clearly then, the spectrum would be an indication of cloud size and the harmonics present would vary dramatically as the cloud size is reduced. This is not the case: correlation traces were taken for cloud sizes of from $5 > N > 50$, in all cases the frequency components present were the same, see figures 6.12 and 6.13.

What is most interesting about the photon correlation traces is that the principal component, which indicates the cloud rotation frequency, is always very precisely twice the magnetron frequency (calculated from the trap voltage, U_0). This shows that the cloud rotates at a frequency very close to the centre of mass magnetron frequency. The photon correlation spectra show the relative motional frequencies of the ion cloud rather than the centre of mass (single ion) motional frequencies and these alone are subject to space charge shifts. These shifts are dependent upon the density of the cloud; the magnetron frequency specifically tends to shift to higher values as the cloud density increases [23]. Observations of the ions under many

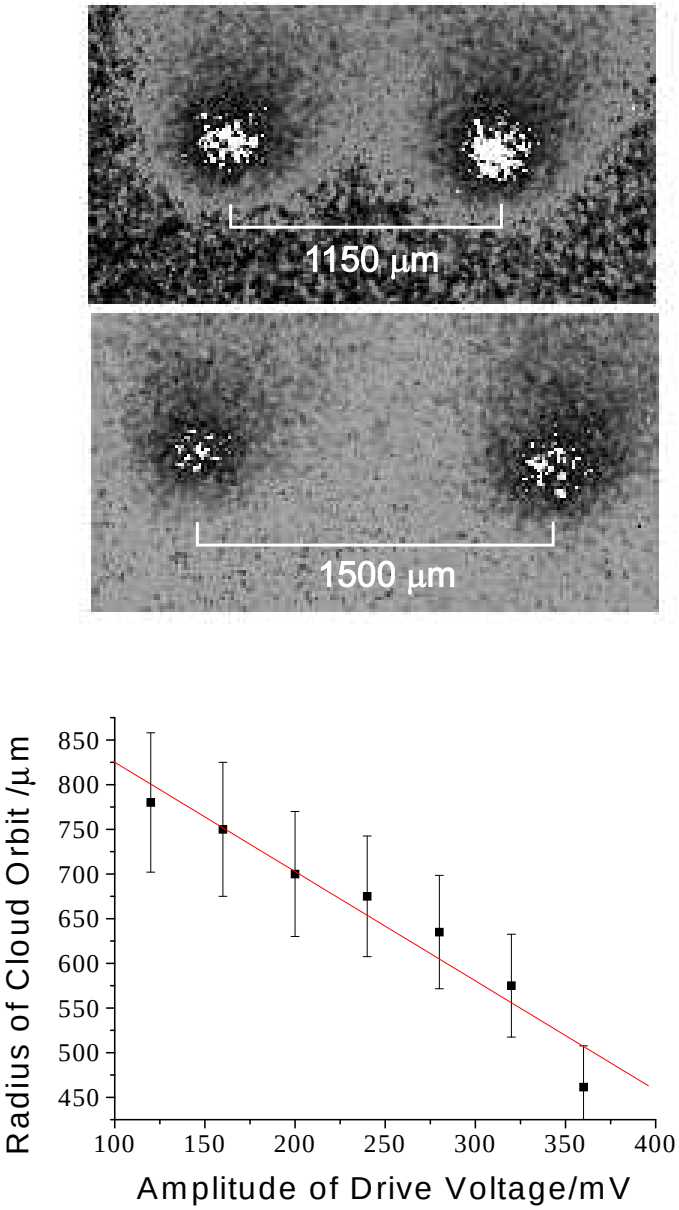

Fig. 6.14: The dependence of ion cloud orbital radii on the amplitude of the axializing drive for a ~ 50 ion cloud. The ICCD images show the same cloud the amplitude of the axializing drive at 0.32 V (top) and 0.16 V (bottom). The graph shows the general form of the dependence of the orbit radius with axializing drive voltage.

different conditions show that the recorded cloud rotation frequency does not stray from the centre of mass value by more than 10 kHz. This suggests that the ions are so distant from each other that the effects of space charge are very weak.

If the space charge effects are almost negligible then the equilibrium radius for N ions rotating at a frequency close to ω_m should be of the same order or even smaller than those observed experimentally. An equilibrium ion orbit can be calculated by considering the forces acting on the trapped ions. The simplest case is where there are two ions in the trap separated by a distance $2r$. It can be assumed that the modified cyclotron motion is well damped so that the only motion present is a rotation at $2\omega_R$. In the frame of reference which rotates at $\omega_c/2$ the forces acting can be related thus [1]:

$$mr\omega_1^2 = mr\omega_R^2 + e^2/(16\pi\epsilon_0 r^2) \tag{6.23}$$

where

$$\omega_m = \omega_c/2 - \omega_1 \tag{6.24}$$

and ω_1 is the radial oscillation frequency in the rotating frame. Where there are N ions in a ring configuration of radius r, the charge dependent term must be modified. In this case, the principal of superposition can be used to give the resultant Coulomb force.

It has been established that the cloud rotation frequency in the lab frame is similar to ω_m. If there is any variation in the cloud rotational frequency as a result of space charge, then this must be very small: no more than 10 kHz. This means that the maximum change in ω_R is from ω_1 to $\omega_1 - 2\pi \times 10 \times 10^3$. Taking this lower value of ω_R, equation 6.23 can be solved for r. Under the conditions set out, it is found that the equilibrium radius for 50 ions in a ring should be of the order of one millimetre. This is almost twice as large as the biggest radii observed. Thus if

the ions were in a ring then our experiment would clearly show the effects of space charge.

It was observed that the orbital radius observed was highly dependent upon the amplitude of the axializing drive. This is expected from the analysis in section 6.3 and is shown in figure 6.14. If the orbital radius alters with the applied drive strength, the cloud density will also change which should then lead to different magnetron frequencies being observed at different drive amplitudes. It has been established that, for 50 ions in a ring configuration the equilibrium radius is much larger than those seen in our experiment. Thus, if it can not be contended that space charge effects are negligible, what might we expect?

Following from equation 6.23 we can formulate an expression for two ions separated by $2r$ which describes the effect of space charge on the cloud rotation frequency in the rotating frame [1]:

$$\omega_R^2 = \omega_1^2 - e^2/(16\pi\epsilon_0 r^3 m) \tag{6.25}$$

The effect this has on the observed (lab frame) magnetron frequency can be found by equation 6.24. This gives a shifted magnetron frequency of: $\omega'_m = \omega_c/2 - \omega_R$. The maximum value of ω'_m occurs when the ions reach a maximum density at which point $\omega'_m = \omega_c/2$.

As before, the charge dependent term of equation 6.25 can be extended to the case of N ions in a ring of radius r. The dependence of ω_R upon orbit radius for a ring of 50 ions is plotted on the graph in figure 6.15. Experimentally, for 50 ions, an orbit radius of 500μm might be expected. If the trap voltage is 10 V then in the absence of space charge $\omega_R/2\pi = 243$ kHz (making $\omega_m = 2\pi \times 72$ kHz). With the ions arranged in an evenly spaced ring of radius 500μm $\omega_R/2\pi$ shifts to $2\pi \times 172$ kHz, giving an ω_m of $2\pi \times 143$ kHz. This is a substantial change. What is

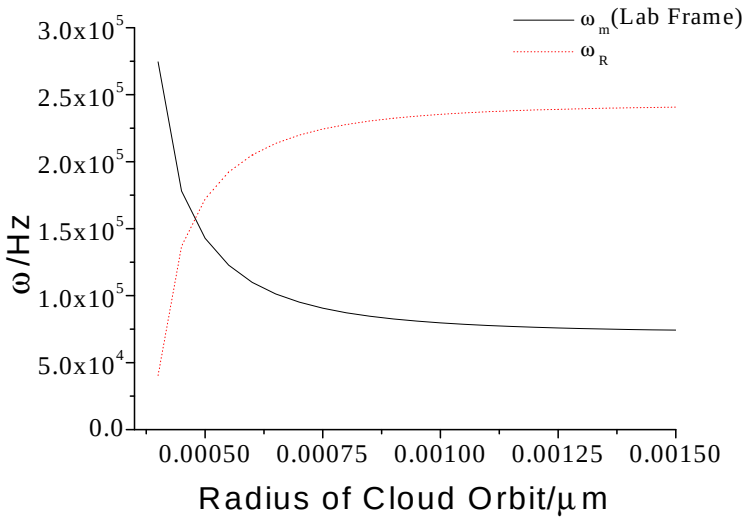

Fig. 6.15: The effect of space charge the cloud rotation frequency and the experimentally observed magnetron frequency in the lab frame. It is assumed that the ions are in a ring formation. The graph approaches $\omega_m = \omega_c/2$ for smaller radii.

more, the experimental radii are in a range ($r \simeq 450$ μm to $r \simeq 780$ μm) where the rate of change in ω_R is very great. This would make any shifts in the magnetron frequency highly noticeable. In fact there is no perceptible change in the magnetron frequency as the drive voltage is altered, which makes it unlikely that the ions do form a ring.

The alternative model to the ring configuration is that the ions remain as a cloud and orbit the trap centre together, as first postulated. The trouble with this picture is that it sounds highly unlikely that charged particles should want to stay together, especially when they are not being cooled strongly. One reason why they might is the relative efficiencies with which internal and external degrees of freedom are cooled.

In Chapter 2 the requirements for laser cooling are discussed. It was determined

that for laser cooling to occur, the following condition needed to be fulfilled:

$$\beta\omega_m < \alpha < \beta\omega_c' \tag{6.26}$$

the particular values of α and β and the motional frequencies being related to the cooling rates for each motion, γ_m and γ_c. It can be shown that in the general case where both magnetron and cyclotron motions are present, the relative ion motional frequencies will experience a shift to greater values. In the lab frame, the magnetron frequency shifts from $\omega_m \rightarrow \omega_m + \xi$ while the modified cyclotron frequency shifts from $\omega_c' \rightarrow \omega_c' + \xi/2$ [1]. This means that the requirement for laser cooling the relative motions is effectively more difficult to fulfill as the range represented by expression 6.26 is smaller for the internal motion than the centre of mass motion. The end result is that the internal degrees of freedom tend to be cooled less efficiently than the external (centre of mass) degrees of freedom. If we refer to the principal equation, equation 6.16, and the conditions set out, this could have the effect that, while the damping coefficients for the centre of mass motion fulfills condition 3, those for the relative motions still comply with condition 2 for axialization.

There is a further consideration in that it is unlikely that the value of δ, the coupling coefficient, should be equal for both the centre of mass and relative motions. In fact it is likely to be reduced for the relative motion. This does seem to contradict the argument of the previous paragraph, but leads to another interesting point. If δ is significantly reduced for the relative motion then it is possible that these motions become largely irrelevant in the axialization process. This seems possible, since the existence and the nature of space charge shifts in the motional frequencies means that the sum frequency of the two radial motions is no longer equal to the cyclotron frequency: they are not in resonance with the drive. In this way axialization becomes a purely centre of mass phenomenon: when cooling conditions are such that the

centre of mass of the cloud is predicted to be in a large orbit, then the only possible configuration is one in which the entire cloud orbits as a whole.

Space charge clearly must play a role in the behaviour of the cloud. There is still considerable work to be completed on the theory before these effects can be fully accounted for and quantified. It has already been stated that axialization is most suitable for application to single ions, thus it is conceivable that the clouds used in this study, containing only tens of ions are *sufficiently small* to allow axialization to dominate. It becomes increasingly difficult to produce cyclotron resonance as cloud size increases leading to the conclusion that with much larger clouds plasma considerations make axialization inefficient.

A Realistic Picture of the Cloud Dynamics

Assuming that our model of the ion cloud is correct then some numerical calculations can be made. As has been discussed, the source of the slow modulation is the magnetron orbit which takes the ions in and out of the laser beam. The width and separation of these peaks will be determined by the relative dimensions of the cloud, the orbital radius and the laser beam waist. Of particular interest is the amplitude α_2. This coefficient represents how much the ion motion brings the ion in and out of resonance with the laser light and may give some indication of how fast the ions are moving when they are within the laser beam. Suitable calculations would allow the modulation amplitude, α_2, to be related to a velocity amplitude.

Consider first the magnetron modulation alone. To simplify the picture, imagine that the ion cloud has no dimensions, as it orbits the trap it enters the laser beam and begins to fluoresce, it passes through a maximum of fluorescence at the centre of the laser beam and when it leaves the laser beam fluorescence stops immediately. If we were to record the fluorescence rate we would see long periods where there is no fluorescence and triangular pulses corresponding to the periods where the ions

are in the laser beam twice in each orbit. The FWHM width of these triangular pulses, τ_p is characteristic of the velocity of the ion cloud, $r\omega_m$ and the laser beam waist, w_0. The spacing of the modulation peaks, τ_s will be the time it takes the ion cloud to complete half an orbit. Expressions can be derived for both τ_p and τ_s:

$$\tau_p = \frac{s}{r\omega_m} \tag{6.27}$$

and

$$\tau_s = \frac{\pi}{\omega_m} \tag{6.28}$$

where $s \simeq w_0$. Taking the more realistic case where the ion cloud does have dimensions the triangular pulses are broadened, by how much depends only on the cloud size. In fact the amount of broadening will be equal to the time it takes for the cloud to travel twice its diameter: fluorescence begins as the leading edge of the cloud enters the laser beam and only ceases when the trailing edge leaves the beam. The value of τ_p in expression 6.27 can be redefined to account for the broadening:

$$\tau_p' = \frac{w_0 + (w_0/n)}{r\omega_m} \tag{6.29}$$

here the cloud dimension are expressed in terms of a fraction of the beam waist: w_0/n = cloud diameter, where n is any real number. Note that the expression uses (w_0/n) and not twice this value, this is because it is the FWHM width of the fluorescence pulses which is required. In the limit of very large clouds (or where the orbit diameter is close to the beam waist dimensions) the pulses will become so broadened that they run into each other and eventually become indistinguishable. In order to asses how visible the modulation will be it is useful to look at the ratio

of the peak width to the peak separation.

$$\frac{\tau_p'}{\tau_s} = \frac{w_0(1+1/n)}{r\pi} \tag{6.30}$$

Larger ratios clearly indicate less visible modulation peaks and would be expected for larger cloud sizes.

Since the beam waist and the sizes of the ion cloud orbits are known it is possible to make some calculations as to the expected widths of modulation peaks. Refer back to figure 6.12 which shows the photon correlation spectrum for a cloud of ~ 50 ions. It can be estimated, from the ICCD images, that the cloud diameter is ~ 400 μm and that the orbit radius is ~ 500 μm. Thus it is calculated that the ratio $\tau_p'/\tau_s = 0.34$, that measured from the correlation traces is $0.30\pm5\%$. Figure 6.13 is the correlation spectrum for a cloud of ~ 5 ions. This data sample gives a smaller ratio, $0.27\pm5\%$, which is consistent with there being very few ions. The value is actually much better than might be expected using only the simple model outlined in the laser few paragraphs: the cloud diameter is ~ 90 μm and the orbit radius is ~ 100 μm which gives $\tau_p'/\tau_s = 0.73$. This would make the modulation peaks nearly indistinguishable. However, since we are dealing with a very small cloud then it is expected that the correlations should be strong: the chance of two photons from the same ion arriving consecutively at the TAC increases as ion number decreases (see section 6.5.4). This same consideration also accounts for the very clear modified cyclotron peaks in comparison to those seen on the trace from the larger cloud.

Imagine now what happens when the cloud of ions is within the laser beam. If the laser cooling frequency is ν_0, the ion motion at a velocity v (due to ω_c'), alters the apparent frequency of the laser light (as a result of the Doppler shift) by an amount $\Delta\nu$ thus:

$$\Delta\nu = \nu_0 \frac{v}{c} \tag{6.31}$$

where c is the speed of light. Depending upon how far detuned the laser light is from the atomic resonance the depth of intensity modulation, ΔI which arises as a result of the frequency change, $\Delta\nu$ will change. It is expected that at small detunings the intensity modulation will be greater than at large detunings; this is a direct result of the Lorentzian lineshape of the atomic transition. The intensity profile of the transition can be expressed thus [25]:

$$I(\nu) = \frac{(\Gamma/2)^2}{\nu^2 + (\Gamma/2)^2} \tag{6.32}$$

By differentiating equation 6.32, the gradient of the line profile can be calculated. With a detuning of $\Gamma/2$, the gradient has a value of $1/\Gamma$. Looking once again at the fluorescence level F (neglecting the magnetron modulation for the moment), the effect of the velocity modulation at a particular detuning can then be assessed:

$$F(t) = I(0) + \frac{dI}{d\nu}\Delta\nu(t) \tag{6.33}$$

where *I(0)* is the average fluorescence level. Thus the value of α_2 can be calculated:

$$\alpha_2 = \frac{\nu_0 v}{c}\frac{dI}{d\nu} \tag{6.34}$$

The quantity $(\nu_0/c)^{-1} = 280nm$ is the laser cooling wavelength.

The actual detuning used in the experiments was around 100 MHz, this gives a value of $dI/d\nu \simeq 1/18\Gamma$. Using the fitted values for α_2 shown in table 6.1 then estimates for v can be found: for data set 1, v = 150 m/s and for data set 2, $v = 120$ m/s. This would be consistent with strong cooling of the modified cyclotron motion.

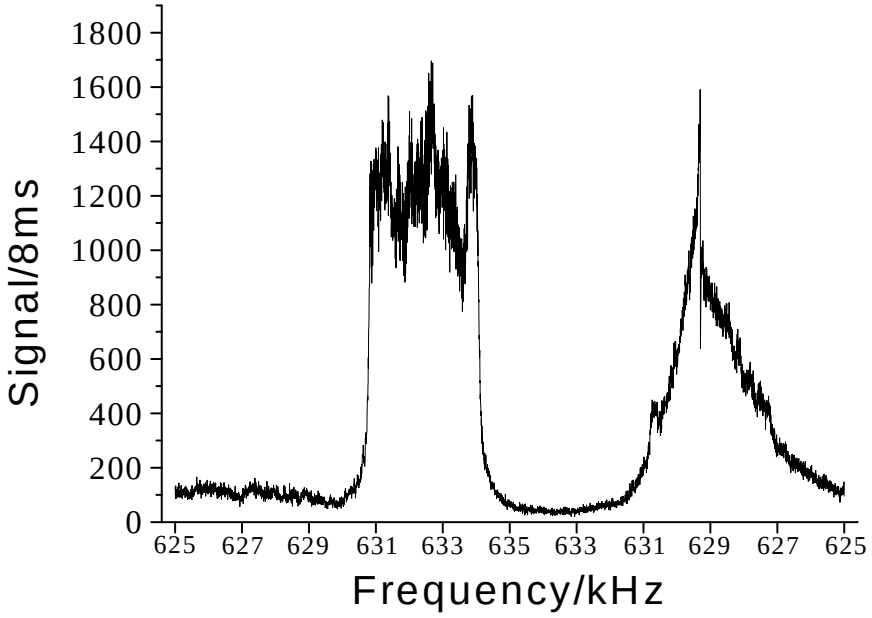

Fig. 6.16: The asymmetry in the resonance feature for a large cloud. The drive frequency is swept first up through resonance then down again.

6.5.6 Large Cloud Dynamics

The dynamics of larger clouds under the influence of the axializing drive is interesting for a number of reasons. The appearance of structure as discussed in the last section is perhaps the most striking feature, but other phenomena were discovered. In particular, it was found that there is a distinct asymmetry in the shape of the resonance curve depending on whether it is approached from above or below in frequency and a near sinusoidal modulation of the fluorescence rate (at a few Hz) when the cloud was held with the drive set on resonance. Using the ICCD camera it was possible to connect both of these effects with physical changes in the ion cloud.

First take the instance of the asymmetric resonance curve, an example of which is shown in figure 6.16. It was observed that the response of ion clouds of any size

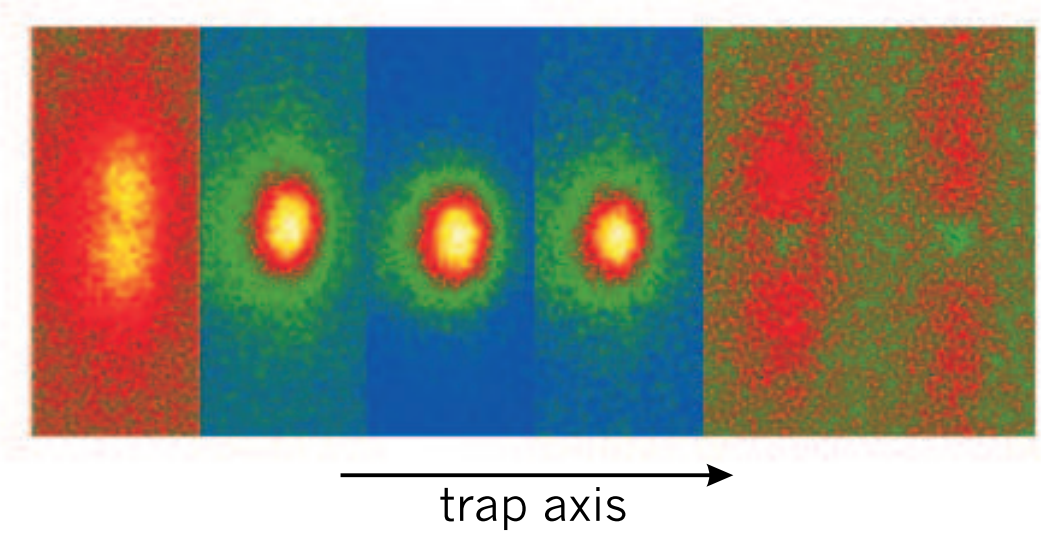

Fig. 6.17: ICCD images of the cloud at 2 kHz intervals as the drive frequency is swept (the start frequency is 621 kHz). Resonance is at 627 kHz in this case (this is slightly lower than the expected value of 630 kHz, this may be due to magnetic field fluctuations during the time taken to record the image).

is somewhat sensitive to whether the drive is slightly above or below resonance. It has also been observed that whereas a cloud may be held indefinitely at a drive frequency *below* the cyclotron resonance, trying to keep a cloud at a drive frequency *above* the cyclotron resonance generally leads to rapid expansion of the cloud and loss of the ions. This may indicate that the heating and cooling rates experienced by the cloud above and below resonance may be quite different. These effects are likely to be exaggerated as ion number increases.

Consider the MCS trace shown in figure 6.16. As the drive frequency is swept upwards there is an abrupt increase in signal to a maximum value where it remains for a broad range of frequencies before dropping to a minimum. Reducing the drive frequency again it can be seen that the resonance is much sharper. It is interesting that the upward going resonance appears to begin at approximately the same frequency as the downward going resonance reaches its sharpest peak. This

frequency has been calculated as the expected value for the cyclotron frequency.

Looking at the evolution of the cloud using the ICCD camera (figure 6.17), with shots taken every 2 kHz, it is possible to see that the ion cloud does actually behave differently above and below resonance. The cloud starts out as a diffuse disk of ions, nearing resonance it becomes dense and quite spherical, immediately above resonance it is forced into a large well defined orbit about trap centre. The size of the orbit above and below resonance is also noticeably different, it is in fact largest above resonance indicating that there may be greater heating effects present.

Reducing the cloud size alters the evolution such that the cloud is forced into a well defined orbit both above and below resonance. When this is so the asymmetry in the MCS trace is reduced. It is probable that the observed effect is related to the effects of space charge, which with larger clouds become predominant over the effects of the driving field leading to the suppression of certain phenomena. When the ions are hotter (above resonance) and therefore further apart the influence of the drive field once again predominates. This could lead to the asymmetry observed.

The modulation which is seen in the fluorescence signal from the driven cloud (figure 6.18) is also intriguing. The modulation appears only for specific laser beam positions, more precisely, when the laser beam is placed slightly on the magnetron heating side of the trap. The drive amplitude and frequency appear to have the greatest influence on the frequency of the modulation. The obvious explanation for this is that the cloud is swapping between the axialized and non-axialized states, indeed ICCD camera evidence does suggest that this is so. The time scale upon which the cloud oscillates is too fast for the camera to resolve entirely, thus images show the cloud in a superposition of states, as shown in figure 6.19.

The dependency of the period of cloud oscillation upon such things as drive amplitude and frequency was investigated. The influence of the drive amplitude is complicated by the fact that it affects not only the strength of the ion response,

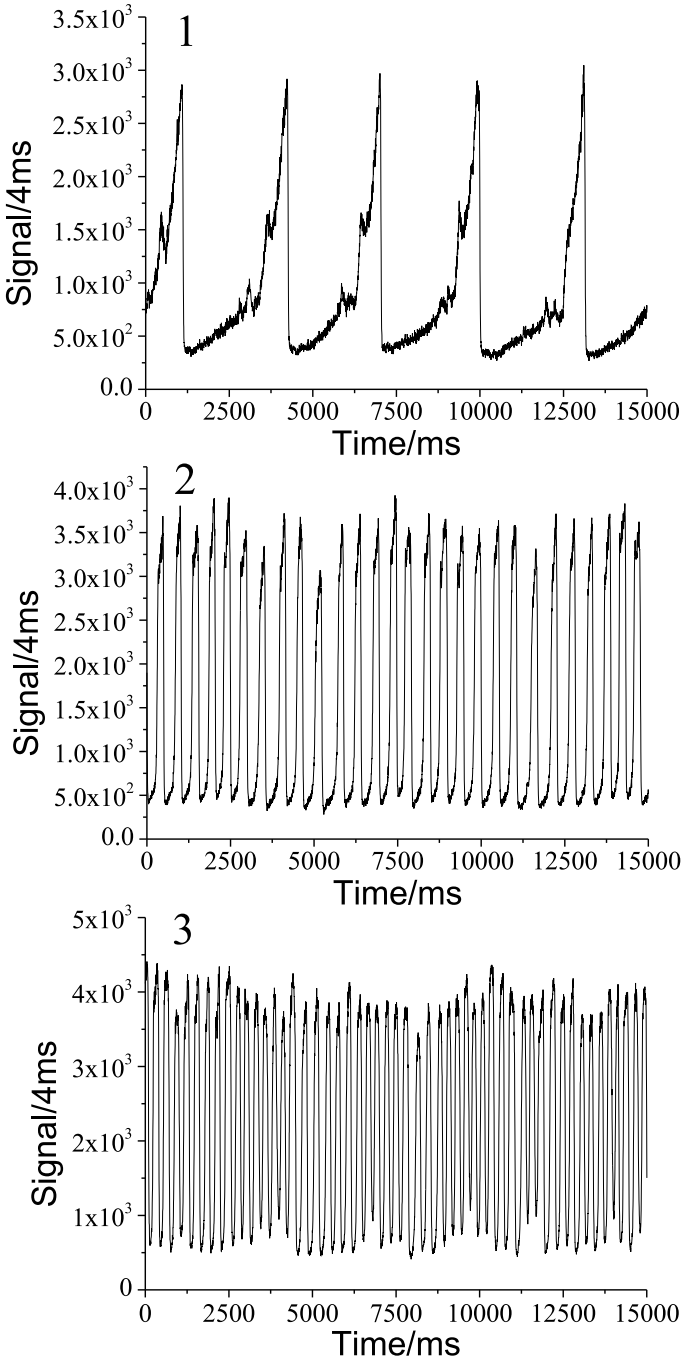

Fig. 6.18: The figure shows how the fluorescence modulation depends upon the drive frequency. The axializing drive frequencies were 625, 630 and 633 kHz for each of 1, 2 and 3 respectively. The drive amplitude was 50 mV.

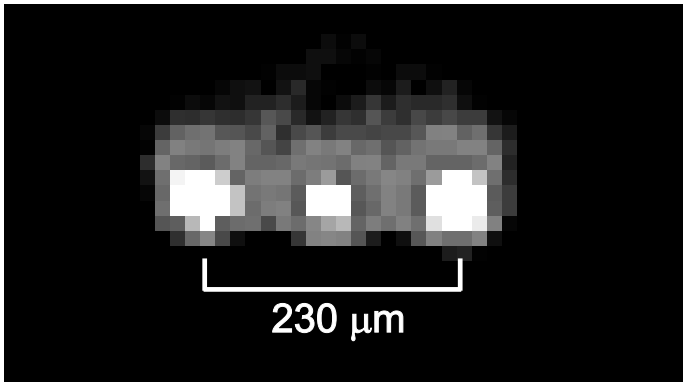

Fig. 6.19: Here the cloud is oscillating between two states: the dense axialized state (central bright spot) and the large orbit, indicated by the two bright spots on either side of the central one, where the large orbit intersects the laser beam.

but also the breadth of the resonance. Experimental results show that the principal effect of the drive amplitude is on the depth of modulation observed: larger drive amplitudes result in deeper modulation (rather the maximum signal reached being higher). The frequency of the applied drive alters the period of modulation observed. Frequencies furthest below resonance resulted in the longest modulation periods.

This kind of oscillation in the fluorescence signal has been observed before [26]. In this instance highly periodic variation in the fluorescence from undriven clouds of $^{24}Mg^{+}$ ions was observed. The particular conditions for which this type of behaviour was seen involved laser positions close to the trap centre. Variation in signal levels was up to 80%. The oscillation period ranged from 0.1 s to 6 s and was strongly dependent upon the laser detuning. As in the present case the reason for the oscillations is a subtle interaction of laser cooling and heating processes: changes in the spatial extent of the cloud combined with the spatially dependent Doppler shift due to the magnetron motion. Where axialization is involved there are clearly very large, rapid changes in the ion cloud.

Other explanations for cloud expansion despite strong cooling involve issues of angular momentum conservation and coupling of the magnetron motion and the

uncooled axial motion [27]. From the analysis outlined in Chapter 2, as the density of an ion cloud is increased, its rotation frequency will also increase. If we add angular momentum to the cloud by laser cooling then the cloud rotation frequency can be made to increase. The increase in rotation frequency however, will not continue indefinitely: it has a limiting value of $\omega_c/2$. At this limiting frequency the density of the ion cloud also reaches a maximum. As more angular momentum is added by the laser then the cloud begins to expand again. Experimentally it has proven difficult to reach the condition of maximum density using only simple laser cooling [14]. The previous discussion also does not predict any compression following periods of expansion which result in the oscillations observed.

The authors turn to effects which prevent the attainment of maximum density. The effect of perturbations of the trapping fields is considered the most likely explanation. Imperfections in the trapping fields could result in coupling of angular momentum into the system producing expansion of the magnetron radius before maximum density is reached.

The condition where the trap symmetry is slightly tilted about the x-axis is considered specifically. Owing to the axial ion motion, such a misalignment is shown to result in what can be interpreted as an oscillating electric field in the y-direction. This electric field, E_y, is thought to be responsible for resonant driving of the radial motion.

$$E_y = \frac{3zU_0}{R_0^2}\sin(2\delta) \tag{6.35}$$

where δ is the tilt angle.

For a single ion, if $\delta << 1$ then this driving term is close to ω_z and clearly non-resonant with either of the radial frequencies: there can be no energy transfer between modes. In a cloud of ions the situation is very different: there will be broadening of the ω_m and ω_c' resonances due to ion-ion collisions, cloud compression increases cloud density and rotation frequency and ω_z is reduced owing to the effects

of space charge. Jointly these effects lead to a situation where the ratio $\omega_z'/\omega_m \rightarrow 1$ (where ω_z' is the space charge shifted axial oscillation frequency). Under these conditions there will be resonant coupling between the magnetron and axial modes, which in the case where the axial motion is *not* cooled leads to an increase in the magnetron radius. At low ion cloud density (and higher temperatures) the resonance condition is not fulfilled. Where there are influences for both compression (laser cooling, axialization) and expansion (resonant coupling to the axial mode) there appears to be the possibility that the cloud will actually expand and contract periodically. However, it is clear that more work is needed to establish the exact mechanisms involved.

6.6 Conclusion

The axialization of laser cooled ions has been demonstrated and imaged for the first time. The ions form a dense cloud at the centre of the trap and both radial motions of the ions are cooled strongly by the laser. The technique can be applied to single ions and results in a tightly localized orbit. Under particular conditions the ions can be driven into a relatively large orbit with a well defined radius comparable to or larger than the laser beam diameter.

The dynamics of large axialized clouds was studied, especially under the conditions where large orbits were formed. Using photon correlation it was found that the ions in these large orbits form two clouds on opposite sides of the trap which orbit the trap at the magnetron frequency. Other phenomena which appeared were also investigated. Using the ICCD camera it was possible to connect these to physical changes in the ion cloud.

References

[1] R. C. Thompson and D. C. Wilson, *Z. Phys. D* **42**, 271 (1997)

[2] R. C. Thompson, *Adv. Atom. Molec. Phys.* **3** (1993), 53

[3] J. I. Cirac, P. Zoller, *Phys. Rev. Lett*, **74**, 4091 (1995)

[4] W. Itano and D. J. Wineland, *Phys. Rev. A.*, **25**, 35 (1982)

[5] W. Itano, L. R Brewer, D, J, Larson and D. J. Wineland, *Phys. Rev. A*, **38**, 5698 (1988)

[6] G. Zs. K. Horvath and R. C. Thompson, *Phys. Rev. A.*, bf 59, 4530 (1999)

[7] R. C. Thompson and J. Papadimitriou, *J. Phys. B.* **33**, 3393 (2000)

[8] L. Schweikhard and A. Marshall, *J. Am. Mass Spectrom.*, **4**, 433 (1993)

[9] F. Mintert and Ch. Wunderlich, *Phys. Rev. Lett.* **87**, 257904 (2001)

[10] H. Imajo, S. Urabe, K. Hayasaka, M. Watanabe, *J. Mod. Opt.* **39**, 317 (1992)

[11] S. Guan, X. Xiang and A. G. Marshall, *Int. J. Mass Spectrom. Ion Proc.* **124**, 53 (1993)

[12] M. König, G. Bollen, H. J. Kluge, T. Otto, J. Szerypo, *Int. J. Mass Spectrom. Ion Proc.*, **142**, 95 (1995)

[13] Ch. Lichtenberg, G, Marx, G. Tommaseo, P. N. Ghosh and G. Werth, *Eur. Phys. J. D.*, **2**, 29 (1998)

[14] J.J. Bollinger and D. J. Wineland, *Phys. Rev. Lett.* **53**, 348 (1984)

[15] D. J. Heinen, J.J. Bollinger, F. L. Moore, W. M. Itano and D. J. Wineland, *Phys. Rev. Lett.* **66**, 2080 (1991)

[16] X-P Huang, J. J. Bollinger, T. B. Mitchell and W. M. Itano, *Phys. Rev. Lett.* **80**, 73 (1998)

[17] G. Gräff and E. Klempt, *Z. Naturforsch* **22a**, 1960 (1967); *Z. Phys.* **222**, 201 (1969)

[18] A. A. Solokov and Yu. G. Pavlenko, *Opt. Spectrosc. (USSR)* **22**, 1 (1967)

[19] H. F. Powell, R. C. Thompson and D. M. Segal, *Phys. Rev. Lett.* **89**, 093003 (2002)

[20] H. F. Powell, D. M. Segal and R. C. Thompson, in preparation (2002)

[21] M. A. van Eijkelenborg, M. E. M. Storkey, D. M. Segal, R. C. Thompson, *Int. J. Mass. Spectrom. Ion Proc.* **188**, 155 (1999)

[22] J. J. Bollinger, D. J. Heinzen, F. L. Moore, W. M. Itano and D. J. Wineland, *Phys. Rev. A.* **48**, 525 (1993)

[23] K. Dholakia, G. Zs. K. Horvath, D. M. Segal, R. C. Thompson, D. M. Warrington and D. C. Wilson, Phys. Rev. A, bf 47, 441 (1993)

[24] R. C. Thompson, D. J. Bate, K. Dholakia, D. M. Segal and D. C. Wilson, *Phys. Scripta.* **46**, 285 (1992)

[25] W. Demtröder, *Laser Spectroscopy: Basic Concepts and Instrumentation*, Springer-Verlag, p 81 (1988)

[26] R. C. Thompson, G. P. Barwood, P. Gill, *Opt. Acta* **33**, 535 (1986)

[27] D. J. Wineland, J. J. Bollinger, W. M. Itano and J. D. Prestage, *J. Opt. Soc. Am. B* **2**, 1721 (1985)

CHAPTER 7

Conclusion and Outlook

7.1 Summary

This thesis describes experiments with laser cooled Mg^+ ions in a Penning trap. The design of a cylindrical Penning trap for use in a quantum Zeno effect experiment is described and its properties analyzed. Although the experiment itself was never completed, the preparatory steps are described and a full discussion of the philosophical and experimental issues surrounding the quantum Zeno effect is given. The quantum jump statistics of the three stable isotopes of Mg^+ are studied and evidence of so called nuclear quantum jumps in $^{25}Mg^+$ is discussed. The possibility of studying these rare nuclear jumps by driving the specific hyperfine transitions is explored. The implementation of axialization, a scheme for improving laser cooling efficiency in the Penning trap, is described. This technique has many advantages and should be widely applicable in future quantum information experiments. The behaviour of the laser cooled ion cloud in the presence of an axializing drive field proved to be very fertile ground for study. Novel ion dynamics were discovered and these were studied in some depth.

7.2 Comments upon the Quantum Zeno Experiment

The quantum Zeno effect highlights one of the important and fundamental difficulties with measurement of quantum systems. The premise of the quantum Zeno effect is that the decay of an unstable system can be inhibited by frequent measurement and completely stopped in the case of continuous measurement. The resolution of how the effect really plays a part in physical systems would be a step forward in our understanding and interpretation of quantum mechanics.

Experiments carried out by Itano et al on a cloud of Be^+ ions [2] went some way to demonstrating the existence of the quantum Zeno effect. In this case the atomic systems are driven coherently between two atomic states and the time evolution of this process is shown to be impeded by frequently applied, discrete measurements (in the form of a laser pulse). Unfortunately, this experiment suffers from certain problems of interpretation, namely in the description of the measurement interaction between the laser pulses and the atomic systems. This can only be resolved by repeating the experiment with a single ion [3]. Even so these experiments do not look at the Zeno phenomenon in its purest form leaving many unanswered questions: the measurement schemes of [2, 3] cannot reach the continuous regime and the atomic systems are driven rather than decaying spontaneously.

At Imperial it was hoped to address both these issues the first by implementing an approach suggested by Beige [4]. This would allow access to a near continuous measurement regime. To look at the second issue a scheme for simulating a spontaneously decaying system was developed by Plenio [5]. The lively debate concerning the quantum Zeno effect continues, with many papers published each year.

Although all systems were in place for the completion of the quantum Zeno ex-

periment, ultimately, difficulties in handling and maintaining the apparatus were its downfall. The lack of easy access to the trap and imaging optics made optimization extremely problematic. The instability of ions in the cylindrical trap was also a continuing difficulty. It is thought that the long optical path length to the trap combined with the erratic behaviour of the dye-laser were principally responsible for the problems and it was hoped that by use of axialization the situation might be improved. It is likely that axialization would have helped, however, the introduction of a split ring into the cylindrical trap may actually have exacerbated its unreliability.

Having outlined the principal barrier to success in the quantum Zeno experiment as being doubts about the adequacy of the system for such high precision experiments it is necessary to suggest some improvements. The laser instabilities were largely due to the use of intracavity frequency doubling using a plane faced crystal. A simple solution involved swapping the original crystal for a Brewster cut crystal. However, it is certain that the best approach would be to produce the UV wavelength in an external cavity so allowing for independent optimization of the laser and the UV production. Building a suitably stable cavity with feedback is certainly not trivial, but could be simplified by the use of a modified dye laser cavity. Such a solution has been used by other groups [1].

A more drastic solution would involve a move away from a dye based system to a solid state laser. As yet there are no sufficiently narrow band diode lasers available for frequency doubling to 280 nm (for Mg^+), however there is the possibility of third harmonic generation. For this purpose, the required fundamental wavelength is 840 nm and two laser sources have been suggested as possible candidates: Ti:Sapphire or Cr:LiSAF. Both of these lasers can be solid state–diode pumped. The tuning range of these lasers is similar, 670–1100 nm (peak at 790 nm) for the former and 780–900 nm (peak at 860 nm) for the latter. Of the two possible lasers, the Ti:Sapphire

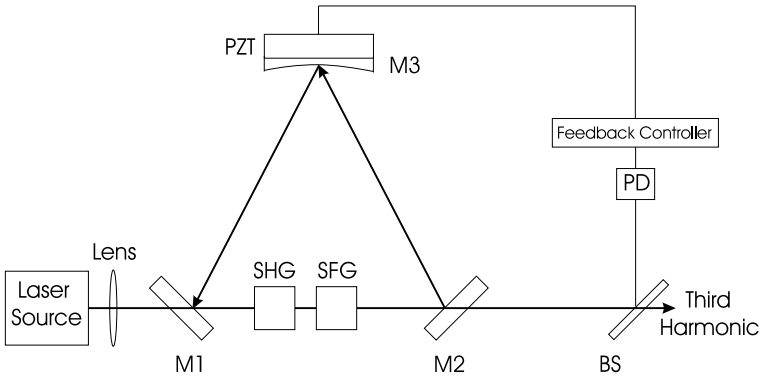

Fig. 7.1: A scheme for the production of the third harmonic by frequency doubling and sum frequency mixing.

would typically give the greater power output: around 600 mW (peak) might be expected if pumping with 5 W diode power, whereas Cr:LiSAF lasers are generally limited to < 230 mW [6][1]. The principal advantage of a Cr:LiSAF laser is that it can be directly diode pumped (the Ti:Sapphire requires a diode pumped–frequency doubled Vanadate laser system) and so represents the cheaper alternative. This may however be outweighed by the fact that it is only the Ti:Sapphire system which would be commercially available as a narrow linewidth source. That the tuning range of the Ti:Sapphire stretches further into the infra–red also makes this laser more attractive as it would be suitable for generation of not only 280 nm but also 313 nm, for laser cooling Be^+ (requiring a fundamental wavelength of 939 nm).

To produce the third harmonic a scheme for frequency doubling plus sum frequency mixing has been suggested as the most efficient method. A diagram of a suitable system is shown in figure 7.1. The fundamental (840 nm for the generation of 280nm UV) enters the cavity and is frequency doubled in the first non-linear crystal, the fundamental and the second harmonic are then mixed in the second non-linear crystal to produce the third harmonic. For good conversion of the fundamental

[1] although this same paper reports 1.1 W of CW power from a Cr:LiSAF using a novel pumping technique

Table 7.1: A summary of results showing the on:off ratios for all three stable isotopes of Mg^+.

Ion Species	On:Off Ratio	
	theory	experiment
$^{24}Mg^+$	16.0	16.1±0.8
$^{25}Mg^+$I	11.8	10.2 ±1.5
$^{25}Mg^+$II	22.8	22.0 ±3.0
$^{26}Mg^+$	16.0	15.8 ±0.7

to the third harmonic the cavity needs to be resonant with both the fundamental and the second harmonic. There will be some dispersion owing to the presence of the second non-linear crystal. In order to optimize the cavity length, part of the output from the frequency conversion cavity is directed into a feed back loop: the piezo–controlled mirror is used to maximize the signal falling on the photodiode.

7.3 Quantum Jumps in Magnesium

This project involved investigation of the jumps statistics of Mg^+. Single ions of each of the three stable isotopes of Mg^+ ($^{24}Mg^+$, $^{25}Mg^+$ and $^{26}Mg^+$) were trapped and quantum jumps observed. An analysis was made of the time spent by the ion in each of its two states: either fluorescing (on) or not fluorescing (off). The principal result of the investigation was experimental verification of the On to Off ratios for each of the three isotopes studied.

The values found show good agreement with theory. The results are summarized in table 7.1. The labels I and II in the case of $^{25}Mg^+$ indicate the use of the lower and upper cooling transition respectively.

The length of quantum jumps was also studied. This revealed some evidence for the nuclear quantum jumps postulated some years ago by the Imperial College Ion Trapping group [9]. These very rare jumps occur only in $^{25}Mg^+$. They occur

between the different hyperfine levels of this isotope and are distinguishable from normal quantum jumps as they are of much longer duration (up to six times as long). Initial studies were inconclusive owing to the low incidence of the nuclear jumps; a fuller investigation of the phenomenon would involve driving the relevant RF transitions. This was attempted, but without success, due to magnetic field instabilities. Nuclear jumps should be of general interest to the wider Ion trapping community as their occurrence is not limited to $^{25}Mg^{+}$: they should be present for any ion which has hyperfine structure.

7.4 Axialization

The implementation of this technique represents an important step forward for experimentalists working on quantum computing in the Penning trap environment. It has proved itself to be an impressive tool for the cooling and localization of single ions and small clouds.

The technique works by applying a quadrupole drive in the radial plane. This couples the strongly cooled cyclotron motion to the unstable magnetron motion. A simple mathematical analysis shows that in the presence of laser cooling, several possibilities exist for how the ions behave. The outcome depends upon the coupling strength, δ, relative to the damping of the cyclotron and magnetron motions, γ_c and γ_m respectively. A computer simulation was used to test the three principal cases: $\gamma_c = \gamma_m = 0$, $\gamma_c\gamma_m < \delta^2$ and $\gamma_c\gamma_m = \delta^2$.

Experimentally the most important result is where $\gamma_c\gamma_m < \delta^2$ and the magnetron motion decays to leave the ions localized at the central axis of the trap. The experiments described in this thesis showed successful demonstration of this process. Images taken of single ions were used to estimate an upper limit of $\sim$10 mK on the temperature of an axialized ion.

In the case where $\gamma_c\gamma_m = \delta^2$, the ion finds an equilibrium magnetron orbit. Studies with clouds show that these orbits can be very large, up to 1500 μm. The structure of these orbits was studied by the use of photon-photon correlation. The results were unexpected as they indicated the presence of a high degree of spatial order even for very large clouds. Evidence suggests that the ions form a dense cloud which orbits the trap centre. This behaviour may result from the difference in the cooling rates for the internal and external degrees of freedom of the cloud.

7.5 Future Experiments

To complete the work on axialization, the cooling rates of the radial motions should be determined with and without the presence of the axializing field. These measurements can be completed quite simply using a photon-RF correlation technique (described at the end of chapter 2).

To reach lower temperatures than those already achieved there are several options. Moving to the superconducting magnet not only has the advantage of a more stable field, but also the trap designed for use with this system enables direct cooling of the axial motion. The angled laser beam path through the trap centre already provides some axial cooling, however, the trap design would also accommodate the passage of a cooling beam along the trap axis. This additional cooling would greatly improve conditions in the trap, however, because the imaging system for this trap is also done along the axis, there would be problems with scattered light. Despite the difficulties posed, this type of geometry with both imaging and laser cooling along the same axis, has been used successfully [7]. If we were able to implement this scheme it would also open the way for providing another cooling method for the magnetron motion. The concept is analogous to axialization, requiring a quadrupole field in the axial plane. This could be achieved using the end-caps and two of the

four sections of the ring. A driving field applied at a frequency $\omega_d = \omega_z + \omega_m$ would result in the coupling of the axial and magnetron motions.

7.6 Outlook

One of the favoured systems for use in quantum information studies is the Ca^+ ion in an RF trap. Recent work at Imperial College has demonstrated laser cooling of $^{40}Ca^+$ in a Penning trap [8]. Future experiments will look at decoherence effects in a Penning trap which is relevant to the use of this type of trap in quantum information science.

The Mg^+ ion is, unfortunately unsuitable for applications in quantum information processing. However, the simplicity of the laser cooling system for this ion is attractive. This means that Mg^+ could still prove useful as a form of *test and measurement* system for exploring the bounds of quantum phenomena. It may therefore be worthwhile continuing with this system in parallel with the Ca^+ experiments.

References

[1] M. G. Boshier, PhD Thesis, University of Oxford, Unpublished (1988)

[2] W. M. Itano, D. J. Heinzen, J. J. Bollinger and D. J. Wineland, *Phys. rev. A* **41**, 2295 (1990)

[3] Ch. Balzer, R. Huesman, W. Neuhauser, P. E. Toschek, *Opt. Comms* **180**, 115 (2000)

[4] A. Beige and G. C. Hegerfeldt, *J. Phys. A* **30**, 1323 (1997)

[5] M. B. Plenio, P. L. Knight, R. C. Thompson, *Opt. Comm.* **123**, 278 (1996)

[6] D. Kopf, U. Keller, M. A. Emanuel, R. J. Beach and J. A. Skidmore, *Opt. Lett.* **22**, 99 (1997)

[7] T. B. Mitchell, J. J. Bollinger, W. M. Itano and D. H. E. Dubin, *Phys. Rev. Lett.* **87**, 183001 (2001)

[8] K.Koo, J. Sudbery, D. M. Segal and R. C. Thompson, in preparation, (2002)

[9] D. J. Bate, PhD Thesis, University of London, Unpublished (1991)

APPENDIX A

A Program to Analyze Quantum Jump Data

This program reads in .dat data files containing mcs traces with quantum jumps. It calculates the detected photon distribution, the the distribution of quantum jump lengths, the average jump time, the total number of quantum jumps, the on-to-off ratio, the length of the data run.

The program is written in Turbo Pascal.

```
$N+,R+,S+ uses dos,crt,graph; const
   threshold     = 5;            (* defines "on" and "off" states          *)
   dwelltime     = 0.500;        (* dwelltime in milliseconds              *)
   screentext    = true;         (* screeninfo = false increases memory    *)
   numberoffiles = 1;            (* number of input files                  *)
   nameout       = 'qjumps.sts'; (* output file name                       *)
   skiplines     = 10;           (* number of lines skipped in input files *)
   directory     = 'f: \data\';  (* defines directory path                 *)
   nameout       = +directory+'qjumps.sts'; (* defines name of output file *)
   maxphotoncount = 60;          (* reduce these to increase memory        *)
```

```
   maxjumplength  = 60;
   classxscale    = 7;           (* scaling values for screen plotting     *)
   classyscale    = 100;
   jumpxscale     = 4;
   jumpyscale     = 20;
var
   class    : array[0..maxphotoncount] of longint;
   jmplength: array[0..maxjumplength] of longint;
   name     : array[1..numberoffiles] of string;
   f,ff     : text;
   grd,grm  : integer;
   texxt    : string;
   averagejumplength : extended;
   t,i,j,photons,maximumx,maximumy,on,off,jumplength,
   numberofjumps,totaljumplength : longint;
   quantumjumped : boolean;
procedure assigninputfiles; begin
  name[1]  := +directory+'n25d4001.dat';
end; procedure openinputfile; begin
  assign(f,name[j]);
  reset(f);
  if ioresult <> 0 then
    begin
      sound(800);delay(1000);nosound; exit;
    end;
    for i:= 0 to skiplines do readln(f);
end; procedure resetcounters; begin
```

```
  for i := 0 to maxphotoncount do class[i] := 0;
  for i := 0 to maxjumplength  do jmplength[i] := 0;
  on:=0; off:=0; numberofjumps := 0;
end; procedure setupscreen; begin
  grd := detect;
  initgraph(grd,grm,'c:\tp\bgi');
  maximumx := getmaxx; maximumy := getmaxy;
  delay(20000);
end; procedure updatestatistics; begin
  if photons > threshold then
    begin
      inc(on);
      if quantumjumped then
        begin
          inc(numberofjumps);
          inc(jmplength[jumplength]);
          putpixel(400+jumpxscale*jumplength,
          maximumy-10-round(ln(jmplength[jumplength])*jumpyscale),
                                                        lightcyan);
        end;
      quantumjumped := false;
    end
    else
    begin
      inc(off);
      if not(quantumjumped) then
        begin
```

```
          jumplength := 1;  quantumjumped := true;
        end
        else
        inc(jumplength);
    end;
end; procedure plotscreentext; begin
  str(threshold,texxt);
  outtextXY(10,220,'threshold = '+texxt+' ');
  str(numberofjumps,texxt);
  outtextXY(220,240,'Total number of jumps = '+texxt+' ');
  str(dwelltime*(on+off)/60000,texxt);
  outtextXY(220,230,'Total time (minutes)  = '+texxt+' ');
  outtextXY(220,250,'Output file name      = '+nameout+' ');
  for i:=0 to 10 do
    putpixel(round(classxscale*(threshold+0.5)),maximumy-20-i,
                                                    lightred);
    for i:=0 to 2 do
      begin
        str(i*20,texxt);
        outtextXY(classxscale*20*i,maximumy-8,texxt);
   end;
   for i := 0 to 4 do
     begin
       str(round(i*10*dwelltime),texxt);
       outtextxy(400+jumpxscale*i*10,maximumy-8,texxt);
     end;
   outtextXY(470,350,'N(T_off)   (ms)');
```

```
   outtextXY(10,350,'P(n)');
end; procedure makeoutputfile; (* for easyplot *) begin
  assign(ff,nameout); rewrite(ff);
  writeln(ff,'/et g  "',nameout,' <T_off> = ',
                                dwelltime*off/numberofjumps,' ms"');
  if screentext then
    begin
      writeln(ff,'/aa 00 10000 "R = ',on/off,' with threshold = ',
                                                    threshold,' "');
      writeln(ff,'/aa 00 20000 "',numberofjumps,' qntjumps in ',
                                                     on+off,' ms"');
      for i := 0 to maxphotoncount do writeln(ff,i,'  ',class[i]);
      writeln(ff,'//nc'); (* end of curve *)
      for i := 1 to maxjumplength do
      writeln(ff,i*dwelltime,'   ',jmplength[i]);
      writeln(ff,'//nc'); (* end of curve *)
      writeln(ff,'/et x "1. n (number of photons)    2. T_off (ms)"');
      writeln(ff,'/et y "1. N(n)                     2. N(T_off) "');
    end;
    close(ff);
end; begin
  assigninputfiles;
  resetcounters;
  setupscreen;
  for j := 1 to numberoffiles do
    begin
      openinputfile;
```

```
      quantumjumped := false;
      jumplength := 0;
      repeat
      readln(f,t,photons);
      if screentext then
      putpixel(round(t/8000*maximumx),maximumy-300-photons,white);
      inc(class[photons]);
      putpixel(classxscale*photons,maximumy-10-round
                          (class[photons]/classyscale),lightcyan);
      updatestatistics;
      until eof(f);
      close(f);
    end;
  str(on/off,texxt);
  outtextXY(220,220,'On to off ratio   R   = '+texxt+' ');
  str(dwelltime*off/numberofjumps,texxt);
  outtextXY(220,260,'Average jump length (ms) = '+texxt+' ');
  if screentext then plotscreentext;
  makeoutputfile;
  repeat until keypressed;
  closegraph;
end.
```

APPENDIX B

Quantum Jumps of Several Ions

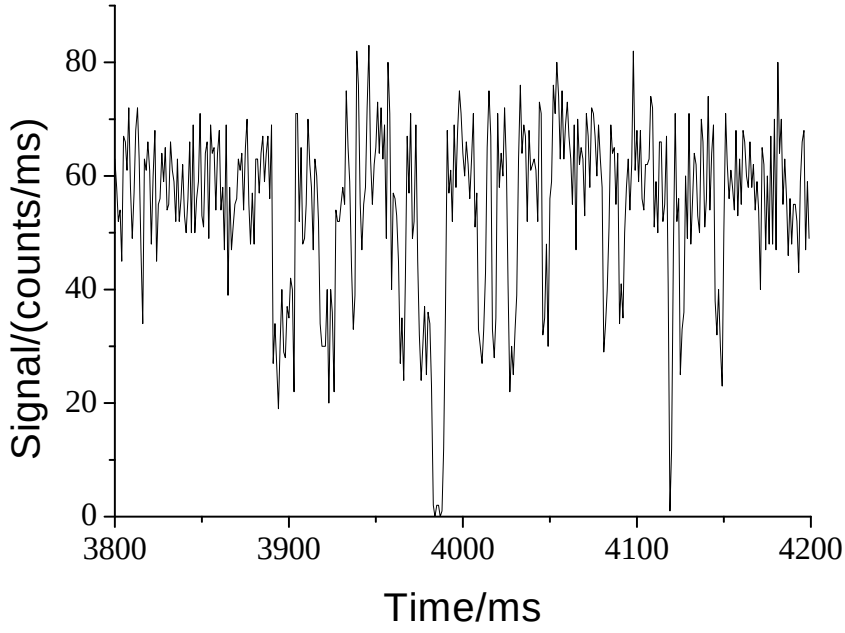

Fig. B.1: A data trace showing the quantum jumps of two ions. There are two distinct fluorescence levels above background in the fluorescence signal corresponding to both or just one of the ions being in the shelving state.

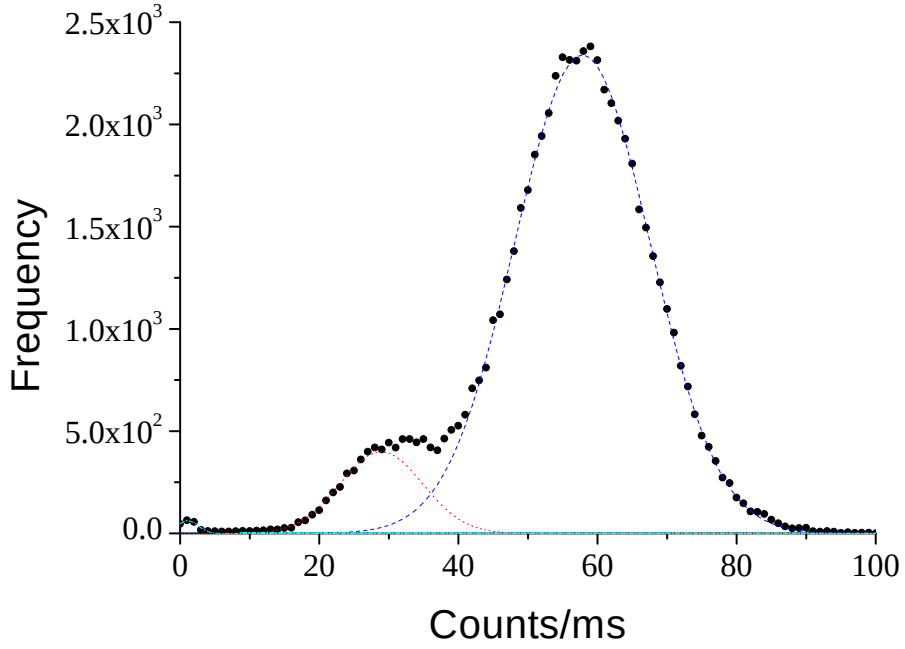

Fig. B.2: The photon statistics of two ions. The graph is produced by passing the raw data shown in figure B.1 through the program shown in Appendix A. There are three peaks corresponding to the fluorescence levels of zero (background count rate), one and two ions.

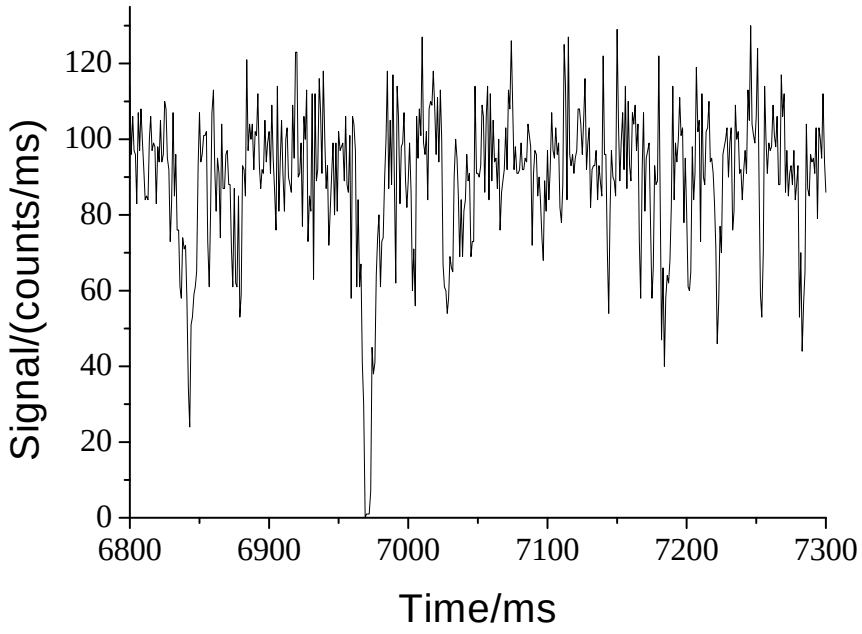

Fig. B.3: A data trace showing the quantum jumps of three ions. Here there are three distinct fluorescence levels above background corresponding to three, two or just one of the ions being in the shelving state.

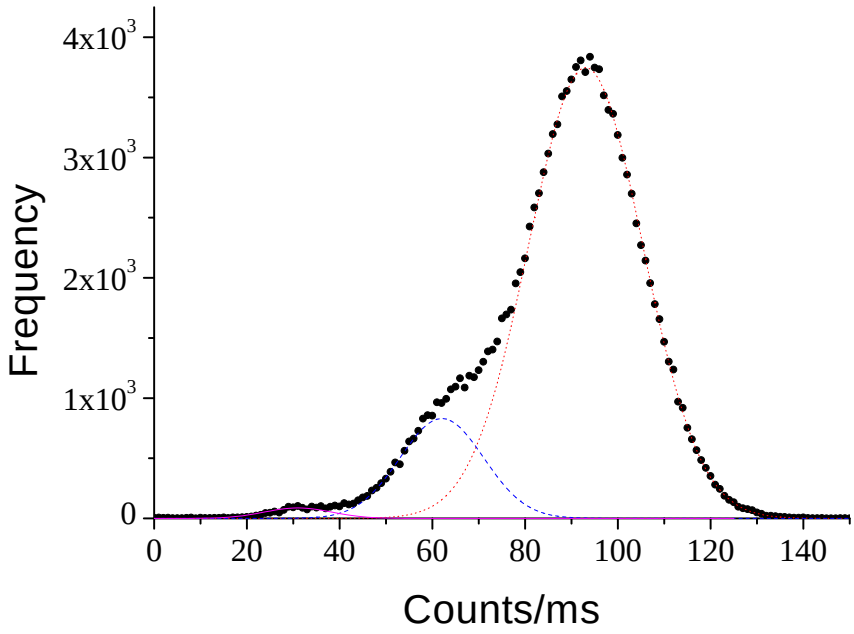

Fig. B.4: The photon statistics of three ions. The graph is produced by passing the raw data shown in figure B.3 through the computer program shown in Appendix A. There are four peaks corresponding to fluorescence levels of zero (background count rate), one, two and three ions.

APPENDIX C

A Program to Simulate the Axialization of Trapped Ions.

This program simulates the motion of ions in a Penning trap. The axializing drive exerts a force on the ions in the x and $-$y directions of magnitude $i(e/m)C\sin(\omega_c t)$ where all constants have been defined previously and i=x,y. If this force is encorporated into the equations of motion then axialization can be simulated. The program integrates the equations of motion over the time step "w" and plots ion positions at each interval. The final positions of the ions can be stored and plotted.

With a slight modification to the program the path of each ion can be plotted over the complete integration time. This was used to produce the plots for single ions shown in chapter 6 (figure 6.5).

The program is written in Turbo Pascal.

```
$N+,R+,S+ uses dos,crt,graph; const
   numberions = 2;
   w = 1e-9;                    (*start integration interval        *)
   m  = 4.0e-26;
   e  = 1.6e-19;
```

```
   Pi = 3.14;
   x0 = 100e-5;   x_0=  20;      (*Ion start parameters in m and m/s *)
   y0 = 100e-5;   y_0=  20;
   z0 = 100e-5;   z_0=  20;
   QQ = 5.768e-3;
   U  = 10;                      (*Trap parameters                   *)
   R0sq = 5.1e-5;
   B    = 1;
   Wzsq = 4*e*U/m/R0sq;          (*axial motion                      *)
   Wc   = e*B/m;                 (*cyclotron motion                  *)
   startmagnif= 100000;          (*Screen parameters                 *)
   taillength = 100;
   saveskip   = 30;              (*Data file saving parameters       *)
   horlength  = 25;
   screentext = true;
   directory  = 'f:\data\';                 (*defines directory path  *)
   nameout    = +directory+'manyax.out';(*output filename             *)
var
   i,magnif : longint ;
   t,h,Wm,Wi,Wcmod,gammaWc,gammaWm,gammaz,alpha,beta,C : extended;
   xx_,yy_,x,x_,y_,y,z,z_,initionr: array [1 .. numberions] of extended;
   grm,grd,originx,originy,q,k,j,n,l :integer;
   answer,option : char;
   madefile : boolean;

(*         Equations of Motion                          *)
function x__:extended; var a: integer; coulomb : extended; begin
```

```
  coulomb := 0;
  for a := 1 to numberions do if a <> j then
  coulomb:= coulomb + QQ*(x[j]*x[a]/sqr(initionr[a]/initionr[a]));
  x__ := 0.5*Wzsq*x[j] + Wc*y_[j] + coulomb - (beta/2)*x_[j] +
                          (alpha/2)*y[j] + e/m*x[j]*C*sin((Wc)*t);
end; function y__:extended; var a: integer; coulomb : extended;
begin
  coulomb := 0;
  for a := 1 to numberions do if a <> j then
  coulomb:= coulomb + QQ*(y[j]*y[a]/sqr(initionr[a]/initionr[a]));
  y__ := 0.5*Wzsq*y[j] - Wc*x_[j]+ coulomb -(beta/2)*y_[j] -
                           (alpha/2)*x[j]- e/m*y[j]*C*sin((Wc)*t);
end; function z__:extended; var a: integer; coulomb : extended;
begin
  coulomb := 0;
  for a := 1 to numberions do if a <> j then
  coulomb:= coulomb + QQ*(z[j]*z[a]/sqr(initionr[a]/initionr[a]));
  z__ := -Wzsq*z[j] + coulomb - 2*gammaz*z_[j];
end; begin
  clrscr;
  writeln('_____________________________________________________________ ');
  writeln('|                                                            |');
  writeln('|  Options:                                                  |');
  writeln('|  e   : exit                                                |');
  writeln('|  +/- : zoom in/out                                         |');
  writeln('|  s/f : slower/faster integration                           |');
  writeln('|  m/l : more or less coupling                               |');
```

```
  writeln('|  d   : create file manyax.out of (x,y,z) at that time   |');
  writeln('|  p   : panic button kills all ions                      |');
  writeln('|                                                         |');
  writeln('|                                                         |');
  writeln('|_________________________________________________________|');
  writeln('  Press a key to start  ');
  repeat until keypressed;
begin
  writeln('Create datafile ? (y/n)'); read(answer);
  if answer = 'y' then
    begin
      assign(output,nameout);
      rewrite(output);
    end;
    for j := 1 to numberions do
      begin
        x[j]:=x0*(random-0.5);
        x_[j]:=x_0*(random-0.5);
        y[j]:=y0*(random-0.5);
        y_[j]:=y_0*(random-0.5);
        z[j]:=z0*(random-0.5);
        z_[j]:=z_0*(random-0.5);
      end;
grd := detect;
initgraph(grd,grm,'c:\tp\bgi' );
originx:= round(getmaxx/2); originy := round(getmaxy/2); for j:= 1
to numberions do i:=0; q:=0; l:=0; t:=0; k:=0;h:=w;
```

```
magnif:=startmagnif; (*                          Define variables
*)
   C := 1e2;             (* couplingstrength (prop. to drive voltage) *)
   Wi:= Sqrt(Wc*Wc - 2*Wzsq);     (*radial frequency in rotating frame*)
   Wcmod:= (0.5*Wc) + Wi;         (*modified cyclotron frequency      *)
   Wm   := (0.5*Wc) - Wi;         (*magnetron frequency               *)
   gammaWm:= -2e1;                      (*damping rates of magnetron, *)
   gammaWc:= -10*gammaWm;               (*cyclotron and               *)
   gammaz := gammaWm;                   (*axial motions               *)
   beta   := 2*(gammaWm+gammaWc);
   alpha  := (2*(Wcmod*gammaWm+Wm*gammaWc));
repeat
  for j := 1 to numberions do
    begin
      for n:=1 to numberions do if j <> n then
      initionr[n] := Sqrt(Sqr(x[n] - x[j]) + Sqr(y[n] - y[j])+
                                            Sqr(z[n] - z[j]));
      x_[j]  := x_[j]+ h*x__ ;    x[j] := x[j] + h*x_[j];
      y_[j]  := y_[j]+ h*y__ ;    y[j] := y[j] + h*y_[j];
      z_[j]  := z_[j]+ h*z__ ;    z[j] := z[j] + h*z_[j];
      putpixel(originx+round(x[j]*magnif),originy-round(y[j]*magnif),cyan);
    end;
    t := t + h;
    if round(i/horlength) = getmaxx then i := 0;
    inc(i);
    if l = taillength then
      begin ClearDevice;
```

```
  l:= 0 ;
end;
inc(l);
if keypressed then
  begin
    option := Readkey;
    if option = 'e' then exit;
    if option = '+' then magnif := magnif*10;
    if option = '-' then magnif := round(magnif/10);
    if option = 'm' then C:= C*10;
    if option = 'l' then C:= C/10;
    if option = 's' then h := h/10;
    if option = 'f' then h := h*10;
    if option = 'p' then exit;
    if option = 'd' then
    if q = saveskip then
      begin
        assign(output,nameout);
        rewrite(output);
       writeln(output,'Penning trap for ',numberions,' magnesium ions');
       writeln(output,'with B =',B,'T, U=',U,'V, R0sq=',R0sq);
       writeln(output,'Coordinates (x,y,z) in meters for all ions');
       writeln(output,'after',t,' secs');
       for j := 1 to numberions do
       writeln(output, x[j],'',y[j],'',z[j]);
       q:=0 ;
       madefile := true;
```

```
      end;
    end;
    inc(q);
    inc(i);
    until false;
    if madefile then close(output);
    closegraph;
end.
```

APPENDIX D

Quadrupole Drive Circuit

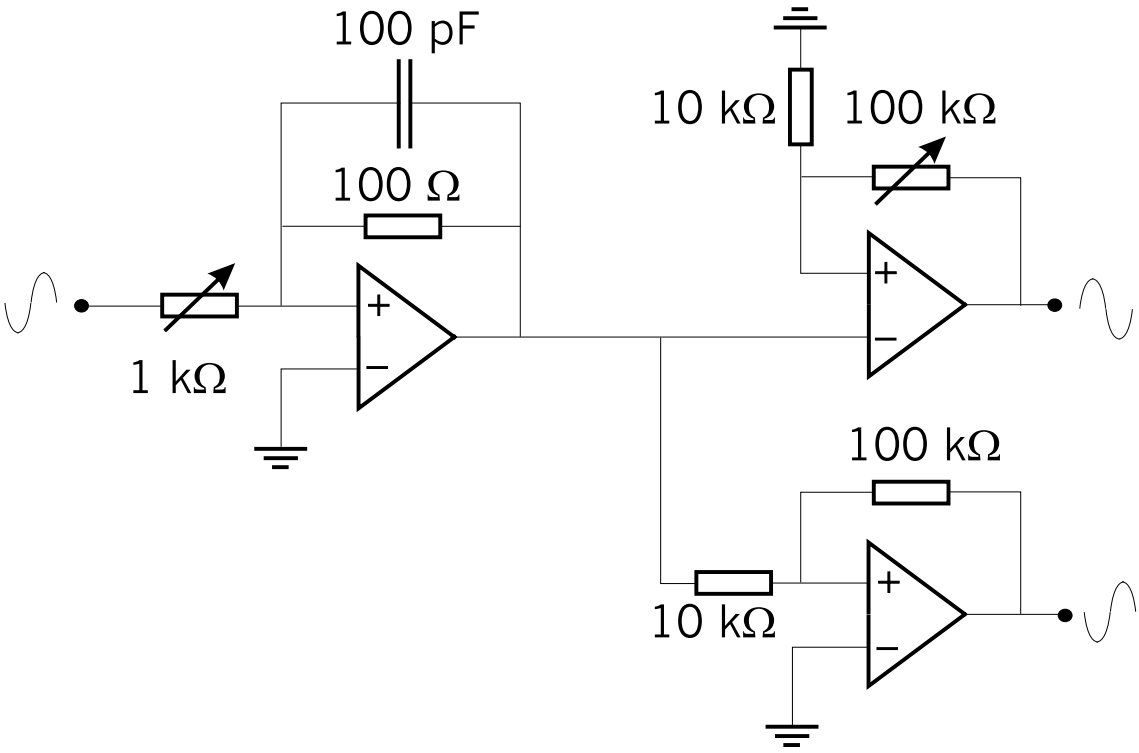

Fig. D.1: The diagram shows the circuit used to generate the axializing drive. The first amplifier controls the gain of the whole circuit. It is designed to pass any signal of $\omega < 2 \times \pi 1.5$ MHz. Two further amplifiers of equal gain, one which is inverting and one which is non-inverting produce two signals which are out of phase by $\pi/2$.